



Lehrstuhl für Elektrische Antriebssysteme und Leistungselektronik
der Technischen Universität München

Model Predictive Control for Electric Drives with Extensive Considerations

Xuezhu Mei

Vollständiger Abdruck der von der Fakultät für Elektrotechnik und Informations-
technik der Technischen Universität München zur Erlangung des akademischen
Grades eines

Doktor-Ingenieurs

genehmigten Dissertation.

Vorsitzender: Prof. Dr.-Ing. Gerhard Rigoll

Prüfer der Dissertation:

1. Prof. Dr.-Ing. Dr. h.c. Ralph Kennel
2. Prof. Dr.-Ing. Fengxiang Wang

Die Dissertation wurde am 10.04.2019 bei der Technischen Universität München
eingereicht und durch die Fakultät für Elektrotechnik und Informationstechnik am
07.07.2019 angenommen.

Acknowledgments

This dissertation is to my parents, Prof. Sheng Mei and Prof. Chunxia Ou, who gave me beautiful life and raised me up to add values into it.

The research in this dissertation was initialized and conducted at the Institute for Electrical Drive Systems and Power Electronics (EAL), Technical University of Munich (TUM), Germany and Quanzhou Institute of Equipment Manufacturing (QIEM), Chinese Academy of Sciences (CAS), China. No part of this work has been plagiarized from unauthorized work and submitted elsewhere for any other degree or qualification, it is all my own work unless reference to the contrary in the text.

My deepest gratitude goes first and foremost to Prof. Ralph Kennel, my supervisor, for his years' long trust, support and guidance. I have come across many obstacles and failures during my doctoral study, and some of them almost made me deny myself and give up trying. Luckily as his student, I am able to learn his humorous and confident way to handle serious topics. And his opening attitude and curiosity towards diversity and understanding of humanity changes my impression of German scientists. His full support and encouraging commends on my ideas and progress is my UPS to chase the technical dream.

I would also like to thank Prof. Fengxiang Wang, my supervisor at QIEM. In the past years, he offered me his cherished experiences of research and gave inspired talks on my project. At work he is so cautious and harsh, while in life he is my brother-like friend. He push me forward to be fearless of different circumstances and build up the leadership, lead me to fight against my weakness and get onto the pace as researcher, rebuild my confidence and forgive my innocence.

I cherished my colleagues and international friendship at EAL. When I was in the sensorless control group, Dr.-Ing. Peter Landsmann and other group members have helped me to understand and solve some problems with simulation and test. After I joined the predictive control group, Dr.-Ing. Felix Rojas and Dr.-Ing. Esteban Fuentes lightened up my passion for work by their Latin American enthusiasm and expressions of new discoveries. Dr.-Ing. Reza Fotouhi has given me suggestions on test bench. Dr.-Ing. Aymen Ayad gave me encouragements during conference and urged me to start writing dissertation. Mohamed Abdelrahem offered me great support on experiments at the final stage of dissertation.

I highly appreciate the support and cooperation in both life and work from the Chinese team at EAL. They are Dr. Jianbo Gao, Dr.-Ing. Zhixun Ma, Dr.-Ing. Zhe Chen, Dr.-Ing. Zhenbin Zhang, Dr.-Ing. Xiaocan Wang, Dr.-Ing. Guangye Si and Dr.-Ing. Xinbo Cai. Dr. Gao is the first one who brought me into the EAL family. His kind personality and intelligence influences

me a lot. Dr.-Ing Zhe Chen spent lots of his time on helping me the fundamentals of electric drive. My first conference paper's inspiration came from Dr.-Ing. Zhixun Ma. Dr.-Ing. Xiaocan Wang cared a lot about me at my doctoral starting phase. And they all shared me plenty of their knowledge with patience and no reservation. Together with them, I gained important experiences and had countless unforgettable memories.

In China, I also joined a harmonic family-like working group, in which we work hard, develop fast and treat each other with sincere heart. They are Dr. Peng Tao, Dr. Anjun Xia, Dongliang Ke, Xinhong Yu, Yiyang Huang, Long He and other engineers in the lab as well as our very helpful master students. And I would also like to thank the peer scholars from other institutes who offer me suggestions and discussion. They are Dr. Xiaoquan Lu, Dr.-Ing. Wei Xie and Dr. Yuanlin Wang.

Also, I would like to thank my mentor, Mr. Manfred Popp, who took me as mentee through alumni program, and Prof. Maarten Kamper from Stellenbosch University as well as Mr. Joubert Martins from South Africa, who handed over me this "chocolate box" by forwarding my Ph.D. application to EAL and thereafter switched on my wonderful journal to Germany by chance.

There are some more people in both Germany and China who gave me influential instructions and encouragement to overcome difficulties. I feel sorry that I could not list all their names here because of limited space.

Following are some important belief-turning sentences that support me to live thorough my last years, as a doctoral candidate, and a female in engineering:

"You are your own project manager."—Prof. Dr.-Ing. Ralph Kennel

"We are a team, we never leave anyone behind."—Prof. Dr.-Ing. Fengxiang Wang

"One can never fail on the thing that he loves."—Dr. -Ing. Felix Rojas

"Be brave, be unique and be yourself."— my father

"Raising a daughter is a lifelong mission and treasure."— my mother

Again, I would like to give my heartfelt appreciation and gratitude to my dearest family, friends, supervisors and all colleagues. Without their persistent love and support, I will not be able to go so far as today I can achieve. And I really miss my loving grandfather in heaven, who helped me to construct my first four-wheel drive model when I was in primary school, and who was the most excited and happiest one before my departure for Germany. Last but not least, I am thankful and proud of my Chinese motherland and the German government, who offer me this chance and financial support to study between countries.

Xuezhu Mei
Munich, Germany
March 21, 2019

Abstract

This work is an extensive research on model predictive control for electric drives. Following are its main contributions: several typical conventional model predictive control strategies for electric motors with both finite control sets and continuous references are compared and analyzed; based on traditional finite control set predictive control, two quasi-continuous predictive control strategies are introduced, which maintain the cost function while generating continuous voltage references for SVPWM; a series of control set minimization strategies are proposed, which can simplify the control and reduce calculation efforts; a disturbance observer for torque disturbance inhibition are designed and investigated on different predictive control systems; two solutions of predictive control without weighting factor, which are easier for implementation and conceptually intuitive, are realized.

***Index Terms*—Predictive control, continuous, finite control set, disturbance observer, weighting factor, voltage source inverter, electric drives.**

Zusammenfassung

Diese Arbeit ist eine umfassende Untersuchung der modellprädiktiven Regelung für elektrische Antriebe. Folgende sind ihre wesentlichen Beiträge: Eine Reihe von prädiktive Regelungsstrategien für Elektromotoren mit sowohl endlichen Steuerungssätzen als auch kontinuierlichen Referenzen werden verglichen und analysiert. Basierend auf der herkömmlichen modellprädiktiven Regelung mit endlichen Steuersätzen werden zwei quasi-kontinuierliche modellprädiktive Regelungsstrategien eingeführt, die die Kostenfunktion aufrechterhalten und gleichzeitig kontinuierliche Spannung für Raumzeigermodulation (SVPWM) erzeugen. Eine Reihe von Strategien zur Minimierung von Sollwerte, die die Regelung vereinfachen und den Rechenaufwand reduzieren, werden vorgeschlagen. Einen Störungsbeobachter für die Unterdrückung der Drehmomentswelligkeit wird entworfen und auf verschiedenen modellprädiktiven Regelungssystemen untersucht. Zwei Lösungen zur prädiktiven Regelung ohne Gewichtungsfaktor, die einfacher zu implementieren und konzeptionell intuitiv sind, werden realisiert.

Table of Contents

Acknowledgments	I
Abstract	III
Zusammenfassung	V
1 Introduction	1
2 Background and Motivation	5
2.1 Three-phase System Notation and Its Space Vector Equivalence	5
2.2 AC Electrical Motors and Their Mathematical Models	7
2.2.1 Induction Machine (IM)	7
2.2.2 Surface-mounted Permanent Magnet Synchronous Machine (SPMSM)	9
2.2.3 Interior Permanent Magnet Synchronous Machine (IPMSM)	10
2.3 Two-level Voltage Source Inverter (VSI) and Its Model	10
2.4 Conventional Control Strategies for Electrical Drives	12
2.4.1 Field Oriented Control	12
2.4.2 Direct Torque Control	15
2.5 Model Predictive Control: A Cutting-edge Drive Strategy	19
2.6 Test Bench Description	20
2.7 Motivation and Contribution of This Work	23
3 MPC for Electrical Drives	25
3.1 Classification and Comparison of MPC	25
3.2 Time Order and Compensation	27
3.3 Finite-control-set Predictive Torque Control	28
3.3.1 Estimation and Prediction	28
3.3.2 Cost Function Optimization	30
3.3.3 Simulation and Experimental Verification	30
3.4 Finite-Control-Set Predictive Current Control	38
3.4.1 Estimation and Prediction	38
3.4.2 Cost Function Optimization	39

3.4.3	Simulation and Experimental Verification	40
3.5	Deadbeat MPC	44
3.5.1	Continuous Reference Voltages Prediction	46
3.5.2	Simulation and Experimental Verification	48
3.6	Conclusion	55
4	Increased FCS-Continuous MPC	57
4.1	Dichotomy-based IFCS-PCC	57
4.1.1	Fan Dichotomy-based Method	57
4.1.2	Circular Dichotomy-based Method	60
4.2	Simulation Verification	60
4.3	Conclusion	68
5	Reduced FCS-MPC	69
5.1	Dichotomy-based RFCS-PCC	69
5.1.1	Simulation Verification	70
5.2	Switching-minimized RFCS-PCC	74
5.2.1	Simulation Verification	74
5.3	Deadbeat Triple RFCS-PCC	78
5.3.1	Simulation and Experimental Verification	79
5.4	Deadbeat Double RFCS-PCC	86
5.4.1	Simulation and Experimental Verification	86
5.5	Deadbeat Null RFCS-PCC	94
5.5.1	Simulation and Experimental Verification	95
5.6	Conclusion	107
6	MPC with Disturbance Observer	109
6.1	DO Basics	109
6.2	Torque Disturbance Observer for Electric Drives	110
6.2.1	Torque Disturbance Observer Design	110
6.2.2	Stability Analysis	112
6.3	Deadbeat PCC with Torque Disturbance Observer	113
6.3.1	Simulation and Experimental Verification	113
6.4	FCS-PTC with TDO	120
6.4.1	Maximum Torque Per Ampere Implementation	120
6.4.2	MTPA-based FCS-PTC with TDO	121
6.4.3	Simulation and Experimental Verification	121
6.5	Conclusion	130
7	FCS-MPC without Weighting Factor	131
7.1	Sequential FCS-PTC	131
7.1.1	Conventional Sequential FCS-PTC	132
7.1.2	Sequential FCS-PTC with Varying Control Sequence	133
7.1.3	Simulation and Experimental Verification	136
7.2	Parallel FCS-PTC	143

7.2.1	Full-Vectors Parallel FCS-PTC	144
7.2.2	Simulation and Experimental Verification	144
7.2.3	Deadbeat Triple Parallel RFCS-PTC	154
7.2.4	Simulation and Experimental Verification	154
7.2.5	Deadbeat Double Parallel RFCS-PTC	159
7.2.6	Simulation and Experimental Verification	159
7.3	Conclusion	164
8	Summary and Outlook	165
8.1	Conclusion	165
8.2	Future Work	167
A	Nomenclature	169
B	Pseudo Codes	173
C	List of Publications	177
	List of Figures	179
	List of Tables	187
	Bibliography	189

CHAPTER 1

Introduction

In 1834, the first electric machine prototype was invented by the German-speaking Prussian Moritz Hermann Jacobi. Since then, this machine has been serving to convert electrical and mechanical energy from each other at all industrial and domestic areas [1]. After almost two centuries' development, various types of electric machines have been invented. With respect to different machines and application requirements, and as the continuous improvement of controllers and electronics components, the system (i.e. electric drive system) as well as corresponding control techniques of electric machines have been an everlasting interest of electrical engineers and control scientists.

The history of the electric drives has experienced the following evolutions:

- ***Change 1- From Analog Control Era to Digital Control Era.***

Before the micro control unit (MCU) was applied as the controller of electric machine, all regulations in electric drive systems are realized by operational amplifiers (OPA). The analog control system is conceptually intuitive and its control signal flow is easy to be understood. However, the fixed and complex circuit makes it inflexible and non-universal. Moreover, the control performance is sensitive to the component characteristics and physical environmental factors such as temperature, humidity, voltage and mechanical vibration. In contrast, the MCU-cored digital control system contains hardware circuit with high standardization, low cost of manufacturing, and is unsusceptible to temperature-caused component characteristic drift. Its software nature of control makes it more flexible, stable and reliable. What's more, it enables the complicated logic judgement and other operations. The application of digital control of electric drives, as computer based control, requires discretization and A/D and/or D/A conversions. Simultaneously, peripheral control hardware and technology corresponding to digital control, such as pulse width modulator (PWM), are therefore designed and developed [2]. Discrete power converters with high frequency switching components, such as IGBT and MOSFET based voltage source inverter (VSI) and current source inverter (CSI) are invented and applied.

- **Change 2- From Differentiated Control to Unified Control.**

As we know that direct current (DC) motors have separate torque (armature) and flux (field) producing windings, thus the control of DC is linear and simple. Alternative current (AC) motors had not been capable of adjustable or smooth speed varying control until the 1970s, when field oriented control (FOC), which decouples the air-gap flux and electromagnetic torque producing components, was introduced by Hasse and Blaschke [1, 3]. This was realized by reference frame transformation and electric circuitry equivalence [4]. Since then, the control of AC machines has become as easy as the control of DC machines and it is equivalent to the control of DC machines under FOC. Thus, the controls of DC and AC machines were unified [5]. As a result, AC motors are widely used and serve as the main machines for high performance servo control systems nowadays [6].

- **Change 3- From Open Loop Control to Close Loop Control.**

The transform process from open loop to close loop control happens parallelly with the discovery of decoupled torque and flux producing components. And it bases also on the space vector notation as well as the theories of reference frame transformation of the machine variables. The coupled sinusoidal currents that contain both torque and flux information could not be fed back to the system. Instead, frequency proportional voltage signal can be controlled in open loop manner to achieve speed variation, which is named the 'V/f control' [7, 8]. This control satisfies the situations when rough control is enough, such as fans and pumps. However, when faster torque and speed response is required, close loop control should be applied. With the direct and quadratic current components corresponding to flux and torque producing currents in the synchronous reference frame, which are constant in steady state, both the currents and rotor speed/position are fed back to the control system. Thus, for most high performance varying speed regulation (VSR) and all servo drives systems, current sensors are necessary and speed encoders are optional, depending on whether the close loop control is encoderless [9–12].

- **Change 4- From Linear Control to Nonlinear Control.**

In close loop control system, the essence of control is to realize a convergence mechanism enabling the real machine to track its reference, which is either torque, speed, or position. PI and PID controller are typical and classic controllers that can realize this tracking process in linear way but with limited bandwidths [13, 14]. For cascade controls such as FOC, in order to guarantee the best control performance, the inner PI control loops should behave at least 10 times faster than the outer PI control loop. Thus, the linear based methods, though simple in concept, have limitations. Moreover, the P, I and D parameters require tuning efforts, which is tedious and irregular for inexperienced workers. An alternative is nonlinear hysteresis based control such as direct torque control (DTC) proposed by Depenbrock and Takahshi in 1984 [15–17], which has faster torque response and is less sensitive to parameter variation. However, it has larger total harmonics distortion (THD) and large torque ripples. In the past two decades, the development of modern control theories in industrial control bring more different nonlinear control methods into the areas of electric drives. This includes artificial intelligence (AI) based control such as fuzzy logic control and neural network control [18–20]. Self-adaptive based control and sliding mode variable structure control [21, 22]. Most of these are optimized control strategies or compensation methods based on the fundamental structures of FOC or DTC,

and have complex algorithms. Model predictive controls (MPC) including genetic predictive control (GPC) [23] and deadbeat control [24, 25] is a class of emerging nonlinear control methods with distinct basic structures as FOC or DTC [26, 27]. Because electric machines are highly nonlinear systems, for nonlinear controls, no matter they are 'white box' based such as DTC and MPC or 'black box' based such as AI controls, require correct design to enable the precise control fitting to the real system model.

A typical close loop digital control system of electric drives is shown in figure. 1.1 [6].

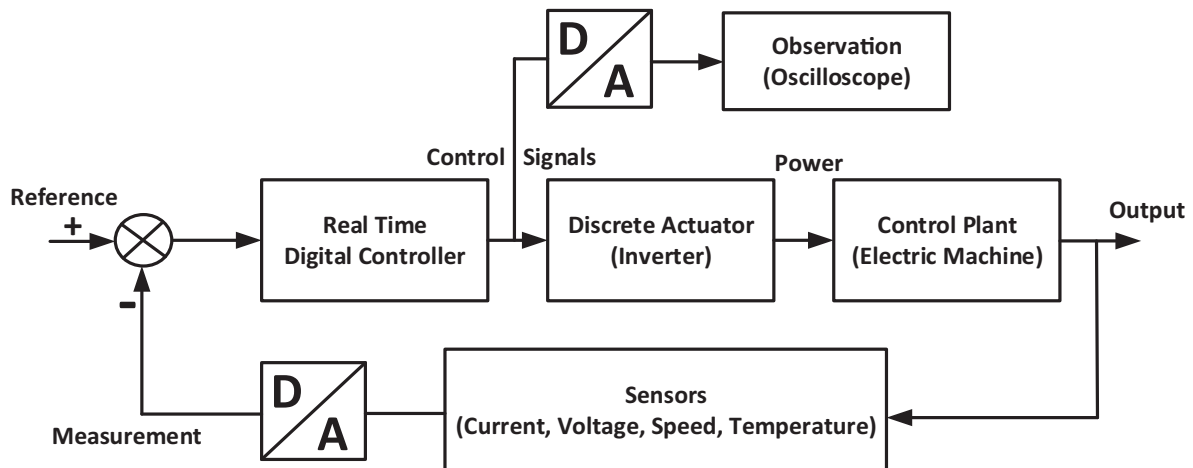


Figure 1.1: Close Loop Control System for Electrical Machine

Figure. 1.1 shows that except the controlled electric machine, there are three parts in the system: digital controller, actuator and sensors. Controllers are usually based on MCU, DSP or FPGA. Actuator refers to inverter which realizes the DC-AC conversion. Sensors are used to measure real machine output indexes such as speed, currents, voltage, and temperature, which may not be all compulsory. These signals, after DA conversion, are compared with the reference. Their error is taken as the feedback to the controller for further regulation and adjustment. In some situation, analog signals are needed for user observation. This work is not interested in the control of generators, so the term 'electric machine', if not separately clarified, refers merely to motor.

The main problems and therewith trend in the control of electric drives are:

- **1. Calculation burden reduction.**

As the development of semi-conductor industry, the calculation speed of micro controllers is increasing exponentially. However, the demanding control performances with various functions and advanced algorithms are still challenging the calculation ability of hardware. Thus, within the current hardware limit, and to realize highest performance with lowest cost, from the system control point of view, control strategies considering calculation optimization are required to reduce calculation redundancy [28–30].

- **2. Growing concerns on reliability.**

To enable wide and durable operation of the drives in modern servo control systems, reliability should be guaranteed. This refers to both the controllability with respect to

varying switching points of inverter and the stability against parameter deviations. As a result, control system with model of adaptivity and robustness is also under research [31–33].

- **3. Demanding steady and dynamic control performances.**

To achieve steady operation and precise control of electric motors, and assure high industrial indexes such as wide speed ratio and short regulation time, control system, that is less sensitive to disturbances influence, especially with varying load rejection ability, is required [34–36].

- **4. Combination of multiple control strategies.**

Due to the wide application conditions and tremendous quantity, electric drive systems should be used in harsh environments with low cost and high efficiency. A typical example is the trend on electric drives without encoder. Thus, in many literatures [37–39], encoderless control is also applied and combined with the core control strategy of this work, i.e. MPC.

With the analysis of the history and trend of modern electric drive controls, and in order to further fill in the blanks of MPC. In this work, MPCs, especially finite control set predictive current control (FCS-PCC) [40,41] is selected as the research target. Further improvements and extensions are made into the controller design. Meanwhile, novel concepts of implementation are introduced for both the control systems with and without PWM and the system with and without cost function.

This work is organized as follows: in the consecutive chapter, the fundamental components in electric drive systems, two AC machines as well as their conventional control methods are reviewed, and MPC is introduced. In chapter 3, conventional MPC methods are compared and the mostly used ones are shown and analyzed. Chapter 4 introduces two variations of continuous FCS-MPC with PWM. Chapter 5 shows several realizations of FCS-MPCs with reduced control set for calculation reduction and simplicity. In chapter 6, to improve system torque disturbance rejection ability, disturbance observer is further added to both FCS-MPC and continuous MPC. And chapter 7 is the highlight of this work, i.e. two ways of FCS-MPCs without weighting factor in cost function. Finally, the work is concluded and future prospect is given in chapter 8.

CHAPTER 2

Background and Motivation

In order to prepare related background for this work and unify conventions, in this chapter, fundamentals of electric drive theories including control reference frame transformation with machine variable space vectors, machine and inverter equivalent mathematics model expressions as well as conventional and novel machine control strategies are reviewed and explained.

2.1 Three-phase System Notation and Its Space Vector Equivalence

The coils of three phase AC electrical motors are equivalently displaced in space as depicted in figure 2.1 [1], with 120° interval in phase from each other. Stator currents are used as an example.

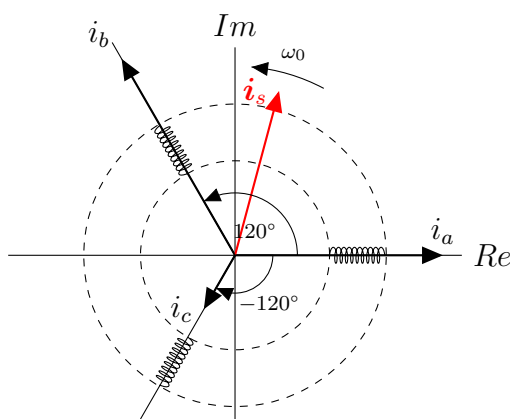


Figure 2.1: Space-vector notation of three-phase currents

These three phase component, with an electrical angular speed of ω_0 , is defined in the stator fixed stationary reference frame as:

$$i_a = I \cdot \sin(\omega_0 \cdot t) \quad (2.1)$$

$$i_b = I \cdot \sin(\omega_0 \cdot t + \frac{2\pi}{3}) \quad (2.2)$$

$$i_c = I \cdot \sin(\omega_0 \cdot t + \frac{4\pi}{3}) \quad (2.3)$$

Their synthetic vector is gained with the introduction of the a-operator as follows:

$$\mathbf{i}_s = i_a + a \cdot i_b + a^2 \cdot i_c \quad (2.4)$$

$$a = e^{j \cdot \frac{2\pi}{3}} = \frac{-1}{2} + j \cdot \frac{\sqrt{3}}{2} \quad (2.5)$$

These three phase components are further expressed within a rectangular two-phase coordinate system in figure 2.2, when the real and imaginary axes are noted as α and β . This is realized by space vector equalization by replacing three-phase components to the two-phase ones as shown in (2.6). Thus, the α - β expression of stator currents are derived as (2.7) and (2.8).

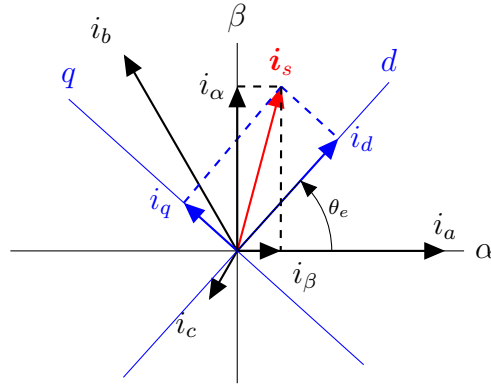


Figure 2.2: Space-vector notation of two-phase currents

$$\mathbf{i}_s = i_\alpha + j \cdot i_\beta \quad (2.6)$$

$$i_\alpha = \frac{2}{3} \cdot (i_a - \frac{1}{2} \cdot i_b - \frac{1}{2} \cdot i_c) \quad (2.7)$$

$$i_\beta = \frac{2}{3} \cdot (\frac{\sqrt{3}}{2} \cdot i_b - \frac{\sqrt{3}}{2} \cdot i_c) \quad (2.8)$$

When written in the matrix form, Clarke transformation is obtained.

$$\begin{pmatrix} i_\alpha \\ i_\beta \end{pmatrix} = \frac{2}{3} \begin{pmatrix} 1 & -0.5 & -0.5 \\ 0 & 0.5\sqrt{3} & -0.5\sqrt{3} \end{pmatrix} \cdot \begin{pmatrix} i_a \\ i_b \\ i_c \end{pmatrix} \quad (2.9)$$

Its inverse form, inverse Clarke transformation, is shown in (2.10):

$$\begin{pmatrix} i_a \\ i_b \\ i_c \end{pmatrix} = \begin{pmatrix} 1 & 0 \\ -0.5 & 0.5\sqrt{3} \\ -0.5 & -0.5\sqrt{3} \end{pmatrix} \cdot \begin{pmatrix} i_\alpha \\ i_\beta \end{pmatrix} \quad (2.10)$$

It should be noticed that (2.9) and (2.10) are not the only forms of Clarke transformation encountered in literature. Hereinbefore mentioned form is based on the vector magnitude equivalence criteria. However, when based on the magnetomotive force (MMF) balance criteria, the matrices (2.9) and (2.10) are multiplied by 1.5 and $\frac{2}{3}$ respectively. And when based on the apparent power balance criteria, the matrix (2.9) and (2.10) are multiplied by $\sqrt{\frac{3}{2}}$ and $\sqrt{\frac{2}{3}}$ respectively.

In order to transform AC components of the current vector in the stator frame into DC signals, formulas of further transformation to a field-fixed revolving reference frame, i.e. Park transformation, are provided in (2.11). The revolving reference frame, d - q frame, is also illustrated in figure 2.2, with θ_e as the angle difference against the α - β frame. This angle is chosen to be rotor flux angle, with e representing "excitation".

$$\begin{pmatrix} i_d \\ i_q \end{pmatrix} = \begin{pmatrix} \cos(\theta_e) & \sin(\theta_e) \\ -\sin(\theta_e) & \cos(\theta_e) \end{pmatrix} \cdot \begin{pmatrix} i_\alpha \\ i_\beta \end{pmatrix} \quad (2.11)$$

Similarly, it also has inverse form:

$$\begin{pmatrix} i_\alpha \\ i_\beta \end{pmatrix} = \begin{pmatrix} \cos(\theta_e) & -\sin(\theta_e) \\ \sin(\theta_e) & \cos(\theta_e) \end{pmatrix} \cdot \begin{pmatrix} i_d \\ i_q \end{pmatrix} \quad (2.12)$$

Other vectors of variables such as voltages, flux linkages can be transformed similarly.

2.2 AC Electrical Motors and Their Mathematical Models

Three different AC motors are introduced and implemented in this work. Below is a review of their mathematics models in both α - β and d - q reference frames.

2.2.1 Induction Machine (IM)

Figure 2.3 is a simplified physical model of a three phase squirrel-cage asynchronous machine (ASM) or induction machine (IM) [7]. It only has windings on the stator, and the rotor back electromotive field (EMF) is induced through the stator windings. Thus, the rotor cage bars can

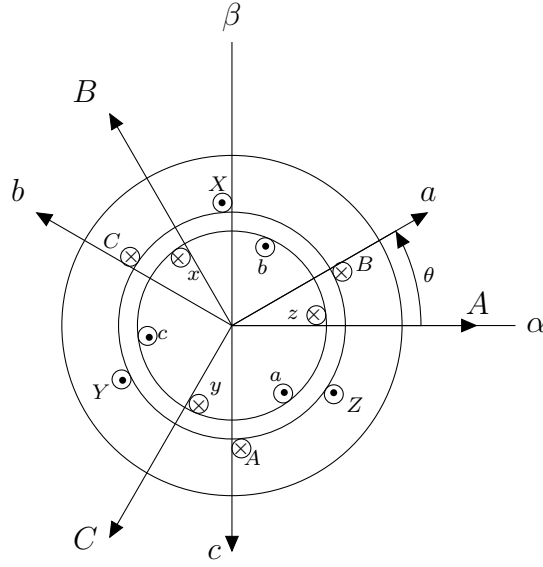


Figure 2.3: Squirrel-cage induction machine model

be equivalently considered as windings having same distribution as the stator, with a slightly speed lag to the stator field.

IM model in α - β frame is expressed with following classic set of equations [42]:

$$\mathbf{v}_s = R_s \mathbf{i}_s + \frac{d\boldsymbol{\psi}_s}{dt} \quad (2.13)$$

$$0 = R_r \mathbf{i}_r + \frac{d\boldsymbol{\psi}_r}{dt} - j\omega_e \boldsymbol{\psi}_r \quad (2.14)$$

$$\boldsymbol{\psi}_s = L_s \mathbf{i}_s + L_m \mathbf{i}_r \quad (2.15)$$

$$\boldsymbol{\psi}_r = L_r \mathbf{i}_r + L_m \mathbf{i}_s \quad (2.16)$$

$$T_e = \frac{3}{2}p(\boldsymbol{\psi}_s \times \mathbf{i}_s) = \frac{3}{2}p(\psi_{\alpha s} i_{\beta s} - \psi_{\beta s} i_{\alpha s}) \quad (2.17)$$

(2.13) and (2.14) are the stator and rotor voltages equations. Because the rotor bars are short-circuited, rotor voltage is 0. ω_e is the rotor electrical speed, which is different from mechanical speed ω_m with a multiplication of pole pairs number p as in (2.18):

$$\omega_e = p \cdot \omega_m \quad (2.18)$$

(2.15) and (2.16) are the stator and rotor fluxes equations including the self inductance and mutual or magnetic inductance. (2.17) calculates the mechanical electromagnetic torque, which is independent of the reference frame of quantities.

Considering the load torque and inertia of rotor, the mechanical differential equation connects the electrical system to the mechanical system. The difference between output electromagnetic torque and input load torque to the rotor shaft decides the acceleration of rotor speed as:

$$J \frac{d\omega_m}{dt} = T_e - T_l \quad (2.19)$$

2.2.2 Surface-mounted Permanent Magnet Synchronous Machine (SPMSM)

Figure 2.4 is a simplified physical model of a surface-mounted permanent magnet synchronous machine (SPMSM). As can be seen from this figure, the permanent magnet is mounted on the outer surface of the rotor. It has extreme small value of magnetic permeability, i.e. large magnetic reluctivity, which is closed to the value of air. Therefore, the magnet can be equally considered as a pair of air-core field windings. With the N direction as the α direction, the rotor inductance in vector form, namely, the inductance tensor, can be expressed as:

$$\mathbf{L}_s^s = \begin{bmatrix} L_s & 0 \\ 0 & L_s \end{bmatrix} \quad (2.20)$$

where L_s is the stator inductance.

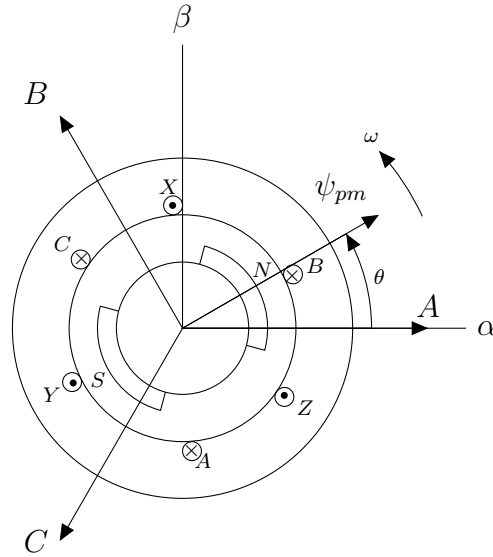


Figure 2.4: Surface-Mounted Permanent Magnet Synchronous Machine

SPMSM model is also represented in α - β frame with following stator voltage and flux equations [43]:

$$\mathbf{v}_s = R_s \mathbf{i}_s + \frac{d\boldsymbol{\psi}_s}{dt} \quad (2.21)$$

$$\boldsymbol{\psi}_s = L_s \mathbf{i}_s + \boldsymbol{\psi}_{pm}^s \quad (2.22)$$

Since rotor side is permanent magnet, its voltage equation is not required for control purpose. And the permanent magnet flux $\boldsymbol{\psi}_{pm}^s$ is transformed from rotor coordinate value $\boldsymbol{\psi}_{pm}^r$ to its stator correspond as:

$$\boldsymbol{\psi}_{pm}^s = \mathbf{C} \boldsymbol{\psi}_{pm}^r = \begin{bmatrix} \cos(\theta_e) & -\sin(\theta_e) \\ \sin(\theta_e) & \cos(\theta_e) \end{bmatrix} \begin{bmatrix} \psi_{pm} \\ 0 \end{bmatrix} \quad (2.23)$$

The electromagnetic torque is not machine type sensitive, therefore, its equation is same as (2.17).

2.2.3 Interior Permanent Magnet Synchronous Machine (IPMSM)

Figure 2.5 is a simplified physical model of an interior permanent magnet synchronous machine (IPMSM). Similar as SPMSM model, the magnet can also be equally considered as a pair of air-core field windings. However, being different from SPMSM, the stator inductance is not equally distributed because the iron core's magnetic permeability is much larger than air and permanent magnet. Therefore, the air gap reluctivity in the N pole magnetic direction, i.e. d axis, is larger than that of q axis, rendering $L_d < L_q$.

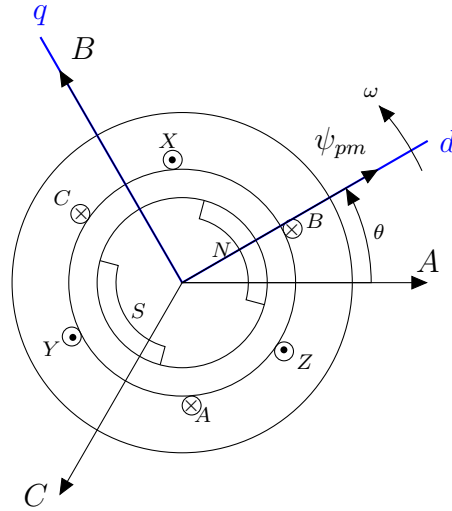


Figure 2.5: Interior Permanent Magnet Synchronous Machine

Because of this non-sinusoidal distribution of stator inductance in the circular area, for control simplicity, IPMSM model is represented in d - q frame with following set of stator voltage and flux equations [44]:

$$\begin{cases} u_d = R_s \cdot i_d + \frac{d}{dt}\psi_d - \omega_e \cdot \psi_q \\ u_q = R_s \cdot i_q + \frac{d}{dt}\psi_q + \omega_e \cdot \psi_d \end{cases} \quad (2.24)$$

$$\begin{cases} \psi_d = L_d \cdot i_d + \psi_{PM} \\ \psi_q = L_q \cdot i_q \end{cases} \quad (2.25)$$

Similarly, because the expression of mechanical electromagnetic torque is independent of the reference frame and machine type, based on (2.17) and (2.25), it is given as:

$$T_e = \frac{3}{2}p (\psi_d i_q - \psi_q i_d) = \frac{3}{2} \cdot p [\psi_f i_q + (L_d - L_q) i_d i_q] \quad (2.26)$$

2.3 Two-level Voltage Source Inverter (VSI) and Its Model

The power module to be controlled in this work is the simplest but mostly applied three phase VSI. It is constructed with three half-bridge inverter circuits, each of which corresponds to one phase and is called an arm in the VSI topology as shown in figure 2.6 [45].

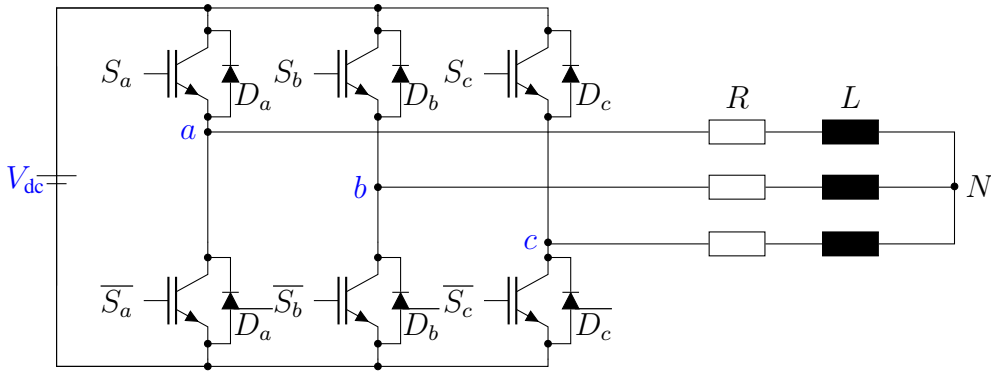


Figure 2.6: Three-phase Two-level VSI.

As is shown in figure 2.6, each arm consists of two switches and each switch is made of an insulated gate bipolar transistor (IGBT) and an anti-parallel freewheeling diode. The load is three phase electrical machines, each phase of whom can be simplified as a pair of series connected resistor R and inductor L . S_x , $x \in (a, b, c)$ and their inverse represent both the IGBT and the complementary switching states of the upper and lower switches on the same arms. And they are given 1 for "on" state and 0 for "off" state. For example, when $S_a = 1$, then it must be $\overline{S}_a = 0$. In real hardware, to prevent short-circuit, dead time is added between the switching actions of upper and lower switches, because of the non ideal characteristics of transistors. The state changing from "on" to "off" mode of each switching process is as follows: after upper switch S_a is switched off, the lower freewheeling diode \overline{D}_a is conducted to let the current flows until it declines to 0. When the current reverses, the lower switch \overline{S}_a is switched on. This is because of the inductive characteristic of the load. The larger the load's impedance angle is, the longer the turn on time of freewheeling diode is.

Review the three-phase to space vector transformation, and according to the vector magnitude equivalence criteria based Clark transform as mentioned in previous sections, a single synthetic space voltage vector can be derived as follows:

$$\mathbf{v}_{out} = \frac{2}{3}V_{dc}(S_a + aS_b + a^2S_c) \quad (2.27)$$

For different switching state combinations, the voltages between the switch and neutral point, i.e. phase voltage, and corresponding voltage vectors are shown in table 2.1.

As can be seen from the table, there are two switching states for null vectors. Therefore, only 7 different switching states exist. And from this table, a diagram of spacial voltage vectors of VSI in a hexagon form is shown in figure 2.7. In this figure, the digits in bracket beside each voltage vector represent the switching states of three phases.

Table 2.1 also implies that with different switching states, two non-zero levels ($V_{dc}/3$ and $2V_{dc}/3$) of values for both positive and negative phase voltages are generated by VSI. As a result, three phase half-bridge voltage source inverter is also named as three-phase two-level voltage source inverter.

Table 2.1: Voltages for Different Switching States

S_a	S_b	S_c	v_{an}	v_{bn}	v_{cn}	\mathbf{v}_{out}
0	0	0	0	0	0	0
0	0	1	$-V_{dc}/3$	$-V_{dc}/3$	$2V_{dc}/3$	$\frac{2}{3}V_{dc}e^{j\frac{4\pi}{3}}$
0	1	0	$-V_{dc}/3$	$2V_{dc}/3$	$-V_{dc}/3$	$\frac{2}{3}V_{dc}e^{j\frac{2\pi}{3}}$
0	1	1	$-2V_{dc}/3$	$V_{dc}/3$	$V_{dc}/3$	$\frac{2}{3}V_{dc}e^{j\frac{2\pi}{3}}$
1	0	0	$2V_{dc}/3$	$-V_{dc}/3$	$-V_{dc}/3$	$\frac{2}{3}V_{dc}$
1	0	1	$V_{dc}/3$	$-2V_{dc}/3$	$V_{dc}/3$	$\frac{2}{3}V_{dc}e^{j\frac{5\pi}{3}}$
1	1	0	$V_{dc}/3$	$V_{dc}/3$	$-2V_{dc}/3$	$\frac{2}{3}V_{dc}e^{j\frac{\pi}{3}}$
1	1	1	0	0	0	0

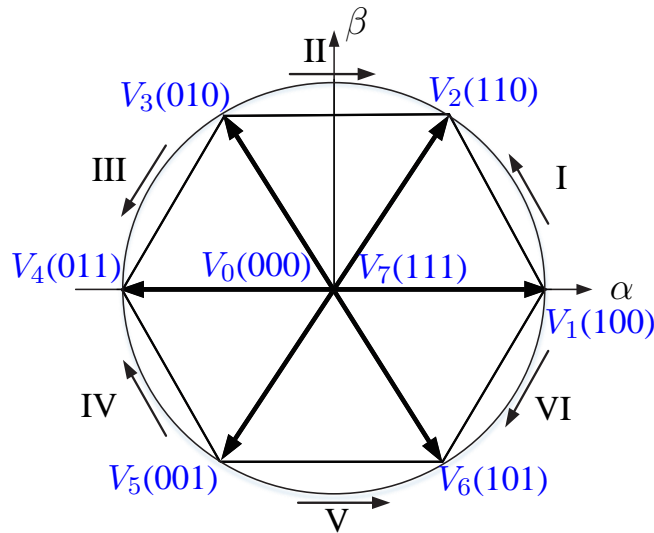


Figure 2.7: Voltage Vectors for VSI.

2.4 Conventional Control Strategies for Electrical Drives

For AC electric drives with high control requirements, two conventional closed loop control strategies have been widely applied by inverter manufacturers in commercial products: Field Oriented Control (FOC) or: Vector Control, and Direct Torque Control (DTC).

2.4.1 Field Oriented Control

From the previous sections, it is known that AC electric machines are highly nonlinear with coupled variables. Therefore, rotor FOC that can achieve separate control of electromagnetic torque and rotor flux, i.e. be equalized to the control of a separately excited DC machine is found [1, 3, 4]. This method orients the AC machine variables onto the rotor flux coordinate, making the torque and rotor flux related control quantities to be decoupled [7]. In contrast to

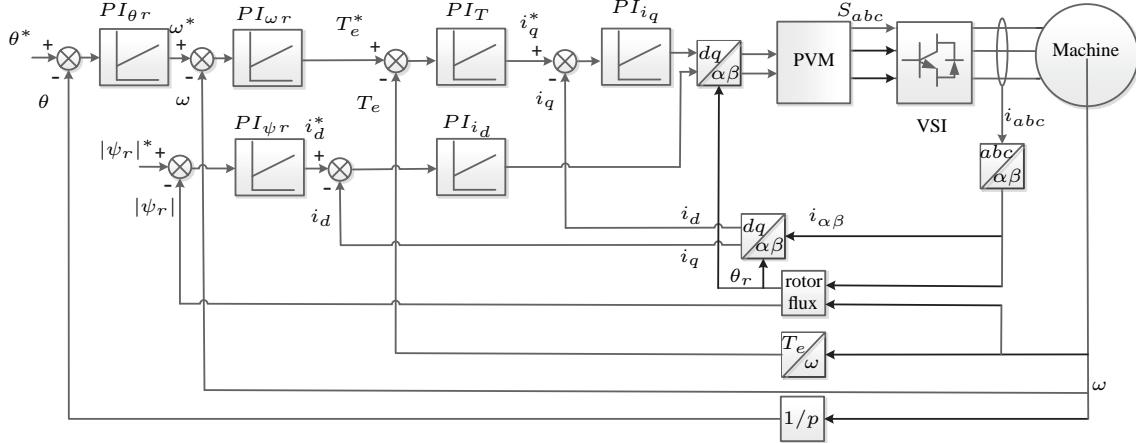


Figure 2.8: FOC Block Diagram.

scalar control, FOC is also called "vector control", because it is the first method that controls machine quantities with their two axis components based vector equivalent circuit model instead of with machine's original three phase physical model.

The schematic of an FOC electric drive system including all control variables are shown in figure 2.8. It is a multiple loops cascaded position control system. The outer loop is rotor angle. For speed control, only the outer position control loop should be removed. For some industrial applications, in which only torque control is concerned, the middle speed control loop can be further removed. As can be seen from figure 2.8, to maintains three phases balance of the machine, only two phases currents are needed to be calculated because the sum of three phase balanced currents are null in light of Kirchhoff laws. And the stator currents are transformed to the rotor flux reference frame through Park transformation. Therefore, the controls are all manipulated in the rotor flux synchronous rotating frame. When the voltage reference values are achieved, an inverse Park transformation is conducted to turn the quantities back to the stator stationary reference frame. Depending on the PWM strategies to be applied, either $\alpha\beta$ voltage references or three phase voltage references after further inverse Clark transformation are given to PWM module to calculate switching signals for VSI to offer deserved power to the machine.

In the following implementation of this work, only speed control is researched and applied to different control strategies.

The basic derivations of the mostly applied FOC method will be explained as follows.

Take the FOC of IM as an example and transform the machine into a rotating reference frame. In order to orient the rotating frame's d axis of the machine variables to the rotor flux vector, the following requirements should be always met:

$$\psi_{rd} = |\psi_r| \quad (2.28)$$

$$\psi_{rq} = 0 \quad (2.29)$$

Substitute the above limitations into (2.13) to (2.16), the d quantity of rotor flux ψ_{rd} , i.e. rotor flux magnitude $|\psi_r|$ is derived as:

$$\frac{d\psi_{rd}}{dt} + \frac{R_r}{L_r} \cdot \psi_{rd} = \frac{R_r}{L_r} L_m \cdot i_{sd} \quad (2.30)$$

As can be seen from (2.30), the rotor flux is only proportionally and derivatively related to the stator current d component.

Since torque is coordinate reference frame independent and review (2.29). (2.17) can be rewritten in the dq frame as follows:

$$T_e = -\frac{3}{2}p(\psi_{dr}i_{qr} - \psi_{qr}i_{dr}) = -\frac{3}{2}p\psi_{dr}i_{qr} \quad (2.31)$$

Moreover, from (2.14) and (2.29), rotor current q component is gained:

$$i_{rq} = -\frac{L_m}{L_r}i_{sq} \quad (2.32)$$

Combine (2.31) with (2.32), the torque of machine is achieved:

$$T_e = \frac{3}{2} \frac{L_m}{L_r} p \psi_{dr} i_{qs} \quad (2.33)$$

(2.33) shows that the torque is only proportional to the rotor current q component. Therefore, the control of rotor flux magnitude and electromagnet are decoupled through orientating the machine variables onto the rotor flux aligned rotating reference frame.

Because the reference frame transformation requires the rotor angle, and flux control requires rotor flux magnitude, rotor flux should be estimated for FOC. There are several ways of rotor flux estimations: closed-loop estimation, which is robust but complicated; and open-loop estimation, which is easier and is mostly used. Open-loop estimation can be further divided into voltage model (or: stator model) based method and current model (or: rotor model) based method [46].

Voltage model combines (2.13) with (2.15), and calculates the rotor flux as:

$$\psi_r = \frac{L_r}{L_m} \cdot \psi_s - \left(\frac{L_r L_s}{L_m} + L_m \right) \cdot i_s \quad (2.34)$$

Current model combines (2.13) with (2.16), thus, the rotor flux is derived as:

$$\psi_r + \frac{L_r}{R_r} \frac{d\psi_r}{dt} = L_m i_s + j\omega_e \psi_r \frac{L_r}{R_r} \quad (2.35)$$

For IM, because there is angular slip between rotor mechanical angle and rotor flux angle, instead of direct measuring, rotor flux angle should be calculated with flux components as:

$$\varphi = \arctan \left(\frac{\psi_{r\beta}}{\psi_{r\alpha}} \right) \quad (2.36)$$

For PMSM, rotor flux angle is exactly rotor angle, therefore, it can be gained through encoder.

In figure 2.8, it is seen that proportional (PI) linear controllers are applied as controllers in all control loops. Therefore, FOC electric drive system is linear controlled. Usually PID controllers should be applied. However, since all controller outputs for the electric drive system under research have only proportional or integral relations to the controlled quantities as the

controller inputs, only PI controllers are adopted. This matches exactly the principles of the applicable range of PID controllers: the inputs and outputs of PID controllers should have one or more relationships of proportion, derivative and/or integral.

For the position PI control, this requirement is met through the simple relation of:

$$\omega_r = \frac{d\theta_r}{dt} \quad (2.27)$$

For the speed PI controller, this is confirmed by (2.19).

Moreover, steady state quantities are only and must be needed to calculate the reference values. Therefore, for the torque and flux PI controllers, the principles are met by (2.33) and (2.30), respectively as below:

$$i_{qs}^* = \frac{2}{3} \frac{L_r}{pL_m} \frac{T_e^*}{|\psi_r|^*} \quad (2.28)$$

$$i_{ds}^* = \frac{|\psi_r|^*}{L_m} \quad (2.29)$$

For the two currents' PI controllers, this can be understood from (2.13), in which except stator currents, stator flux is also required for the calculation of stator voltage references. However, since for control references, only steady state quantities are considered. Therefore, the principles still work for single control input of stator currents.

Moreover, by properly reducing the reference of the rotor flux reference, flux weakening can be applied for operations that of higher speed than the rated.

2.4.2 Direct Torque Control

Direct torque control (DTC) is another early control method for AC drives that can separately control flux and torque [17, 45]. Figure 2.9 shows the schematic of basic DTC. Instead of controlling rotor flux as in FOC, it controls stator flux magnitude.

Different from FOC, and through the control decision making strategy, DTC selects directly the switching states and output the gating signals to VSI. Therefore, PWM calculation module is no more required.

Similar to FOC, electromagnetic torque is gained with an outer speed PI controller. For inner torque and stator flux control, hysteresis controllers are applied. Hysteresis controller is a typical nonlinear controller for coupled nonlinear systems which output discrete values for continuous input values. It is simply a two-bands regulator that limits the errors of torque or stator flux magnitudes within predefined ranges of band. As a result, it is also intuitively named as "Bang-bang" control to mimic the sounds when the control actions lead the controlled values hitting the bands. The widths of the band are the error tolerances. When these band widths are reduced, the oscillation magnitudes of both control quantities will be reduced. However, smaller band widths lead to higher switching frequency and loss as well as reducing the system operation efficiency. Moreover, the higher switching frequency has higher requirements of switching power electronics components. Therefore, the band values of hysteresis controllers in DTC should be correctly tuned for proper overall performance.

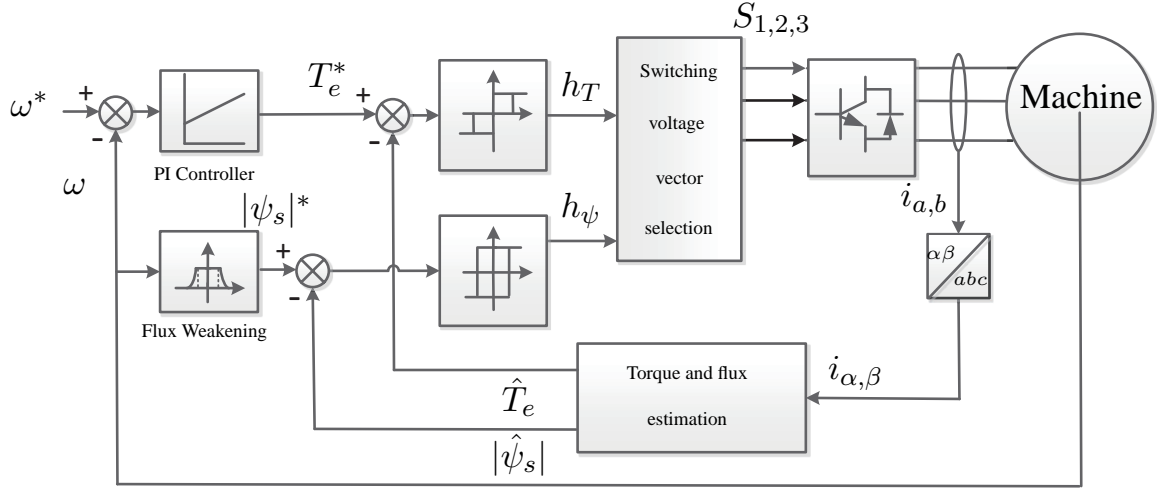


Figure 2.9: DTC Block Diagram.

The outputs from torque and flux hysteresis controllers, together with the sector information of stator flux vector, are given to a 3-D look-up table to select the switching voltage vectors. Similar as FOC, stator flux (both magnitude and angle) and torque are also estimated. The stator flux is estimated with voltage model (2.13) and torque is calculated with (2.17). Assume the control bands of torque and flux magnitudes are $[-\Delta T, \Delta T]$ and $[-\Delta\psi_s, \Delta\psi_s]$. The most common rules of setting the hysteresis controller outputs are as follows:

$$h_T = \begin{cases} -1, & e_T < -\Delta T, \text{ torque should be decreased} \\ 0, & e_T < -\Delta T, \text{ torque should be kept at the current value} \\ 1, & -\Delta T \leq e_T < 0 \text{ and } h_T > 0, \text{ or } 0 \leq e_T \leq \Delta T \text{ and } h_T \leq 0, \text{ torque should be increased} \end{cases} \quad (2.40)$$

$$h_{\psi_s} = \begin{cases} -1, & e_{\psi_s} > \Delta\psi_s, \text{ flux should be decreased} \\ 1, & e_{\psi_s} < -\Delta\psi_s, \text{ flux should be increased} \\ \text{same as last value,} & -\Delta\psi_s \leq e_{\psi_s} \leq \Delta\psi_s, \text{ flux should be kept at the current value} \end{cases} \quad (2.41)$$

The torque control is dominant and has higher priority, therefore, compared to flux control, it has one more "0" output signal level. This "0" action can alleviate the severe variations of torque, i.e. reduce the magnitude of torque ripples.

To judge the location of stator flux, the vector complex plane is equally divided into six consecutive angles with the VSI feasible voltage vectors lying on the angle bisectors, and as shown in figure 2.7. Assume the first sector of $(-30^\circ, 30^\circ)$ is named as S_1 , the other sectors are S_2 to S_6 in the angular increase direction.

With above rules, the decision making look-up table for optimal voltage vector selection is illustrated in table 2.2. The explanation of the mechanism in this table will be clarified in the following derivations.

Table 2.2: Lookup table for DTC

h_{ψ_s}	h_t	S_1	S_2	S_3	S_4	S_5	S_6
1	1	110	010	011	001	101	100
1	0	111	000	111	000	111	000
1	-1	101	100	110	010	011	001
-1	1	010	011	001	101	100	110
-1	0	000	111	000	111	000	111
-1	-1	001	101	100	110	010	011

From the voltage model (2.13), when the rotor speed is high enough for neglecting the voltage drop on stator resistance, the stator flux error, after the first order Euler forward discretization as shown in (2.42), has and only has the linear relation with the stator voltage as (2.43).

$$\frac{dx}{dt} = \frac{x(k+1) - x(k)}{T_s} \quad (2.42)$$

$$\psi_s(k+1) - \psi_s(k) = T_s \cdot \mathbf{v}_s \quad (2.43)$$

Replace the \mathbf{i}_s in the (2.17) with the combined derivation of (2.15) and (2.16), torque equation can be rewritten as:

$$T_e = \frac{3}{2}p \cdot \frac{L_m}{\sigma L_s L_r} \cdot (\boldsymbol{\psi}_r \times \boldsymbol{\psi}_s) = \frac{3}{2}p \cdot \frac{L_m}{\sigma L_s L_r} \cdot |\boldsymbol{\psi}_r| |\boldsymbol{\psi}_s| \sin(\epsilon) \quad (2.44)$$

where ϵ represents the angle between the rotor and the stator fluxes.

From (2.15) and (2.16), the rotor current can be calculated as:

$$\mathbf{i}_r = \frac{1}{\sigma L_r} (\boldsymbol{\psi}_r - k_s \boldsymbol{\psi}_s) \quad (2.45)$$

where the coefficient $k_s = L_m/L_s$ and leakage factor $\sigma = (L_s L_r - L_m^2)/(L_s L_r)$.

Substitute (2.45) into rotor voltage equation (2.16), it derives:

$$\boldsymbol{\psi}_r = \frac{k_s}{\sigma \cdot \tau_r \cdot s + 1} \cdot \boldsymbol{\psi}_s \quad (2.46)$$

where $\tau_r = L_r/R_r$ is the rotor time constant.

From (2.46), it is found that if the stator flux $\boldsymbol{\psi}_s$ changes, the rotor flux response lags the stator flux changes. So in the dynamic control, as long as the control response time is much faster than the rotor time constant, the rotor flux $\boldsymbol{\psi}_r$ can be considered as invariant in a single control period. Moreover, for an extreme small angle, its sinusoidal is small enough to be considered as the same as the angle itself. As a result, torque can be considered as proportional to the angular increment of stator flux vector as:

$$T_e \propto \angle(\boldsymbol{\psi}_s(k), \boldsymbol{\psi}_s(k+1)) \quad (2.47)$$

Figure 2.10 takes the DTC control process for the first control sector as an example to describe the working principles of DTC and to understand table 2.2.

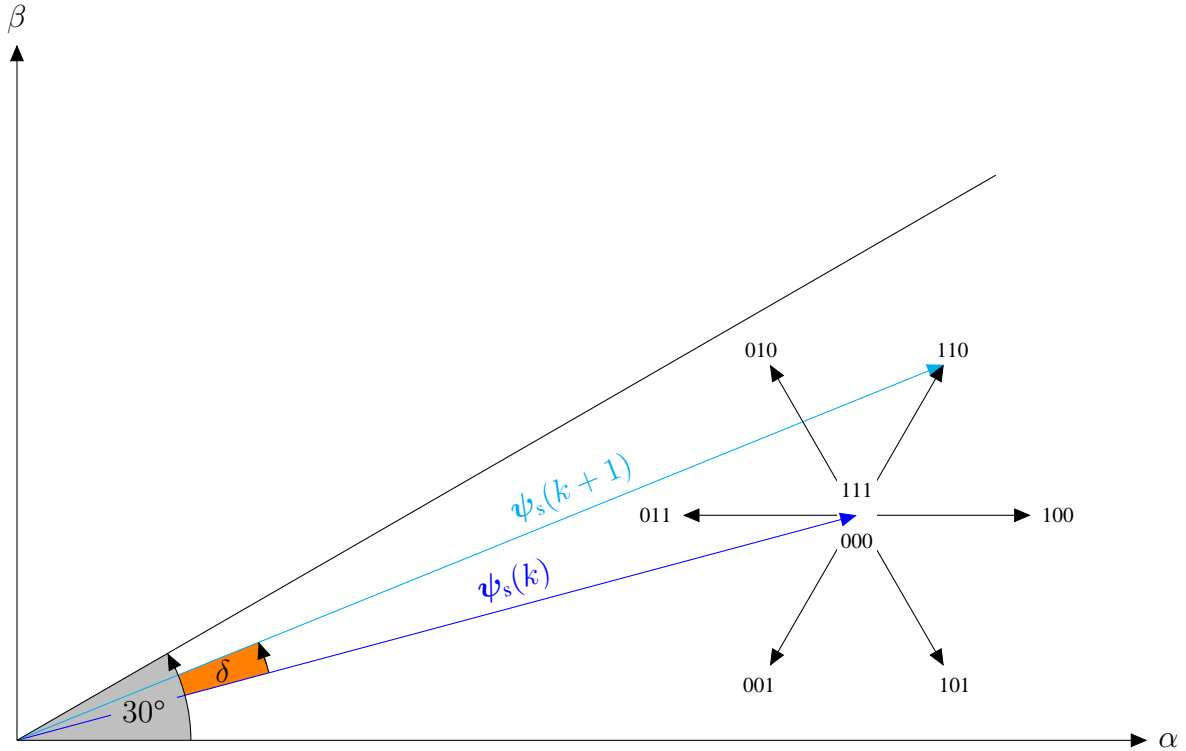


Figure 2.10: Determination of the DTC lookup table for sector 1

When the controller output of hysteresis controllers are $h_T = 1$ and $h_{\psi_s} = 1$, and the current stator flux vector is in sector S_1 . From the controller output values and when refer to (2.47) and (2.43), the applied stator voltage vector should firstly make the stator flux vector's angle of next step larger than the angle of current vector. Therefore, the selection range is limited to stator voltage vectors 011, 010 and 110. Meanwhile, the next step's stator flux should also has larger amplitude than the current's value, thus, the selection range is vectors 011, 100 and 101. As a result, the only mutual vector 011 of both sets is the optimal and is chosen by the LUT as the reference. If $h_T = 0$, whatever value h_{ψ_s} is, a null value should be selected, because voltage control always has higher priority. When choosing the null vectors, the switching number/loss minimization is considered, so either 000 or 111 can be chosen depending to the previous state.

Review figure 2.9, the flux weakening is also shown with the rotor speed as the input for a nonlinear function of stator flux reference calculation.

As can be seen from the previous section, the decision of the stator flux and torque actions shown in LUT depend on the values of stator flux value of next control cycle. Therefore, except being a direct control strategy, DTC can be also considered as the initial form of another important control strategy for electric drives—model predictive control (MPC), with the decision making based on the rough location and magnitude of stator flux vector. In another word, it is an qualitative machine model based predictive control. In contrast, most MPC is quantitative based control when considering the decision making criteria. This will be described in details in the consecutive section.

2.5 Model Predictive Control: A Cutting-edge Drive Strategy

Though DTC strategy, given its merits such as simple structure, fast torque response as well as the elimination of PWM and inner current PI controllers, is widely adopted in industry, it has drawbacks caused by its rough Bang-bang manner of control with limited states subjecting to predefined look-up-table (LUT). For example, it contains large torque ripples. And its switching frequencies are not fixed and it is torque and flux hysteresis controllers' bands dependent [47].

Predictive control (PC) is a class of control strategies which generates the future system outputs based on its past and currents states through certain controllers. It can be generally classified as: hysteresis PC, trajectory PC and model PC (MPC).

MPC as the most popular form among PCs, has been started to be researched for industrial applications since 1960s [48]. The basic mechanism of MPC is to pre-calculate (or: predict/estimate) the concerned physical systems' variables for control by its dynamic models (usually linear empirical ones) in advance, and utilizes these future behavior information containing variables to select an optimal control signal as the input for the control plant's actuator through an optimization evaluation criterion in receding horizon (or: time window) manner. It can be easily used for systems, whose physical models are known. Moreover, it can also handle multiple-variable systems and their constraints problems. However, a feature of MPC is its comparative high calculation burden. Therefore, it used to be widely but limitedly applied to slow process industries such as petrol chemical and oil refineries engineering since 1980s [26].

Thanks to the exponentially developing of semiconductors techniques and microprocessors such as digital signals processor (DSP), complex programmable logic device (CPLD) and field-programmable gate array (FPGA), the calculation amount of MPC is acceptable for faster real-time industrial applications such as power system balancing, control of power converters and electrical drives [49, 50]. Since 1980s, MPC has become an emerging and ever-advancing non-linear model based control strategy for electric drives and power electronics [51, 52]. According to the application requirements and situations, MPC have many variations and therefore can be implemented both with and without modulation modules.

Figure 2.11 shows the general block diagram of MPC for electric drives. Following the signal flow direction, it is seen that the values of control targets, e.g. rotor position, speed or electromagnetic torques is set to the outer controller, which is usually a proportional-integral(-derivative) (PI(D)) controller, for rough control. The output of outer controller is further sent to the the inner MPC controller, which is either hysteresis, trajectory or cost function-based, for precise control of intermediate states such as torque, flux or/and currents. Therefore, either the continuous reference voltage or switching states of inverter's finite feasible voltage set are generated through the corresponding predictive control mechanisms. A modulator is here optional: if the reference voltage is generated, a modulator (e.g. sinusoidal pulse width modulation (SPWM) or space vector modulation (SVM)) is required to generated the switching states; if switching states are generated, it is directly given to the inverter as control input. In this figure, a VSI is chosen as example. Modulator, together with the VSI, is treated as actuator, i.e. power supply for the electric machines. The machine output states including speed, currents and voltages are measured and given as the feedback to the controllers.

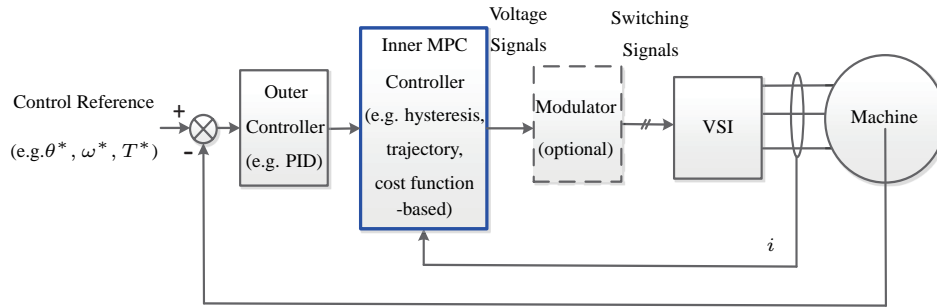


Figure 2.11: General Block Diagram of MPC for Electric Drives.

Compared to conventional control methods for electric drives, MPC has in general the following advantages:

1. The control of nonlinearities is enabled with the models of the nonlinear control plants, i.e. electric machines.
2. Multiple control terms such as flux, torque and/or currents can be simultaneously controlled with different weightings (i.e. importances).
3. System constraints such as switching loss reduction, voltage and current limitations can be realized and control with priorities through cost function.
4. Modulators that causes extra cost and nonlinearities, are not a necessity for system.
5. Compared to DTC, MPC has even simpler concept of design and faster dynamics. Compared to linear control systems such as FOC, it replaces the inner PI current controllers with nonlinear controllers, rendering the current control bandwidth to be infinite.

Therefore, nowadays, MPC is becoming a promising advanced control methods for electric drives, and for this reason, it is chosen as the control strategy under research in this work.

2.6 Test Bench Description

The test of this work is conducted on a system consisting of two machines as illustrated in figure 2.12. It consists of an SPMSM, an SRM, and a DS1007 dSPACE based fast prototype controller that can generate real-time control code of the algorithms directly from MATLAB/Simulink models. Except the main control program, an extra interrupt program triggered by the malfunction signals from the drive's IPM interfaced board is executed in parallel for the purpose of software protection.

The output switching signals for drive switches' triggers can be sent with two different modes through two different output boards: DS5101 DWO board of 7-sectors-based SVPWM 0/5 V signal generator; CLP4003 direct I/O board direct switching signals generation for FCS-MPC.

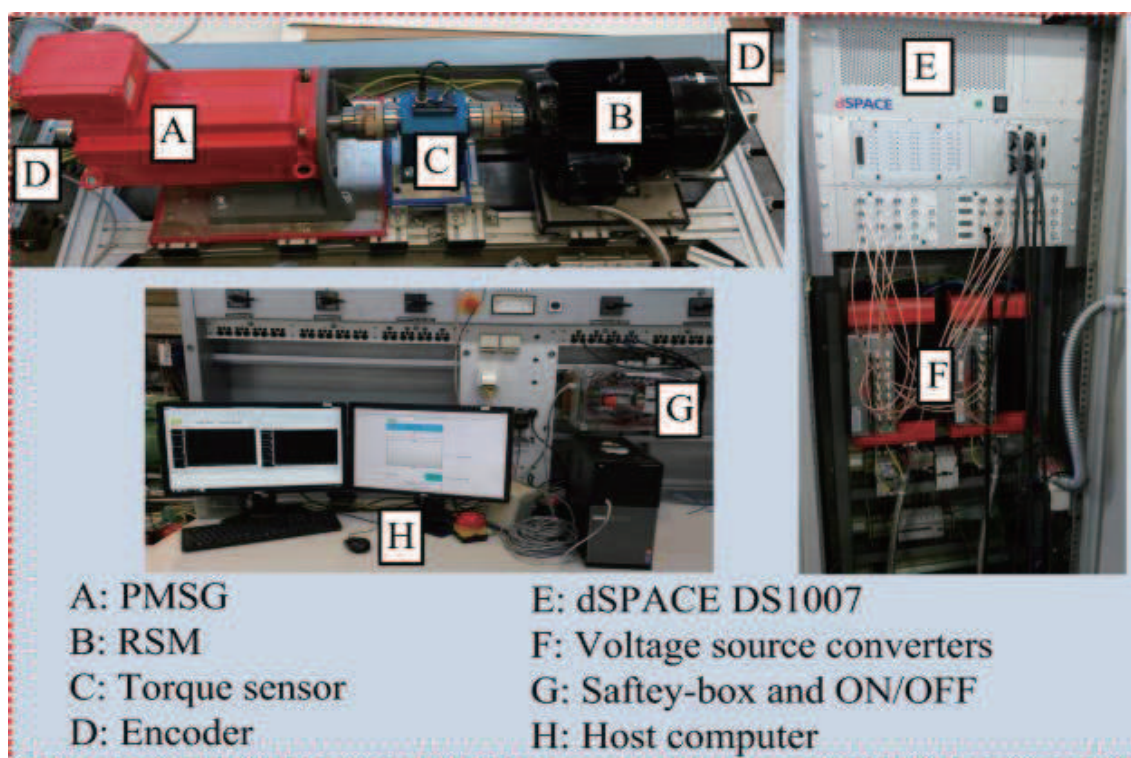


Figure 2.12: Test Bench.

Measured currents and DC voltages signals are sampled with the 16-channels DS2004 AD signal conversion board. An Omron 1024 PPR encoder is adopted and its signal is fed to the controller through a DS3002 incremental encoder board.

Because application or design of more advanced topologies of power converters is not in the scope of this work, the most popular SEW user-defined switching triggered 2-level 3-phase voltage source inverter (VSI) with hardware interlock protection against short-circuit is applied. The AC machines experimented on test bench in this work are the SPMSM and IM, though IPMSM is also simulated. The load is applied through the SRM driven by another SEW commercial Inverter. A torque meter is used for comparison and monitoring purpose. All control variables and parameters can be supervised and modified online in real-time through the Control Desk GUI platform. If not specially mentioned, both sampling frequency and PWM frequency are set to be 10 kHz in simulations and experiments. The detailed control plants' data and system parameters are shown in table 2.3.

Table 2.3: Data of Eletrical Drive Systems.

Parameters	Symbols	Rated Values
Control		
Sampling period	T_s	100 μs
Prediction horizon	N_s	1
VSI		
DC-Link voltage	U_{dc}	560 V
SPMSM		
Rated power	P_{nom}	14.5 kW
Rated speed	ω_{nom}	157 rad/s
Rated torque	T_{nom}	29 Nm
Pole pairs number	p	3
Inertia	J	0.0352 kg · m ²
Stator resistance	R_s	0.15 Ω
Stator inductance	L_s	3.40 mH
IPMSM		
Rated power	P_{nom}	1.8 kW
Rated speed	N_{nom}	1500 rpm
Rated torque	T_{nom}	12 Nm
Pole pairs number	p	3
Inertia	J	0.0175 kg · m ²
Stator resistance	R_s	0.3083 Ω
Stator direct axis resistance	L_d	4.50 mH
Stator quadrature axis resistance	L_q	7.85 mH
IM		
Rated power	P_{nom}	2.2 kW
Rated speed	N_{nom}	2772 rpm
Rated torque	T_{nom}	7.5 Nm
Pole pairs number	p	1
Inertia	J	0.005 kg · m ²
Stator resistance	R_s	2.68 Ω
Rotor resistance	R_r	2.13 Ω
Stator inductance	L_s	283.4 mH
Rotor inductance	L_r	283.4 mH

2.7 Motivation and Contribution of This Work

In spite of the various merits of MPC mentioned in chapter 2.5, for its more economic and stable and therefore wider application to the extent of practical and industrial level, two main aspects should be further and continuously improved:

Control Performances - including dynamic performance such as sufficiently fast response of control targets, and steady performance such as acceptable torque ripples, speed oscillations and current THDs. If the comparable performance of MPC with better dynamics can be achieved, it will take the place of FOC and DTC in drive controls in near future.

Calculation Efficiency - not only the calculation time should be reduced, but the concept of this reduction should be also intuitive with lower requirement and cost for micro-controllers without deterioration to the control performances. This is actually a more crucial problem limiting the wide application of MPC, especially for the cases of long predictive horizons and multilevel inverters.

For the above two purposes, different control algorithms as possible solutions are proposed, derived, verified and analyzed based on the aforementioned test bench in the following chapters as follows:

Chapter 3: as fundamental, it reviews, explains and compares conventional MPC strategies according to their classifications. Their working mechanisms, mutual features as well as differentiations are presented. Moreover, the essences of MPC are therewith discussed. Supportive simulations and experimental results are demonstrated.

Chapter 4: gives a novel solution of continuous Increased FCS-MPC with both PWM and cost function, which combines the advantages of FOC with FCS-MPC, such as fixed switching frequencies and can be applied to the situations where continuous voltage references are required, e.g. continuous voltage signal injection. Though it requires comparative high calculation efforts, it maintains both the advantages of FCS-MPC with cost function and has comparable performance as FOC. Two variations of the strategy are proposed and verified through simulation and experiments.

Chapter 5: aims at reducing the calculation efforts, it presents five variations of reduced FCS-MPC methods that can reduce the size of finite control set for voltage vectors. The number of voltage vectors is therewith reduced from 7 to 0. Moreover, switching loss minimization is also considered in one of these methods reducing switching frequencies. All strategies have simulation and experimental verifications.

Chapter 6: introduces disturbance observer (DO) to inhibit torque variations and disturbances, therefore, the system response and reliability are further improved. Moreover, the tuning work of PI parameters is reduced. And it is implemented on both continuous and FCS-MPC. Meanwhile, maximum torque per Ampere (MTPA) control is included to improve the efficiency and reliability through reduction of current value and therefore heat loss.

Chapter 7: discovers the potentials of two recent proposed FCS-MPC strategies without weighting factor adjustments: sequential FCS-MPC and a parallel FCS-PTC. Without weighting factors in cost functions, system complexity and uncertainty are further decreased. Thus, it is less dependent on experiences, and quantitative restrictions for control terms can be included.

Chapter 8: summarizes this work and proposes future topics of MPCs for electric drives.

Contributions of this work are:

1. Both continuous MPC and FCS-MPC are researched and their applications with various performance improving and calculation optimizing strategies are conducted on different AC machines for different operation conditions. The effectiveness of proposed strategies and system performances are shown through test results.
2. Control performances are improved with application of DO in dynamics and guaranteed with increased FCS-MPC at both dynamics and steady states with extensive nonlinear control capabilities.
3. Calculation efficiency is ensured through calculation and time reduction strategies. And the improvement are verified under test conditions.
4. Control is eased with reduced number of parameters to be adjusted with the application of DO and sequential/parallel FCS-MPC.

CHAPTER 3

MPC for Electrical Drives

3.1 Classification and Comparison of MPC

The classification of PC of electric drives has been generally mentioned in chapter 2.5. Table 3.1 is a detailed summation and comparison of PC for electric drives including all classes of MPCs [53, 54].

Table 3.1: Classification of Predictive Controls for Electric Drives.

Predictive Control (PC)				
Classes	Hysteresis PC	Trajectory PC	Continuous MPC	FCS-MPC
Horizons	one step		one step/long horizon	
Features	no modulator varying switching simple	no modulator varying switching non-cascaded	with modulator fixed switching has constraints	no modulator varying switching optimized
Examples	DTC		GPC, explicit MPC, deadbeat MPC, IFCS-MPC	FCS-MPC, deadbeat FCS-MPC, modulated VSP-MPC

The left two in table 3.1 are two primitive classes of PC. Hysteresis PC restrains errors of control variables within a hysteresis predefined boundaries. Therefore, DTC is a hysteresis PC. There are also other forms of hysteresis PCs for electric drives, such as predictive current controller proposed in [55]. Trajectory PC forces the control terms to track their predefined trajectories, such as the direct speed controller in [56].

The right two in table 3.1 belong to the class of MPC, which can be divided into continuous MPC and finite-control-set MPC (FCS-MPC) [57, 58]:

Continuous MPC generates continuous or quasi-continuous reference voltage vectors as actuator inputs. Since until now all inverters for electric drives can only realize voltage vectors in discrete form instead of arbitrary space voltage vectors, a PWM module is always required for continuous output reference from controller. Therefore, fixed switching frequencies are achieved with continuous MPC. A typical and early form of continuous MPC for electric drives is GPC [59, 60] proposed in 1987. GPC obtains reference voltages by solving analytical equations and has good performance. However, it is complex to be implemented and its concept is comparatively sophisticated to understand, so it is usually not preferred. Other forms of continuous MPC are the explicit MPC [61] and model inverse deadbeat MPC [62] as well as increased-finite-control-set (IFCS)-MPC [63–65], among which the later two will be introduced in details in the following parts of this chapter and chapter 5.

Finite-control-set model predictive control (FCS-MPC), also named as Finite-set MPC (FS-MPC), belongs to the control family of predictive direct control methods. In contrast to continuous MPC, it utilizes the discrete nature of inverters' feasible output voltages. Therefore, it directly introduces a cost function. In contrast to continuous MPC, FCS-MPC selects the switching states for inverters and no PWM is needed. FCS-MPC calculates the reference voltage vectors in a numerical manner by introducing a reference voltage vectors deciding cost function and substituting all feasible discrete voltage vectors of inverter into this cost function. The voltage vector leading to minimize value of cost function is considered as the optimal vector, thus the reference. Though FCS-MPC has no fixed switching frequencies, it is on another hand an advantage to achieve variable average switching frequencies. No modulator is required, but modulated strategies are still extendable, such as the cases of various modulated or varying-switching-point (VSP) MPCs [66]. FCS-MPC, according to the terms to be tracked through inner MPC controllers, has two branches [40]: FCS-Predictive Torque Control (FCS-PTC) and FCS-Predictive Current Control (FCS-PCC), which are the base control strategies for all the rest variations and extensive controls in this work. Therefore, these two FCS-MPCs will be explained in details in the following parts of this chapter.

Both FCS-PTC and FCS-PCC, when implemented in model inverse manner, i.e. instead of substituting candidates voltage vectors into cost function to find out the optimal when compared to the references, calculating directly the optimal reference voltage vectors with references. Thus, the corresponding continuous MPC: Deadbeat PTC and Deadbeat PCC is achieved, which will be explained in details in later parts of this chapter.

Both Continuous MPC and FCS-MPC can be implemented in one-step and multiple-step (long horizon) manners, according to the number of steps for predictions in advance [67–69]. And the switching state at the nearest step should be implemented in the next control period. In next control period, the predictive controller moves one step forward with fixed number of predictions in a time receding horizon way. As a result, the number of prediction iterations will increased exponentially with the increased prediction horizon. The total number of possibilities N with m different switching states of each possibility to be evaluated for an n horizon predictive control is:

$$N = m^n \quad (3.1)$$

Actually, all PCs are model-based, because they all utilize the system mathematical models. However, they are differentiate through above names based on their error elimination methods, except MPC that are designed with a error minimization process with reference control signal prediction and evaluation. Therefore, in more generalized sense, DTC and model inverse dead-

beat MPC, an even earlier form of FCS-MPC, can also be classified as MPC. For simplicity and clarity, in this work, only FCS-MPC and deadbeat MPC are in name of "MPC".

In the following parts of this chapter, several conventional MPCs will be reviewed and compared. The consecutive sub-chapters will introduce and derive the two main FCS-MPCs: FCS-PTC and FCS-PCC; and one typical continuous MPC: Deadbeat MPC. For the comprehensiveness of verification results, all simulations are conducted on an IPMSM model, and all experiments are conducted on an SPMSM. The parameters of both machines are given in table . Moreover, because both IM and SPMSM equations can be considered as special cases of that of IPMSM, therefore, if applied to IM or SPMSM, their corresponding equations can be easily modified based on the equations of IPMSM.

3.2 Time Order and Compensation

To better understand the discrete time implementation of these control strategies and in general model predictive controls, the time order and the concept of time compensation should be firstly explained.

For conventional FCS-MPC, in each control period, only one fixed switching state is given to inverter for the whole control period. Therefore, in a control system, the optimized voltage reference cannot be predicted and applied to the plant in the same control/sampling period. This is actually a intrinsic conflict of all predictive based control that not merely exists in digital control system [70]. This can be understood through figure 3.1 [40, 62] , in which the switching state corresponding to reference voltage for control period time k is $v_s^*(k)$. This value must be readily calculated no later than the end of the control period $k-1$, and applied to the system at the beginning of control period k . From the later prediction equations in chapter 3.3, we will see that to obtain $v_s^*(k)$, $T_e^*(k+1)$ should be predicted, which is the predicted torque value at the end of period k (i.e. the beginning of period k).

Similarly and taken predictive torque control as example, when the time window is shifted one period/step forward, if we want to obtain the desired reference voltage, $v_s^*(k+1)$, of next control period, $k+1$, we should in the present control period, k , predict the torque $T_e^*(k+2)$ corresponding to its real value at the end of the $k+1$ period (i.e. beginning of $k+2$ period) in advance. Therefore, the predictions should consists of two steps: 1. predict $T_e^*(k+1)$ with $i(k)$ and existing $v_s^*(k-1)$, and predict $i(k+1)$; 2. predict $T_e^*(k+2)$ with $i(k+1)$ and candidate $v_s^*(k)$. Therewith, $v_s^*(k)$ can be obtained.

Above is exactly the concept of "time compensation" —one more step forward prediction of desired control variables for the next step's voltage reference.

Time compensation is especially important. Because it enables the control to be closer and preciser with consideration of time order. And it is proved to be crucial in experimental implementations, which ensures the control order is correctly manipulated. In the following chapters, all "one-step" predictions are essentially this kind of "two-steps" predictions with time compensation. With this pre-knowledge, the algorithms of three different MPCs with one-step prediction will be explained as example in the following sub-chapters.

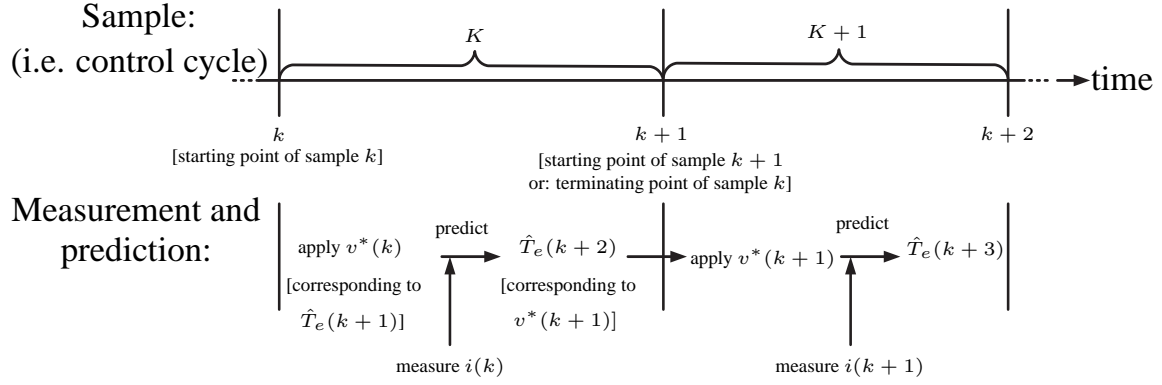


Figure 3.1: Time Order and Compensation of FCS-MPC.

3.3 Finite-control-set Predictive Torque Control

For the control of IPMSM in most applications such as electric vehicles and railway locomotion, torque response time and ripples should be controlled in a suitable range to achieve good dynamics and performance. For this purpose, some extended DTC, e.g. DTC with PWM or direct mean torque control (DMTC) have been investigated to improve conventional DTC respecting to high torque ripples, but they all increase the system complexity. FCS-PTC has been proven to be a very promising MPC method for motors [57, 71], and has smaller torque ripples than DTC and even has comparable performances with those of the FOC method [72].

Therefore, FCS-PTC is a good alternative that can both reduce the torque ripples and maintain a fast system dynamics, and with simple design and implementation. The schematic of FCS-PTC for IPMSM is shown in figure 3.2. It consists of three parts: stator flux and current estimation and prediction; torque and current prediction and current Park transformation from $\alpha\beta$ to dq frame; and cost function optimization.

3.3.1 Estimation and Prediction

For PTC, stator flux should be firstly estimated and discretized from stator voltage equation (2.13). Afterward, both stator flux magnitude and electromagnetic torque should be predicted. To achieve this, (2.13) is again applied and discretized, so that the next step stator flux linkage can be predicted as:

$$\begin{cases} \hat{\psi}_\alpha(k+1) = \psi_\alpha(k) + T_s \cdot [u_\alpha(k) - R_s \cdot i_\alpha(k)] \\ \hat{\psi}_\beta(k+1) = \psi_\beta(k) + T_s \cdot [u_\beta(k) - R_s \cdot i_\beta(k)] \end{cases} \quad (3.2)$$

Instead of using the measured value, the voltage reference, i.e. voltage of last cycle's optimal is applied in calculation for this work. Transform the stator currents $i_{\alpha,\beta}$ and voltage $u_{\alpha,\beta}$ to its rotor flux reference frame form $i_{d,q}$ and $u_{d,q}$ through Park transformation, and combine (2.24) and (2.25), the current derivative is obtained:

$$\begin{cases} \frac{d}{dt} i_d = (u_d - R_s \cdot i_d + \omega_e \cdot L_q \cdot i_q) / L_d \\ \frac{d}{dt} i_q = (u_q - R_s \cdot i_q - \omega_e \cdot L_d \cdot i_d - \omega_e \cdot \psi_{pm}) / L_q \end{cases} \quad (3.3)$$

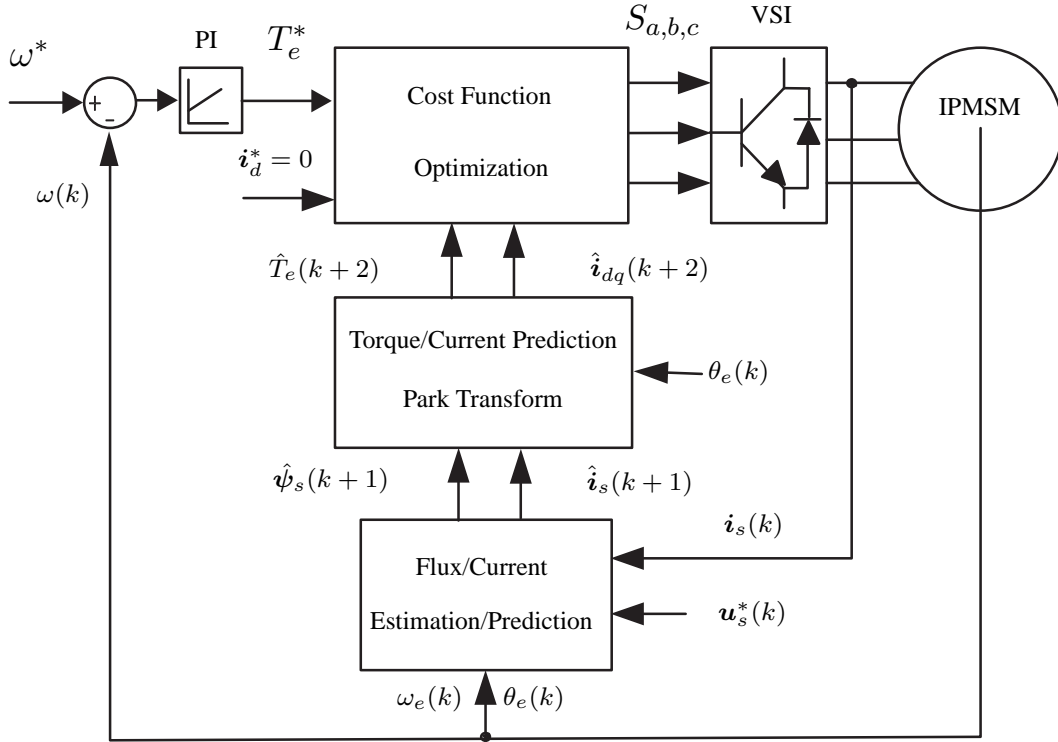


Figure 3.2: FCS-PTC for IPMSM.

The discrete stator predicted currents are therefore derived:

$$\begin{cases} \hat{i}_d(k+1) = i_d(k) + \frac{T_s}{L_d} \cdot [-R_s \cdot i_d(k) + \omega_e(k) \cdot L_q \cdot i_q(k) + u_d(k)] \\ \hat{i}_q(k+1) = i_q(k) + \frac{T_s}{L_q} \cdot [-R_s \cdot i_q(k) - \omega_e(k) \cdot L_d \cdot i_d(k) + u_q(k) - \omega_e(k) \cdot \psi_{pm}] \end{cases} \quad (3.4)$$

For this work, three-phase two-level VSI is applied and for the conventional FCS-MPC, and all 7 available VSI VVs are substituted into the above currents equations for further evaluations to select the 1-out-of-7 optimal VV, i.e. $\mathbf{u}_s^*(k)$, which is the complex vector of the dq components, $u_d(k)$ and $u_q(k)$.

After transforming $i_{d,q}(k+1)$ to their stator frame correspondence $i_{\alpha,\beta}(k+1)$, the stator flux and current predictions are finished and electromagnetic torque prediction can be therewith calculated. However, since the optimal voltage vector (VV) (or: reference VV) can only be applied in the next control period as $\mathbf{v}_s^*(k+1)$ when predicting the next of next step to increased control precision and system dynamics, time compensation, i.e. a further step's stator flux prediction is conducted as:

$$\begin{cases} \hat{\psi}_\alpha(k+2) = \hat{\psi}_\alpha(k+1) + T_s \cdot [u_\alpha(k+1) - R_s \cdot \hat{i}_\alpha(k+1)] \\ \hat{\psi}_\beta(k+2) = \hat{\psi}_\beta(k+1) + T_s \cdot [u_\beta(k+1) - R_s \cdot \hat{i}_\beta(k+1)] \end{cases} \quad (3.5)$$

And the magnitude of predicted stator current is calculated:

$$\|\hat{\mathbf{i}}_s(k+2)\| = \sqrt{\hat{i}_\alpha^2(k+2) + \hat{i}_\beta^2(k+2)} \quad (3.6)$$

Transform $\hat{\psi}_{\alpha,\beta}(k+1)$ to their rotor flux frame correspondences $\hat{\psi}_{d,q}(k+1)$. And from (2.25), the discrete stator currents' prediction in dq frame are:

$$\begin{cases} \hat{i}_d(k+2) = (\hat{\psi}_d(k+2) - \hat{\psi}_{pm})/L_d \\ \hat{i}_q(k+2) = \hat{\psi}_q(k+2)/L_q \end{cases} \quad (3.7)$$

Therefore, with (2.26), the prediction of electromagnetic torque is derived:

$$\hat{T}_e(k+2) = \frac{3}{2} \cdot p[\hat{\psi}_d(k+2) \cdot \hat{i}_q(k+2) - \hat{\psi}_q(k+2) \cdot \hat{i}_d(k+2)] \quad (3.8)$$

For SPMSM, the only difference lies in machine equations is: $L_d = L_q$.

3.3.2 Cost Function Optimization

With the predicted values, for single step PTC, the control system's cost function can be designed with torque and flux-related current error terms as:

$$g_j = |T_e^* - \hat{T}_e(k+2)_j| + \lambda_g \cdot |i_d^* - \hat{i}_d(k+2)_j| + I_m(k+2)_j \quad (3.9)$$

j refers to the 7 different switching states. Because T_e^* has proportional-integral relation with the speed errors, it is obtained with the outer speed PI controller. i_d^* is the stator current d axis reference, which is for simplicity of control set with $i_d^* = 0$ for neither rotor flux weakening nor increasing operation. λ_g is the weighting factor. According to experiences, it is usually set to be the ratio of control terms' rated values ,i.e. $\lambda_g = T_{nom}/\|\mathbf{i}_s\|_{nom}$, for a fair control between torque and flux corresponding terms, whose attributes are different. $I_m(k+2)_j$ is the predicted current magnitude judgement term for overcurrent protection, which is defined as:

$$I_m(k+2) = \begin{cases} 0 & \text{if } \|\hat{\mathbf{i}}_s(k+2)\| \leq \|i_{max}\| \\ \gamma >> 0 & \text{if } \|\hat{\mathbf{i}}_s(k+2)\| > \|i_{max}\| \end{cases} \quad (3.10)$$

where $\|i_{max}\|$ is a predefined current limit, whose value can not only realize protection, but also roughly adjust the average magnitude of current. More system constraints similar as I_m and nonlinear control terms can be further added into cost function according to the requirements.

3.3.3 Simulation and Experimental Verification

FCS-PTC is simulated on IPMSM model and experimented on SPMSM at different speed ranges and load conditions. The simulations and experimental results are shown and analyzed in the following parts.

Simulation 1 is to find out the speed step startup and reversal process.

Figure 3.3 shows speed, torque, current and flux of this process. The speed reference is given in ramp form. As can be seen from the figure, the motor under FCS-PTC has fast response for speed tracking (within 0.5 s for 3000 rpm variation). During both speed startup and reversal processes, the output electromagnetic torque is controlled with its maximum feasible value (rated value of 12 Nm) to offer fastest acceleration and deceleration. Moreover, because the current limitation term in cost function, the stator one phase current i_{sa} 's maximum is also maintained around 10 A, which is within the nominal limit of 13.8 A.

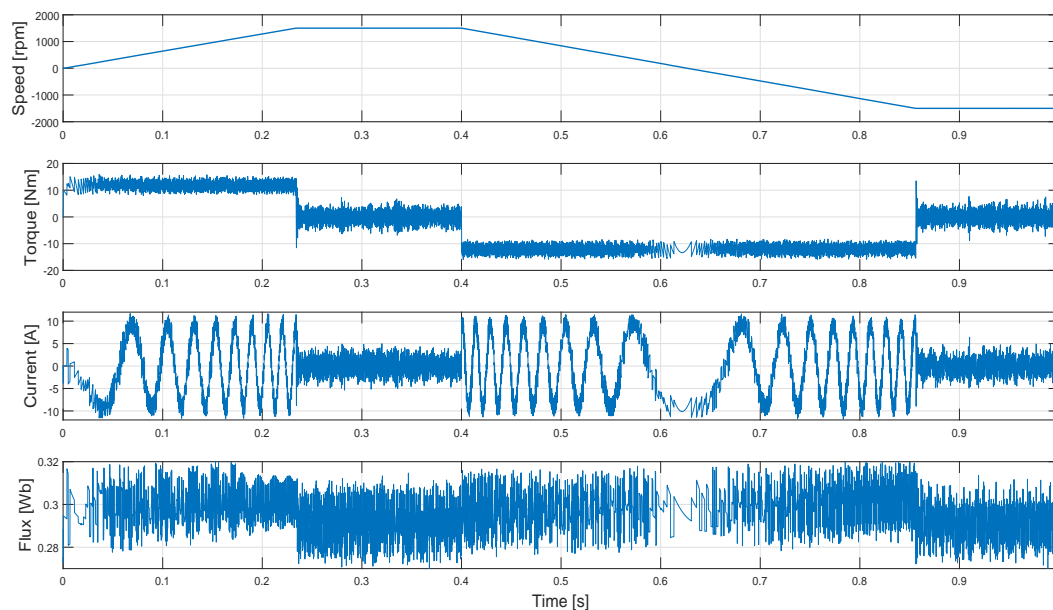


Figure 3.3: Simulation: IPMSM Rated speed start up and reversal under FCS-PTC.

Figure 3.4 shows torque and flux related current i_d 's tracking performance. From both the sub-figures, it is seen that both torque and current predictions can track their references, which shows the effectiveness of the FCS-PTC. It is also seen that the real value has one control period's delay than the predicted value, which is self-evident, because the IPMSM model's output with the reference calculated in current step is actually given to inverter one step later than controller's prediction in the current step (otherwise it is not feasible and there exists algebraic loop). This shows the successful realization of time compensation. For experiments, the prediction and real values may be not so highly matched because of the various extents of model deviations.

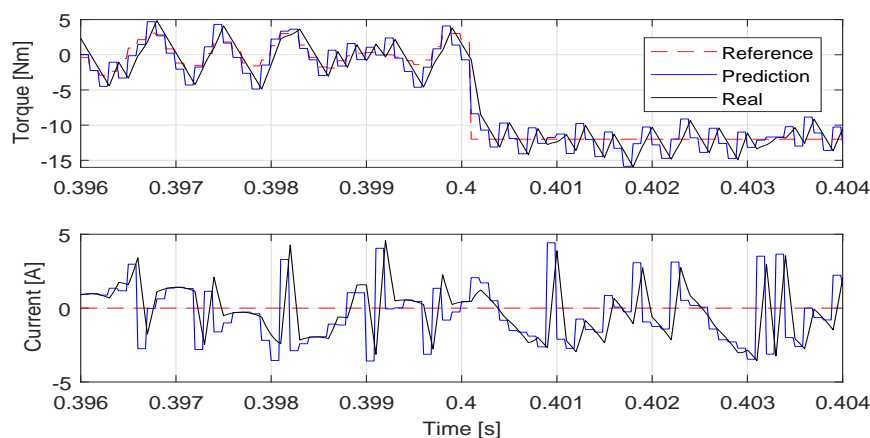


Figure 3.4: Simulation: IPMSM Torque and Flux Tracking Performance under FCS-PTC.

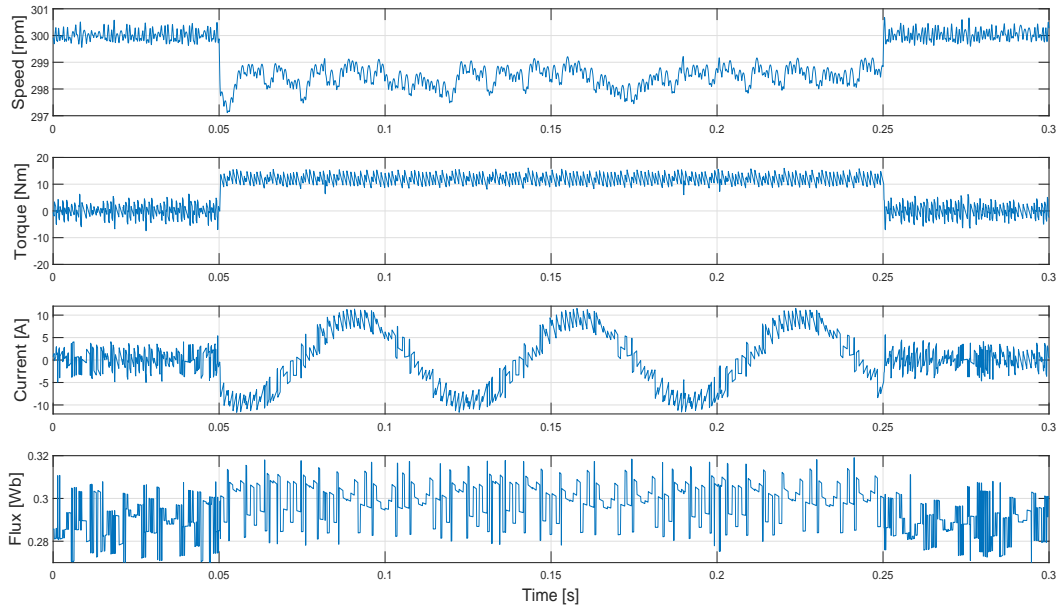


Figure 3.5: Simulation: IPMSM FCS-PTC Performance under Torque Variations.

Simulation 2 is to find out the speed performance under torque variations.

Figure 3.5 shows speed, torque, current and flux of this process. Since low speed range is the most difficult control range of IPMSM with torque control, it is constantly controlled with speed reference of 300 rpm (20% of rated). A sudden rated load $T_l = 12 \text{ Nm}$ is added and hold for 0.2 s . It is shown in figure that the system can instantly track the load and its removal, with only a slight speed drop of 2 rpm under load conditions. This speed variation is caused by the non-optimal speed PI parameters, because these parameters are operation point sensitive that should be adjusted with respect to different speeds and loads. Many researches have been done for the self-adjustment of PI parameters, such as self-adaptive online parameters and wavelet PI adjustments. In the later chapter 6, a strategy with DO, which is essentially a model based PI parameters adjustor in manner of feed-forward compensation will be proposed to solve this problem as well as increase the torque dynamics. Similar as the speed startup and ramp down transients in the previous simulation, maximum torque is output to track the torque variations instantly in several mini seconds.

Figure 3.6 zooms in the torque and switching states during torque variation transient. Vector number 0 to 6 represent the switching states of 000 to 111 as shown in table 2.1. As can be seen from this figure, the torque can track its reference quickly within 0.5 ms , which shows a fast response. When the torque is loaded, more null vectors are applied. This is because higher torque requires larger stator current. However, large current is closer to the current control limit set in cost function. Therefore, the selection of reference voltage is more "conservative" with more null vectors instead of active vectors leading to large current ripples that will exceed the current limits.

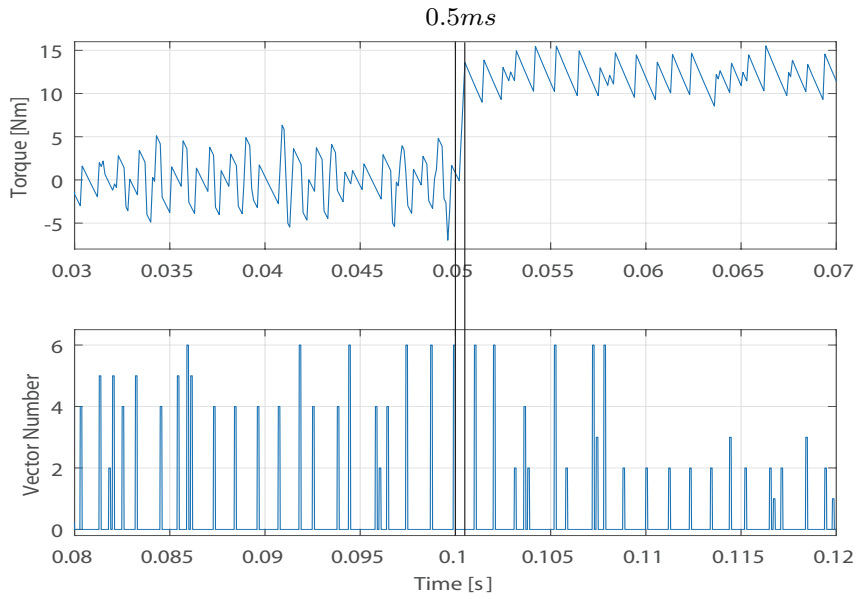


Figure 3.6: Simulation: IPMSM Torque and Voltage Vectors of FCS-PTC under Torque Variations.

Simulation 3 tests the robustness of FCS-PTC. The maximum as well as minimum values of the parameters' deviation ranges are chosen with the criteria that no obvious deterioration is found in the current and torque values, when compared with the situation without parameter deviations. Figure 3.7 to figure 3.9 show the system performances against the variations of R_s , L_d and L_q . The motor is operated at half rated speed (750 rpm) with half load (6 Nm). It can be seen from the figures that FCS-PTC controlled IPMSM system is very robust against parameters variations. And R_s , which is sensitive for most model based control and observers, shows a wide range of robust range of deviations of [10%,1000%], while L_d and L_q have similar ranges around [60%,120%].

The similar experiments are conducted on the SPMSM. Figure 3.10 shows the speed step startup and reversal performance in experiment. Similar as IPMSM's simulation, the startup and reversal processes take within 0.5 s. Since the step startup requires faster acceleration than the ramp reversal, keeping on the rated value of 40 Nm, the startup required torque is larger than the reversal one. And the current is proportional to the output torque. In this figure and all following experiments results, the flux related current, which is constantly controlled with $i_d = 0$, is shown.

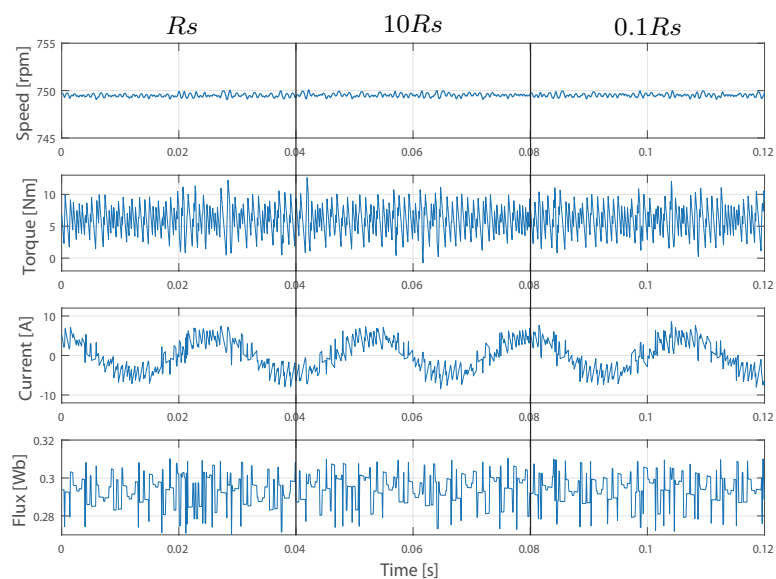


Figure 3.7: Simulation: IPMSM FCS-PTC performance with R_s Variations.

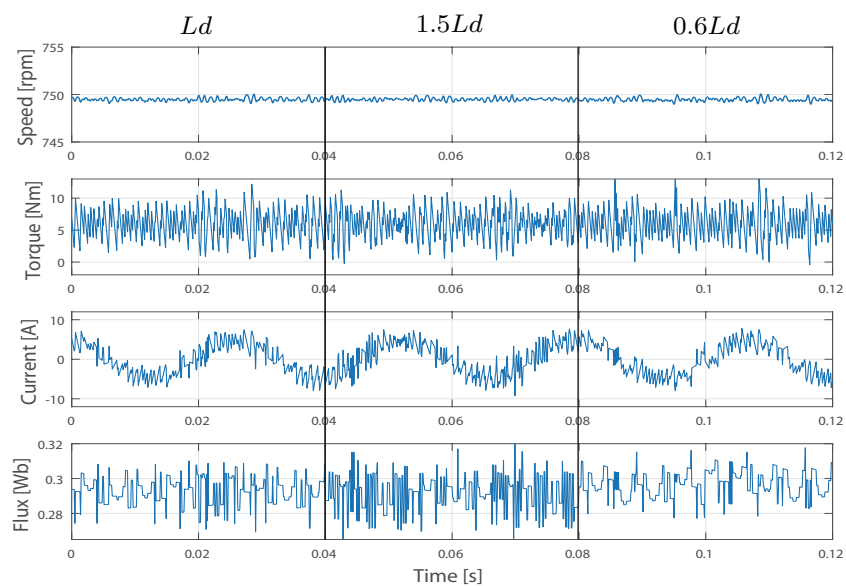


Figure 3.8: Simulation: IPMSM FCS-PTC performance with L_d Variations.

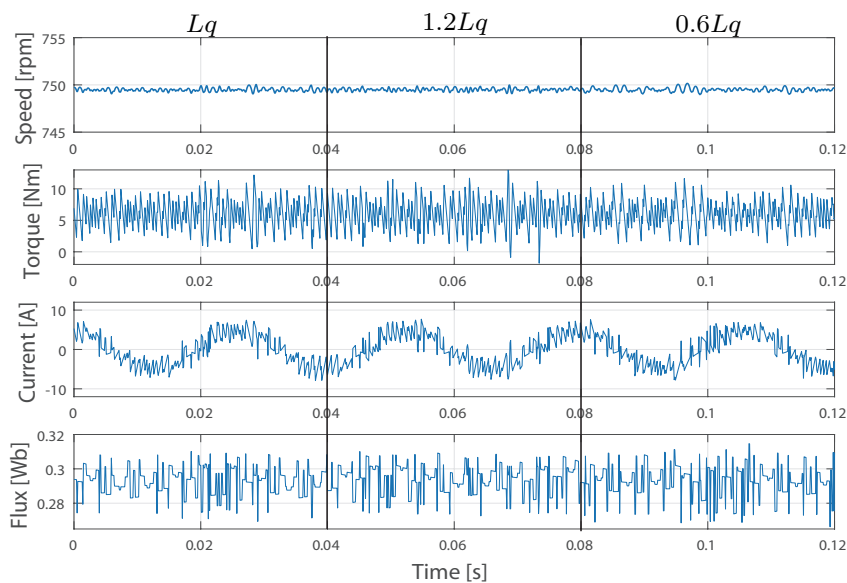


Figure 3.9: Simulation: IPMSM FCS-PTC performance with L_q Variations.

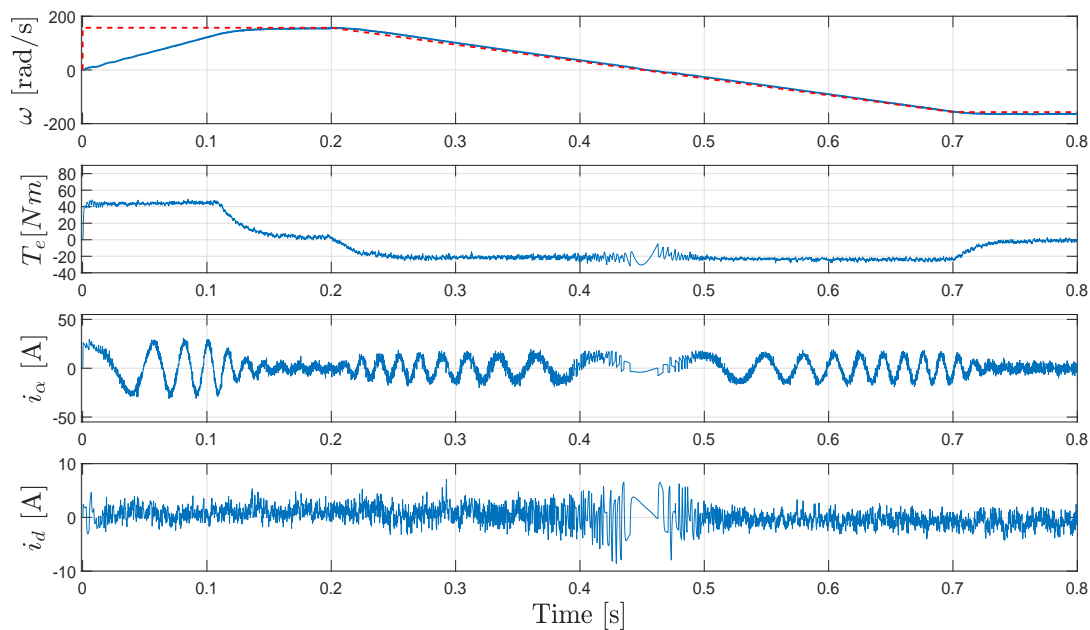


Figure 3.10: Experiment: SPMSM Rated speed startup and reversal under FCS-PTC.

Figure 3.11 is the torque and flux current tracking performance. The predicted value tracks the reference well, therewith, the (filtered) real value also highly aligns with the reference.

The system under load variations are tested. In figure 3.12, the load torque are given in steps for both directions and the machine works at both generator and motor modes. The torque tracks its reference fast, and as a result, the speed drop is comparatively small.

Similarly, the robustness of system parameters are also tested. Figure 3.13 shows the stator resistance value has almost no sensitivity when it has 50% increase and decrease.

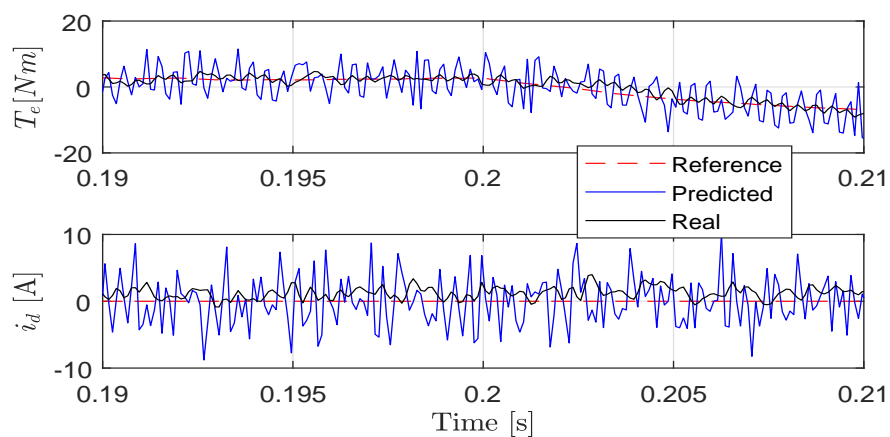


Figure 3.11: Experiment: SPMSM Torque and Flux Tracking Performance under FCS-PTC.

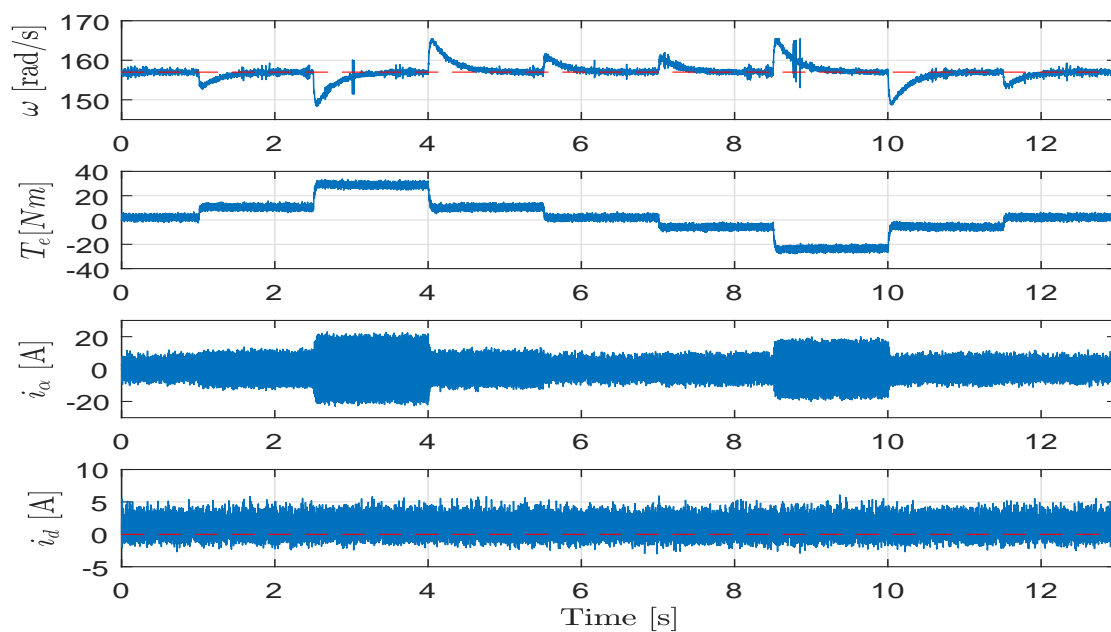


Figure 3.12: Experiment: SPMSM FCS-PTC Performance under Torque Variations.

For parameter sensitivity tests, figure 3.13 shows the R_s robustness in experiment.

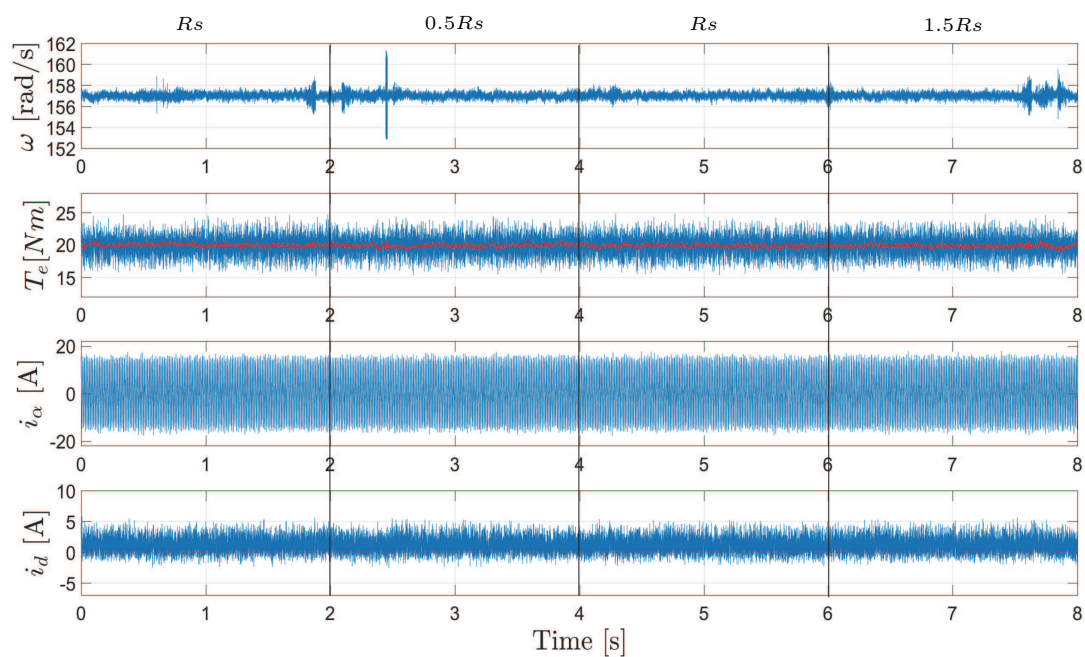


Figure 3.13: Experiment: SPMSM FCS-PTC Performance under R_s Variation.

Figure 3.14 shows that the stator inductance variations also lead to minor miscontrol.

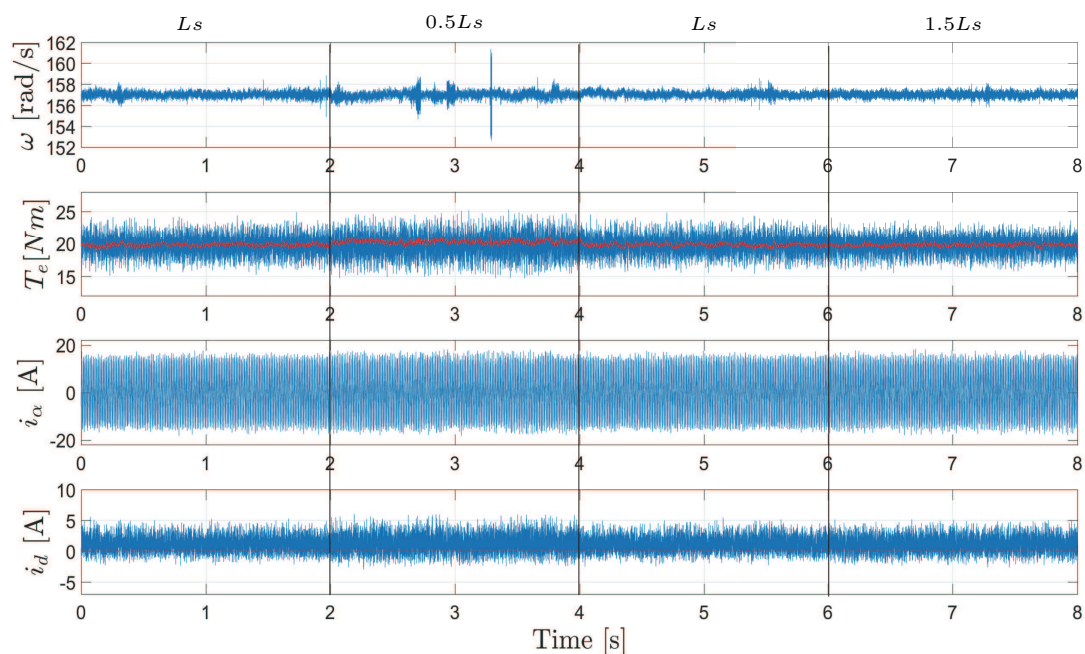


Figure 3.14: Experiment: SPMSM FCS-PTC Performance under L_s Variation.

However, the system is sensitive but only in short time to permanent magnet variable variations with 30% mismatch in parameters. For example, in figure 3.15, when the permanent

magnet flux in control is decreased to 0.7 of the real value, the control is therefore disturbed and speed increases above reference. As a result the torque control force the torque reference (red line in figure) to reduce thereafter to balance this speed variation. However, the real torque is only instantly increased. After around 0.2 s, the new balance with the deviated torques reference and real values is achieved, thanks to the self adjustment of the close loop. Since the permanent magnet flux value doesn't change frequently, this robustness is acceptable.

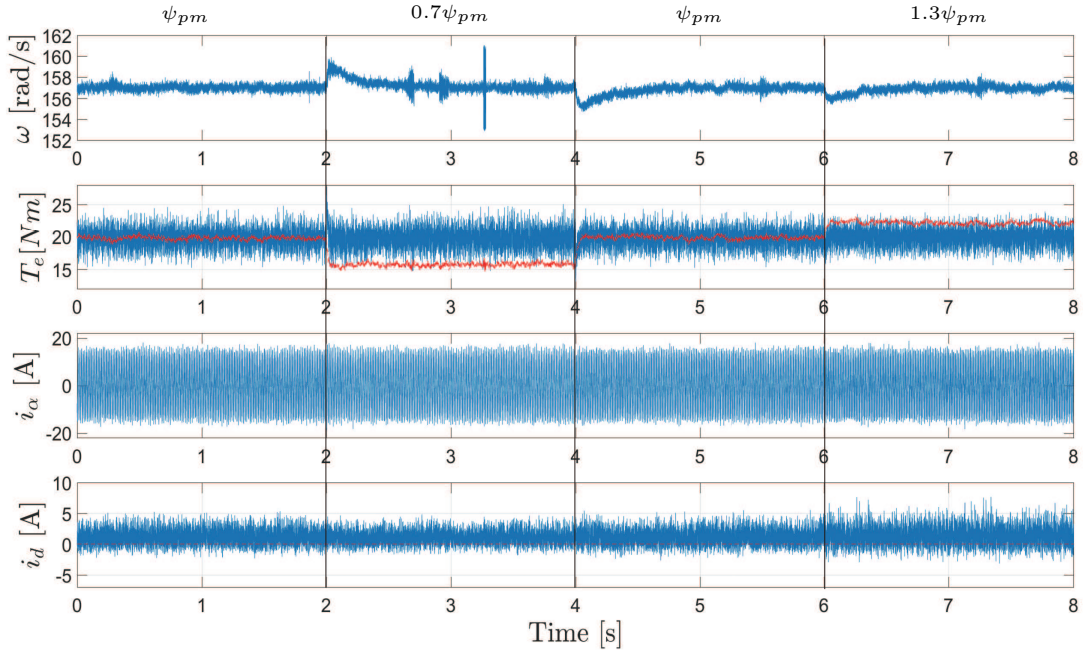


Figure 3.15: Experiment: SPMSM FCS-PTC Performance under ψ_{pm} Variation.

3.4 Finite-Control-Set Predictive Current Control

FCS-PCC method was firstly proposed in 2007 [73]. It is also named as FCS-PFOC [62], because its reference currents are firstly given in the dq frame, which is similar as FOC, and then transferred back to $\alpha\beta$ frame terms for the cost function. The schematic of FCS-PCC for IPMSM is shown in figure 3.16. Except the outer speed PI controller, FCS-PCC's inner current controllers consist of three parts: stator flux and current estimation and prediction; current prediction and Park inverse transformation from dq to $\alpha\beta$ frame; and cost function optimization.

3.4.1 Estimation and Prediction

FCS-PCC also requires the estimation and prediction of stator flux and prediction of stator currents. Its calculation is actually similar and comparatively simpler than FCS-PTC. The prediction steps are the same as that of FCS-PTC from (3.5) to (3.7). After that, the predicted currents are further transformed into the stator $\alpha\beta$ frame through Park transformation as:

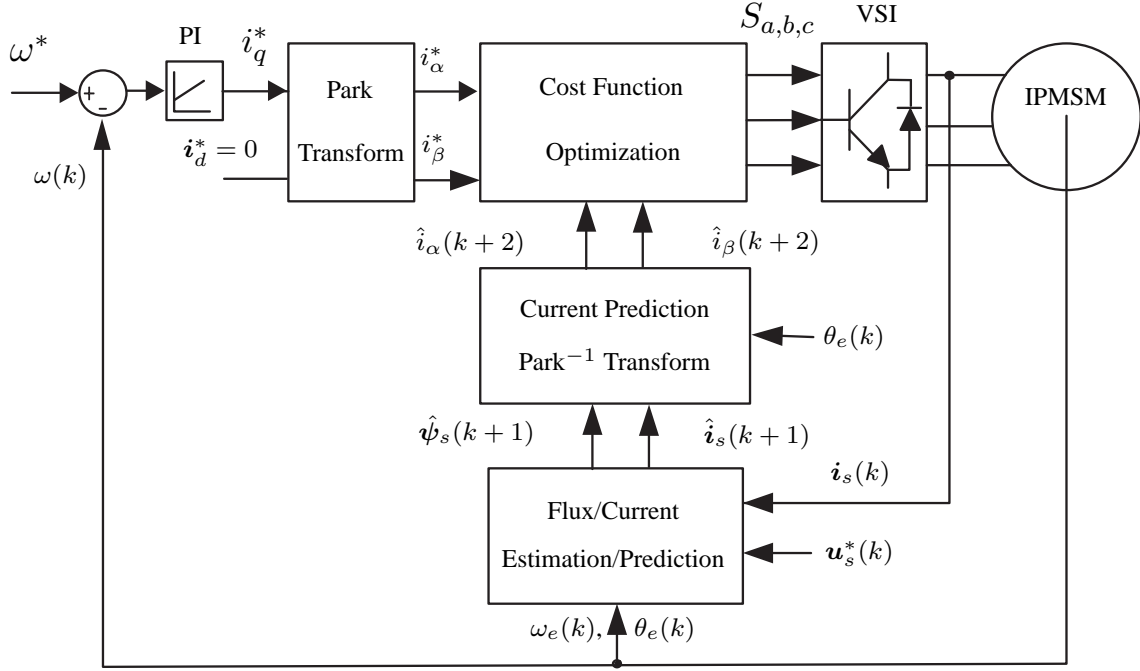


Figure 3.16: FCS-PCC for IPMSM.

$$\begin{cases} \hat{i}_\alpha(k+2) = \cos(\theta_e) \cdot \hat{i}_d(k+2) - \sin(\theta_e) \cdot \hat{i}_q(k+2) \\ \hat{i}_\beta(k+2) = \sin(\theta_e) \cdot \hat{i}_d(k+2) + \cos(\theta_e) \cdot \hat{i}_q(k+2) \end{cases} \quad (3.11)$$

where θ_e is the electrical angle of rotor. And similarly, the reference currents from dq frame is also transformed into stator reference frame as:

$$\begin{cases} i_\alpha^* = \cos(\theta_e) \cdot i_d^* - \sin(\theta_e) \cdot i_q^* \\ i_\beta^* = \sin(\theta_e) \cdot i_d^* + \cos(\theta_e) \cdot i_q^* \end{cases} \quad (3.12)$$

where i_d^* is still set as 0 for simplicity of control and fair comparison between FCS-PCC with the previous FCS-PTC. i_q^* is directly obtained through PI speed controller, because when $i_d = 0$, and according to (2.26), i_q^* is proportional to T_e^* .

3.4.2 Cost Function Optimization

The design of cost function differentiates the control of FCS-PCC from FCS-PTC, where the currents instead of torque and flux are set as the control terms as:

$$g_j = |i_\alpha^* - \hat{i}_\alpha(k+2)_j| + |i_\beta^* - \hat{i}_\beta(k+2)_j| + I_m(k+2)_j \quad (3.13)$$

$I_m(k+2)_j$ is defined the same as in FCS-PTC. No weighting factor is required in FCS-PCC for fair control, because both current control terms are of same attribute.

One thing should be noticed here is that currents should be controlled in $\alpha\beta$ frame instead of dq synchronous reference frame. Otherwise, FCS-PCC is controlling the torque related and flux related terms, and therefore it is essentially still FCS-PTC instead of FCS-PCC.

3.4.3 Simulation and Experimental Verification

Similar to FCS-PTC, FCS-PCC is also simulated on IPMSM and experimented on SPMSM at different speed ranges and load conditions. The simulations and experimental results are shown and analyzed in the following parts. For easiness of control, the operation conditions and speed PI parameters of FCS-PCC are set to be the same as FCS-PTC in both simulations and experiments.

Simulation 1 is to find out the speed startup and reversal process.

Figure 3.17 shows speed, torque, current and flux of this process. Compare this figure with figure 3.3, it is seen that the dynamics as well as steady state performance of FCS-PCC are almost identical as FCS-PTC, except the torque ripples' range of FCS-PCC is slightly larger than that of FCS-PTC, which is consistent of the phenomenon found on the comparison tests on IM conducted in [40].

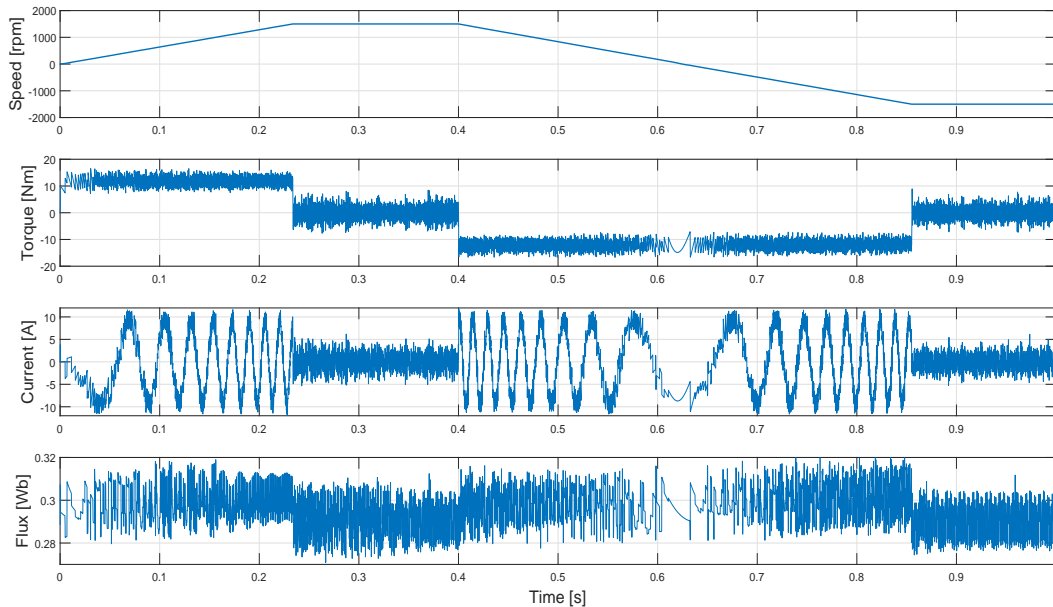


Figure 3.17: Simulation: Rated speed start up and reversal of FCS-PCC.

Figure 3.18 shows currents' tracking performance, which is as good and precise as the torque and flux tracking performance in FCS-PTC.

Simulation 2 is to find out the speed performance under torque variations.

Figure 3.19 shows speed, torque, current and flux of this process, similar as the same simulation of FCS-PTC, there is a slight speed drop. Since the discussion of PI parameters compensation is not in the scope of this chapter and this problem also exists in FOC and other control strategies, it will not be considered as a drawback for the predictive control itself.

The zoomed-in torque and switching states during torque variation transient are shown in figure 3.20, whose torque response is similar to the case of FCS-PTC in figure 3.6, but the band of ripples are larger because of FCS-PCC's indirect control of torque leads to larger ripples than the case in FCS-PTC with direct control of torque.

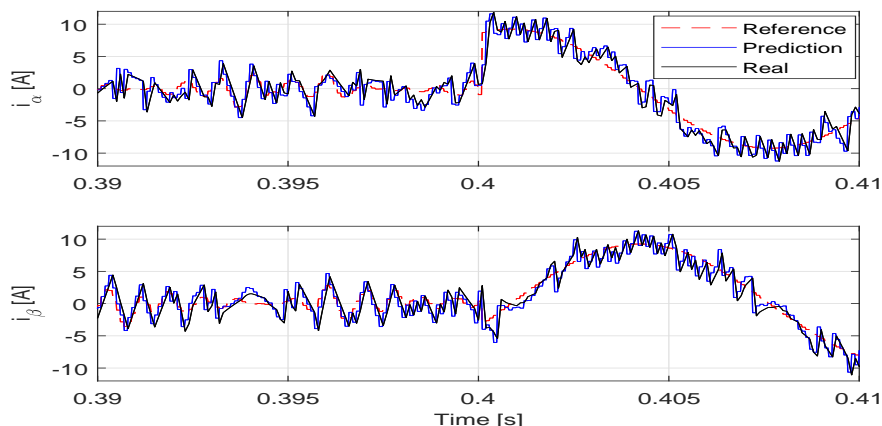


Figure 3.18: Simulation: Current Tracking Performance of FCS-PCC.

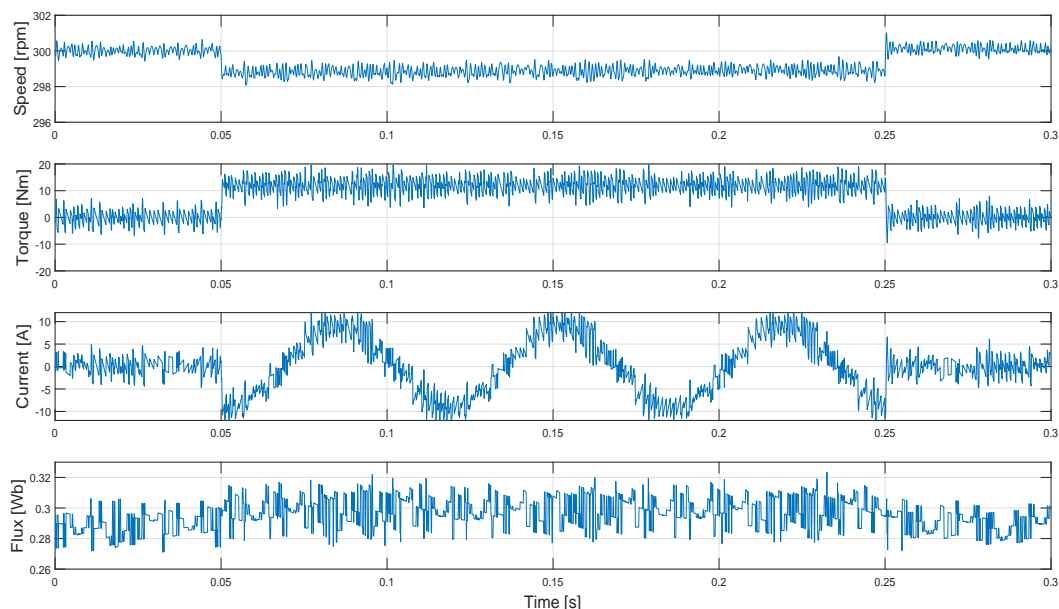


Figure 3.19: Simulation: FCS-PCC Performance under Torque Variations.

Simulation 3 tests the robustness of FCS-PCC.

Figure 3.21 shows the system performance against the variations of R_s . Compared to FCS-PTC, FCS-PCC has a much larger robust range of R_s of [1%,150%].

Figure 3.22 shows the system performance against the variations of L_d . Compared to FCS-PTC, FCS-PCC has a slightly smaller robust range of L_d .

Figure 3.23 shows the system performance against the variations of L_q . Compared to FCS-PTC, FCS-PCC has a similar robust range of L_q .

The robustness differences between FCS-PTC and FCS-PCC are also consistent with the test results found in the FCS-MPC of IM [40].

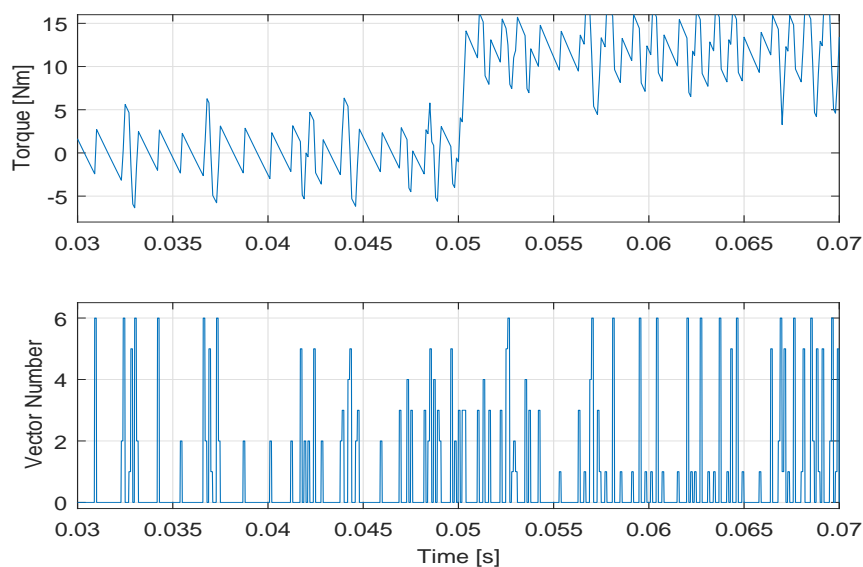


Figure 3.20: Simulation: Torque and Voltage Vectors of FCS-PCC under Torque Variations.

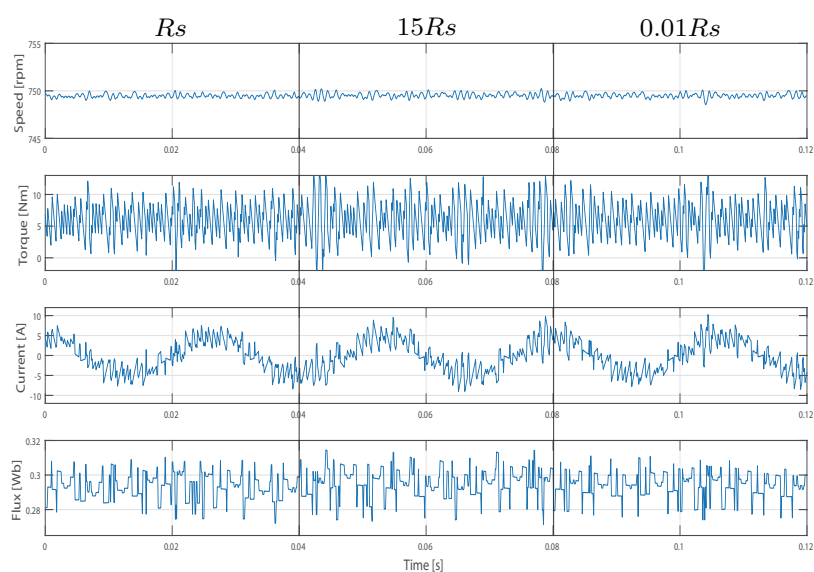


Figure 3.21: Simulation: FCS-PCC performance with R_s Variations.

Experiments of FCS-PCC is also conducted on SPMSM.

Figure 3.24 is the speed startup and reversal performance. The step startup process is slightly faster than FCS-PTC because the current limit is increased. And the ramp reversal is also well tracked therefore having the same reversal time. Same as the previous simulation results, FCS-PCC contains larger torque ripples, which can be considered as a tradeoff of better current performance (i.e. less ripples).

Figure 3.25 is the zoomed-in current tracking performance at the starting short transient of

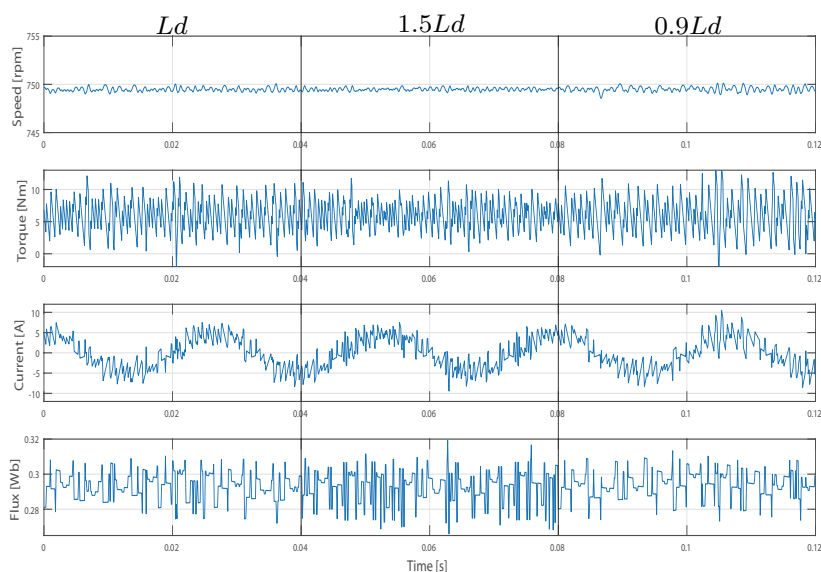


Figure 3.22: Simulation: FCS-PCC performance with L_d Variations.

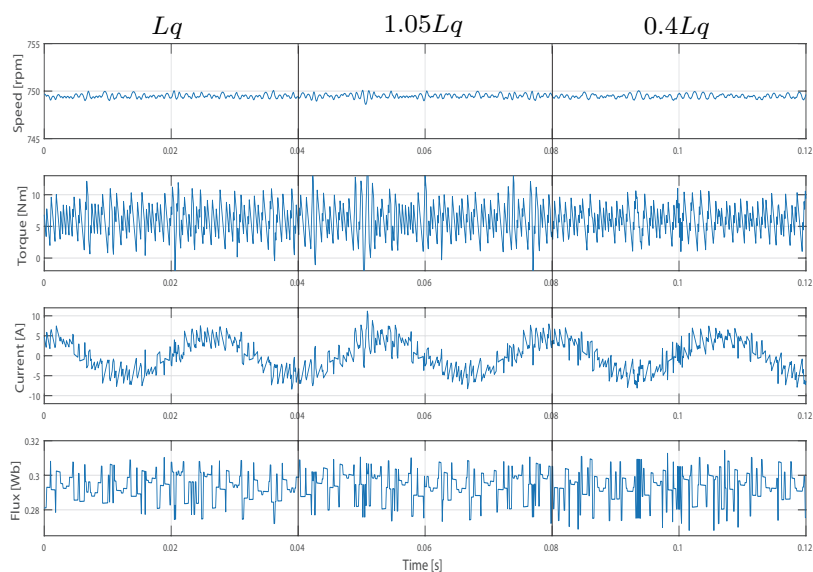


Figure 3.23: Simulation: FCS-PCC performance with L_q Variations.

speed reversal. Similar as FCS-PTC, the predicted and therefore the real current tracks the reference well. Though the predicted and real current ripples are not small, which is intrinsic in light of the small stator inductance.

From the torque variation experimental result in figure 3.26, the torque and current (including the flux related current) relation are the consistent to the previous experiment.

Figure 3.27 shows FCS-PCC's similarly good R_s robustness as in FCS-PTC.

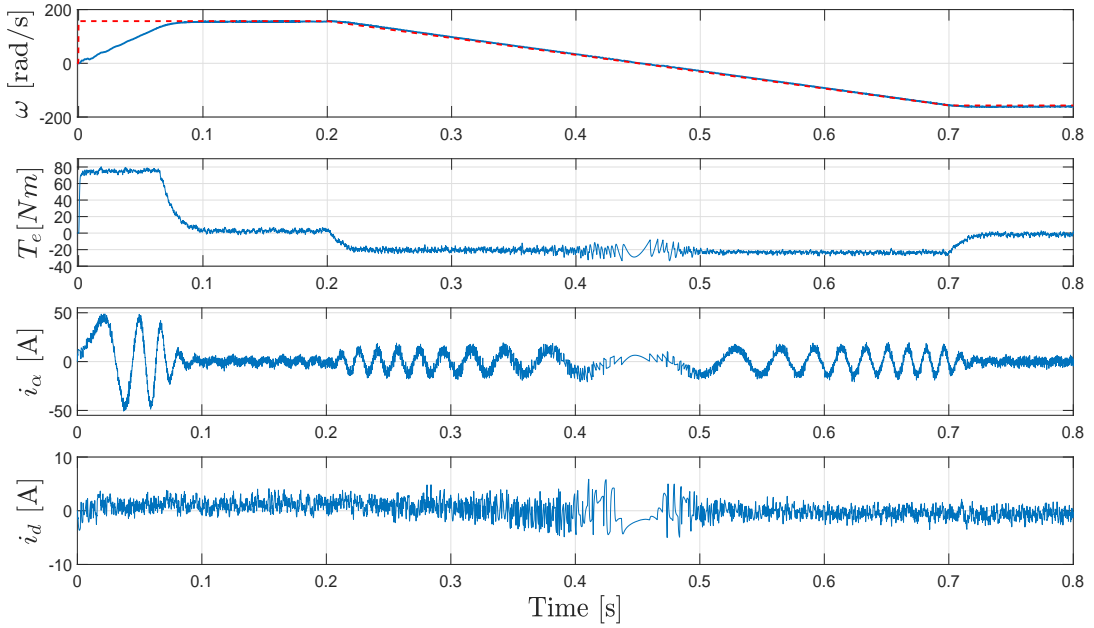


Figure 3.24: Experiment: Rated speed startup and reversal of FCS-PCC.

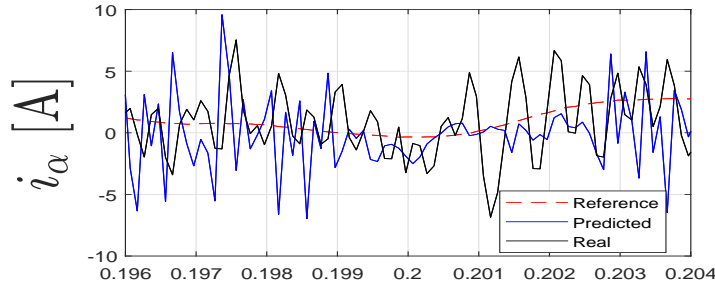


Figure 3.25: Experiment: Current Tracking Performance of FCS-PCC.

And figure 3.28 shows FCS-PCC's similar L_s robustness as in FCS-PTC.

In figure 3.29, compared to the correspond in figure 3.15, FCS-PCC has slightly better ψ_{pm} robustness as in FCS-PTC in light of its smaller speed change when the same values of sudden ψ_{pm} variation is conducted in control.

3.5 Deadbeat MPC

As mentioned in chapter 3.1, FCS-MPC, when implemented in the model inverse way, achieves its corresponding deadbeat form, i.e. deadbeat MPC (DBMPC). Since PCC has in general less calculation effort, simpler control algorithms when compared to PTC, so as to deadbeat PCC (DBPCC). As a result, DBPCC for IPMSM is designed and verified in this sub-chapter as example for continuous and deadbeat MPCs.

The schematic of DBPCC of this work is shown in figure 3.30. It is similar as FCS-PCC,

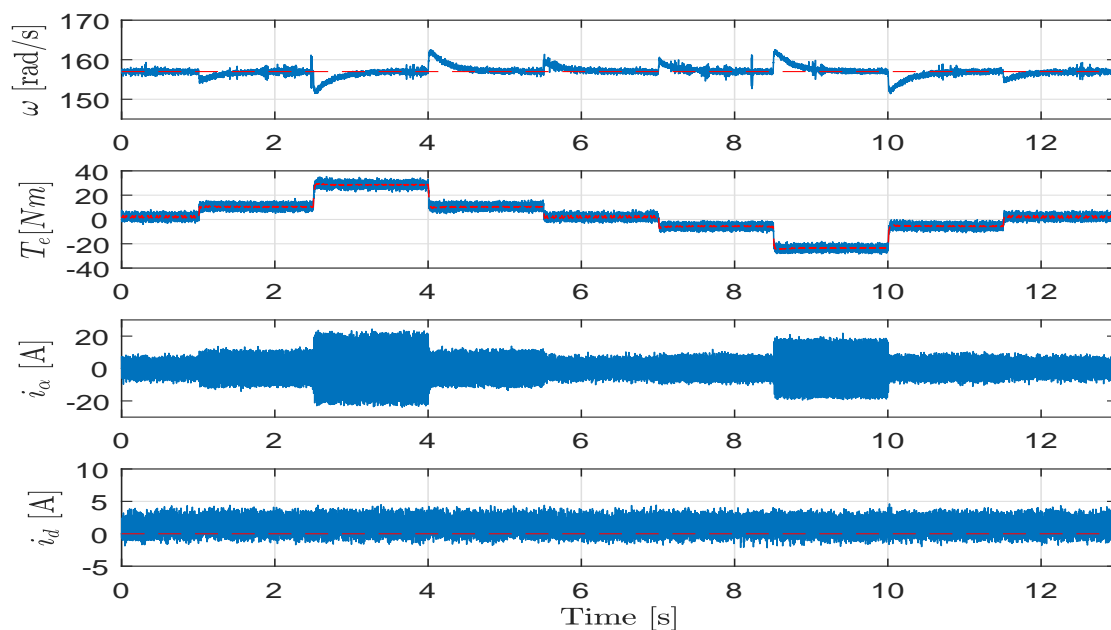


Figure 3.26: Experiment: FCS-PCC Performance under Torque Variations.

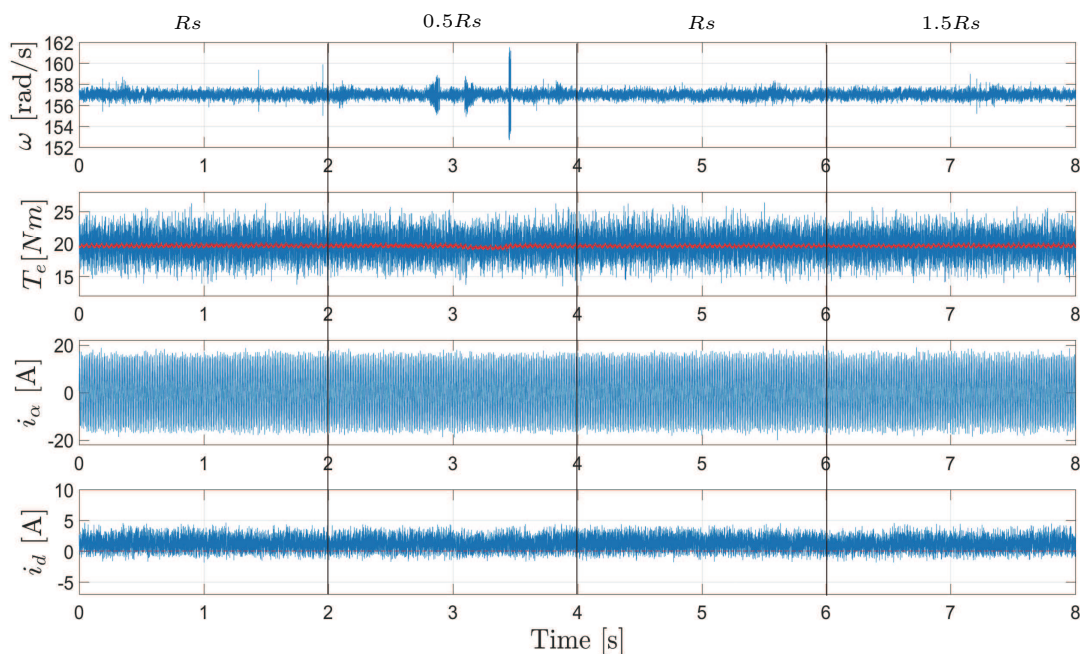


Figure 3.27: Experiment: FCS-PCC Performance under R_s Variation.

except the cost function optimization is replaced by a deadbeat controller that calculates the continuous reference voltages by equating the current references and predictions in analytical manner instead of selecting discrete voltage vectors from finite candidate set through cost function optimization in numerical manner.

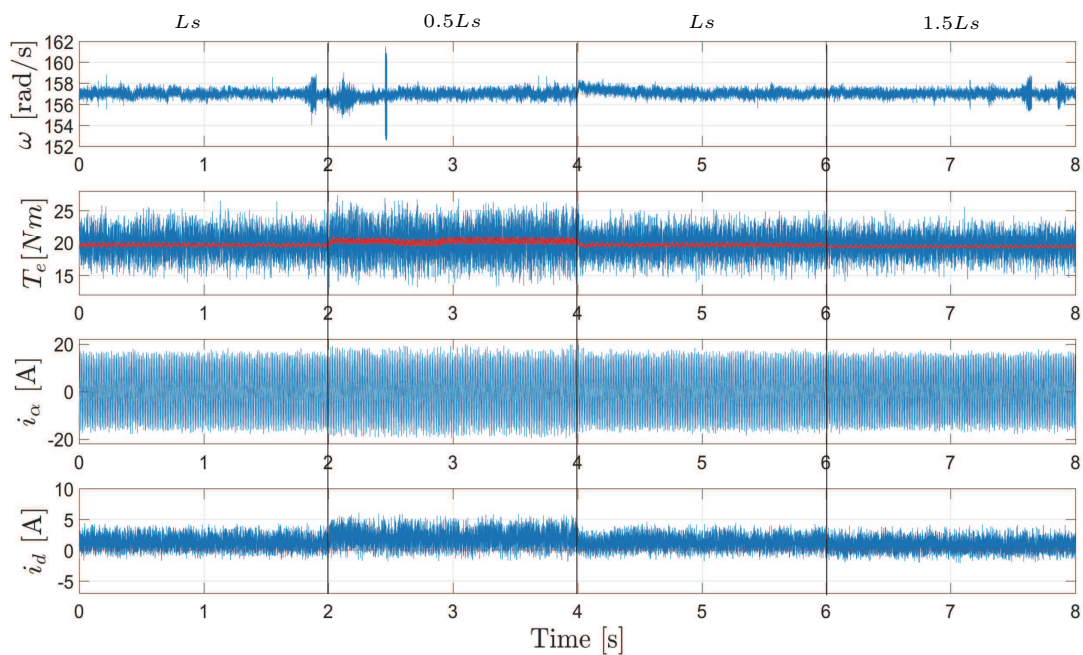


Figure 3.28: Experiment: FCS-PCC Performance under L_s Variation.

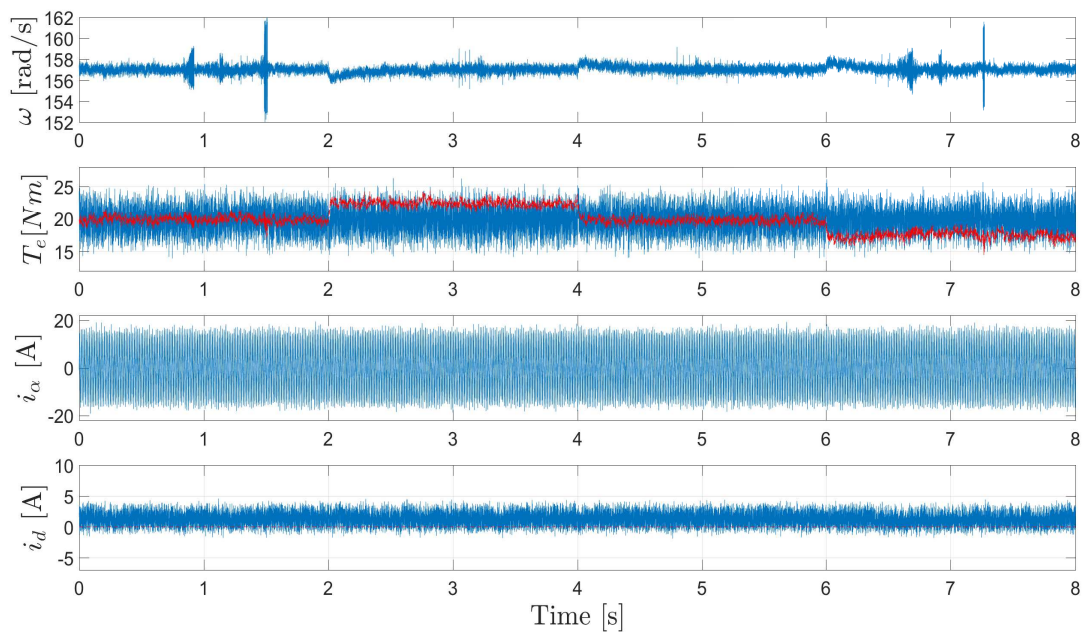


Figure 3.29: Experiment: FCS-PCC Performance under ψ_{pm} Variation.

3.5.1 Continuous Reference Voltages Prediction

The derivation of DBPCC is very simple and intuitive, based on the previous equations for the derivations of FCS-PTC and FCS-PCC. Review the sub-chapter 3.3, instead of using predicted

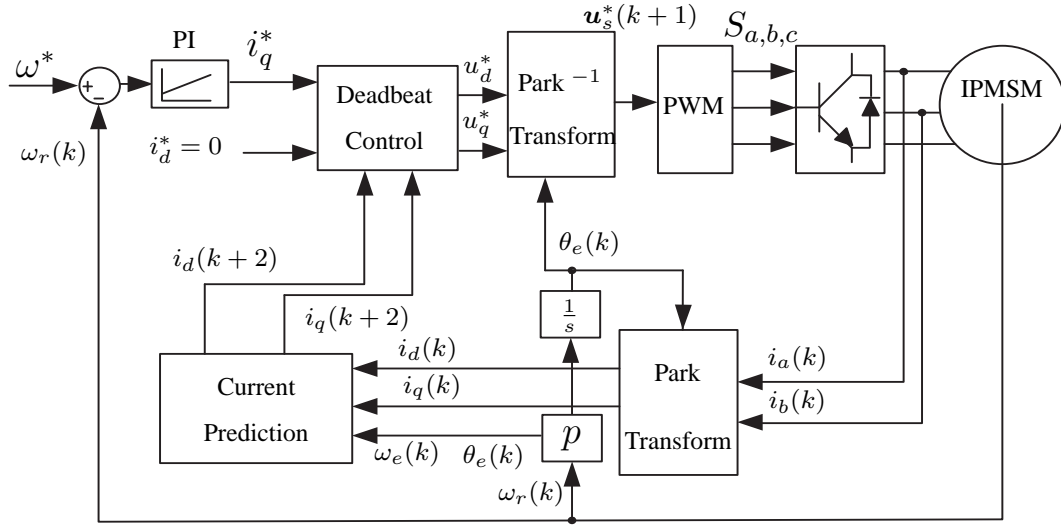


Figure 3.30: DBPCC.

flux equation to predict $i_d(k+2)$ and $i_q(k+2)$ as in (3.7), the current prediction is obtained with one step forward as in (3.4):

$$\begin{cases} \hat{i}_d(k+2) = \hat{i}_d(k+1) + \frac{T_s}{L_d} \cdot [-R_s \cdot \hat{i}_d(k+1) + \\ \quad \omega_e(k+1) \cdot L_q \cdot \hat{i}_q(k+1) + u_d(k+1)] \\ \hat{i}_q(k+2) = \hat{i}_q(k+1) + \frac{T_s}{L_q} \cdot [-R_s \cdot \hat{i}_q(k+1) - \\ \quad \omega_e(k+1) \cdot L_d \cdot \hat{i}_d(k+1) + u_q(k+1) \\ \quad - \omega_e(k+1) \cdot \psi_{pm}] \end{cases} \quad (3.14)$$

In fact, during experimental implementation, the next step's electrical speed $\omega_e(k+1)$ is replaced by the value of its current control cycle, $\omega_e(k)$, because the speed prediction requires the measurement of the real load torque, which increases hardware cost with extra torque meter. Actually, this approximation is ignorable in light of the large time constant of electrical angular speed ω_e of IPMSM that is proportional to rotor mechanical speed ω_r . It is found in (3.14) that the reference voltages $u_d(k+1)$ and $u_q(k+1)$ are exclusively dependent on the stator currents predictions $\hat{i}_d(k+1)$ and $\hat{i}_q(k+1)$. Therefore, the continuous reference voltages for the next control period is predicted through the calculation by substituting current references i_d^* and i_q^* into to (3.14) to replace $\hat{i}_d(k+1)$ and $\hat{i}_q(k+1)$ as following:

$$\begin{cases} u_d^*(k+1) = \frac{L_d}{T_s} \cdot [i_d^* - \hat{i}_d(k+1)] + R_s \cdot \hat{i}_d(k+1) \\ \quad - \omega_e(k) \cdot L_q \cdot \hat{i}_q(k+1) \\ u_q^*(k+1) = \frac{L_q}{T_s} \cdot [i_q^* - \hat{i}_q(k+1)] + R_s \cdot \hat{i}_q(k+1) \\ \quad + \omega_e(k) \cdot L_d \cdot \hat{i}_d(k+1) \\ \quad + \omega_e(k+1) \cdot \psi_{pm} \end{cases} \quad (3.15)$$

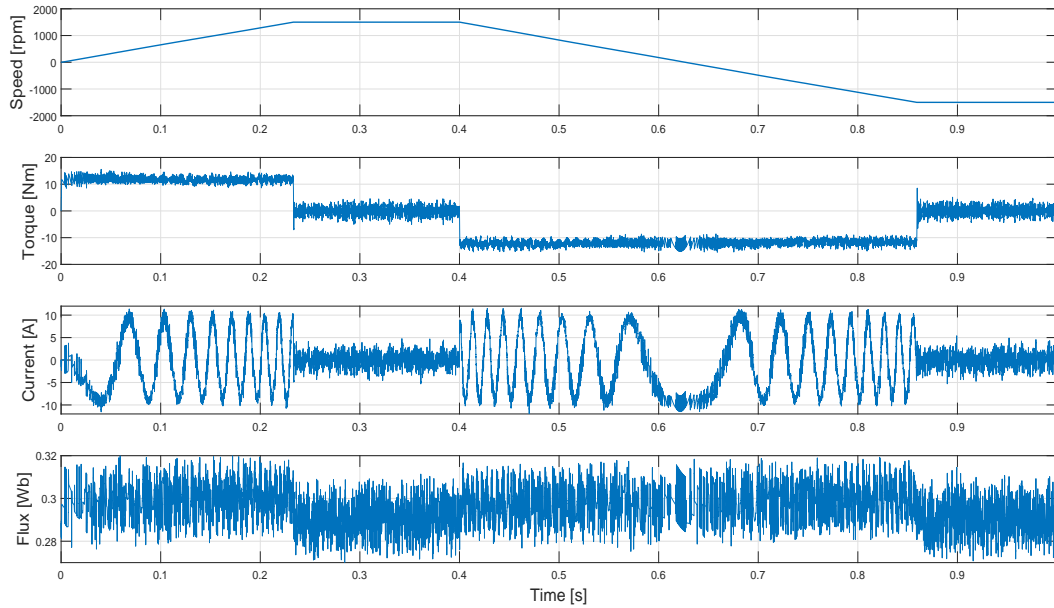


Figure 3.31: Simulation: Rated speed start up and reversal of DBPCC.

3.5.2 Simulation and Experimental Verification

All simulation and experiments of DBPCC are conducted with the same sampling/control frequency ($10k Hz$) on the same IPMSM and SPMSM with the same speed PI controller parameters as the previous two FCS-MPCs. The PWM frequency is set to be the same as sampling frequency.

Simulation 1 is to find out the speed startup and reversal process.

Figure 3.31 shows speed, torque, current and flux of this process. Compare this with figure 3.17 with the previous same simulation results for both PTC and PCC, it is found that DBPCC system have better torque and current performance with smaller ripples. But the dynamics (i.e. response time) are very similar. This shows that DBPCC has comparable dynamics and better steady state performance as FCS-MPC at same sampling frequency. This is because the precise alignment of the stator currents on their references through deadbeat control and the adoption of PWM (SVPWM, or: SVM is used in this work as PWM) for a fixed higher average switching frequency than the FCS-MPCs. However, in light DBPCC has SVM in system, which means higher switching frequency and therewith "smoother" values of variables as in FOC, it is not fair to conclude that DBPCC has better performance—it depends on the hardware/software ability and application requirements.

Simulation 2 is to find out the speed performance under torque variations.

Figure 3.32 shows speed, torque, current and flux of this process, similar as FCS-MPC, there is a slight speed drop.

The zoomed-in torque and switching states during torque variation transient are shown in figure 3.33. It is seen that only active vectors are given during torque increasing transient to offer fastest response. This is because DBPCC, with the PWM which offers shorter duty ratio

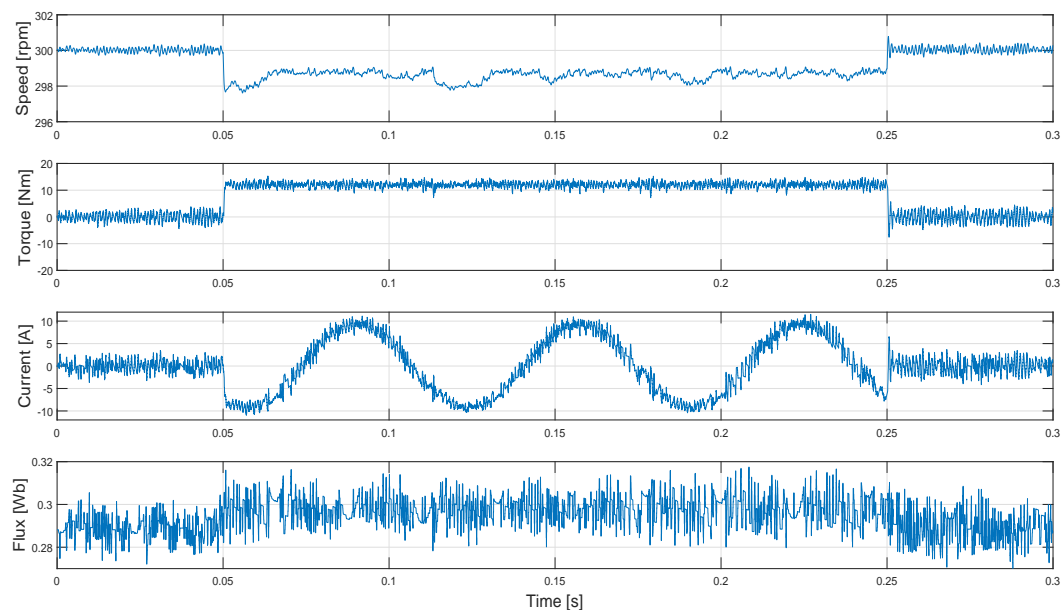


Figure 3.32: Simulation: DBPCC Performance under Torque Variations.

(for FCS-MPC, duty ratio is 100%) for different vectors, zero vectors are not needed as in FCS-MPC overshoot caused by active vectors hold for the comparatively long whole control period. The switching frequency of DBPCC is $30kHz$, which is almost 10 times as that of FCS-MPC as shown in figure 3.43.

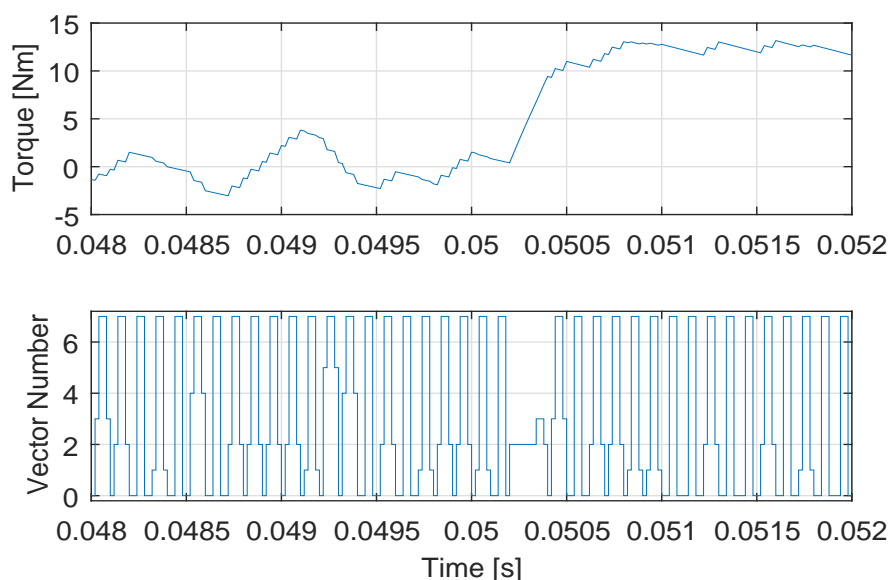


Figure 3.33: Simulation: Torque and Voltage Vectors of DBPCC under Torque Variations.

Simulation 3 checks the robustness of DBPCC.

Figure 3.34, 3.35 and 3.36 show the system performance against the variations of R_s , L_d and L_q , respectively. Compared to FCS-PTC and FCS-PCC, DBPCC has similar robust ranges of L_d and L_q but a smaller range of R_s , which means FCS-MPCs are robuster against R_s variation. Though when there is no parameter deviation, DBPCC can achieve preciser control and less ripples at same sampling frequency condition at FCS-MPC, it is at the same time more sensitive against parameter mismatch. Therefore, it has higher requirements for model precision to guarantee its good performance.

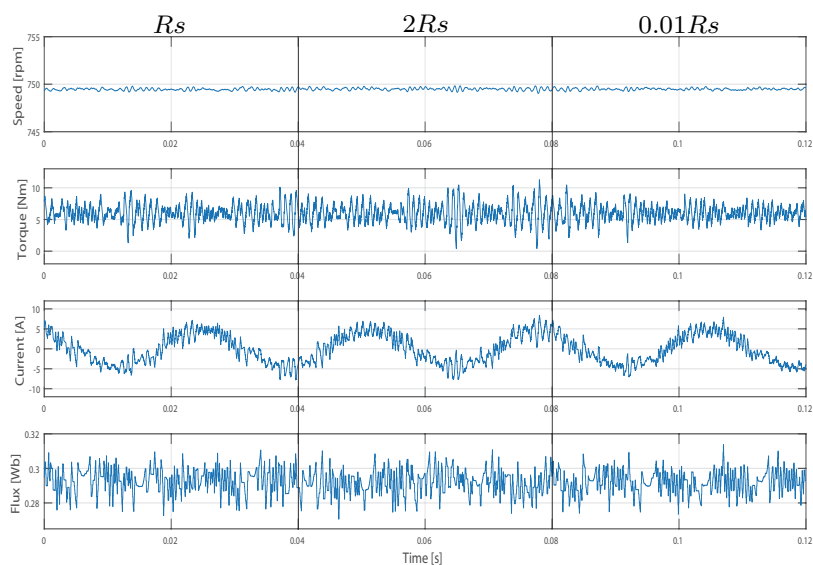


Figure 3.34: Simulation: DBPCC performance with R_s Variations.

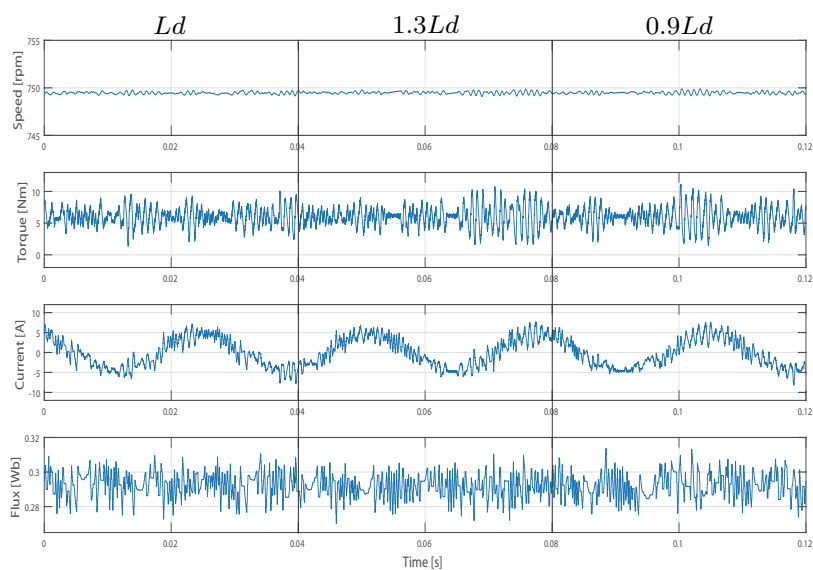


Figure 3.35: Simulation: DBPCC performance with L_d Variations.

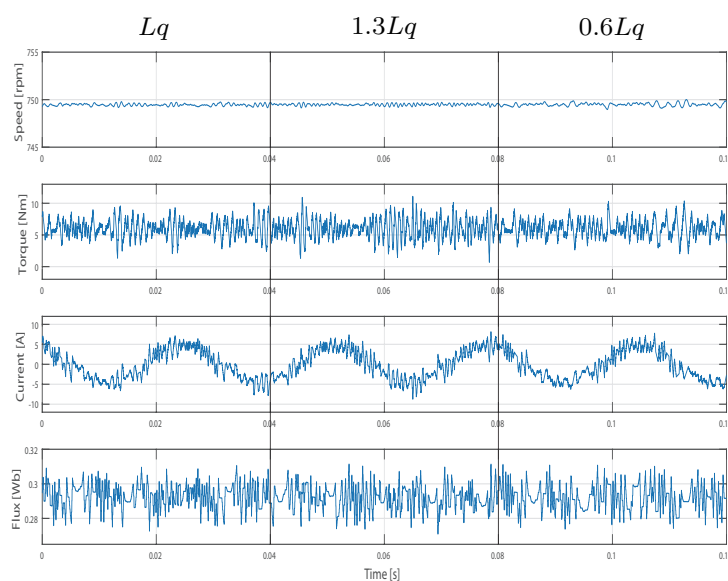


Figure 3.36: Simulation: DBPCC performance with L_q Variations.

Figure 3.37 is the speed reversal experiment of DBPCC on SPMSM. Compared to the one of PCC, it has exactly the same dynamics and much smaller torque and current ripples.

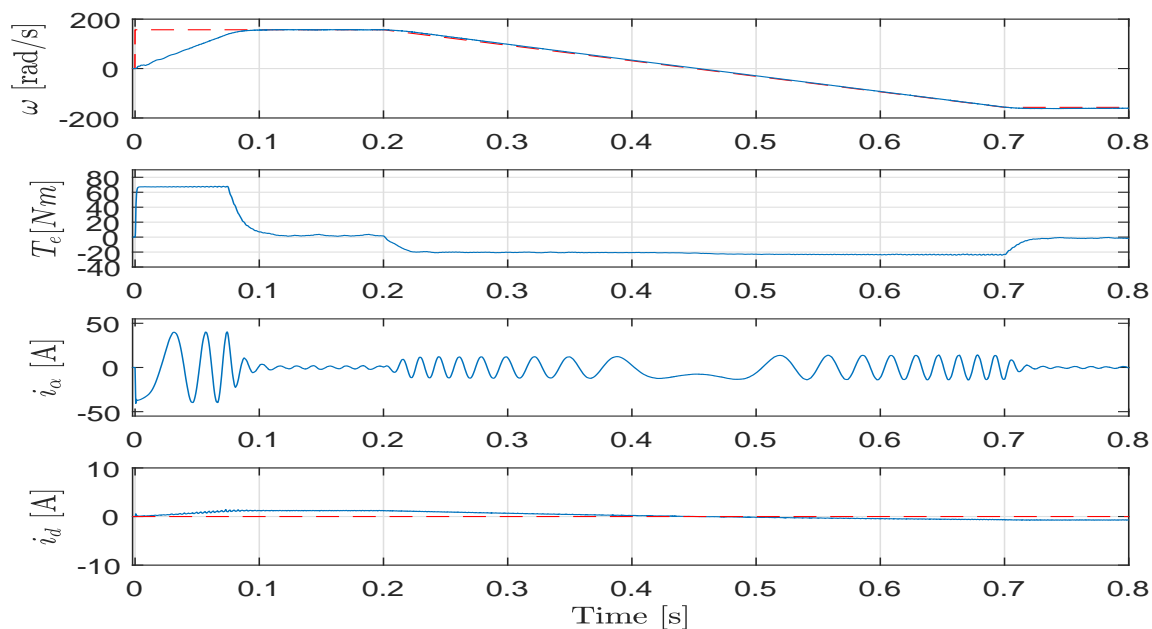


Figure 3.37: Experiment: Rated speed start up and reversal of DBPCC.

Figure 3.38 shows reference voltages during the speed deceleration transient. It is seen that when the torque and current magnitude are kept as their maximum constant values for fastest deceleration, as speed reduces, the magnitude of stator voltages are also reduced.

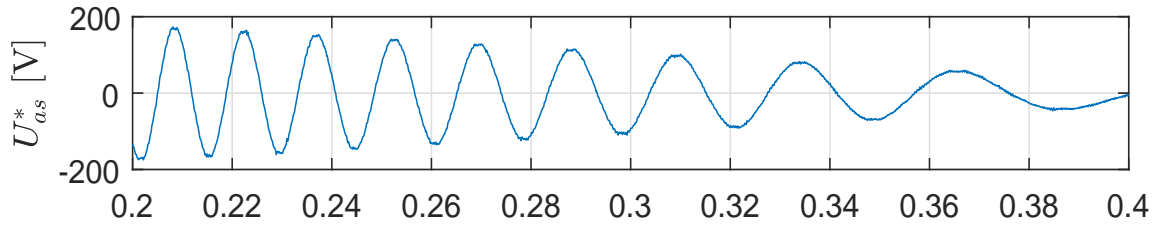


Figure 3.38: Experiment: Stator Reference Voltages during speed deceleration of DBPCC.

The torque variation performance of DBPCC in figure 3.39 shows that the speed oscillations are also smaller, which is directly decided by the torque performance.

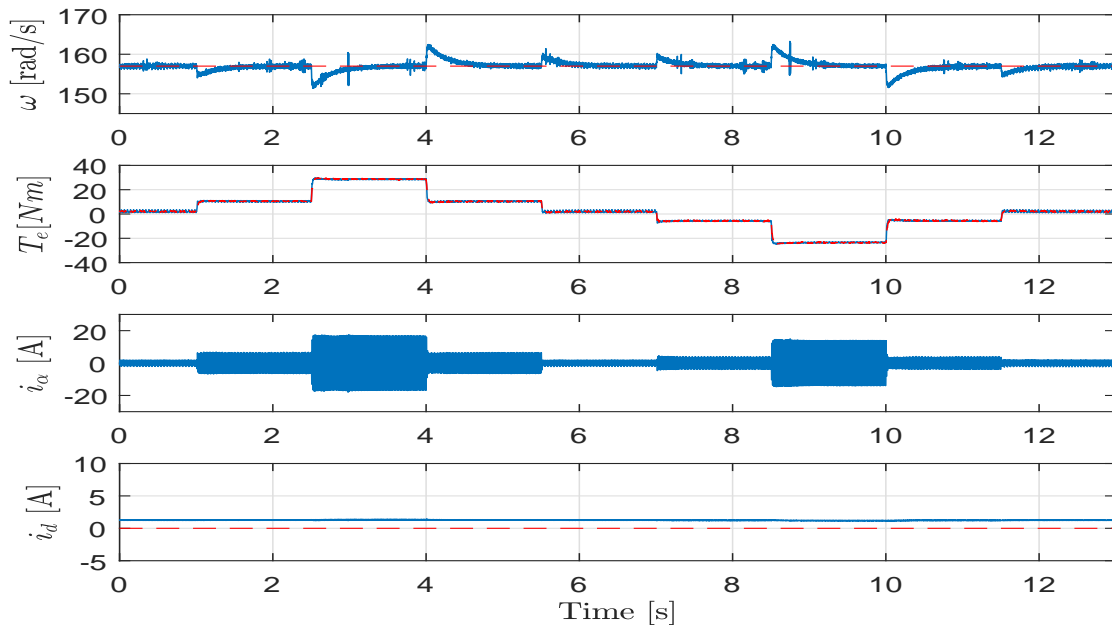
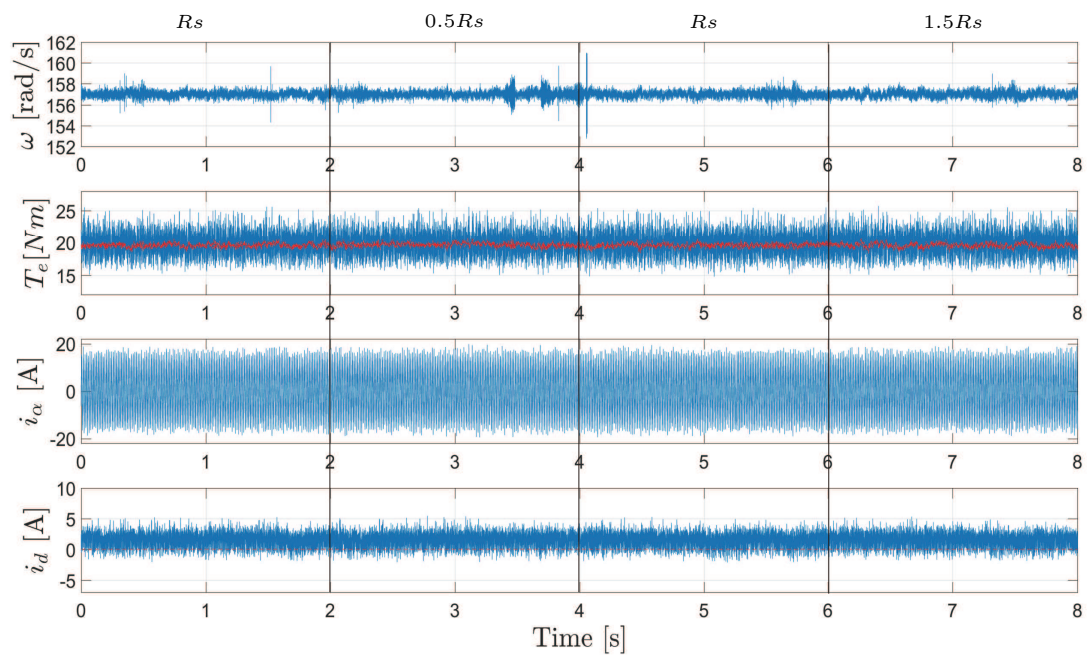
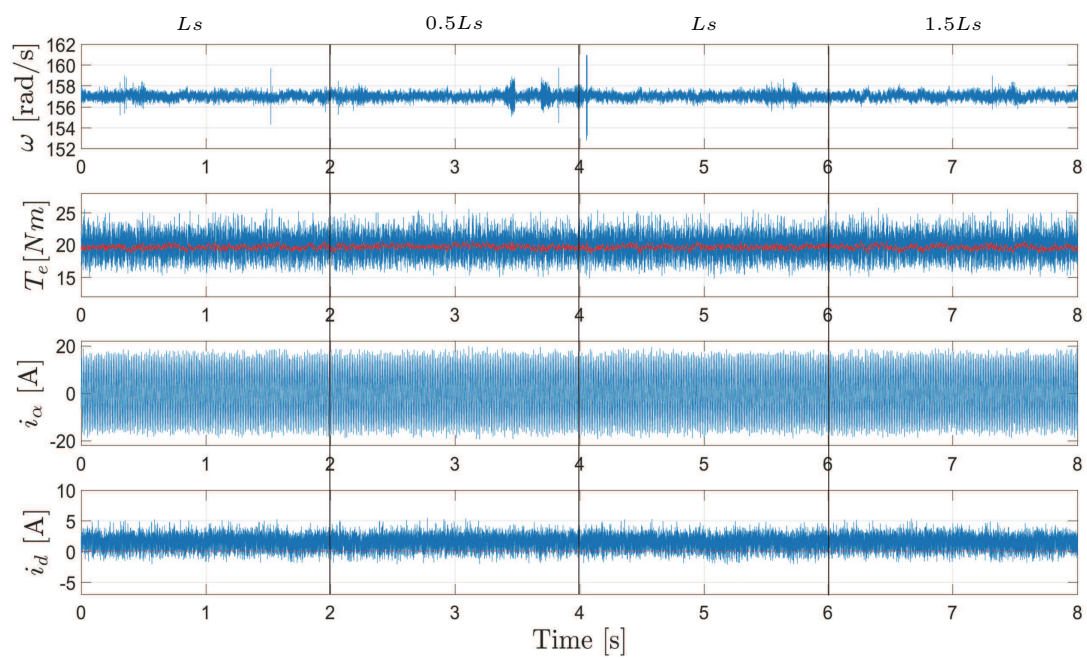


Figure 3.39: Experiment: DBPCC Performance under Torque Variations.

The R_s , L_s and ψ_{pm} robustness of DBPCC in figure 3.40 to figure 3.42 show that DBPCC is much robust than both previous FCS-MPCs. The reason of this lies again in that DBPCC has higher switching frequency and shorter individual vector application sector, which enable refinement and faster control, when the extra PWM module and increased switching frequency and loss is not in consideration.

The average algorithm's turnaround time of DBPCC in experiments is around $17\mu s$, which is only 65% of the average turnaround time ($26\mu s$) of FCS-MPC.

Figure 3.40: Experiment: DBPCC Performance under R_s Variation.Figure 3.41: Experiment: DBPCC Performance under L_s Variation.

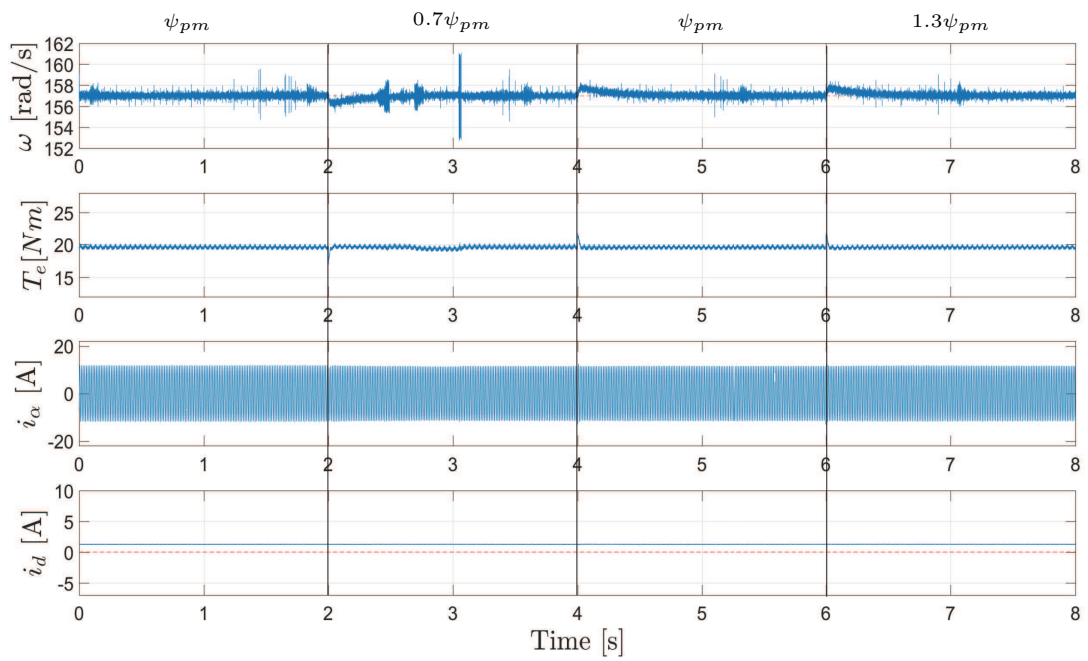


Figure 3.42: Experiment: DBPCC Performance under ψ_{pm} Variation.

3.6 Conclusion

In this chapter, two FCS-MPCs and a typical continuous MPC are explained and analyzed through simulations and experiments.

The analysis of all three methods on IPMSM of the loaded state is shown in the bar chart in figure 3.43. As can be seen that both MPCs have similar performance, except PCC has smaller speed variations but larger torque variations and PCC has slightly higher current THD. It is because in PTC, torque is directly and more precisely controlled in cost function. Therefore, generally speaking, both FCS-MPCs have similar performances. DBPCC as a continuous MPC is actually hard to be fairly compared with FCS-MPCs. As can be seen from the chart, it has small variances in both speed and torque as well as THD in sacrifice of much lower switching frequencies.

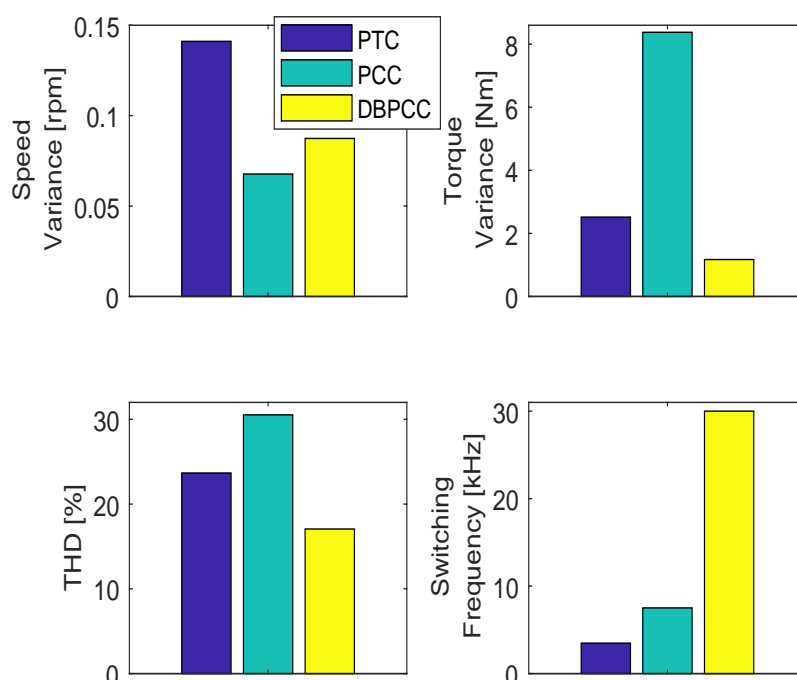


Figure 3.43: Analysis of FCS-PTC, FCS-PCC and DBPCC.

A detailed comparison for different aspects of performance related values for both FCS-MPC and deadbeat MPC is shown in table 3.2.

From this table, it can be concluded that both FCS-MPCs have similar good performances in light of their dynamics, low switching frequencies and nonlinear control/constraint inclusion potential. And no PWM, which means extra software and hardware costs, is required. Therefore, they are promising for many applications.

Meanwhile, since the calculation efforts of DBPCC is much less than that of FCS-MPC, when PWM module is acceptable and system constraints or nonlinearities are not required to be controlled, it is as good an option as FCS-MPC in light of its merits of fast dynamics like

Table 3.2: Comparison of FCS-PTC/PCC and DBPCC.

Features	PTC	PCC	DBPCC
Conceptual complexity	Low	Low	Low
Complexity of implementation	Low	Lower	Lowest
Calculation efforts	Higher	High	Low
PI-current controllers	NO	NO	NO
Use of PWM	NO	NO	YES
Switching frequency	Variable Low	Variable Low	Fixed High
Dynamics	Fast	Fast	Fast
Torque ripples (transient)	Lower	Higher	Lowest
Stator current THD	Lower	Higher	Lowest
System Constraints Included	Easy	Easy	Impossible
Sensitivity to R_s	Low	Lower	High
Sensitivity to L_d	Lower	Low	Low
Sensitivity to L_q	Low	Low	Low
Turn around time	$29\mu s$	$23\mu s$	$17\mu s$

other MPCs. Moreover, its THD and variances of torque and speed as well as other indexes can be further reduced with smaller sampling/control periods. Therefore, it can be considered as an ideal nonlinear alternate of other linear controls with continuous voltage reference and PWM, such as FOC.

CHAPTER 4

Increased FCS-Continuous MPC

In the previous chapter, continuous MPC with deadbeat control method was proposed. This method is simple and has low calculation efforts, but it includes no cost function. Therefore, system constraints and nonlinearities cannot be controlled. To overcome this drawback, in this chapter, two cost-function-including solutions for continuous MPC with constant switching frequency through an increased finite-control-set are proposed and verified by simulations and experiments. Since their number of candidate voltage vectors in control set has been largely increased to generate more voltage vectors covering the voltage plane, they are considered as continuous or quasi continuous MPC, and PWM can be applied. As a results, they are named as "Increased FCS-Continuous MPC" or "IFCS-MPC" for short.

4.1 Dichotomy-based IFCS-PCC

A class of numerical method of quasi-continuous reference voltage calculation based on dichotomy is applied in the sub-chapters to generate the optimized reference voltage vectors selected as the input of PWM before switching the inverter. Since this method is an extension and selection mechanism for control set and it is not directly related to the base control strategies of FCS-MPC, only FCS-PCC will be taken for example of application.

4.1.1 Fan Dichotomy-based Method

The first method is initially proposed and applied on an FCS-PTC SPMSM by Ma [63]. It is firstly called "dichotomy-base method" by us in [65] with the application on an FCS-PCC IM. And in this work, to differentiate it with the other method in this method, it is named with more detail of its vector selection range as "fan dichotomy-base method". For extension of application and comparison purposes, it will be verified on an FCS-PCC controlled IPMSM system.

Fan Dichotomy-based IFCS-PCC has exactly the same process of flux and current estimation and prediction as in the conventional FCS-PCC introduced in the last chapter, except its candidate voltage vectors' formation and selection principles enable it to generate continuous reference as the one calculated from deadbeat, though its calculation and implementation complexity is higher than deadbeat PCC. Therefore, its schematic diagram, as shown in figure 4.1, is similar as the one of FCS-PCC in figure 3.16, except SVM is added as in Deadbeat MPC of figure 3.30.

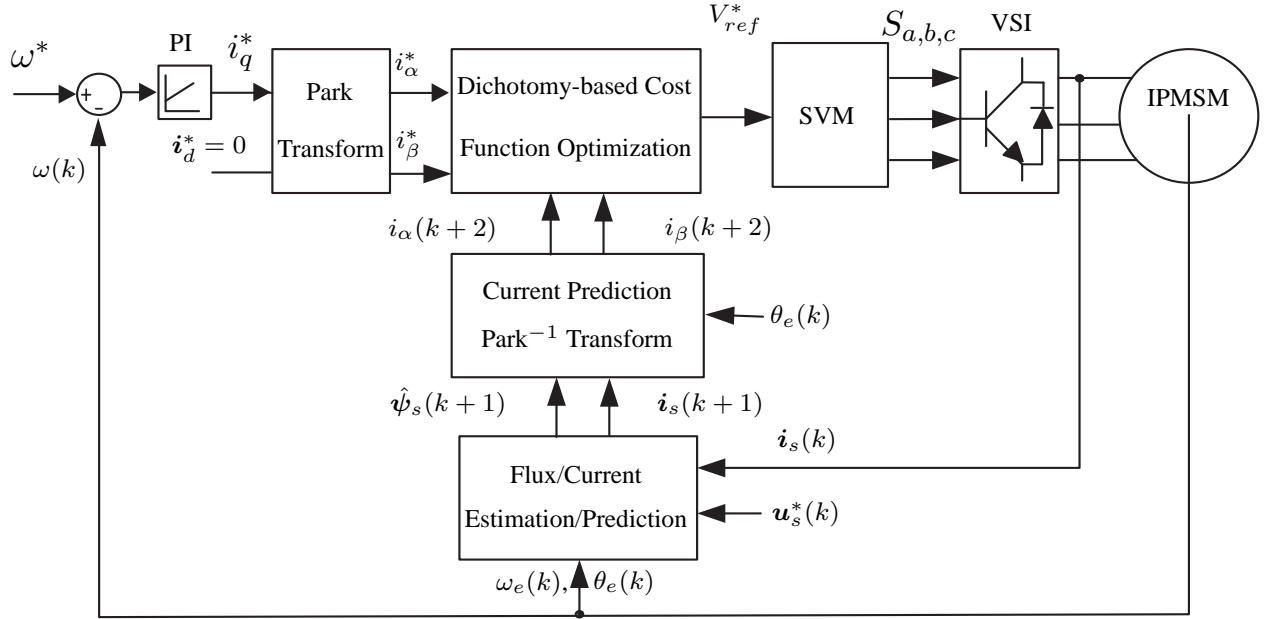


Figure 4.1: Dichotomy-based IFCS-PCC for IPMSM.

Instead of substituting and choosing from only 7 discrete vectors for the cost function, the proposed FCS-PCC calculates the voltage vectors for the cost function by a numerical method. This is realized by increasing the number of candidate reference voltage vectors through dichotomy. This method ensures that the optimal voltage vectors are found at its fastest rate among the possible candidate voltage vectors that equally cover the full-scale of the circular or hexagonal plane of reference voltage vectors.

The selection of optimal voltage vectors is an iteration process, where the amplitude of the next batch's candidate voltage vectors of the loop are based on the last step's voltage vector by adding and subtracting half of the last round's optimal vector's amplitude. The search scale of phase angle is reduced to half of the last step by excluding the dominating area other than the last step's optimal voltage vector. This method increases the calculation effort, but is acceptable, because dichotomy removes calculation redundancy in each new iteration. This is different from the calculation intensive enumeration method. Figure 4.2 shows the first two steps of one iteration of the optimal voltage vector selection mechanism in a circular plane.

In this figure, the selected vector is in red (or: bold for black and white print) for each step and V_m is the maximum available output voltage vector's magnitude. In order to avoid over-modulation and its nonlinear distortion for voltage formation, for the aforementioned inverter, only the inscribed circular area of hexagon is considered. Thus, $V_m = 0.866 \cdot V_{dc}$. To fully use the dc link voltage, voltage vectors can also be calculated in the hexagonal plane or include

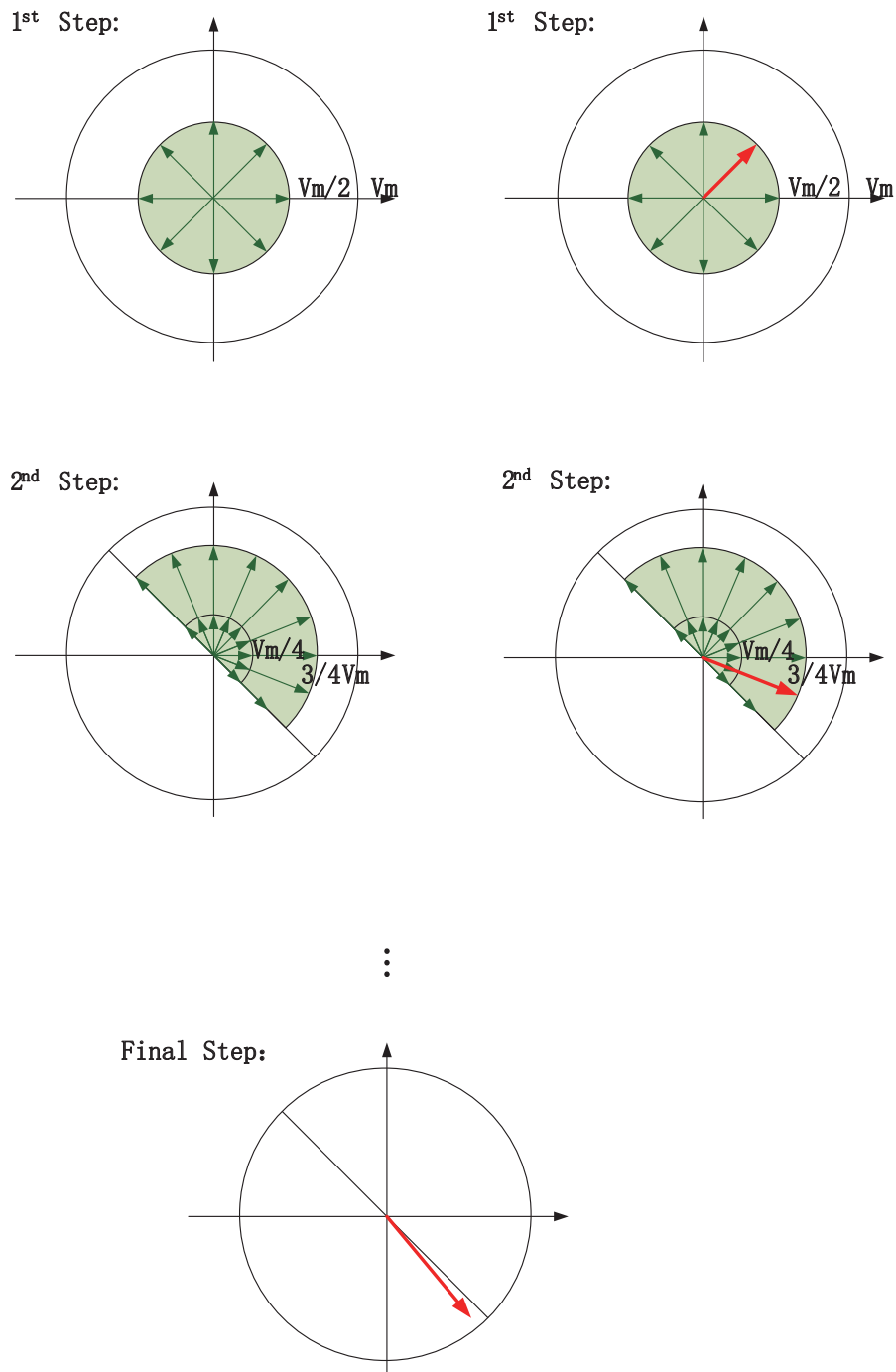


Figure 4.2: One iteration of the fan dichotomy-based IFCS-MPC's reference voltage vector selection.

over-modulation with $V_m = V_{dc}$. However, this will either increase the torque ripples and 6th order harmonics or reduce the control precision.

Since the solution of the next sub-chapter is a similar variation of this method, for easiness of comparison, the simulation and experimental results of Fan Dichotomy-based IFCS-PCC for IPMSM will be shown together with the upcoming method in the later sub-chapter.

4.1.2 Circular Dichotomy-based Method

In this sub-chapter, another new method calculating voltage vectors in circular area for each of the next vector optimization loop in the iteration process will be proposed. Since it is still a numerical method to generate quasi-continuous reference voltage that is similar as the previous solution, SVM can be applied and fixed switching frequency of the inverter is ensured. Its schematic diagram is the same as the previous solution as shown in figure 4.1 [64].

Similarly as dichotomy-based IFCS-MPC, the proposed Circular Dichotomy-based Method enlarges the scale of candidate voltage vectors for the cost function by a numerical dichotomy method. Figure 4.3 shows the first 3 steps of one iteration of the optimal voltage vector selection mechanism in a circular plane. Instead of using only the 7 different discrete voltage vectors to evaluate cost function, the circular dichotomy enlarges the scale of candidate voltage vectors for cost function through dichotomy. Based on previous voltage vector, the magnitude of next step's candidate voltage vectors is set with adding and subtracting half of last step's optimal reference vector's magnitude. And the angle between the adjacent candidate voltage vectors of the same step is set to be half of the last step's value. Similar but different from the fan dichotomy, fan dichotomy's voltage vector's magnitude of next step's candidate voltage vectors is calculated by adding vectors, whose magnitude are half of last step's optimal vector's magnitude. But the next step's voltage vectors' angles equally divides the circular areas instead of fan areas.

4.2 Simulation Verification

This chapter shows the test results of the fan and circular dichotomy-based IFCS-PCC on PMSM. Similarly, same tests designed with same speed PI controller parameters as last chapter are applied. In the tests, both Fan and Circular Dichotomy-based Methods have 4 iterations, with 2 divisions in angles for each iteration.

Simulation 1 is to find out the performance of the speed step up and reversal process for IPMSM. Figure 4.4 shows speed, torque, current and flux of this process. Figure 4.5 shows the current tracking performance of both systems during the speed reversal process.

Simulation 2 is to find out the speed performance under torque variations. Figure 4.6 shows speed, torque, current and flux of this process.

Simulation 3 tests their robustness. Same variations range of parameters as the tests of FCS-PCC are set. Figure 4.7 to figure 4.9 show the system performance against the variations of R_s , L_d and L_q .

All three parameters' variations tests confirm the good and similar robustness of Deadbeat Null RFCS-PCC.

Compared to the Circular Dichotomy-based Method, Fan Dichotomy-based Method reduces the calculation complexity, which alleviates the main problem of Dichotomy-based IFCS-MPC,

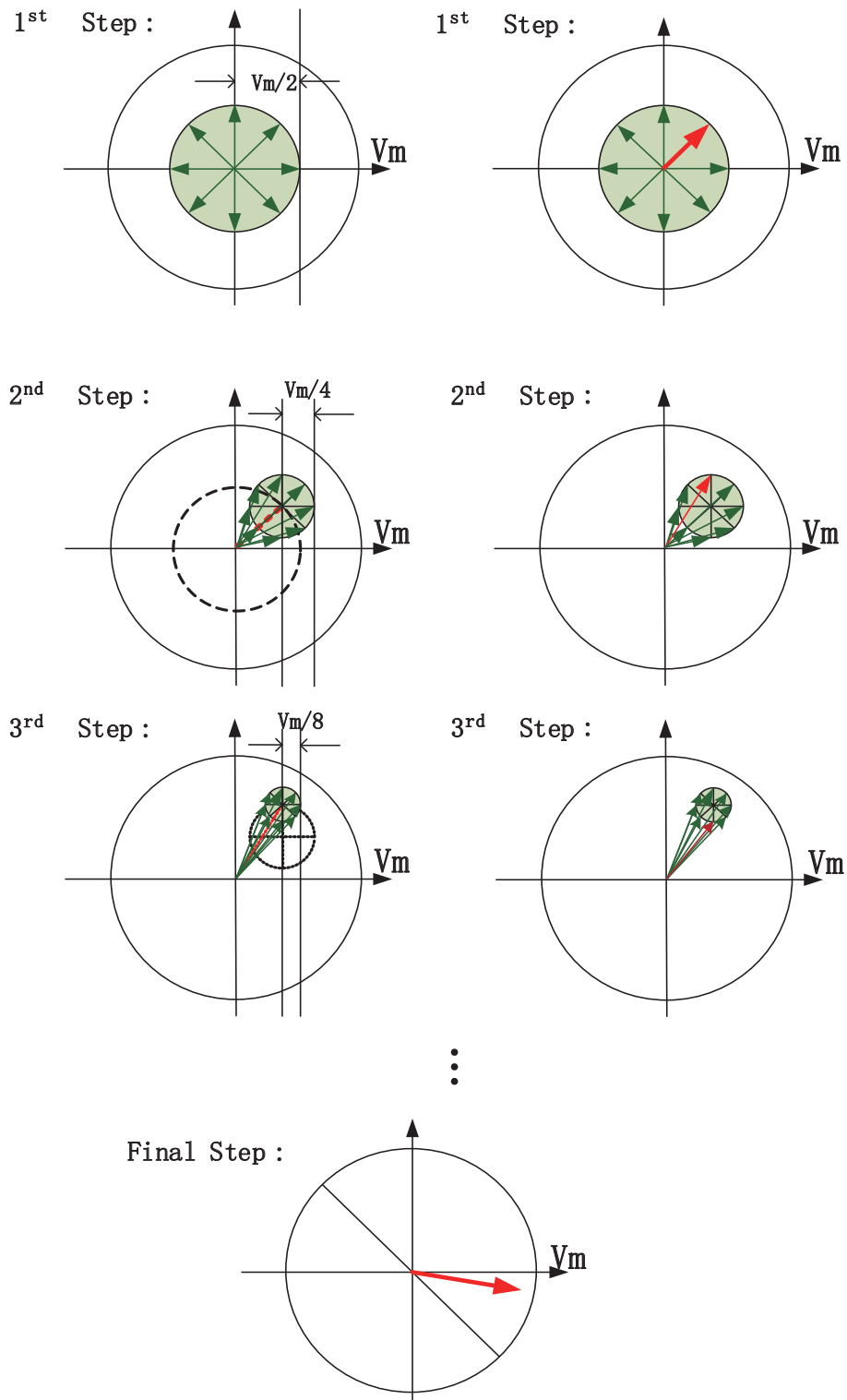
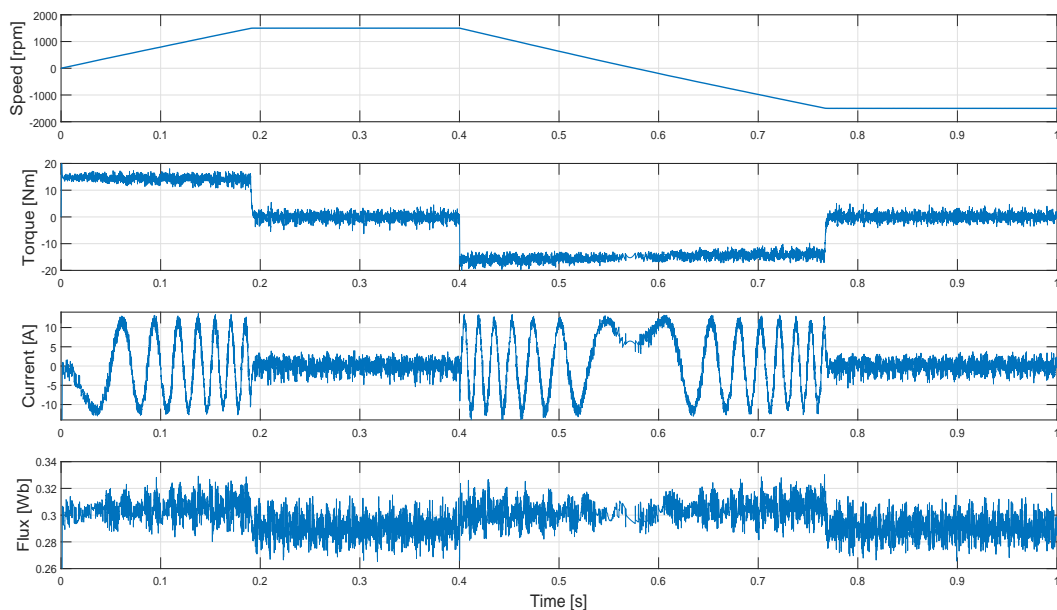
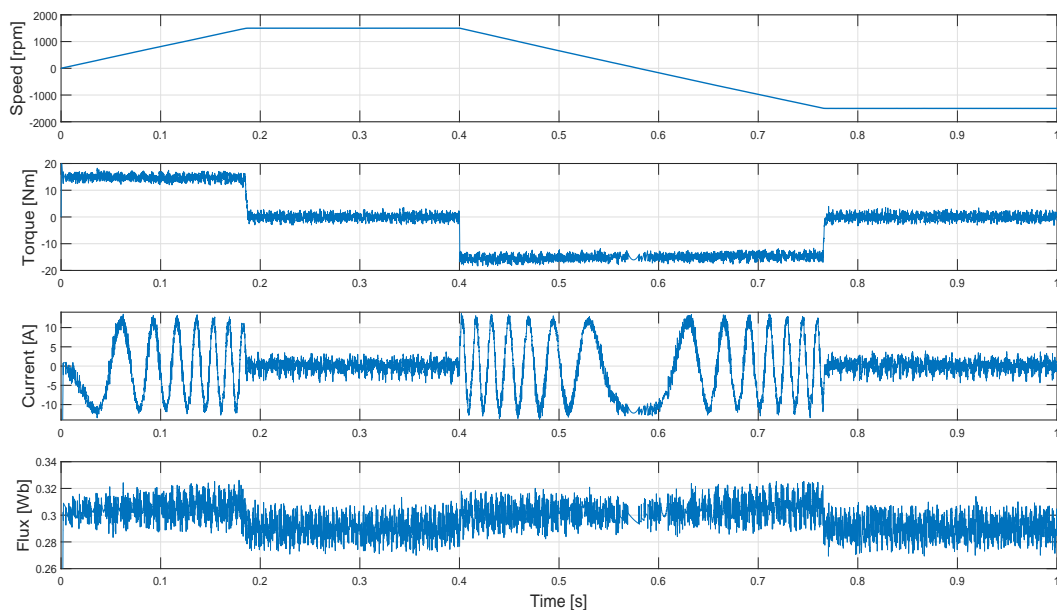


Figure 4.3: One iteration of the circular dichotomy-based IFCS-MPC's reference voltage vector selection.



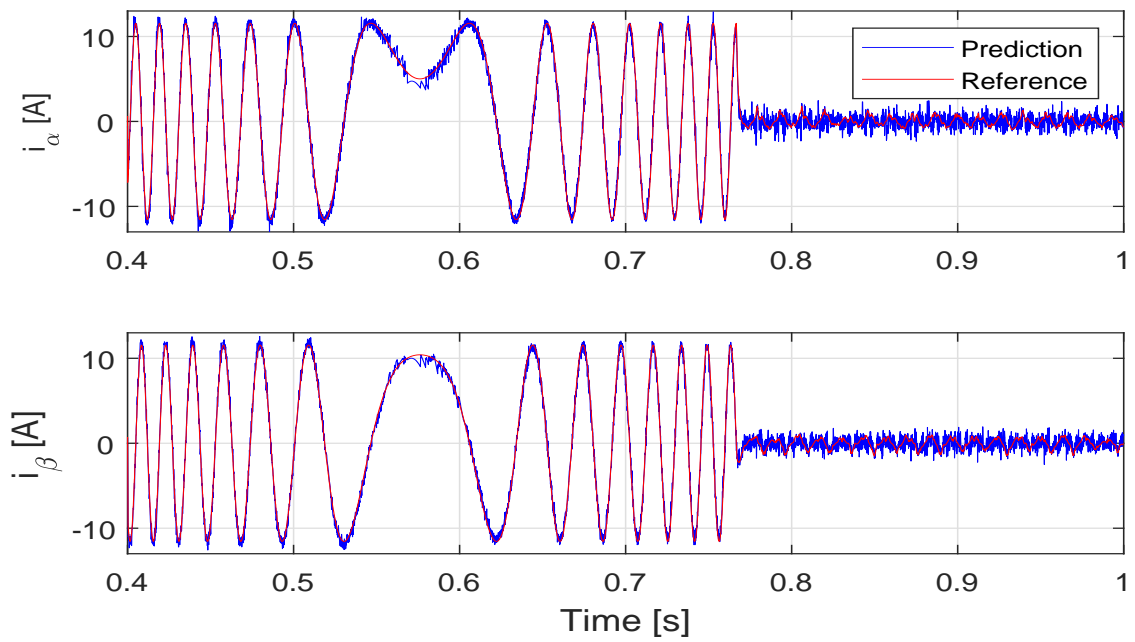
(a) Fan Dichotomy-based IFCS-PCC.



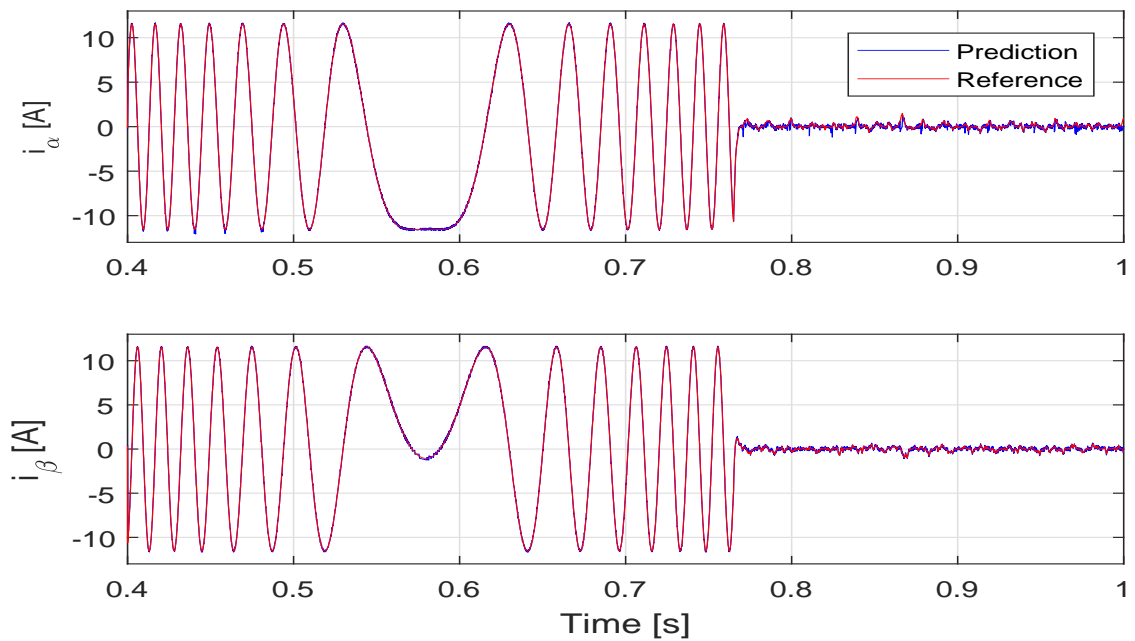
(b) Circular Dichotomy-based IFCS-PCC.

Figure 4.4: Simulation: Rated speed start up and reversal of Dichotomy-based IFCS-PCC for IPMSM.

and makes it considerate for the application for long horizon predictive control, whose crucial limitation is the amount of calculation. And with respect to the dynamic performance and robustness, the proposed method is comparable and even slightly better than the existing FCS-



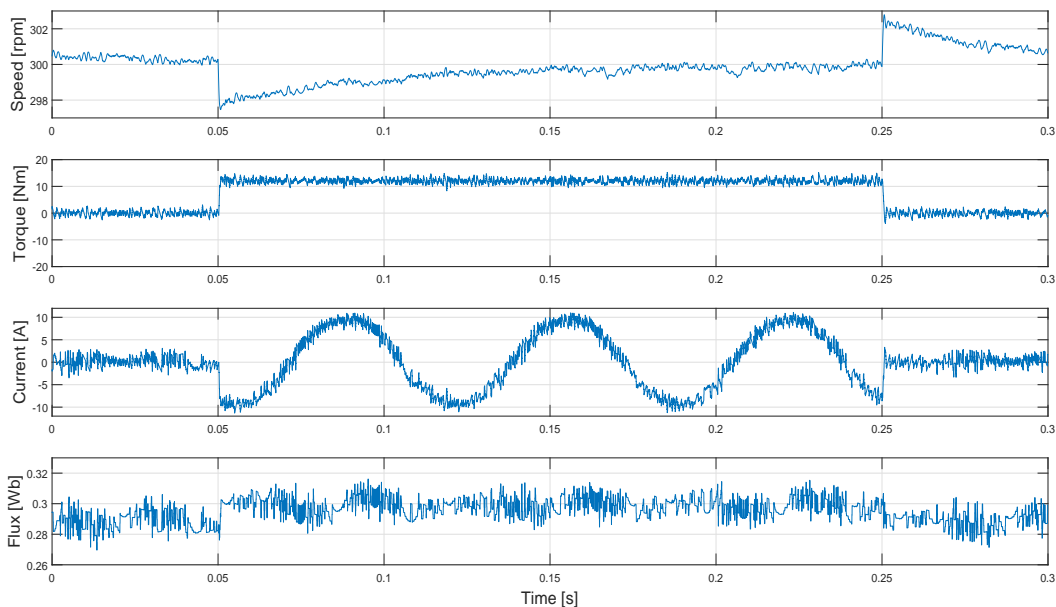
(a) Fan Dichotomy-based IFCS-PCC.



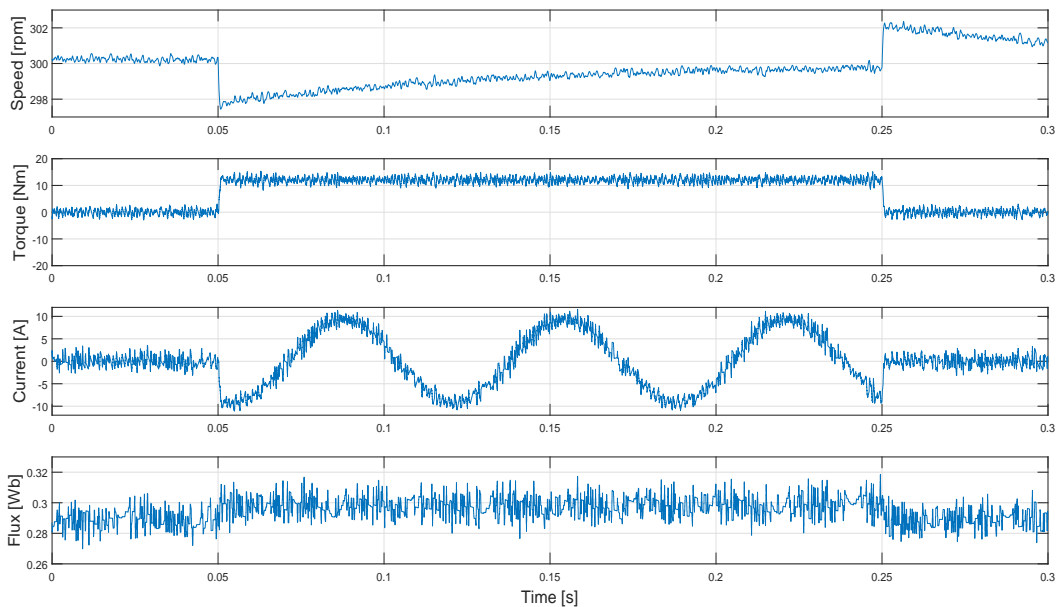
(b) Circular Dichotomy-based IFCS-PCC.

Figure 4.5: Simulation: Current Tracking of Dichotomy-based IFCS-PCC for IPMSM

PCC and DBPCC in chapter 2.

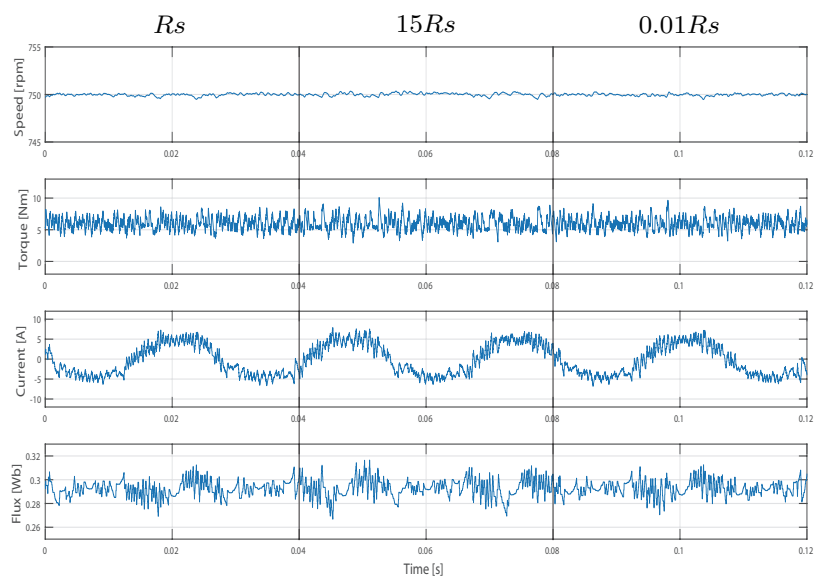


(a) Fan Dichotomy-based IFCS-PCC.

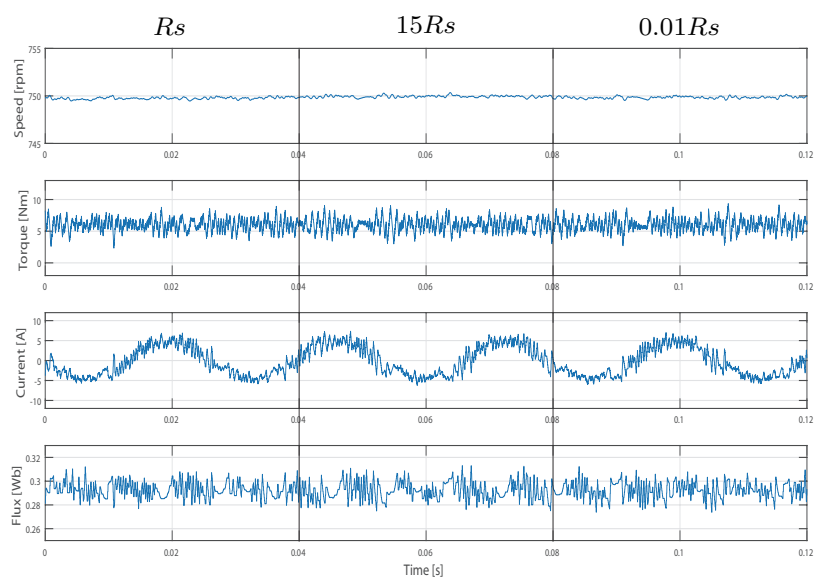


(b) Circular Dichotomy-based IFCS-PCC.

Figure 4.6: Simulation: Dichotomy-based IFCS-PCC Performance for IPMSM under Torque Variations.

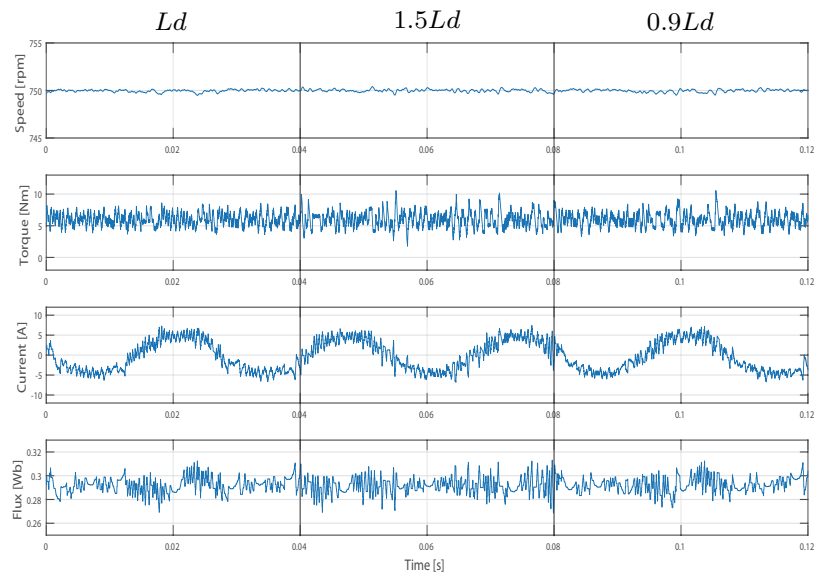


(a) Fan Dichotomy-based IFCS-PCC.

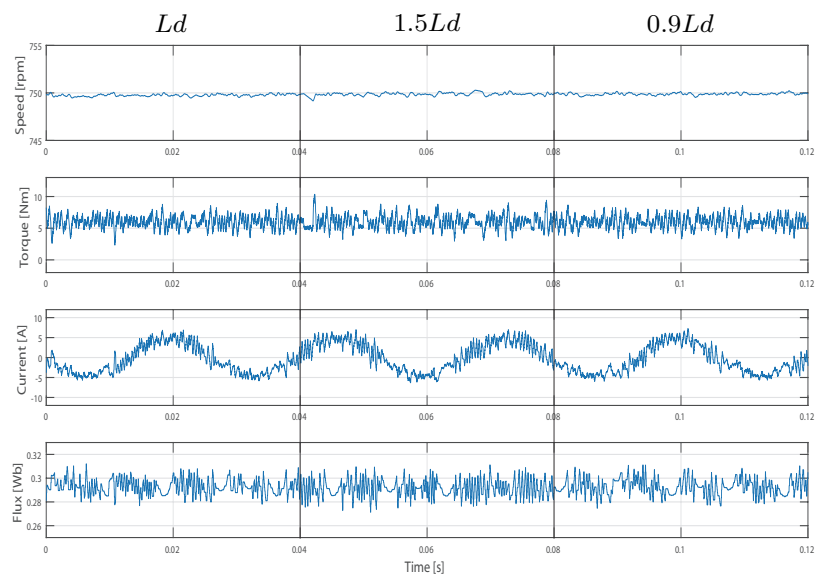


(b) Circular Dichotomy-based IFCS-PCC.

Figure 4.7: Simulation: Dichotomy-based IFCS-PCC performance for IPMSM with R_s Variations.

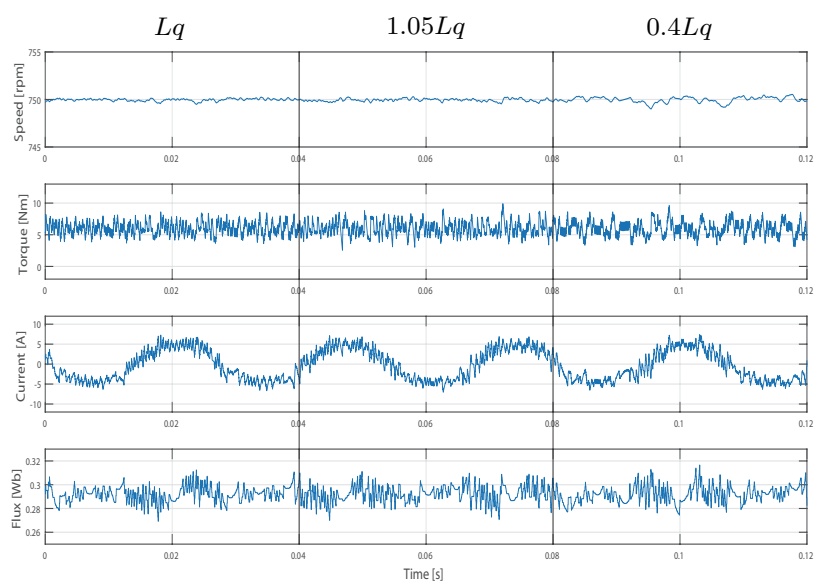


(a) Fan Dichotomy-based IFCS-PCC.

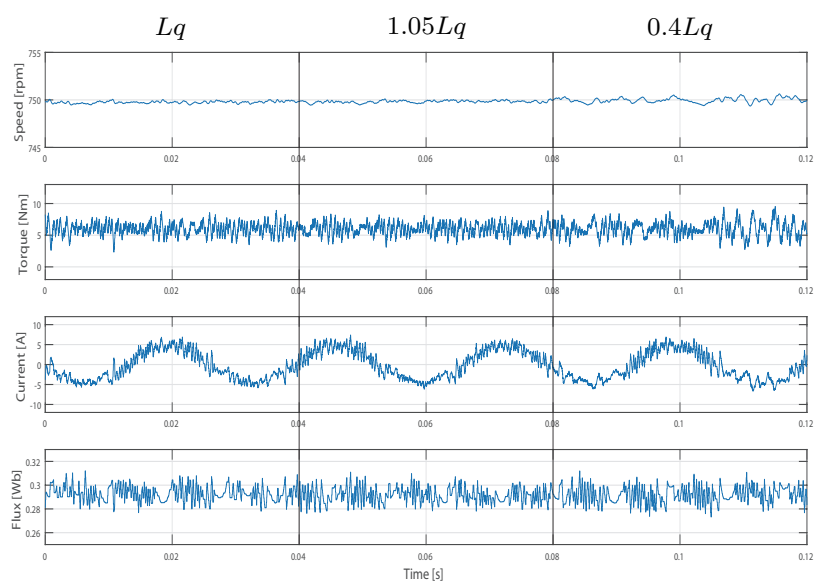


(b) Circular Dichotomy-based IFCS-PCC.

Figure 4.8: Simulation: Dichotomy-based IFCS-PCC performance for IPMSM with L_d Variations.



(a) Fan Dichotomy-based IFCS-PCC.



(b) Circular Dichotomy-based IFCS-PCC.

Figure 4.9: Simulation: Dichotomy-based IFCS-PCC performance for IPMSM with L_q Variations.

4.3 Conclusion

The IFCS-MPC proposed in this chapter, when compared to conventional FCS-PCC, maintains the fixed switching frequency of the inverter, and improves the current quality and reduces the torque ripples significantly due to its quasi-continuous reference voltage generation mechanism to apply multiple switching states in each PWM period. Therewith, the system's reliability can be ensured. And it has better control accuracy, especially when with regard to the current tracking and quality.

Though the calculation efforts of IFCS-MPC is increased, it has meanings for special application where calculation is not the main consideration but system with multiply-objects nonlinear control and fast dynamics of MPC or continuous reference voltage are required.

CHAPTER 5

Reduced FCS-MPC

In contrast to last chapter with IFCS-MPC, this chapter deals with the matter of FCS-MPCs reducing the number of candidate voltage vectors for cost function optimization to reduce the calculation efforts [74, 75]. Therefore, the methods proposed in this chapter are named "Reduced FCS-MPC" or "RFCS-MPC" for short. With RFCS-MPC, instead of substituting all feasible voltage vectors into the vector related terms of cost function in a exhaustive way, only a sub-set of the voltage vectors is chosen as the control set and applied for cost function minimization. This is especially important for system with limited calculation resources, e.g. for higher precision applications that must be controlled with long horizon FCS-MPCs.

However, different from IFCS-MPC, RFCS-MPC still generates discrete voltage vectors. Therefore, no PWM is required. The following sub-chapters propose five different solutions of RFCS-MPC that can reduce the number of candidate voltage vectors in control set for cost function from 7 (or: 8 with both zero/inactive vectors) to 5, 4, 3, 2 and 0 [76], respectively.

All control set reduction principles are only dependent on VSI topology, and theoretically also not electric machine type dependent for different control strategies in this work. Therefore, the methods make no differences on variables estimation, prediction and cost function design of FCS-MPC. FCS-PCC for both IPMSM and SPMSM are taken as examples for the purpose of explanation and verification of algorithms.

5.1 Dichotomy-based RFCS-PCC

This method is another implementation of dichotomy on FCS-MPC, which can reduce the number of candidate voltage vectors in control set for cost function to 5.

The design of this method is very simple and intuitive with the mechanism of dichotomy, which sorts the relevance of vectors by distance and gives instructions for redundancy exclusion. Figure 5.1 gives an example of this method. As shown in this figure, firstly, any 2 vectors of opposite directions (e.g. v_3 and v_6) out of the 6 feasible voltage active vectors from VSI voltage

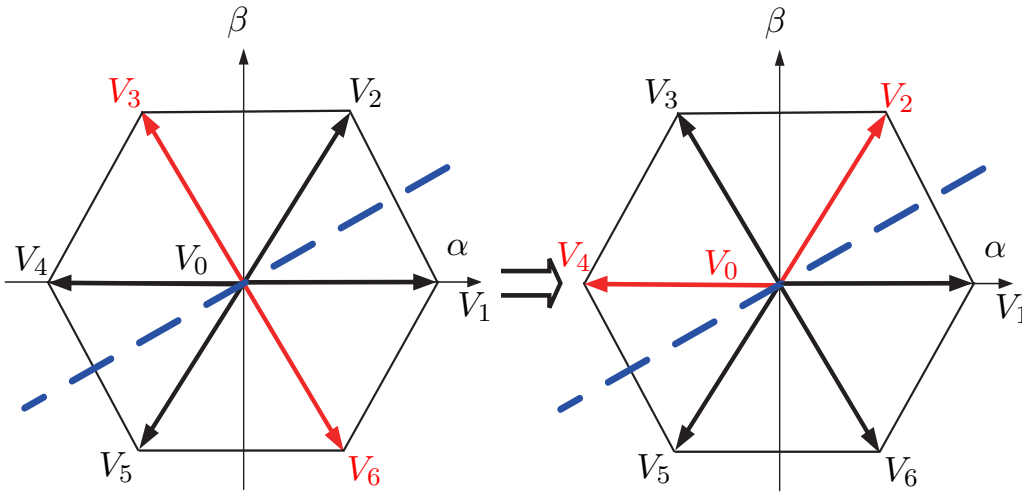


Figure 5.1: Vector Selection of Dichotomy-based RFCS-MPC

hexagon are selected. And the perpendicular line passing through the origin of these two vectors equally divides the plane into two parts. After that, both vectors are substituted into the cost function and the vector (e.g. v_3) that leads to smaller cost function value is considered to be more relevant and closer to (or: may be exactly) the optimal vector in hexagon plane. Therefore, all 3 active vectors (i.e. v_5 , v_6 and v_1) of the opposite side of the perpendicular line, where v_1 is not in, can be considered as less relevant, and thus be excluded. However, since the other 2 active vectors of the same side (i.e. v_2 and v_4) as well as the inactive vector v_0 's relevance is unsure, they cannot still be excluded. As a results, the adjacent 2 vectors (i.e. v_2 and v_4) of v_1 as well as v_0 are finally given to the cost function for further optimization to choose the reference vector. After these two steps of Dichotomy-based RFCS-PCC, only 5 vectors including a null vector are required to shrink the number of candidate voltage vectors in control set for cost function optimization. Therefore, the calculation efforts will theoretically be reduced around 28.6%.

5.1.1 Simulation Verification

As mentioned at the beginning of this section, only FCS-PCC with the proposed RFCS methods for IPMSM will be given as example for verification. Therefore, this sub-chapter will show the test results with the modification in the same FCS-PCC system as proposed in Chapter 3.4 with the proposed Reduced FCS principle. Same test conditions with identical speed PI controller parameters as well as current and torque limitations in control are applied for fair comparison.

Simulation 1 is to find out the performance during speed step-up and reversal process. Figure 5.2 shows speed, torque, current and flux of this process. The speed dynamics and torque ripples' ranges are almost the same as the results of conventional FCS-PCC in figure 3.17. But the current and flux ripples range are slightly larger. The reason of the slight deterioration should be caused by the criteria of distance relevance, which is only vector angles dependent. However, the optimal vector's effectiveness for cost function's values depend both on its angle and magnitude. The possibility still exists that the optimal vector found by this method with

only angular distant criteria leads to larger cost function value than any one of the two excluded vectors (should be adjacent to the found optimal vector) who is more relevant to the real optima in magnitude. However, since for such a radial allocation of feasible voltage vectors of VSI, where angles are the more influential and deciding differences between vectors, it is reasonable and preferable to consider angular distances as relevant criteria as adopted in this method. Figure 5.3 shows the corresponding currents' tracking performance. For better comparison, the scale of current in figure is set to be the same as the one in figure 3.18 of FCS-PCC. It is seen in this figure, its tracking performance is as good as that of the conventional FCS-PCC.

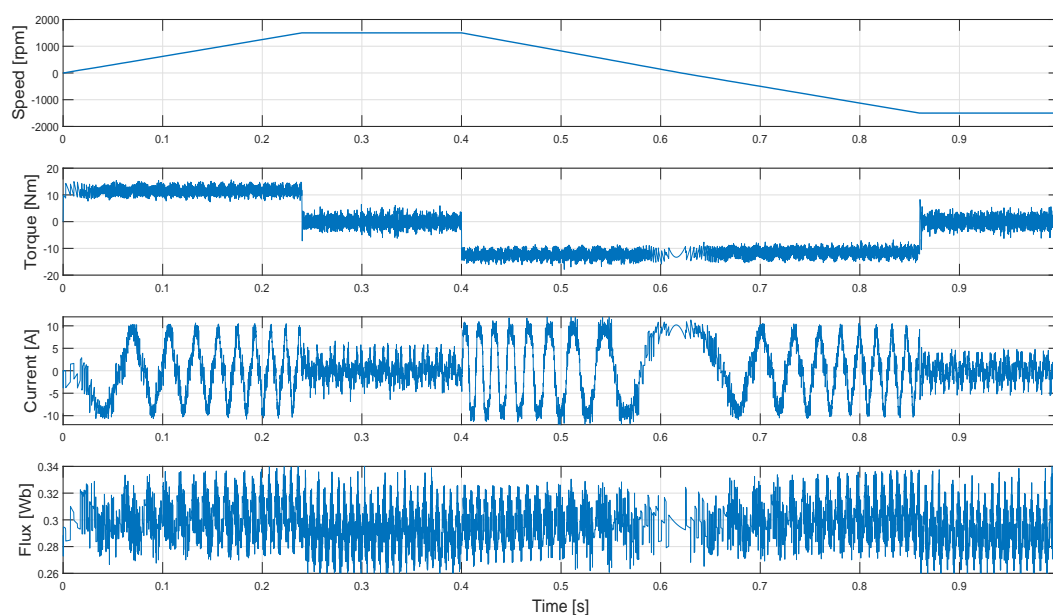


Figure 5.2: Simulation: Rated speed startup and reversal of Dichotomy-based RFCS-PCC.

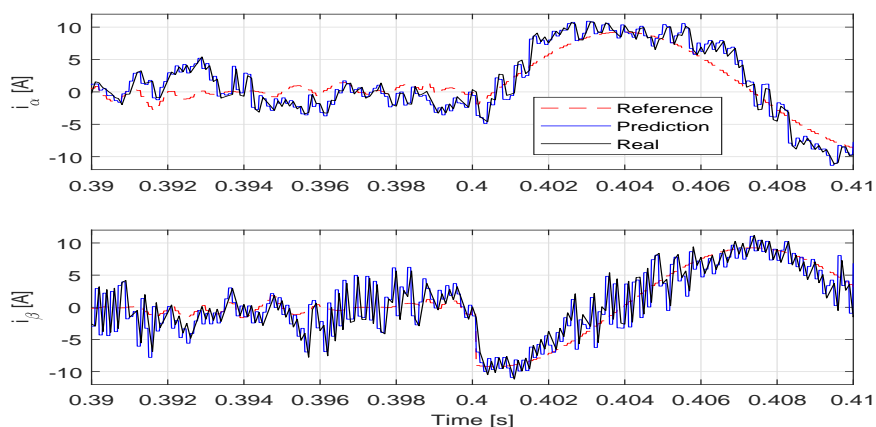


Figure 5.3: Simulation: Current Tracking Performance of Dichotomy-based RFCS-PCC.

Simulation 2 is to find out the speed performance under torque variations. Figure 5.4 shows

speed, torque, current and flux of this process. Similar as in the last test, the flux and current ripples have slight increase. The zoomed-in torque and switching states during torque variation transient are shown in figure 5.5.

Simulation 3 studies the robustness of Dichotomy-based RFCS-PCC. Same variations range of parameters as the tests of FCS-PCC are set. Figure 5.6 shows the system performance against the variations of R_g . Figure 5.7 shows the system performance against the variations of L_d . Figure 5.8 shows the system performance against the variations of L_q . All three parameters' variations tests confirm the good and similar robustness of Dichotomy-based RFCS-PCC.

Since the current ripples are comparatively large with this method, for the protection of machine and inverter, experiments of are not conducted with this Dichotomy-based RFCS-PCC.

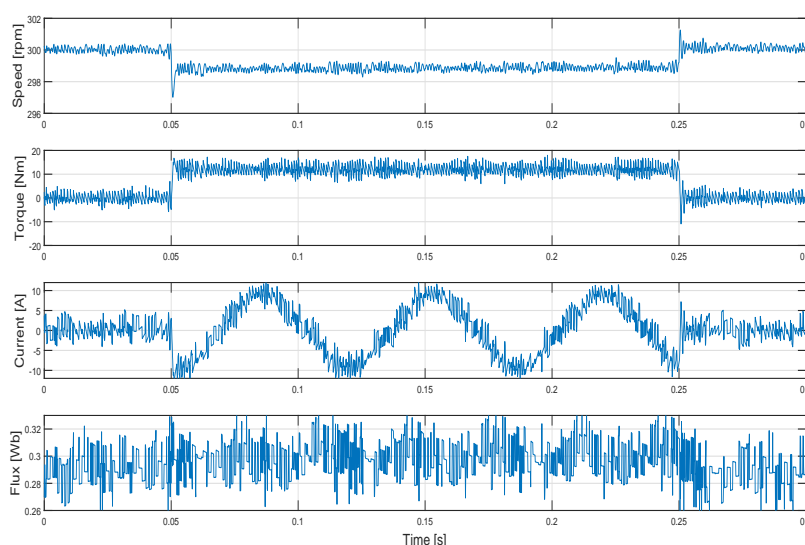


Figure 5.4: Simulation: Dichotomy-based RFCS-PCC Performance under Torque Variations.

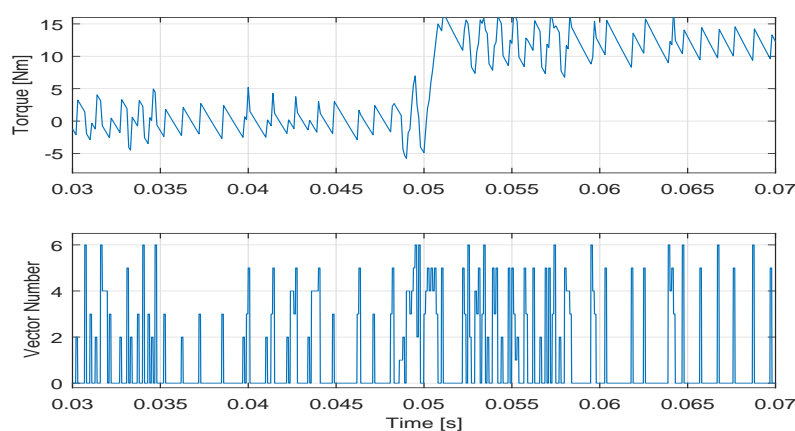


Figure 5.5: Simulation: Torque and Voltage Vectors of Dichotomy-based RFCS-PCC under Torque Variations.

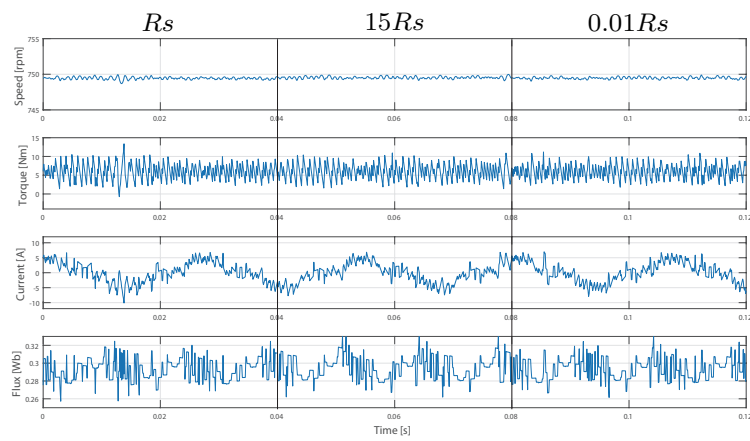


Figure 5.6: Simulation: Dichotomy-based RFCS-PCC performance with R_s Variations.

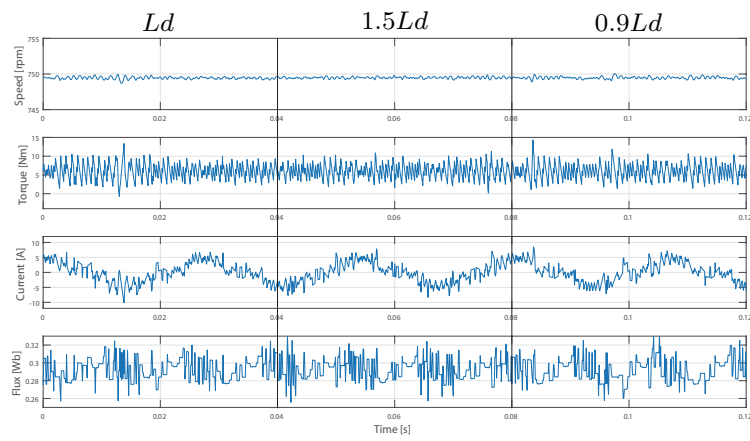


Figure 5.7: Simulation: Dichotomy-based RFCS-PCC performance with L_d Variations.

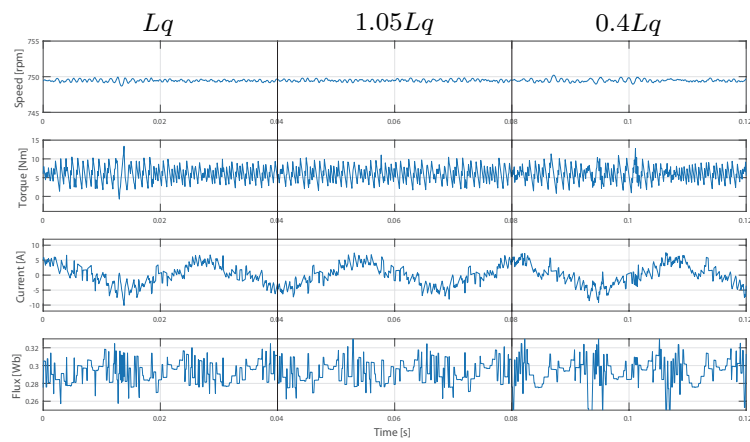


Figure 5.8: Simulation: Dichotomy-based RFCS-PCC performance with L_q Variations.

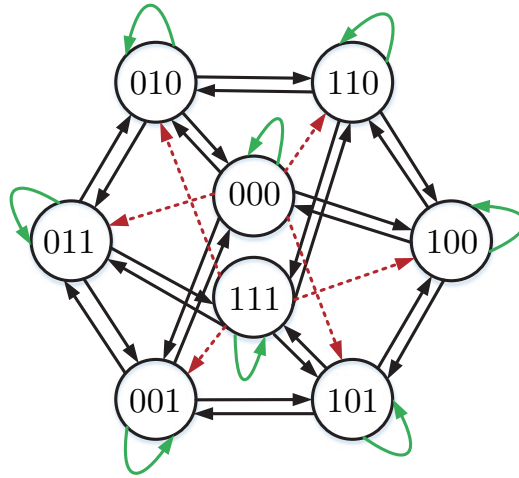


Figure 5.9: Switching states transitions for 2-level 3-phase VSI.

5.2 Switching-minimized RFCS-PCC

This method can reduce the number of candidate voltage vectors in control set for cost function to 4.

It was originally proposed in [28] and applied for FCS-PTC. Its basic principle of vector number reduction is based on minimization of switching number for each period. In each control period, the vectors selected for the sub-set should require maximum one switching transition of one pair of IGBTs on one leg of VSI from the last applied vector. Figure 5.9 shows all switching states transitions for 2-level 3-phase VSI with different types of lines representing different the transition numbers between all vectors from each other. In the figure, only the state transitions with green double dashed lines and blue dashed lines are selected according to the principle for this method.

Moreover, with this principle, the maximum average switching frequency of the inverter becomes:

$$f_{SWmin} = f_c \quad (5.1)$$

Therefore, in this work with the control/sampling frequency $f_c = 10 \text{ kHz}$, the peak switching frequency is 10 kHz . With this reduction of candidate voltage vector number in control set for MPC, 42.86% of the calculation effort of vector selection process can be saved. Meanwhile, with this strict switching number limitation, switching heat loss is also reduced (The percentage of average switching frequency reduction will be measured in the following parts).

5.2.1 Simulation Verification

This chapter shows the test results of PCC with this RFCS principle.

Simulation 1 is to find out the speed step up and reversal process. Figure 5.10 shows speed, torque, current and flux of this process. The ripples are also slightly increased, when compared

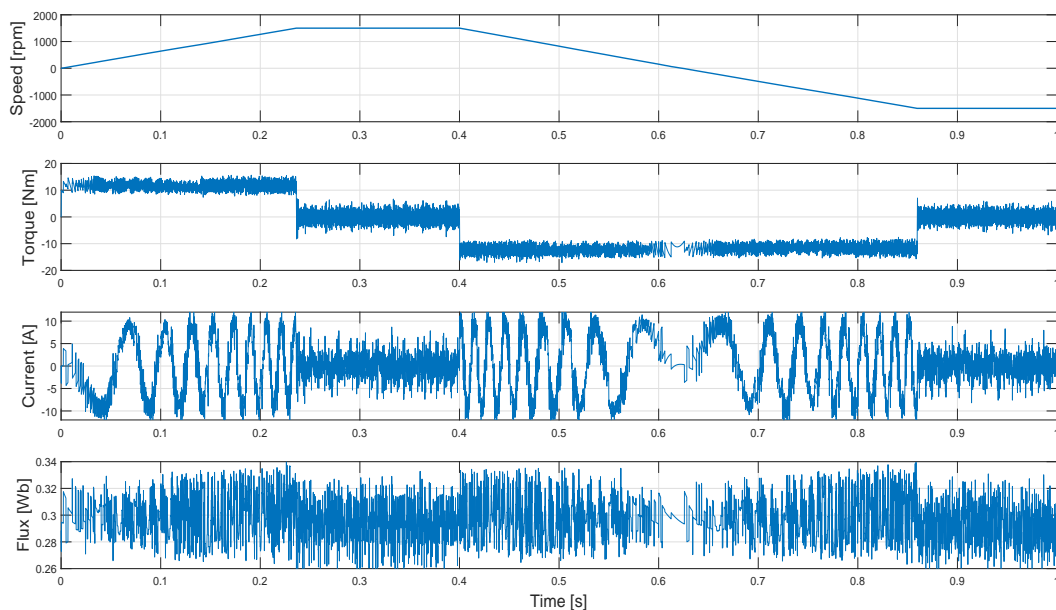


Figure 5.10: Simulation: Rated speed start up and reversal of Switching-minimized RFCS-PCC.

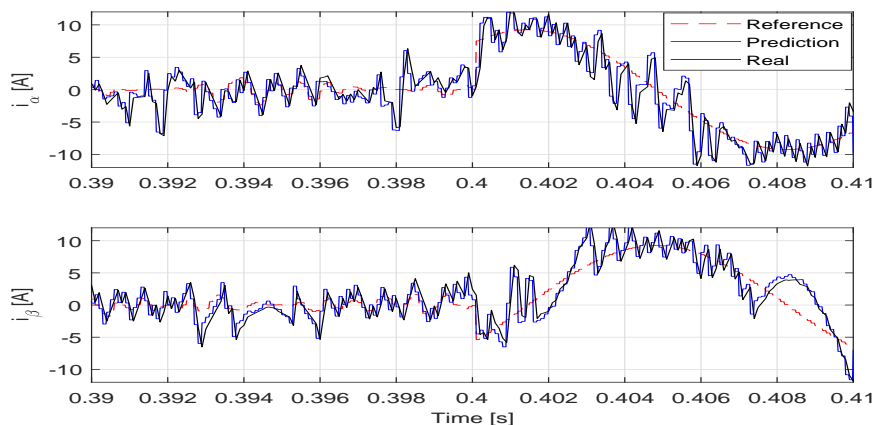


Figure 5.11: Simulation: Current Tracking Performance of Switching-minimized RFCS-PCC.

to conventional FCS-MPC. Figure 5.11 shows the good currents' tracking performance.

Simulation 2 is to find out the speed performance under torque variations. Similarly, in figure 5.12, there is a slight speed drop, but the general performance is quite similar. The zoomed-in torque and switching states during torque variation transient are shown in figure 5.13, which is as fast as FCS-PCC.

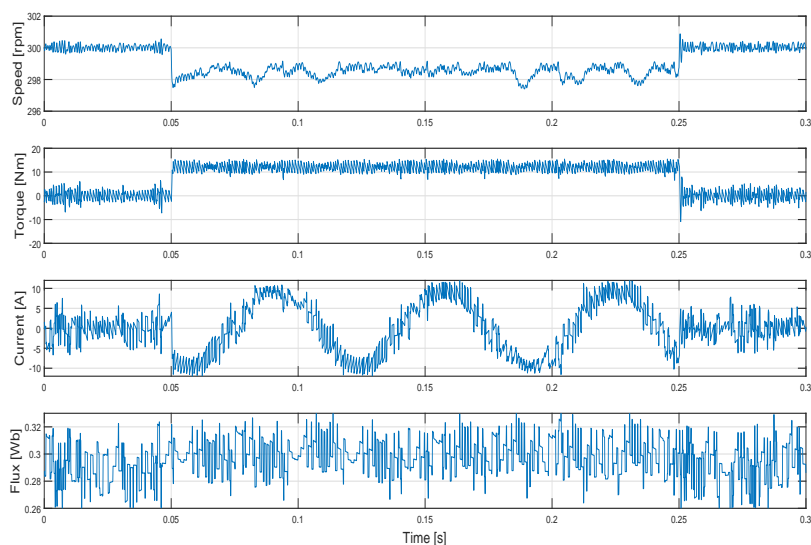


Figure 5.12: Simulation: Switching-minimized RFCS-PCC Performance under Torque Variations.

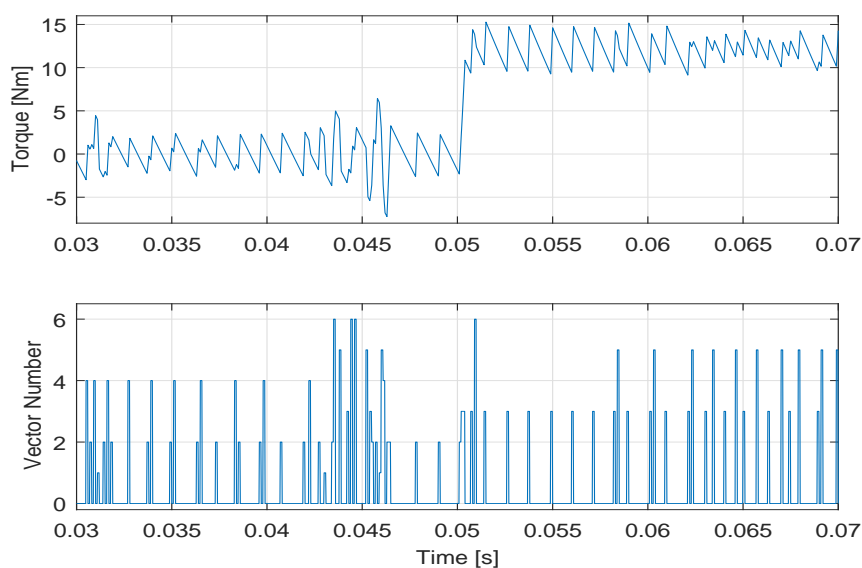


Figure 5.13: Simulation: Torque and Voltage Vectors of Switching-minimized RFCS-PCC under Torque Variations.

Simulation 3 tests the robustness of Switching-minimized RFCS-PCC. Figure 5.14 shows the system performance against the variations of R_s . Figure 5.15 shows the system performance against the variations of L_d . Figure 5.16 shows the system performance against the variations of L_q .

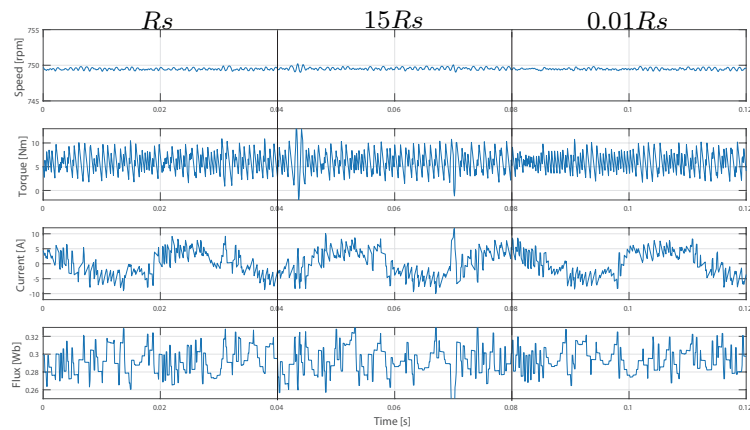


Figure 5.14: Simulation: Switching-minimized RFCS-PCC performance with R_s Variations.

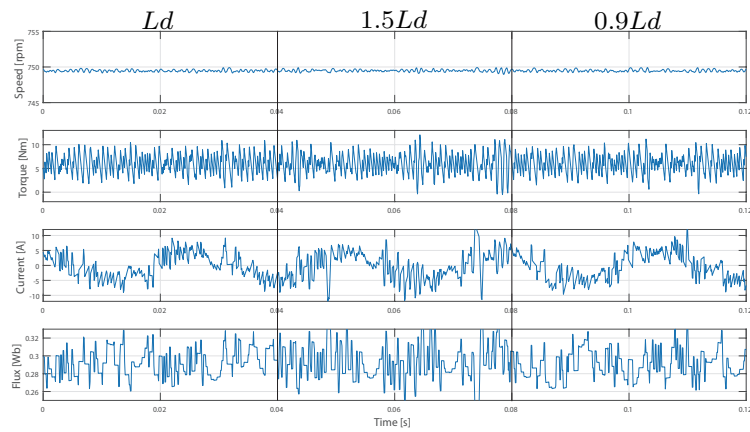


Figure 5.15: Simulation: Switching-minimized RFCS-PCC performance with L_d Variations.

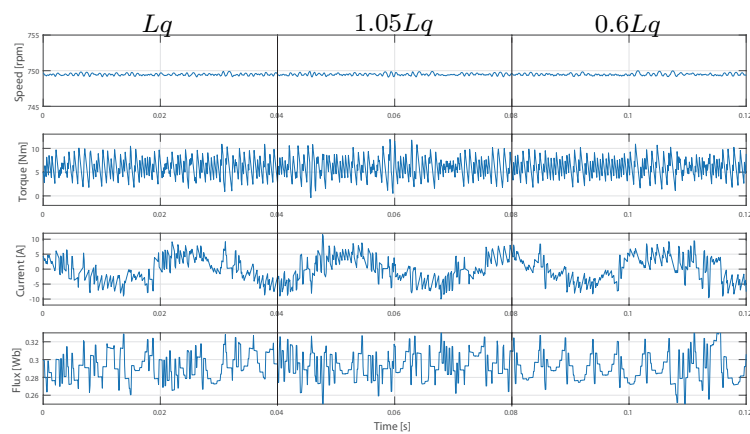


Figure 5.16: Simulation: Switching-minimized RFCS-PCC performance with L_q Variations.

All three parameters' variations tests confirm the good and similar robustness of Switching-minimized RFCS-PCC.

Based on the same reason as in the Dichotomy-based RFCS-PCC, in light of the comparatively large current ripples in Switching-minimized RFCS-PCC, in order to protect machine and inverter, experiments of Switching-minimized RFCS-PCC are not conducted.

5.3 Deadbeat Triple RFCS-PCC

This sub-section will explain a method that can reduce the number of candidate voltage vectors in control set to 3 [77].

Its fundamental principle is based on the deadbeat continuous MPC, but it is still a FCS-MPC with reduced number of candidate voltage vectors in the control set. The reference voltage vectors are calculated in the same way as deadbeat continuous MPC. Instead of giving this vector directly to the PWM as in continuous MPC, it is used to firstly in this method to locate the exact fan sector in the VSI hexagon. The way to obtain the angle of vector for sector decision is usually through the arctangent function as shown in (5.2). By doing this, only 3 voltage vectors: 2 adjacent vectors of the located sector as well as 1 zero vector are chosen to form the control set. Therefore, it is named as Deadbeat Triple RFCS-MPC. Again, it will be based on FCS-PCC for IPMSM as example in this section. For example, in figure 5.17, the vectors selected for control set is the blue ones v_1 , v_2 and zero vector v_0 .

$$\theta_s^* = \tan^{-1} \frac{u_\beta^*}{u_\alpha^*} \quad (5.2)$$

However, since for most system, the output range of arctangent is $[-\pi/2, \pi/2]$, in order to find out θ_s^* in the range of $[0, 2\pi)$ covering all areas of VSI voltage hexagon, a sector decision algorithm as follows is adopted:

Sector number decision:

$$\begin{cases} u_1^* = u_\beta^* \\ u_2^* = \sqrt{3}u_\alpha^* - u_\beta^* \\ u_3^* = -\sqrt{3}u_\alpha^* - u_\beta^* \end{cases} \quad (5.3)$$

If $u_1^* > 0$, $A = 1$, else $A = 0$;

If $u_2^* > 0$, $B = 1$, else $B = 0$;

If $u_3^* > 0$, $B = 1$, else $B = 0$.

The number of sector is calculated as:

$$N_{sec} = A + 2 * B + 4 * C$$

The corresponding relationship of sector N_{sec} of sector in figure 5.17 is:

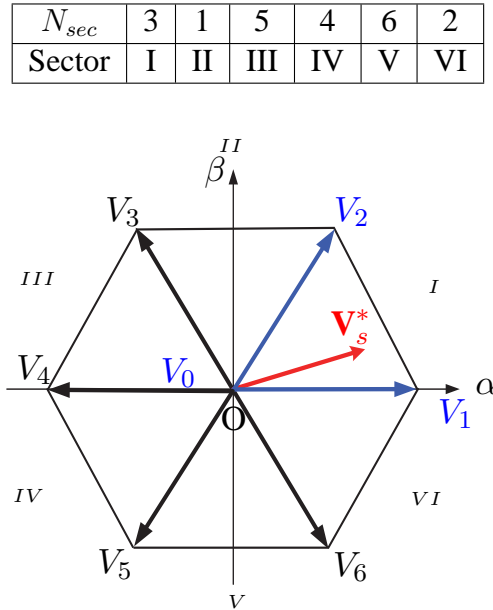


Figure 5.17: Vector Sector Location for Deadbeat Triple RFCS-PCC.

5.3.1 Simulation and Experimental Verification

This chapter shows the test results of the Deadbeat Triple RFCS-PCC system.

Simulation 1 is to find out the speed step-up and reversal process. Figure 5.18 shows speed, torque, current and flux of this process. The dynamics as well as steady state performance is similar to FCS-PCC. Figure 5.19 shows currents' tracking performance.

Simulation 2 is to find out the speed performance under torque variations. Figure 5.20 shows speed, torque, current and flux of this process. Compare to the same results of FCS-PCC, the performance of Deadbeat Triple RFCS-PCC at loaded condition is even better, with less speed drop as that in figure 3.19. This means that the voltage vector of all 7 vectors with minimized current errors in cost function may not guarantee an optimized reference, in stead, the voltage vectors with less angular errors as the reference vector may be even better (at least can be seen from the case of Deadbeat Triple RFCS-PCC in this test). As a result, the following sub-sections after this one will propose two more extended methods based on Deadbeat Triple RFCS-PCC, which also give the angular error or related distance of vectors higher importance for vector selection. The zoomed-in torque and switching states during torque variation transient are shown in figure 5.21, whose torque response and switching are extremely similar to the case of FCS-PCC in figure 3.20.

Simulation 3 tests the robustness of Deadbeat Triple RFCS-PCC. Figure 5.22 to figure 5.24 show the system performance against the variations of R_s , L_d and L_q .

All three parameters' variations tests confirm the good and similar robustness of Deadbeat Triple RFCS-PCC.

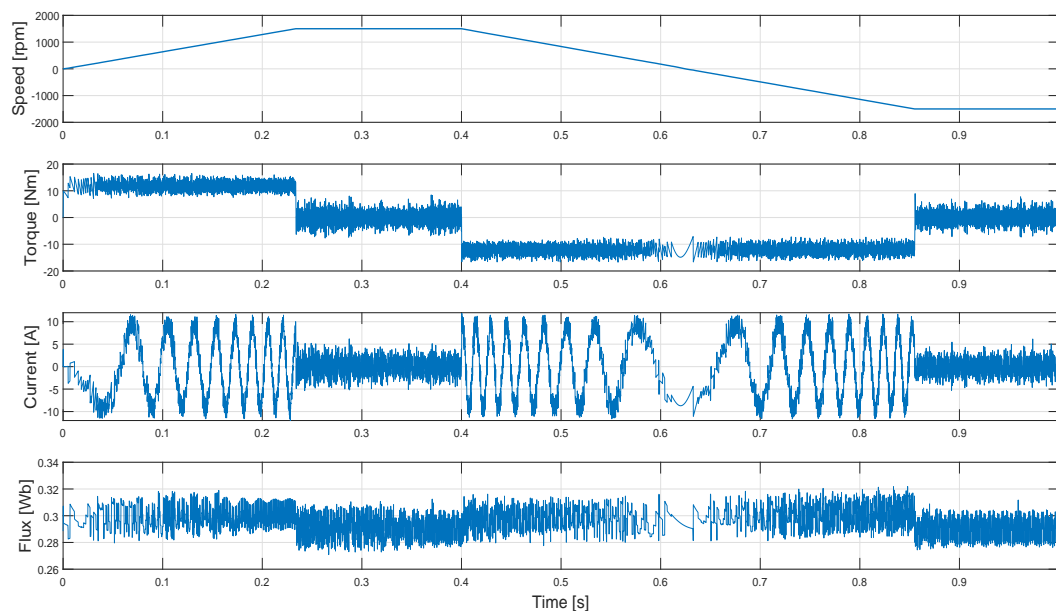


Figure 5.18: Simulation: Rated speed start-up and reversal of Deadbeat Triple RFCS-PCC.

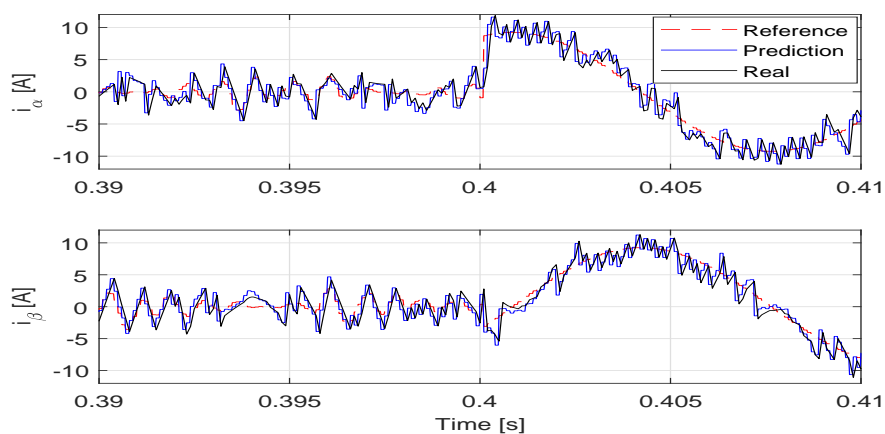


Figure 5.19: Simulation: Current Tracking Performance of Deadbeat Triple RFCS-PCC.

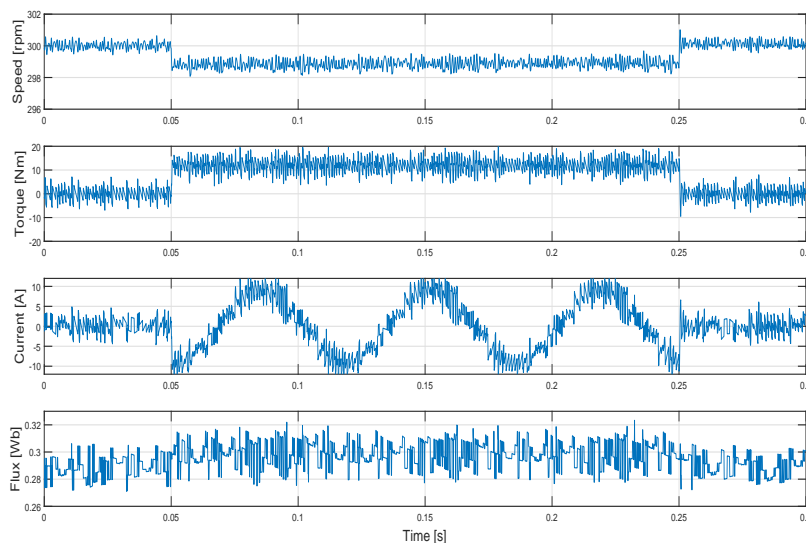


Figure 5.20: Simulation: Deadbeat Triple RFCS-PCC Performance under Torque Variations.

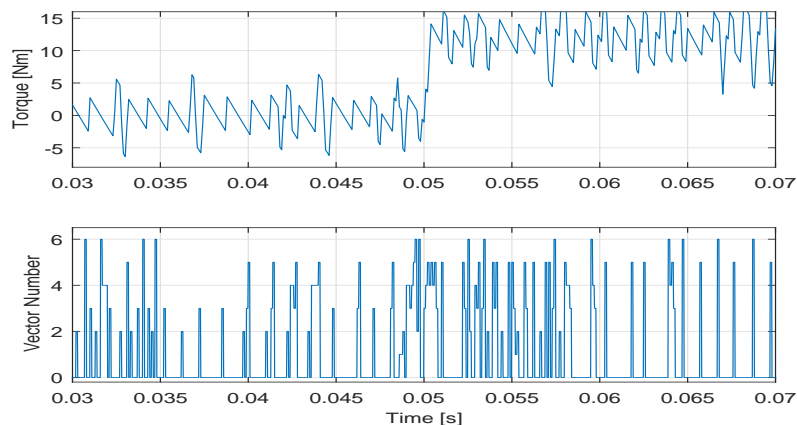


Figure 5.21: Simulation: Torque and Voltage Vectors of Deadbeat Triple RFCS-PCC under Torque Variations.

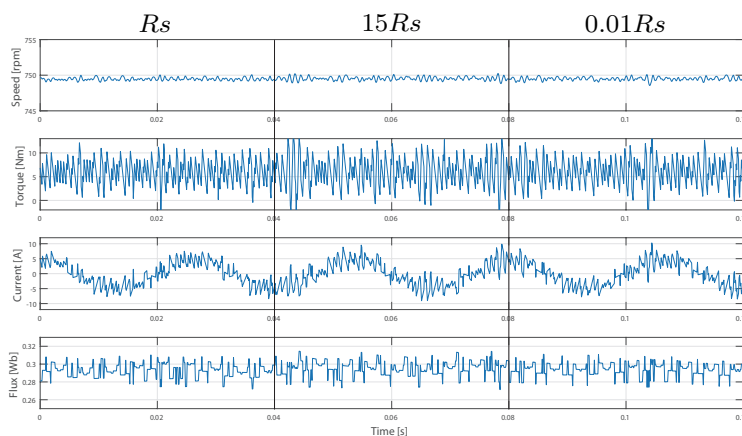


Figure 5.22: Simulation: Deadbeat Triple RFCS-PCC performance with R_s Variations.

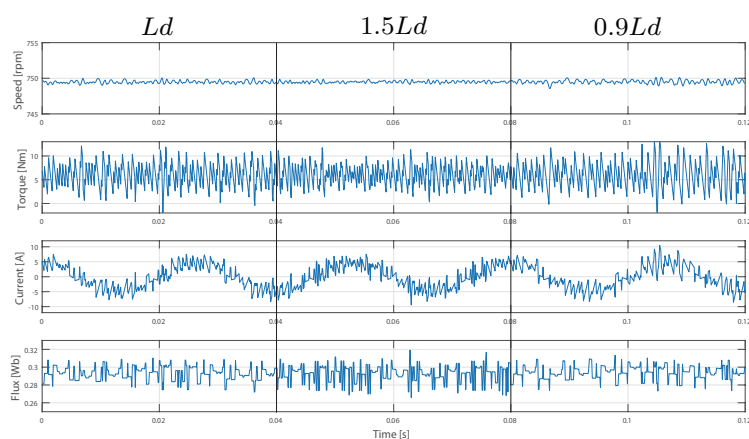


Figure 5.23: Simulation: Deadbeat Triple RFCS-PCC performance with L_d Variations.

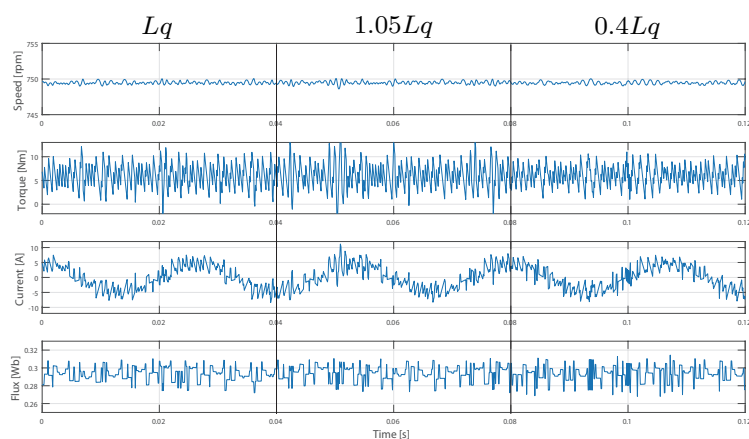


Figure 5.24: Simulation: Deadbeat Triple RFCS-PCC performance with L_q Variations.

Experimental verifications are conducted on SPMSM, whose results are shown in figure 5.25 to 5.30.

Figure 5.25 is the speed start-up and reversal process. It has extremely similar performance as in the same process of FCS-PCC in figure 5.25, which shows the simplification of Deadbeat Triple RFCS-PCC is not in cost of any deterioration of system performance.

Figure 5.26 shows the successful current tracking.

Figure 5.27 are the torque tracking test under step reference variations.

Figure 5.28 to 5.30 are the robustness tests of R_s , L_s and ψ_{pm} . Same as the previous FCS-MPCs, the system is only transiently sensitive to ψ_{pm} deviation, which verifies the good sensitivity of Deadbeat Triple RFCS-PCC.

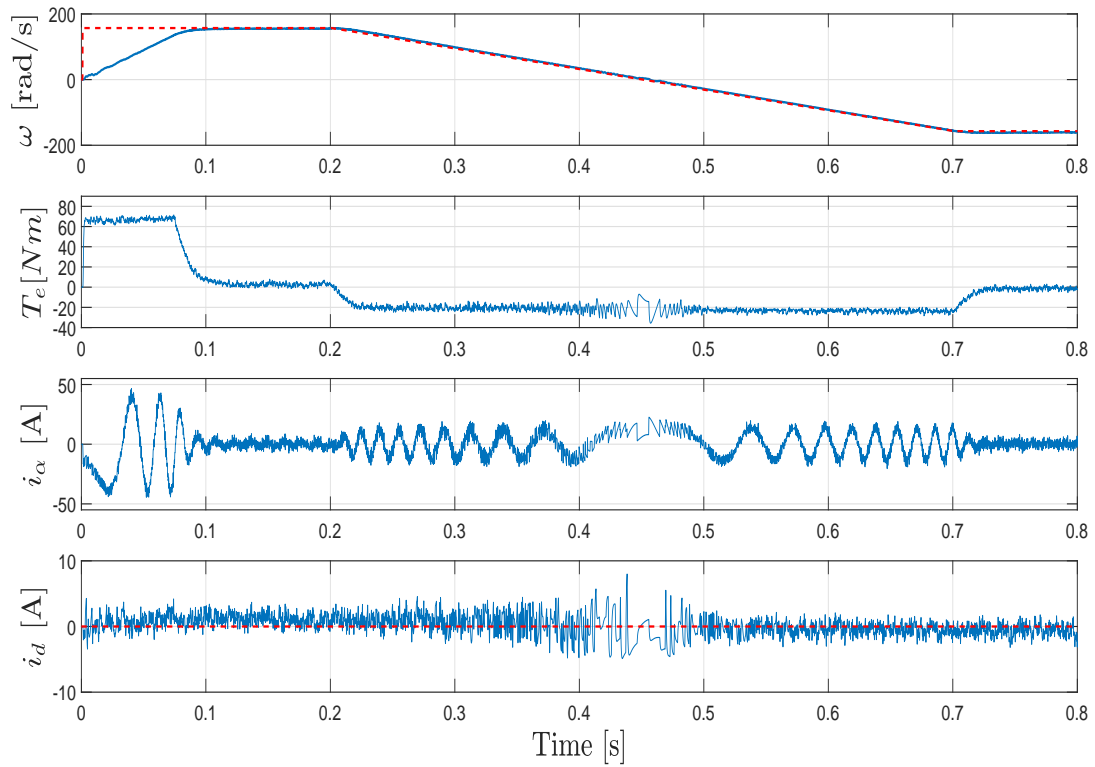


Figure 5.25: Experiment: Rated speed start-up and reversal of Deadbeat Triple RFCS-PCC.

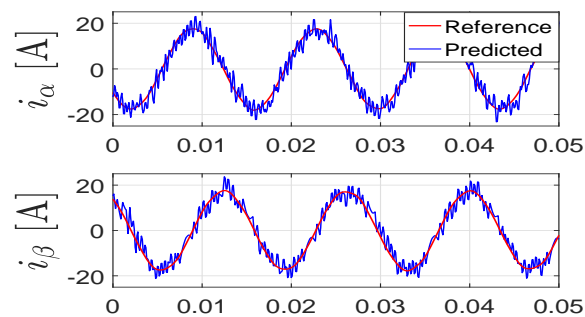


Figure 5.26: Experiment: Current Tracking Performance of Deadbeat Triple RFCS-PCC.

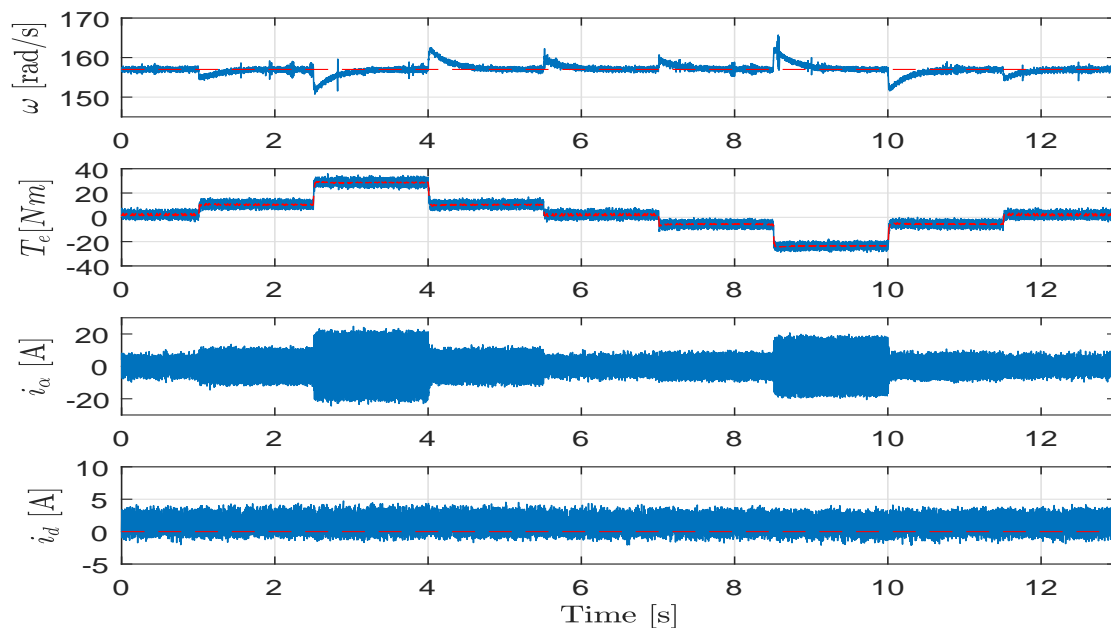


Figure 5.27: Experiment: Deadbeat Triple RFCS-PCC Performance under Torque Variations.

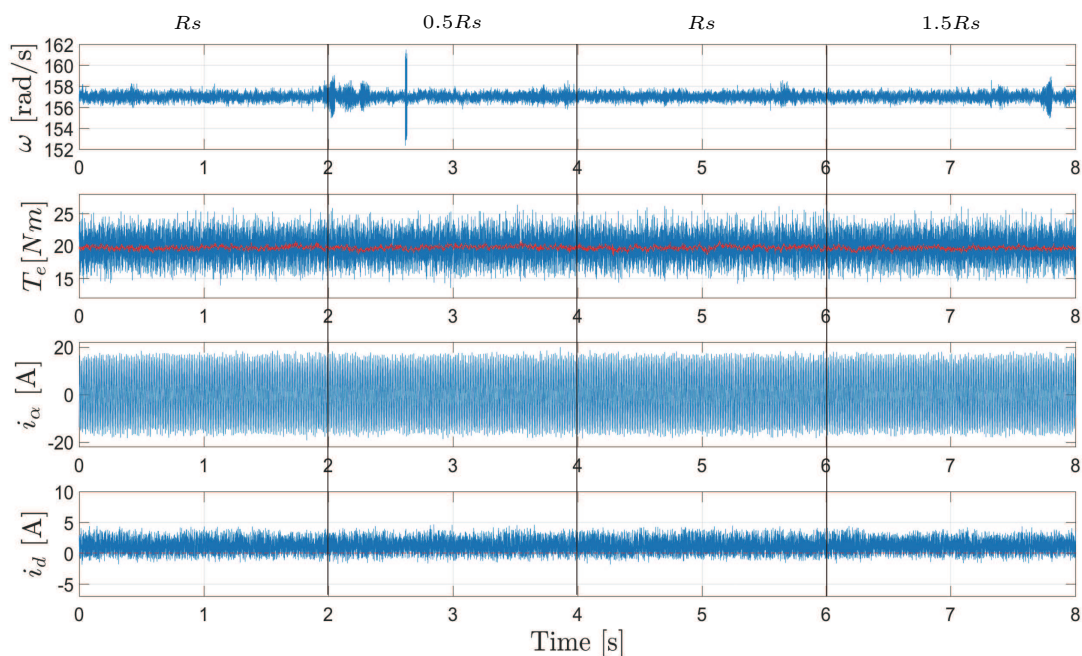


Figure 5.28: Experiment: Deadbeat Triple RFCS-PCC Performance under R_s Variation.

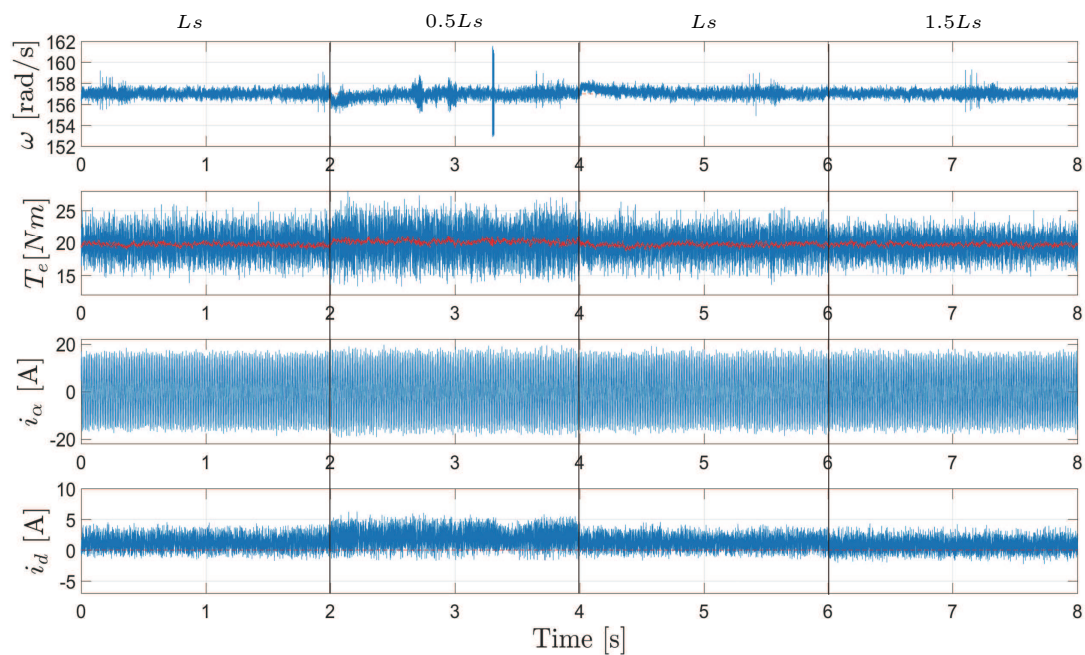


Figure 5.29: Experiment: Deadbeat Triple RFCS-PCC Performance under L_s Variation.

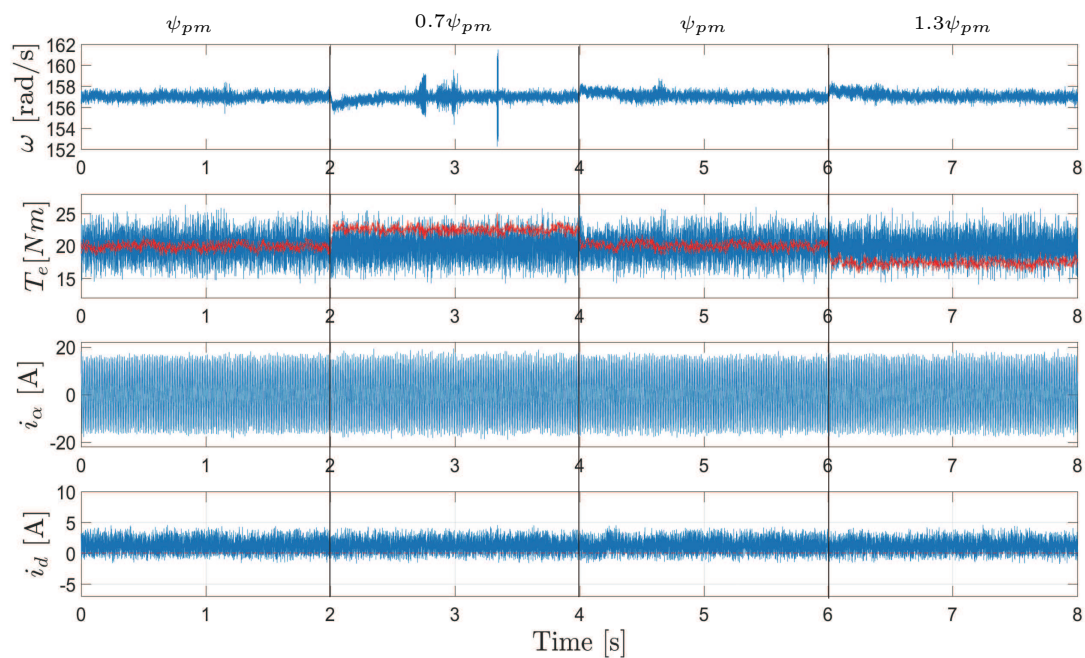


Figure 5.30: Experiment: Deadbeat Triple RFCS-PCC Performance under ψ_{pm} Variation.

5.4 Deadbeat Double RFCS-PCC

This method can reduce the number of candidate voltage vectors in control set to 2.

It also obtains firstly the reference voltage vector through the deadbeat MPC. However, instead choosing the adjacent and zero vectors of this reference as the vectors for reduced control set, only one active adjacent vector that is closest to the reference with smallest angular error is chosen. This will be explained with figure 5.31.

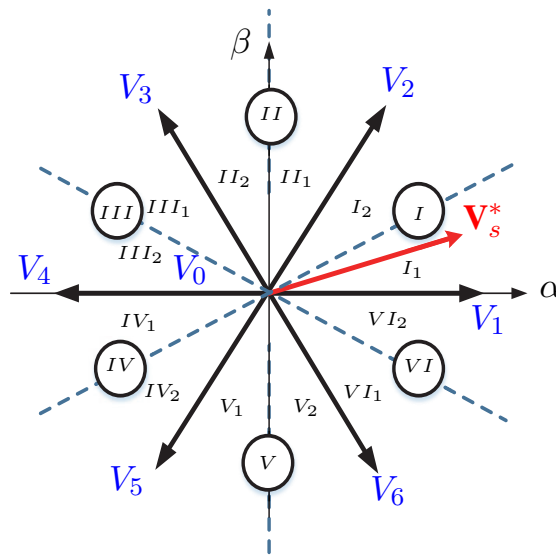


Figure 5.31: Hexagon of reference voltage vector selection for Deadbeat Double RFCS-PCC.

In figure 5.31, the hexagon plane is divided into 6 sectors with the angular bisectors between the six active vectors, where only one active vector is included in each sector. For example, as shown in this figure, v_1 is chosen as the vector that is nearest to the reference.

To realize this, the original sectors divided by 6 active vectors are further equally divided into 12 parts, i.e. $I_1, I_2, \dots, VI_1, VI_2$. And the reference vector is further decided to be in which one of these smaller sub-sectors. For example, if v_s^* is in either I_1 or VI_2 , v_1 is chosen as the vector that is nearest to the reference. However, this method cannot exclude the potential of zero vector as optima. Therefore, except the selected active vector, zero vector should also be always included into the candidate voltages' control set for cost function.

The flowchart of the proposed method is shown in figure 5.32. Within the dotted line of this figure is the detailed vector selection process for control set, whose pseudo code of algorithms can be found in APPENDIX B.

5.4.1 Simulation and Experimental Verification

This chapter shows the test results of the Deadbeat Double RFCS-PCC system.

Simulation 1 is to find out the performance of speed step-up and reversal process. Figure 5.33 shows speed, torque, current and flux of this process. It is similarly good as FCS-PCC.

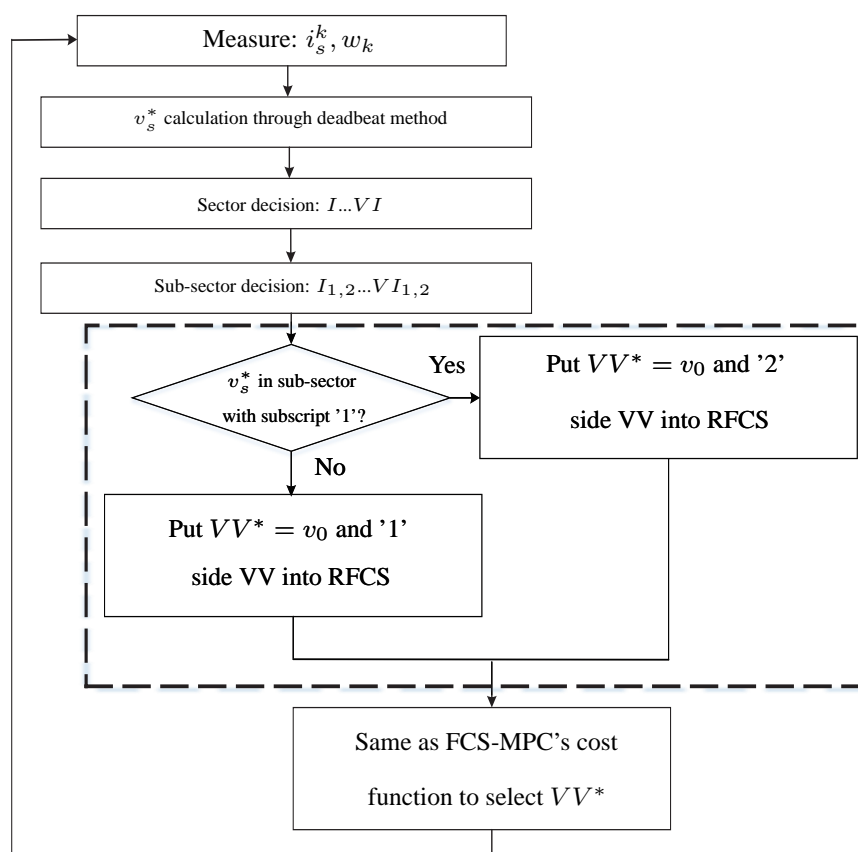


Figure 5.32: Flowchart of Deadbeat Double RFCS-PCC.

Figure 5.34 shows currents' tracking performance, which is also good as previous proposed methods.

Simulation 2 is to find out the speed performance under torque variations. Figure 5.35 shows speed, torque, current and flux of this process. The zoomed-in torque and switching states during torque variation transient are shown in figure 5.36. The band of oscillations is also similar as previous methods.

Simulation 3 tests the robustness of Deadbeat Double RFCS-PCC. Same variations range of parameters as the tests of FCS-PCC are set. Figure 5.37 to figure 5.39 show the system performance against the variations of R_s , L_d and L_q .

All three parameters' variation tests confirm the good and similar robustness of Deadbeat Double RFCS-PCC.

Experiment results of deadbeat double RFCS-PCC are found in figure 5.40 to figure 5.45. Figure 5.40 is the speed reversal process. Compared with previous Triple method, the Deadbeat Double RFCS-PCC has smaller torque ripples. Figure 5.41 illustrates the currents' tracking performance. Figure 5.42 illustrates the performance under torque variations. The speed transient variations are also similar as previous methods. Figure 5.43 to 5.45 are the robustness test results. Still the system is very robust against R_s variations but somehow sensitive to L_s and ψ_{pm} variations in transient.

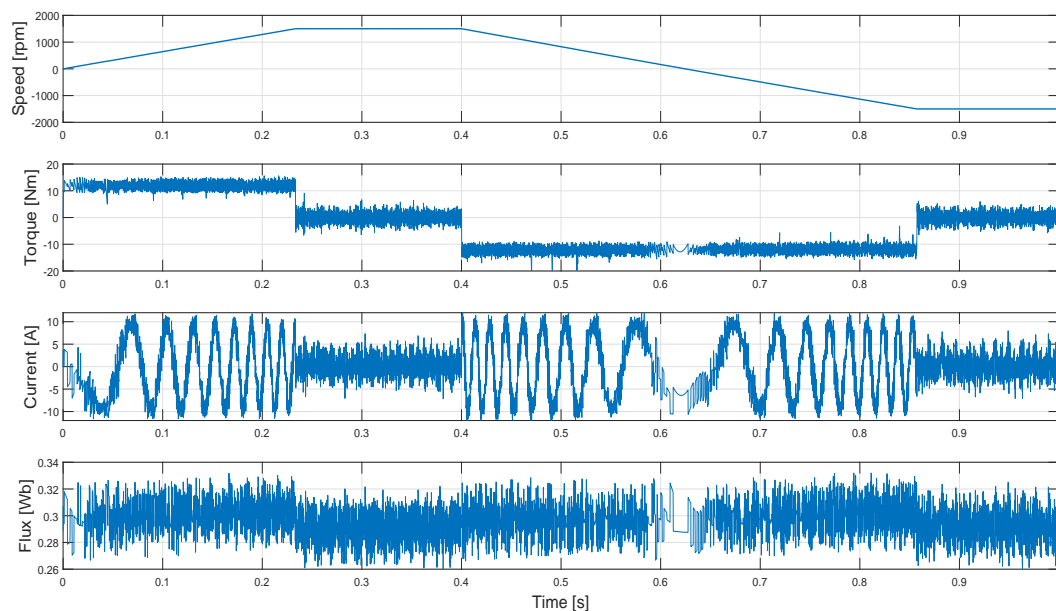


Figure 5.33: Simulation: Rated speed start up and reversal of Deadbeat Double RFCS-PCC.

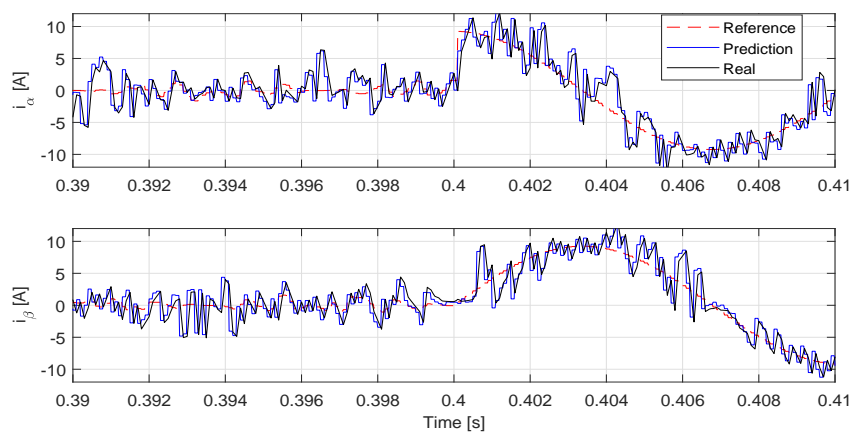


Figure 5.34: Simulation: Current Tracking Performance of Deadbeat Double RFCS-PCC.

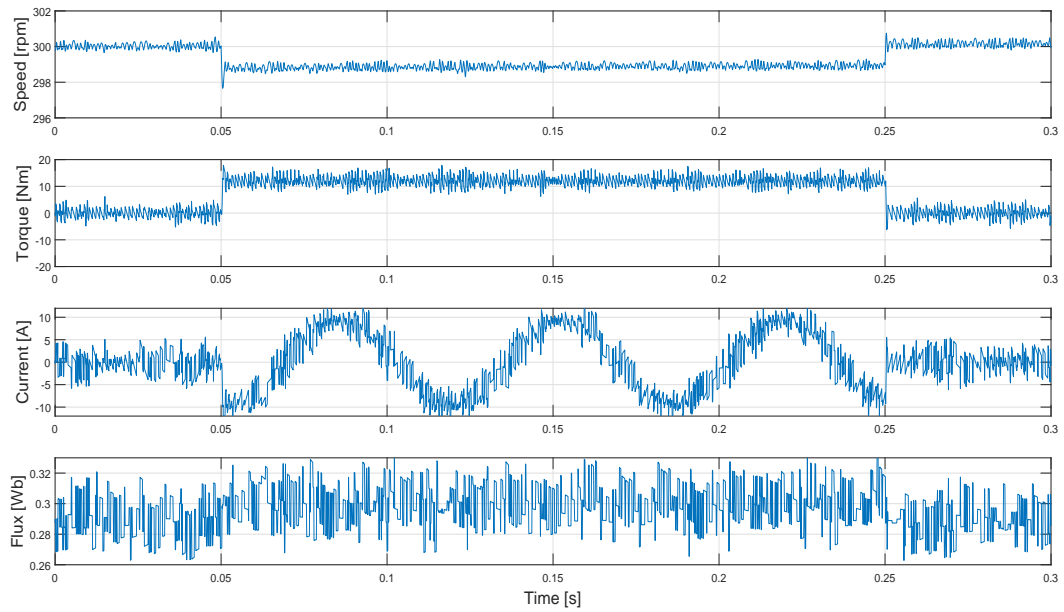


Figure 5.35: Simulation: Deadbeat Double RFCS-PCC Performance under Torque Variations.

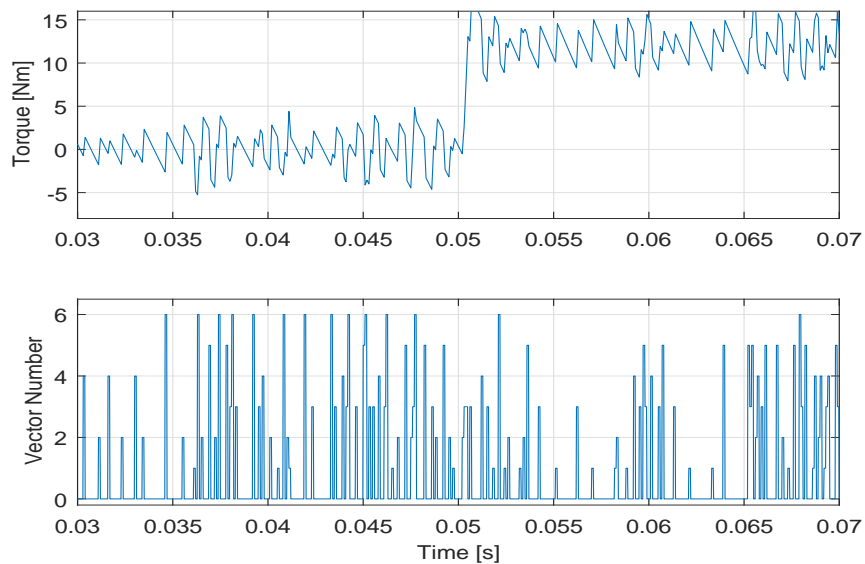


Figure 5.36: Simulation: Torque and Voltage Vectors of Deadbeat Double RFCS-PCC under Torque Variations.

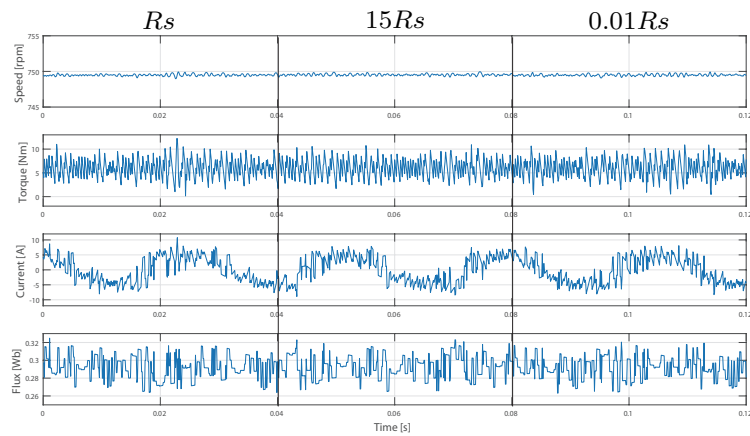


Figure 5.37: Simulation: Deadbeat Double RFCS-PCC performance with R_s Variations.

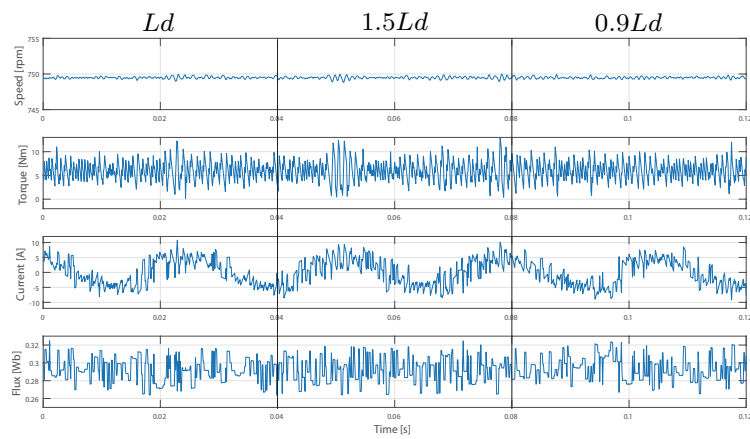


Figure 5.38: Simulation: Deadbeat Double RFCS-PCC performance with L_d Variations.

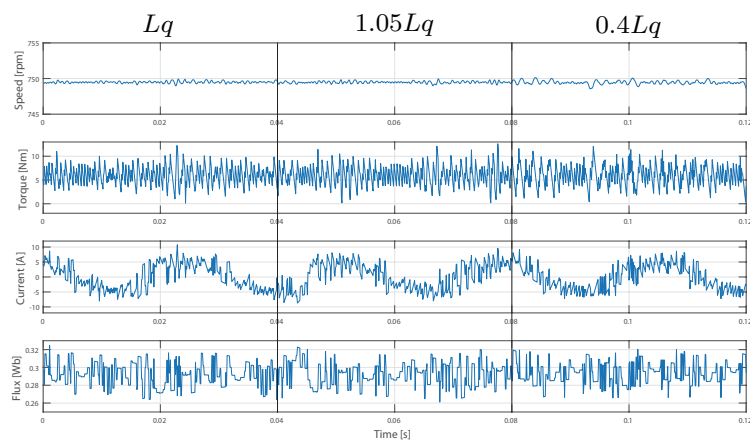


Figure 5.39: Simulation: Deadbeat Double RFCS-PCC performance with L_q Variations.

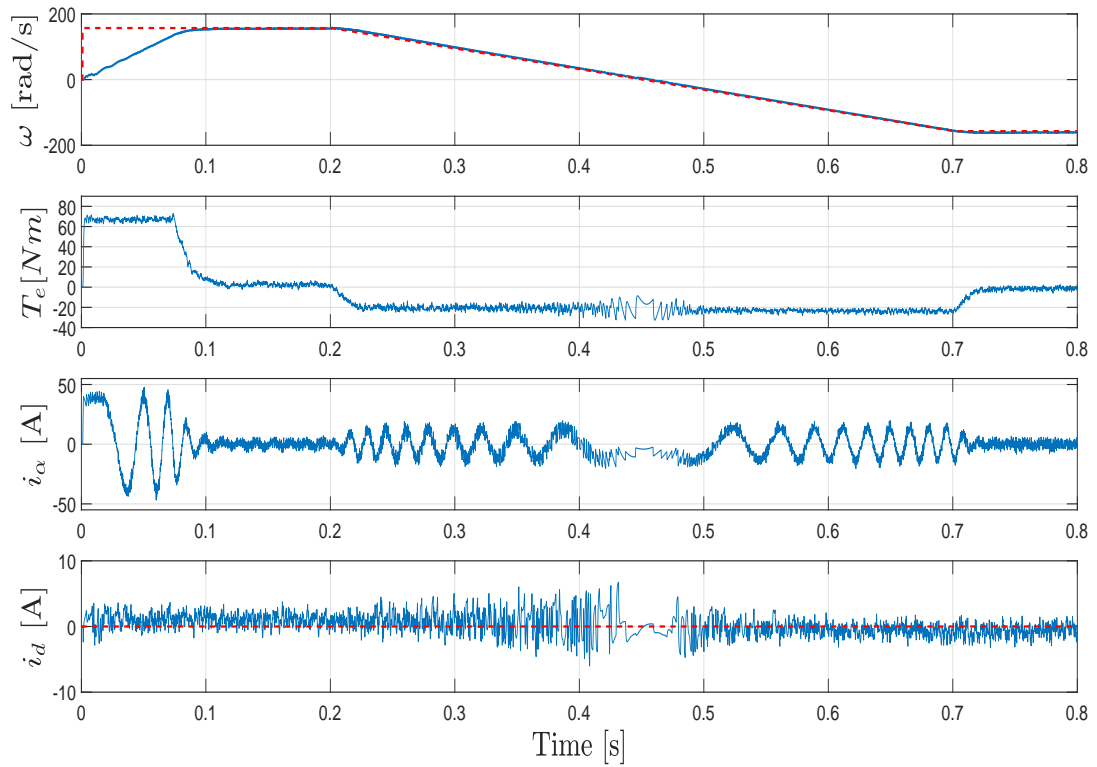


Figure 5.40: Experiment: Rated speed start-up and reversal of Deadbeat Double RFCS-PCC.

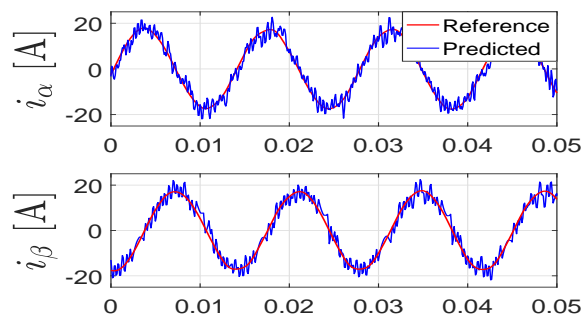


Figure 5.41: Experiment: Current Tracking Performance of Deadbeat Double RFCS-PCC.

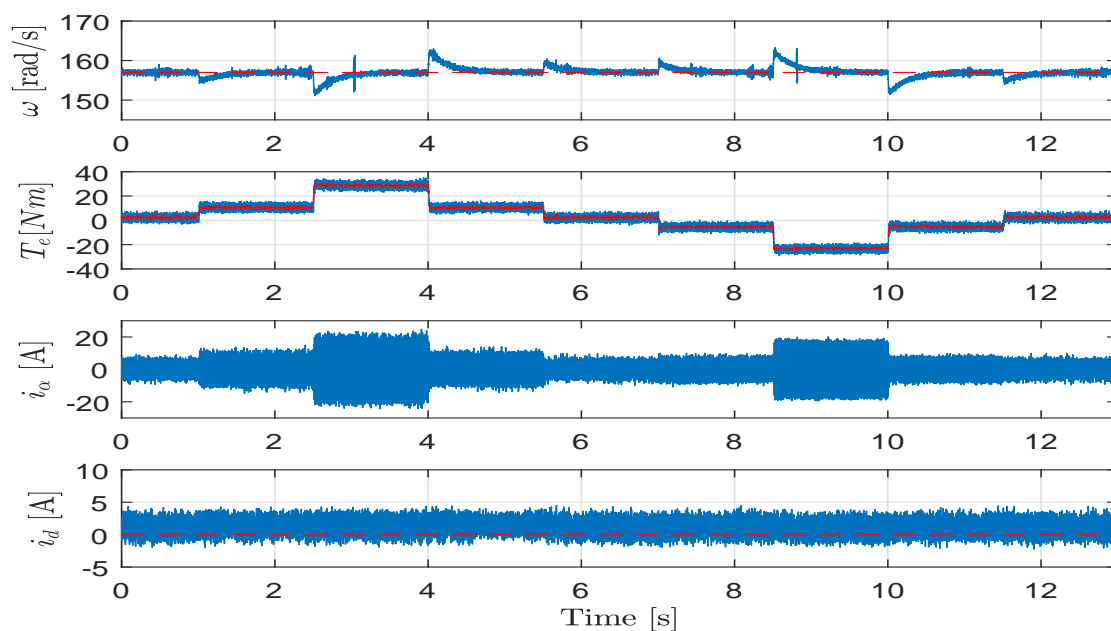


Figure 5.42: Experiment: Deadbeat Double RFCS-PCC Performance under Torque Variations.

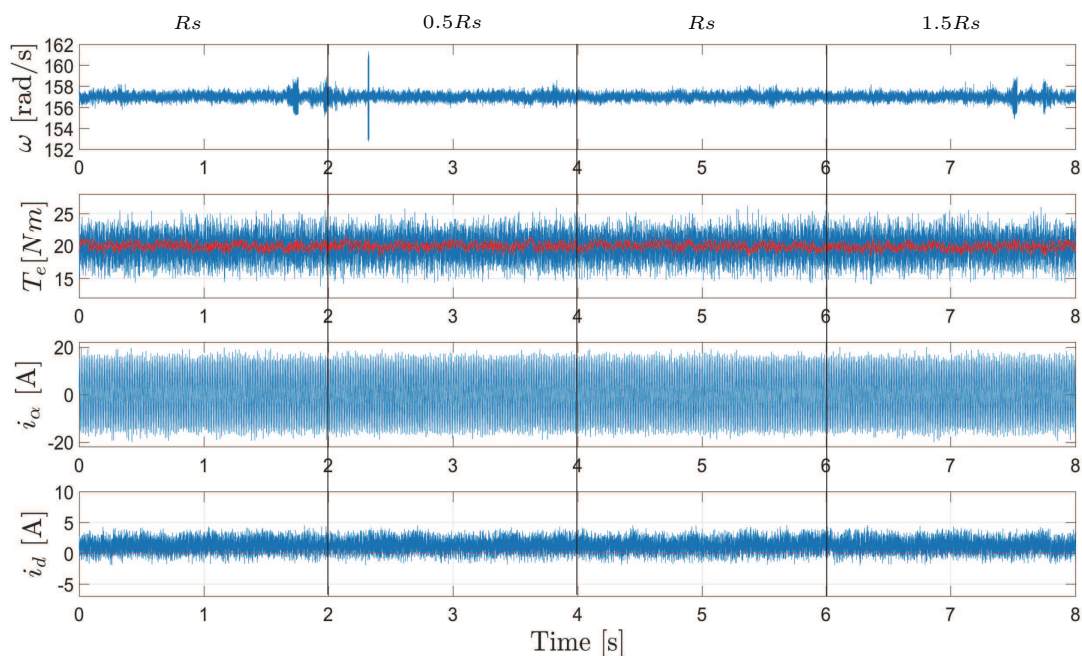


Figure 5.43: Experiment: Deadbeat Double RFCS-PCC Performance under R_s Variation.

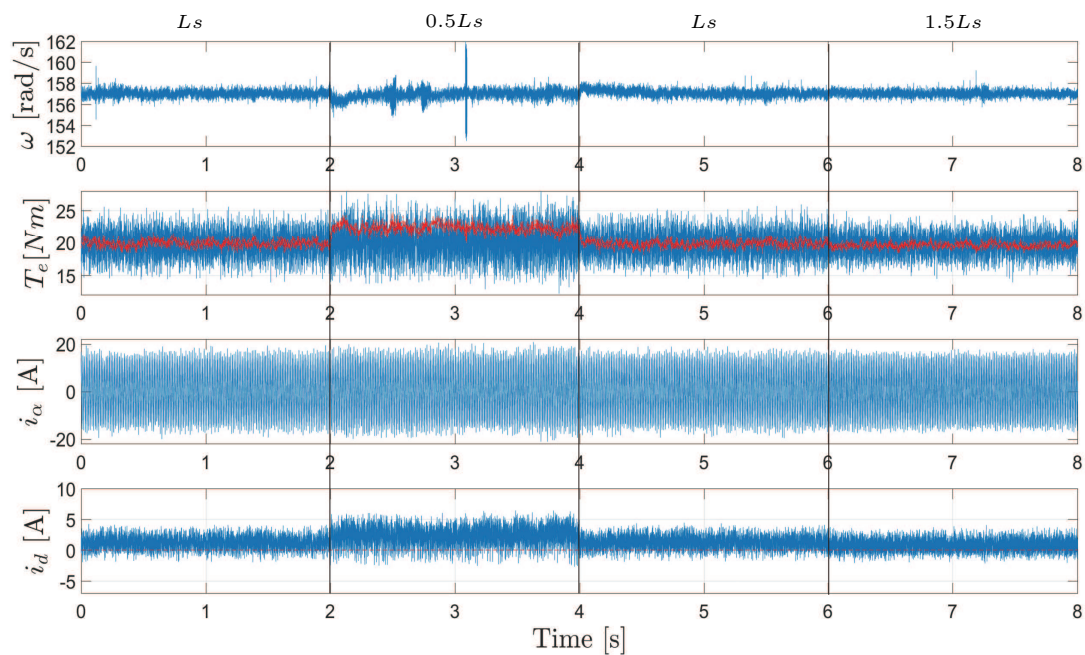


Figure 5.44: Experiment: Deadbeat Double RFCS-PCC Performance under L_s Variation.

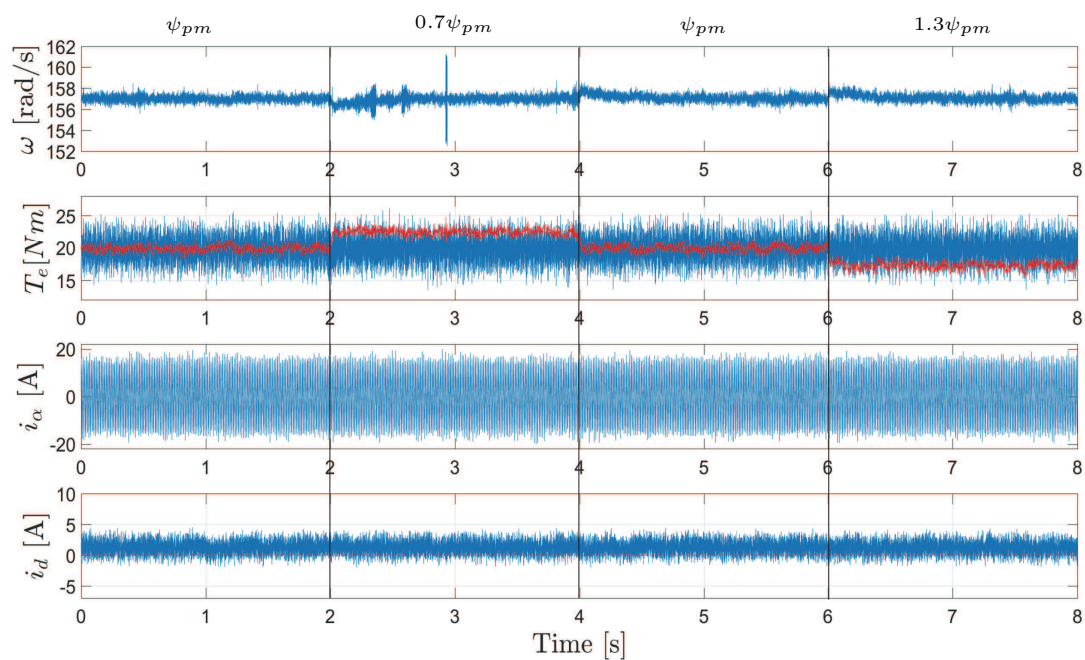


Figure 5.45: Experiment: Deadbeat Double RFCS-PCC Performance under ψ_{pm} Variation.

5.5 Deadbeat Null RFCS-PCC

This method can reduce the number of candidate voltage vectors in control set to 0. Therefore, no cost function is needed and exists in with this method [76].

In this sub-chapter, based on the proposed Deadbeat Double RFCS-PCC, a RFCS-MPC method called Deadbeat Null RFCS-PCC will be proposed. In contrast to the FCS-MPCs that through the minimization of cost function as the criteria for optimization and vector selection. With the calculated continuous voltage, deadbeat null RFCS-PCC selects the reference voltage vectors through a geometrical graphical optimization method. Thus, it reduces the number of candidate voltage vectors in control set to be null. Since 0 is surely a finite number, this method is also classified as RFCS-MPC. For simplicity, it is also exclusively named as Null-Control-Set-MPC (NCS-MPC).

This method also divides the VSI output voltage hexagon into 12 sectors as in previous Deadbeat Double RFCS-PCC. Different from the previous method, it compares the length of the reference vector to the line segment form by origin and edge of hexagon to decide the vector is closer to zero vector or to the contained active vector in one of the 12 sub-sectors. Therefore, by doing this, no cost function is needed. Figure 5.46 shows the way of vector selection.

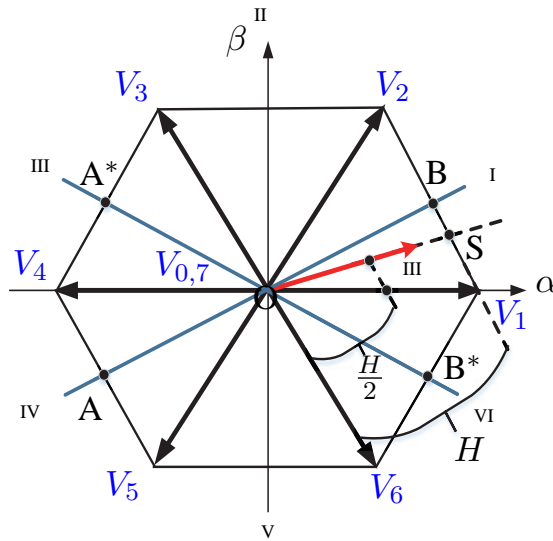


Figure 5.46: Hexagon of reference voltage vector selection for Deadbeat Null RFCS-PCC.

In figure 5.46, the length of the line segment form by origin and edge of hexagon is OS , whose length is H . If $|v_s^*|$ is longer than $H/2$, it is considered to be closer to active vector v_1 within the sector formed by I_1 and VI_2 . Therefore, v_1 is selected as the reference. Otherwise, if $|v_s^*|$ is no longer than $H/2$, v_0 is selected.

The flowchart of the proposed method is shown in figure 5.47. Within the dotted line of this figure is the detailed process for vector selection process, whose pseudo code of algorithms can also be found in APPENDIX B. Since H is periodically varying according to the angle of v_s^* , its calculation is a little tricky. This calculation of H for different sectors are also shown in APPENDIX B.

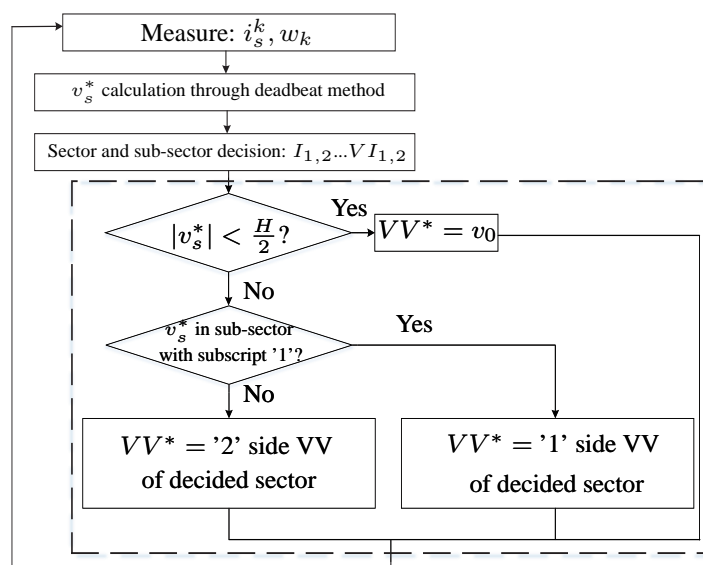
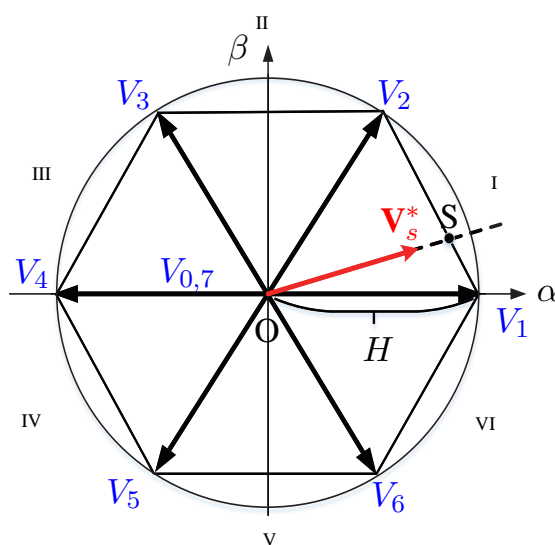


Figure 5.47: Flowchart of Deadbeat Null RFCS-PCC.

Figure 5.48: H approximation with V_{dc} .

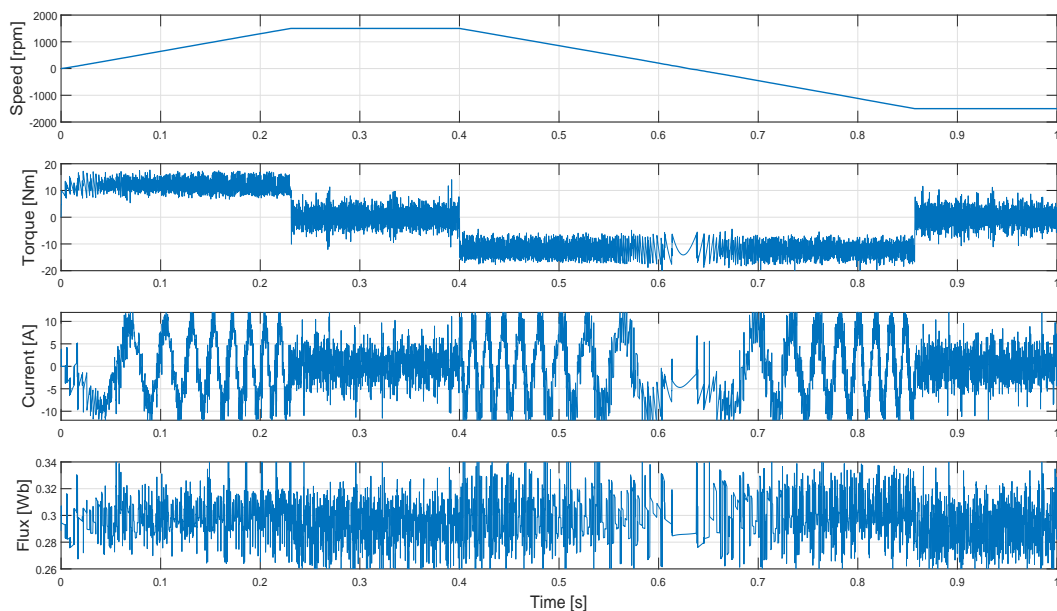
For simplicity of calculation, a fixed value of V_{dc} can be used to approximate the calculated H as shown in figure 5.48.

5.5.1 Simulation and Experimental Verification

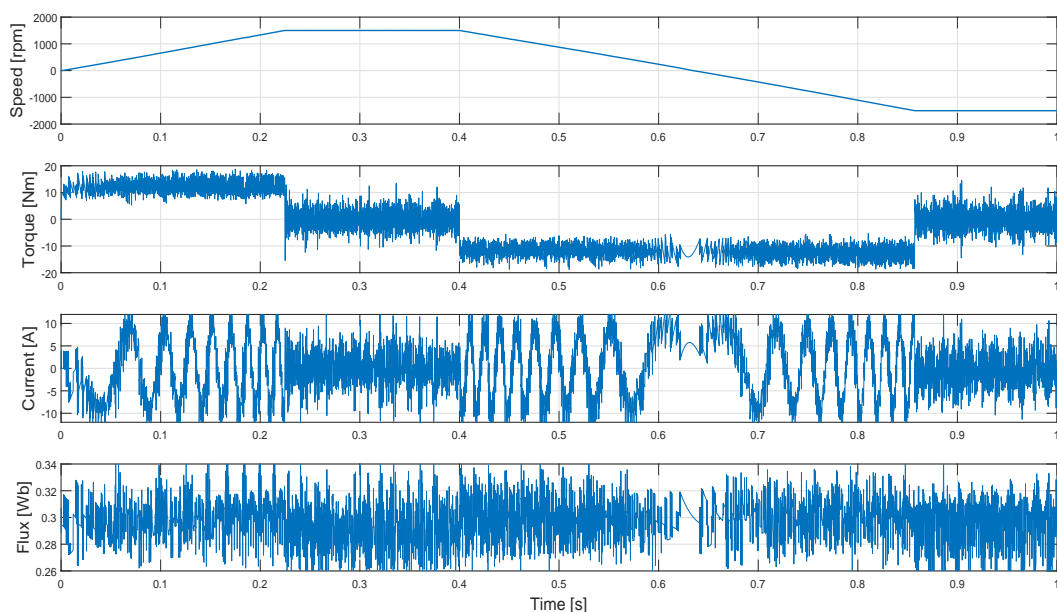
This chapter shows the test results of the Deadbeat Null RFCS-PCC system and its simplified form with $H = V_{dc}$ approximation. Similarly, same tests designed with same speed PI controller parameters are applied.

Simulation 1 is to find out the performance of the speed step-up and reversal process.

Figure 5.49 shows speed, torque, current and flux of this process. It's seen that with the Deadbeat Null RFCS-PCC, the ripples are comparatively large and but the transient performances are still similar as the results of previous deadbeat double RFCS-PCC system.



(a) H is line segment between origin and hexagon edge.



(b) Approximate: $H = V_{dc}$.

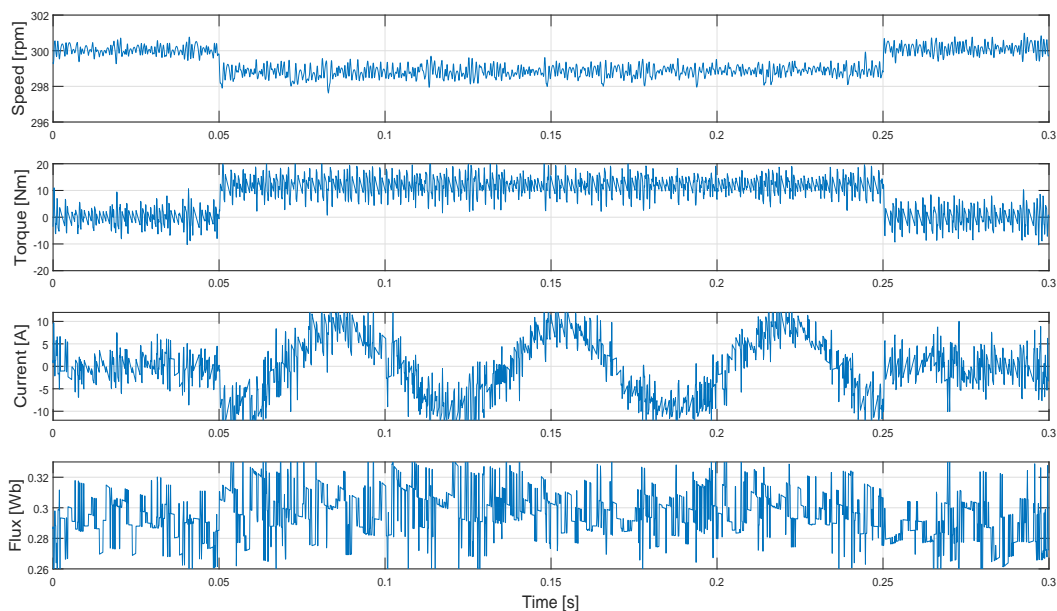
Figure 5.49: Simulation: Rated speed start-up and reversal of Deadbeat Null RFCS-PCC.

Since there is no cost function and predicted variables, no current tracking exists and thus to

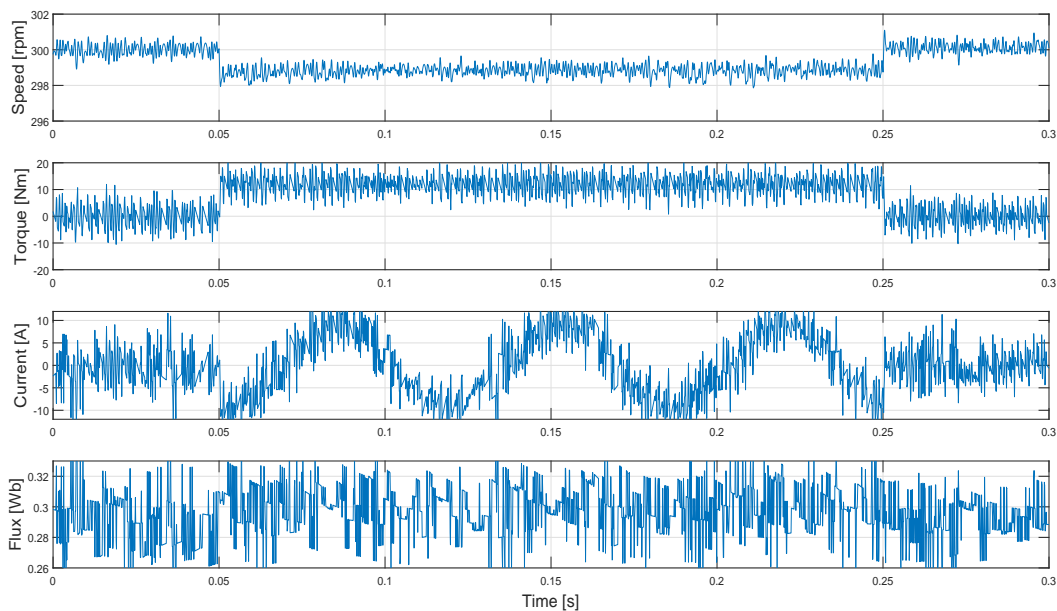
be shown.

Simulation 2 is to find out the speed performance under torque variations.

Figure 5.50 shows speed, torque, current and flux of this process.



(a) H is line segment between origin and hexagon edge.



(b) Approximate: $H = V_{dc}$.

Figure 5.50: Simulation: Deadbeat Null RFCS-PCC Performance under Torque Variations.

The zoomed-in torque and switching states during torque variation transient are shown in

figure 5.51.

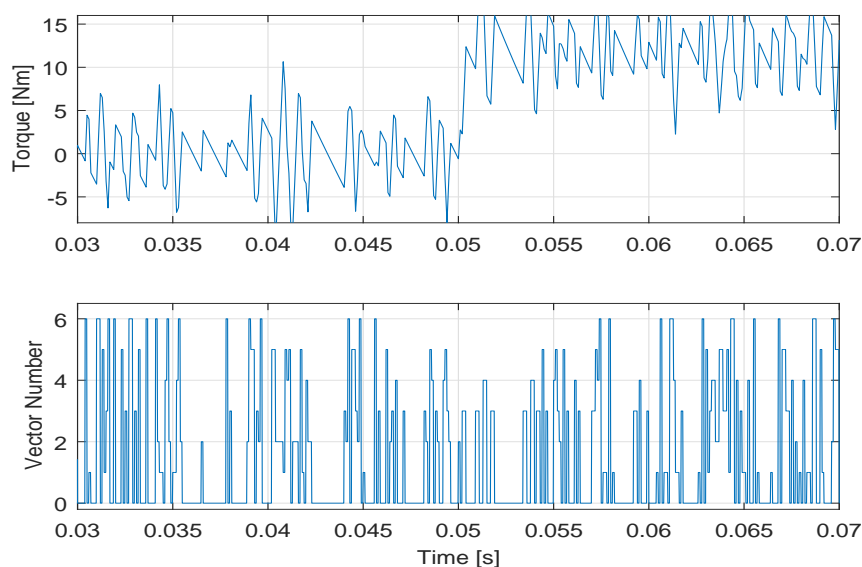
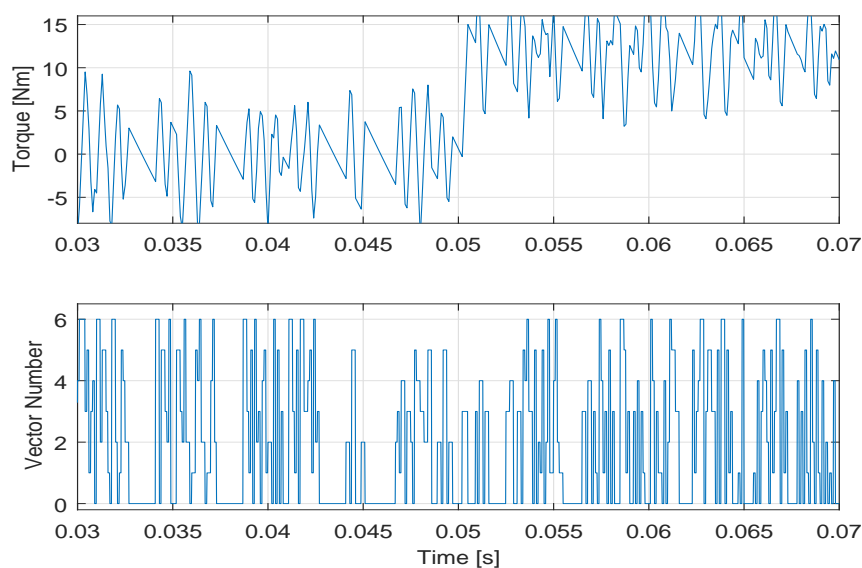
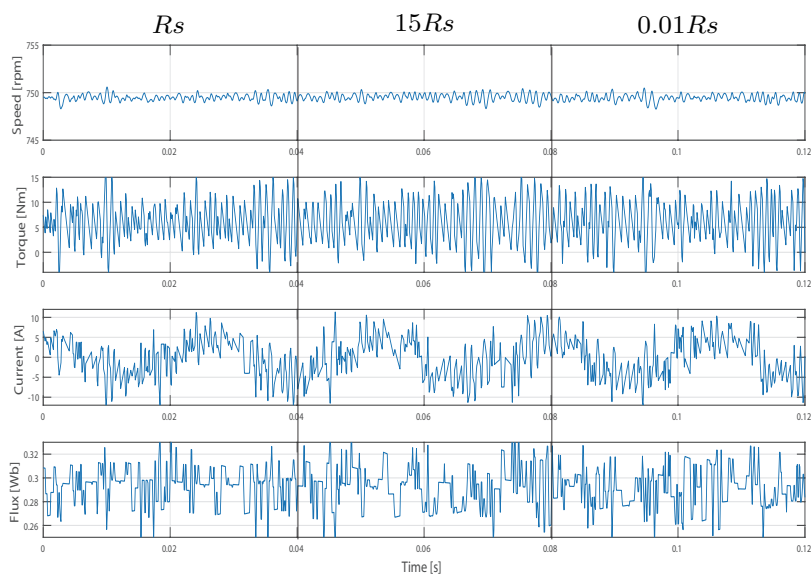
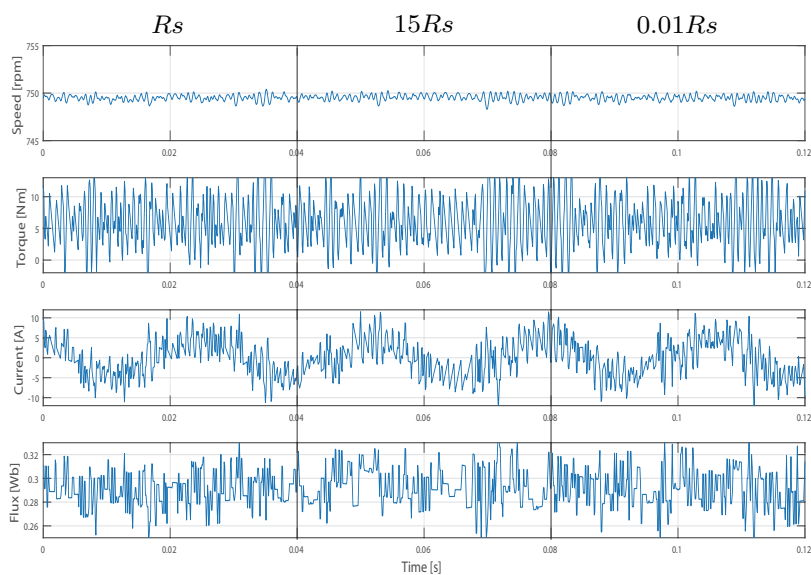
(a) H is line segment between origin and hexagon edge.(b) Approximate: $H = V_{dc}$.

Figure 5.51: Simulation: Torque and Voltage Vectors of Deadbeat Null RFCS-PCC under Torque Variations.

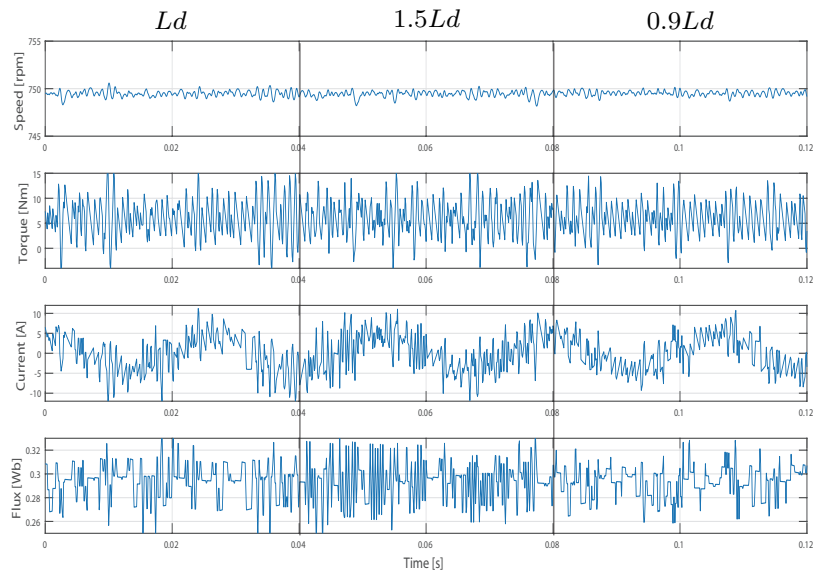
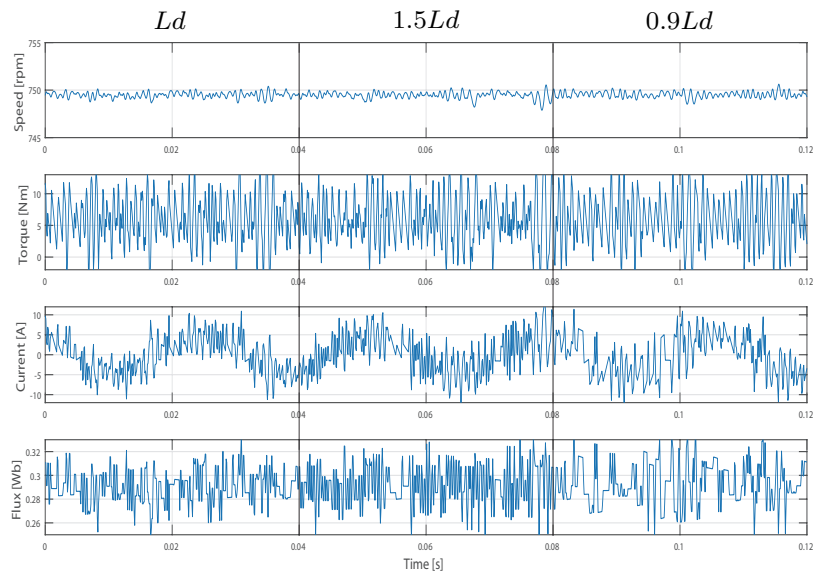
Simulation 3 tests the robustness of Deadbeat Null RFCS-PCC. Same variations range of parameters as the tests of FCS-PCC are set. Figure 5.52 to figure 5.54 show the system performance against the variations of R_s , L_d and L_q .

All previous simulation results show the slightly reduced steady state performance but similar dynamics performance and robustness of Deadbeat Null RFCS-PCC, when compared with conventional FCS-PCC and previous RFCS-PCC with more vectors in control set.

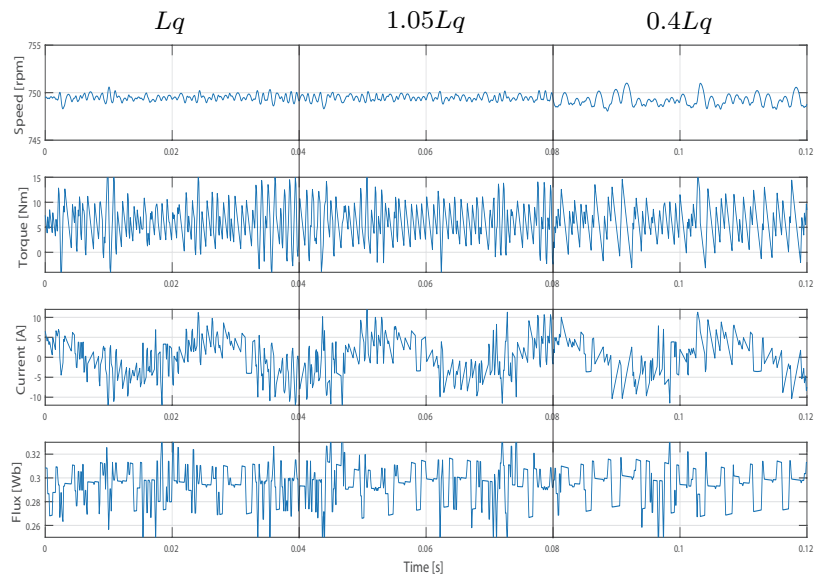
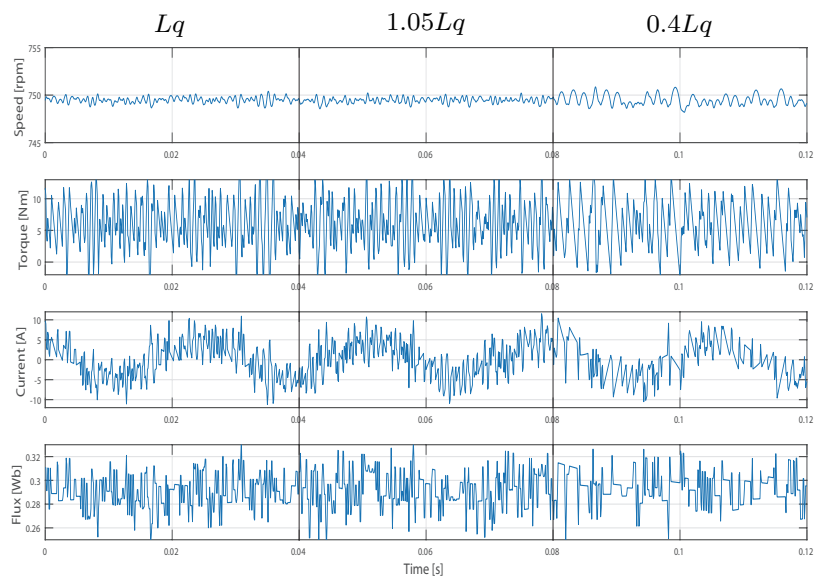
(a) H is line segment between origin and hexagon edge.(b) Approximate: $H = V_{dc}$.Figure 5.52: Simulation: Deadbeat Null RFCS-PCC performance with R_s Variations.

Though comparatively large torque and current ripples exist, experiments are also conducted on SPMSM, because the large reduction of control set of Deadbeat Null RFCS-PCC increases the necessity of experiments. Figure 5.55 is the speed reversal process of Deadbeat Null RFCS-PCC with its H approximation. No obvious difference in these test with two methods is found.

Figure 5.56 are the load tests of both methods. Zoomed in the torque sub-figures, it is found that the system with approximated torque reference has offsets, which shows the control deviations caused by approximation of H . Thanks to the outer speed loop, these deviations don't obviously deteriorate the real torque tracking to the reference given at the load machine side.

(a) H is line segment between origin and hexagon edge.(b) Approximate: $H = V_{dc}$.Figure 5.53: Experiment: Deadbeat Null RFCS-PCC performance with L_d Variations.

However, the drawbacks of approximated H are shown in the robustness tests in figure 5.57 to 5.59, especially in the L_s deviation test, where the method with approximated H to V_{dc} has longer speed respond time thus larger speed drop. Nevertheless, what must be noticed and surprising is that the method with approximated H has actually similar L_s robustness as the previous methods. However, the method without H approximation has best L_s robustness than all the previous RFCS-PCC methods and is as good as that of the conventional FCS-PCC. This shows that difference methods contains different aspects of characteristics and advantages. In light of its good robustness, largely reduction of control set vectors' number and elimination of

(a) H is line segment between origin and hexagon edge.(b) Approximate: $H = V_{dc}$.Figure 5.54: Deadbeat Null RFCS-PCC performance with L_q Variations.

cost function, Deadbeat Null RFCS-PCC is applicable even there are slightly larger ripples in variables.

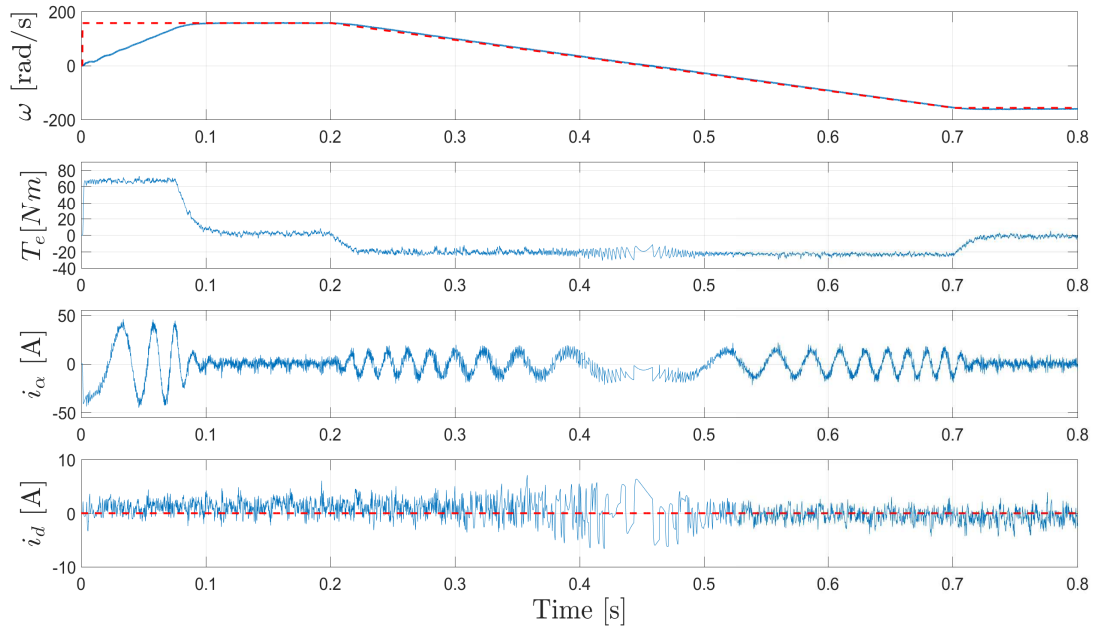
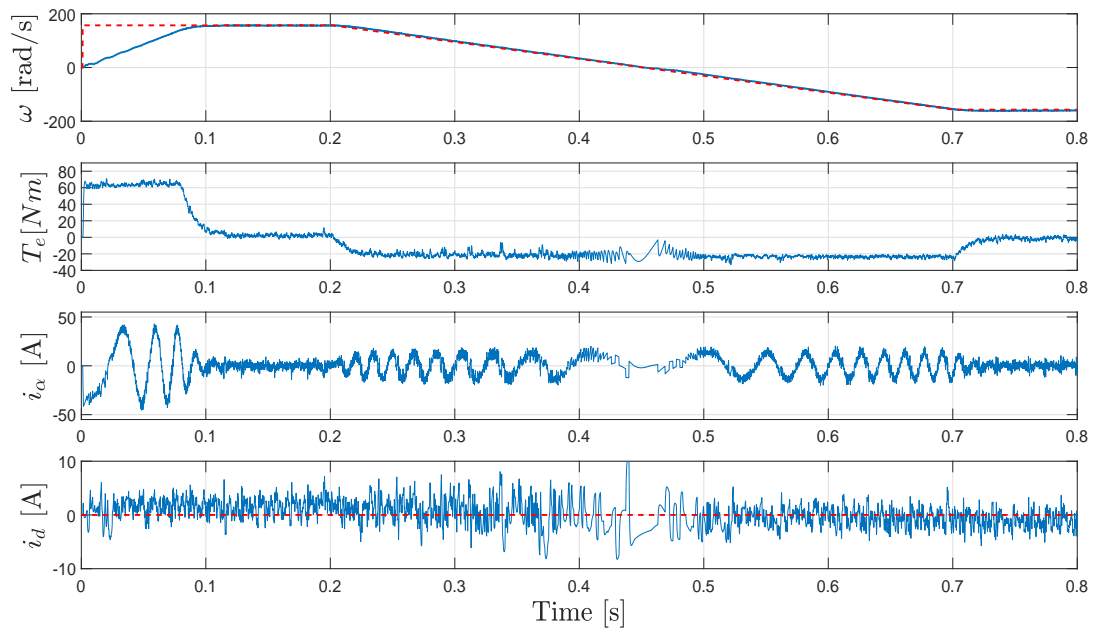
(a) H is line segment between origin and hexagon edge.(b) Approximate: $H = V_{dc}$.

Figure 5.55: Experiment: Rated speed start up and reversal of Deadbeat Null RFCS-PCC.

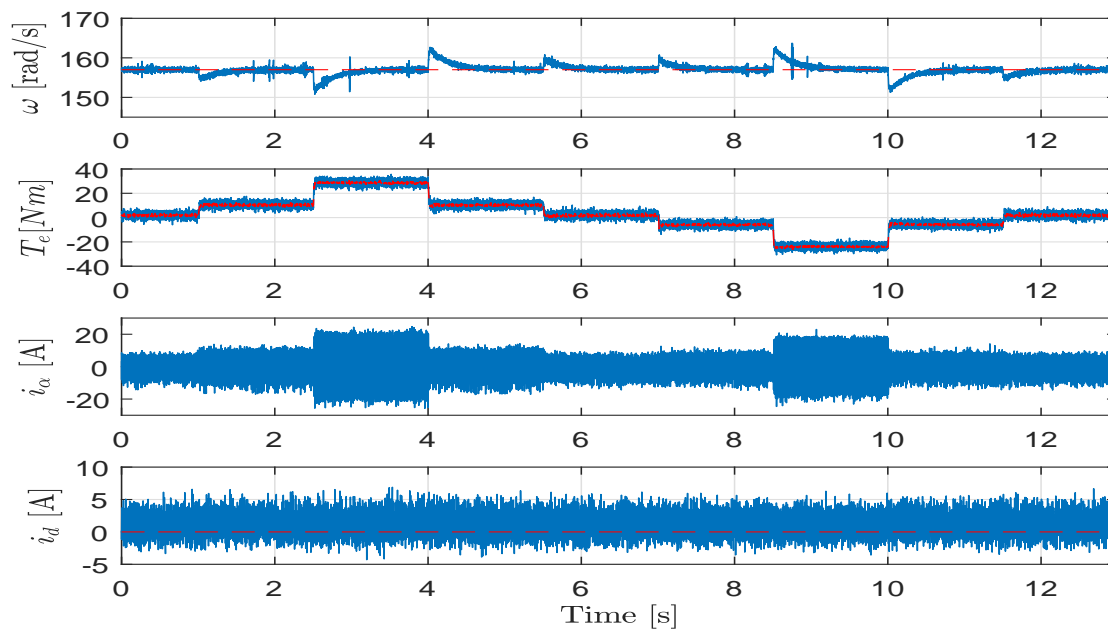
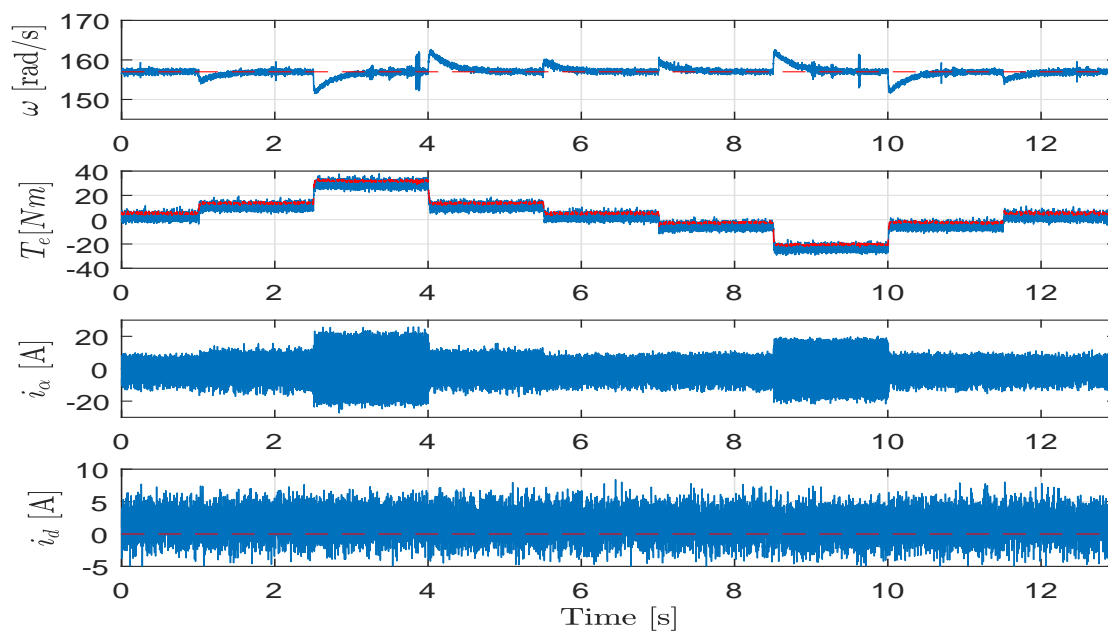
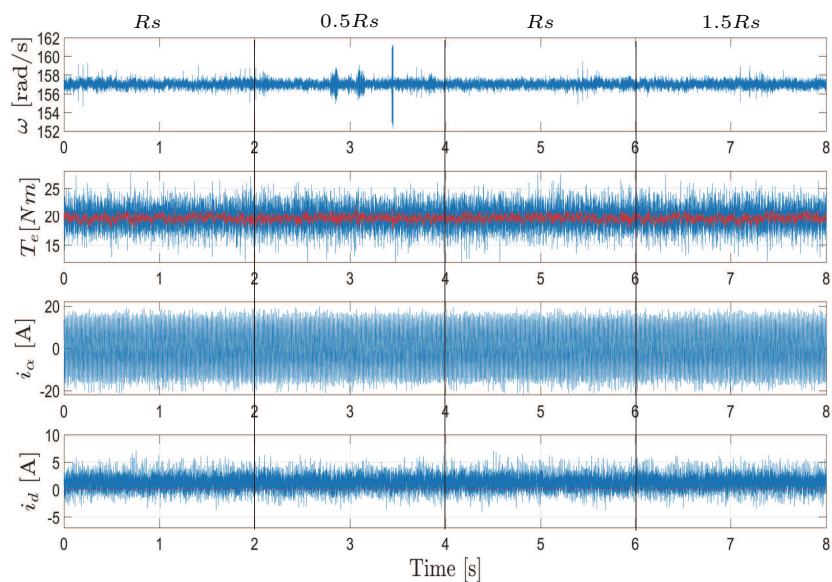
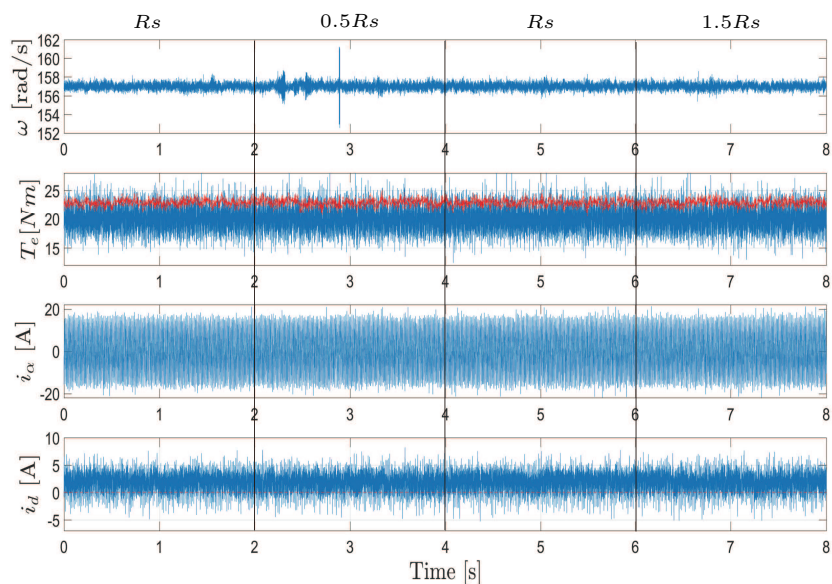
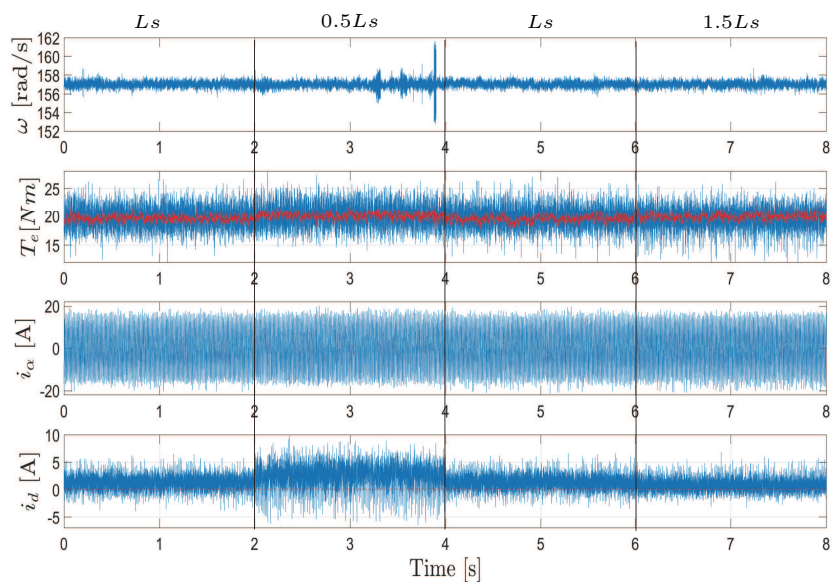
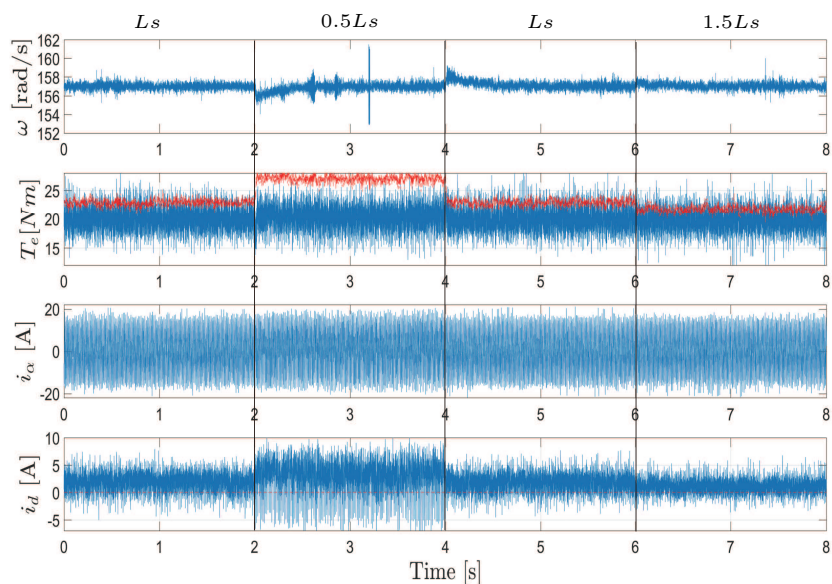
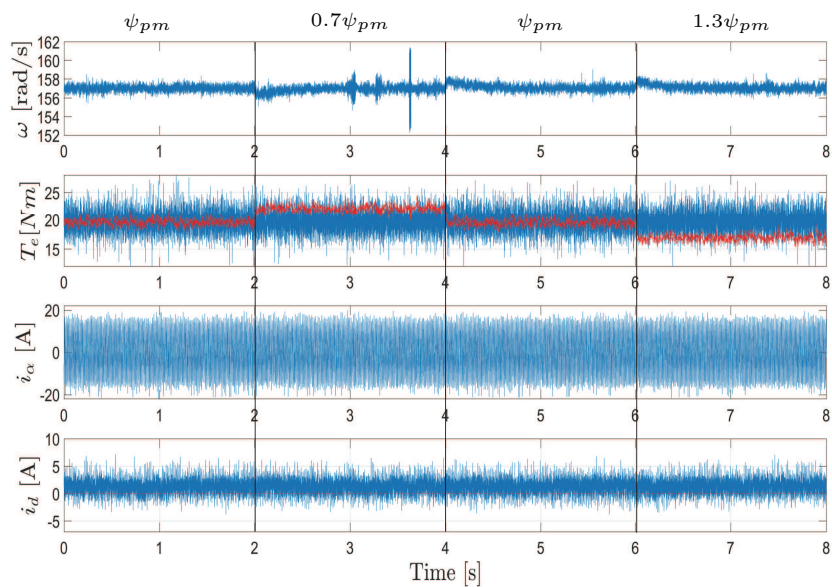
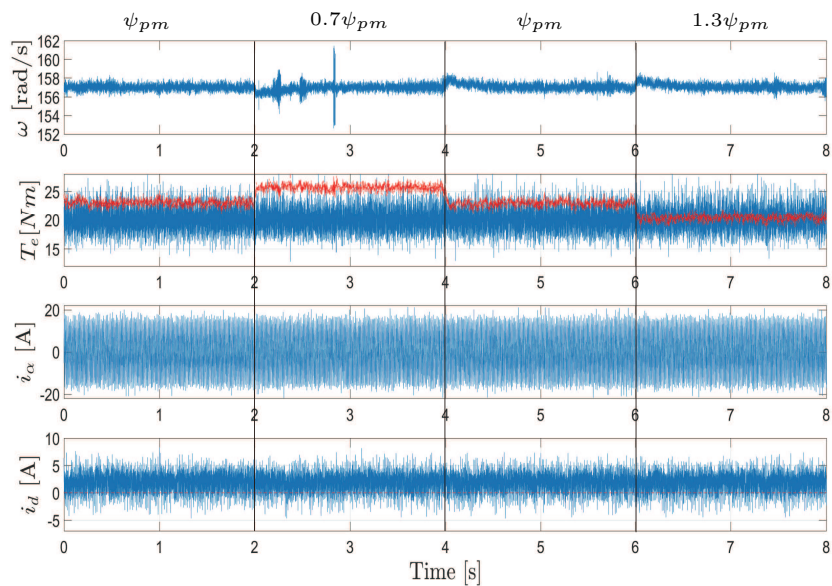
(a) H is line segment between origin and hexagon edge.(b) Approximate: $H = V_{dc}$.

Figure 5.56: Experiment: Deadbeat Null RFCS-PCC Performance under Torque Variations.

(a) H is line segment between origin and hexagon edge.(b) Approximate: $H = V_{dc}$.Figure 5.57: Experiment: Deadbeat Null RFCS-PCC performance with R_s Variations.

(a) H is line segment between origin and hexagon edge.(b) Approximate: $H = V_{dc}$.Figure 5.58: Experiment: Deadbeat Null RFCS-PCC performance with Ls Variations.

(a) H is line segment between origin and hexagon edge.(b) Approximate: $H = V_{dc}$.Figure 5.59: Experiment: Deadbeat Null RFCS-PCC performance with ψ_{pm} Variations.

5.6 Conclusion

The analysis of all previous proposed Reduced FCS-PCC methods of the loaded state in their corresponding test 2 are shown in the bar chart of figure. 5.60. For thorough comparison, conventional FCS-PCC without control set reduction and the simplified version of deadbeat null RFCS-PCC with the approximation that $H = V_{dc}$ is also shown in the chart.

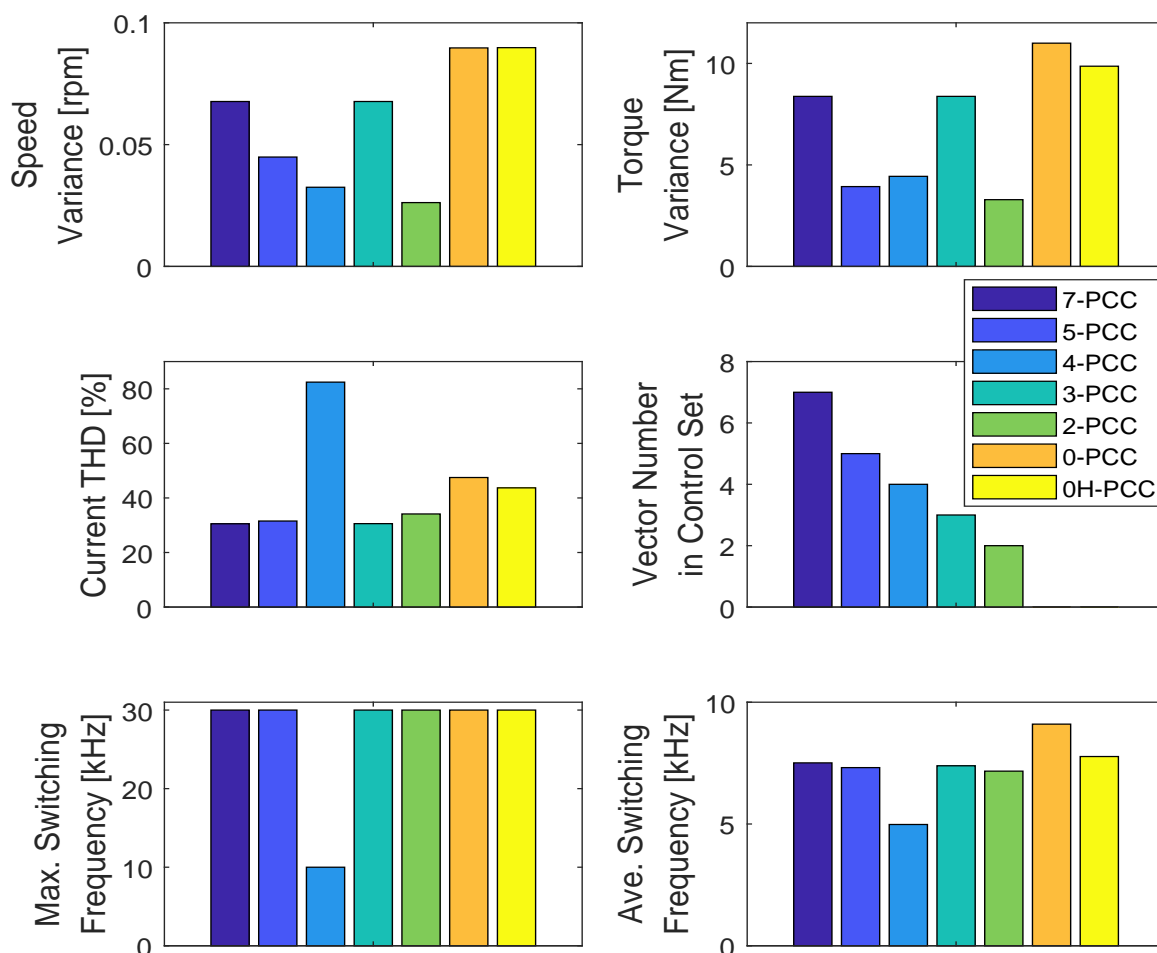


Figure 5.60: Analysis of FCS-PCC (7-PCC), Dichotomy-based RFCS-PCC (5-PCC), Switching-minimized RFCS-PCC (4-PCC), Deadbeat Triple RFCS-PCC (3-PCC), Deadbeat Double RFCS-PCC (2-PCC), Deadbeat Null RFCS-PCC (0-PCC) and its $H = V_{dc}$ approximated method (0H-PCC).

For speed variance: dichotomy, switching-minimized, and deadbeat double methods have smaller speed variances than the other methods. And the deadbeat null methods have larger variances than the others.

For torque variance: dichotomy, switching-minimized and deadbeat double methods have smaller variances. And the deadbeat null methods still have bigger variances than the others.

For current THD: dichotomy, deadbeat triple and deadbeat double methods have similarly good current quality as FCS-PCC but the switching-minimized has higher THD as tradeoff of lower switching frequency.

For vector number: being consistent with intuition, it is found that the methods eliminating voltage vectors with or partially with no cost function, though can reduce the calculation efforts to some extent, cannot fully ensure selecting the optimized vector, when compared with the conventional FCS-PCC with merely cost function as criteria of vector selection.

For maximum switching frequency: except the switching-minimized method, all other methods are possible to reach the full switching frequency of 3 times of sampling frequency of $30H_z$.

For average switching frequency: FCS-PCC is still better and it has even lower average switching frequency than the switching-minimized method. The other methods all have comparatively high average switching frequency, with the deadbeat null methods' to be the highest. Except switching-minimized method has not much lower switching frequency and the two deadbeat null methods have slightly higher frequencies, the average switching frequencies of all RFCS-MPCs are similar.

Therefore, it can be concluded from the previous test results that all proposed reduced FCS-MPC methods in this chapter work effectively. According to the requirements and calculation limitations of systems, they can all be good optional alternatives to replace the conventional FCS-MPC, with reduction of calculation efforts and even better steady state performances. And some of them have even the ability of torque and speed ripples inhibitions, when compared to FCS-MPCs. Deadbeat double RFCS-PCC is the optimal amongst all, in light of its good and average indexes at all aspects for comparison as shown in figure. 5.60.

CHAPTER 6

MPC with Disturbance Observer

"It's all about PI parameters adjustment."—The essence of disturbance observer.

Disturbance Observer (DO), as its name implies, is initially invented based on disturbance related physical systems' observation models to reduce the disturbances [78]. It belongs to observers/estimators, and works also as model predictive controller and a form of deadbeat control in more general classification [79, 80].

In order to achieve fast system response at different load conditions at different speeds, time-varying nonlinear P,I parameters are required to achieve optimal operation performance. As is known that MPC removes the inner current PI controllers, therefore, only speed PI controller exists in the system. Conventional speed PI is tuned by experiences. Though there are different methods of PI tunings [81–84], it is sometimes tedious and complicated. Therefore, a mechanical model based DO is designed in this chapter to ease, even partially remove the PI parameters' tuning work. Therefore, it can say that DO is designed to improve or somehow simplify outer speed PI controller for better system performance.

In the following sub-chapters, the basic concepts and working principles of DO will be firstly introduced and explained, thereafter, a specially designed DO for torque disturbance inhibition for IPMSM will be designed and applied to both continuous MPC and FCS-MPC to verify the its effectiveness.

6.1 DO Basics

The most general state-space (SS) representation of a linear system is in the following form [36, 85]:

$$\begin{cases} \dot{\mathbf{x}} = \mathbf{A} \mathbf{x} + \mathbf{B}_0 \mathbf{u} + \mathbf{B}_1 \mathbf{d} \\ \mathbf{y} = \mathbf{C} \mathbf{x} \end{cases} \quad (6.1)$$

where \mathbf{x} , \mathbf{u} and \mathbf{d} represent the state, input and the lump disturbance vectors, respectively,

and A , B_0 and B_1 are their corresponding coefficient matrices in the state function. C is the coefficient for output equation.

With the above equations, a DO can be designed as shown in fig. 6.1.

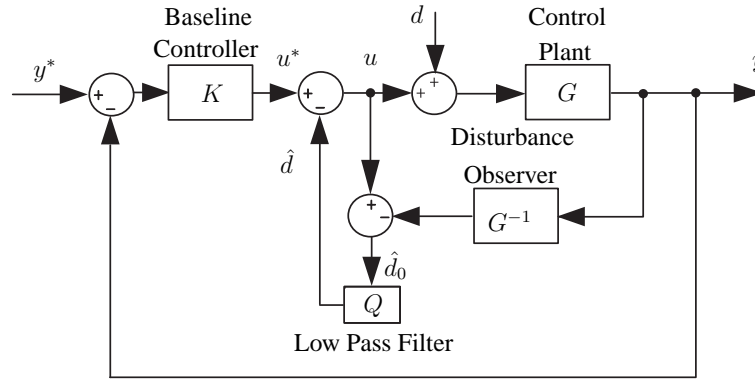


Figure 6.1: DO.

If the disturbance of the control system can be measured in finite consecutive control periods, a baseline controller can be applied. In this figure, before given the control reference directly from the controller to the control plan, a DO is cascaded connected after the baseline controller to compensate the disturbance' influences. The control effort of DO is realized through a positive feedback. This implementation can make the control plant to be equally "disturbance free" for the forward channel. This compensation of disturbance, based on the disturbance related machine model, can also be considered as a form of deadbeat control.

Assume the the control output of the baseline controller is:

$$\mathbf{u}^* = f(x) \quad (6.2)$$

If the the disturbance and input affects the state through the same channel, i. e. $B_0 = B_1$, the integrated control of DO is shown as follows.

$$\mathbf{u} = \mathbf{u}^* - \hat{\mathbf{d}} \quad (6.3)$$

DO contains high flexibility and versatility, rendering the design of it and the form of baseline controller to be independent. In another word, it is not system and control method sensitive.

6.2 Torque Disturbance Observer for Electric Drives

A DO specially for torque disturbance is designed to improve the system dynamics and thus guarantee the precision of control [86]. Criteria to guarantee system stability is also achieved through Lyapunov method [87].

6.2.1 Torque Disturbance Observer Design

Since DO can be considered as an estimator of disturbance, the estimation error can be defined as:

$$e_d = \hat{d} - d \quad (6.4)$$

where \hat{d} and d are the estimated and real disturbances. Therefore, it can be derived that:

$$\hat{d}(k+1) = \hat{d}(k) - \hat{e}_d(k) \quad (6.5)$$

A prerequisite of effective estimation is that the disturbance can be considered as time invariant, with the approximation:

$$\dot{d} = 0 \quad (6.6)$$

The derivative of disturbance estimation can be written as:

$$\begin{aligned} \dot{\hat{d}} &= \frac{-e_d(k)}{T_s} = \frac{-(\hat{d} - d)}{T_s} \\ &= -\frac{\lambda_T}{B_1 T_s} \cdot (B_1 \hat{d} - B_1 d) \end{aligned} \quad (6.7)$$

where a coefficient of λ_T is multiplied as the observer gain to achieve varying convergence rate or dynamics, and with emphasis on different control variables.

With previous SS of linear system in (6.1), (6.7) can be derived as:

$$\dot{\hat{d}} = -\frac{\lambda_T}{B_1 T_s} \cdot B_1 \hat{d} + \frac{\lambda_T}{B_1 T_s} \cdot (\dot{x} - Ax - B_0 u) \quad (6.8)$$

Flux weakening/increasing is still not considered in this work. Therefore, in the dq reference frame, by setting rotor flux magnitude $|\psi_r|^* = 0$, it gains:

$$i_d^* = 0 \quad (6.9)$$

Since electromagnetic torque and the mechanical equation of the motor can be expressed as:

$$T_e = T_e^* = \frac{3}{2} \cdot p[\psi_{PM} i_q^* + (L_d - L_q) i_d^* i_q^*] = \frac{3}{2} \cdot p\psi_{PM} i_q^* \quad (6.10)$$

$$T_e - T_l = J\dot{\omega}_m + B\omega_m \quad (6.11)$$

where p is the pole pair number, T_l is the load torque, J and B are the inertia of moment and friction coefficient. Omitting the friction, i.e. $B = 0$, for a speed controlled IPMSM drive system, it derives:

$$\begin{cases} \dot{\omega}_m = \frac{3}{2} \cdot \frac{p\psi_{PM} i_q^*}{J} - \frac{T_l}{J} \\ y = \omega_m \end{cases} \quad (6.12)$$

Compare (6.12) with (6.1):

$$\begin{cases} \mathbf{x} = \omega_m, & \mathbf{A} = 0 \\ \mathbf{u} = i_q^*, & \mathbf{B}_0 = \frac{3}{2} \cdot \frac{p\psi_{PM}}{J} \\ \mathbf{d} = T_L, & \mathbf{B}_1 = -\frac{1}{J} \\ \mathbf{y} = \omega_m, & \mathbf{C} = 1 \end{cases} \quad (6.13)$$

From (6.13), it is seen that the system is linear time invariant (LTI), with the state space functions' coefficients to be constant. Substitute (6.13) into (6.7), the derivative of estimated torque is:

$$\dot{\hat{T}}_L = \frac{J\lambda_T}{T_s} \cdot \left(-\frac{1}{J}\right) \cdot \hat{T}_L - J\lambda_T \cdot \left(\omega_m - \frac{3}{2} \cdot \frac{p\psi_{PM}i_q^*}{J}\right) \quad (6.14)$$

Backward equivalence of (2.42) is applied for discretization:

$$\frac{dx}{dt} = \frac{x(k) - x(k-1)}{T_s} \quad (6.15)$$

Therefore, (6.14) can be expanded as:

$$\begin{aligned} \hat{T}_L(k) &= \frac{1}{1 + \lambda_T} \cdot [\hat{T}_L(k-1) + J\lambda_T \cdot \\ &\quad \frac{\omega_m(k-1) - \omega_m(k)}{T_s} + \frac{3}{2} \lambda_T p \psi_{PM} i_q^*] \end{aligned} \quad (6.16)$$

6.2.2 Stability Analysis

Review the estimation error of disturbance:

$$e_d = \hat{d} - d \quad (6.17)$$

Since the disturbance change \dot{d} is relatively faster than the error dynamics \dot{e}_d of the observer, and review (6.7), it is derived that:

$$\dot{e}_d + \lambda_T B_1 e_d = \dot{e}_d - \frac{\lambda_T}{J} \cdot e_d = 0 \quad (6.18)$$

where e_d converges to zero as long as \dot{d} is stable for all states. To achieve the input to state stability (ISS) of DO based closed-loop feedforward system, Lyapunov method is applied. The stability function is:

$$V_e = \frac{1}{2} e_d^2 \quad (6.19)$$

This yields the derivative:

$$\dot{V}_e = e_d \dot{e}_d = \frac{\lambda_T}{J} e_d^2 \quad (6.20)$$

Regardless the value of ω_m , the closed loop system is globally exponentially stable when \dot{V}_e is negative definite, i.e. $\lambda_T < 0$.

6.3 Deadbeat PCC with Torque Disturbance Observer

The designed torque disturbance observer (TDO), when integrated into the aforementioned Deadbeat PCC drive system for IPMSM, is displayed in figure 6.2. The control effort of TDO is realized through a positive feedback. In this system, only the estimated torque of the last cycle is shown with $(k - 1)$. Other variables that without sequence number are of current control cycle.

Moreover, when the system is turned into a "torque disturbance free" system with the proposed TDO as a feed-forward compensator, the integral part is no more necessary in speed PI controller, because TDO acts against disturbance variations at much faster rate than the speed changes. Therefore, it doesn't require the comparatively slow integral part in the PI controller, rendering it to simply become a P controller. Because the PI parameters are operation points sensitive, i.e. they must be changed to achieve proper and optimized performance with respect to different load and speed states, TDO simplifies and reduces the tuning work of baseline controllers.

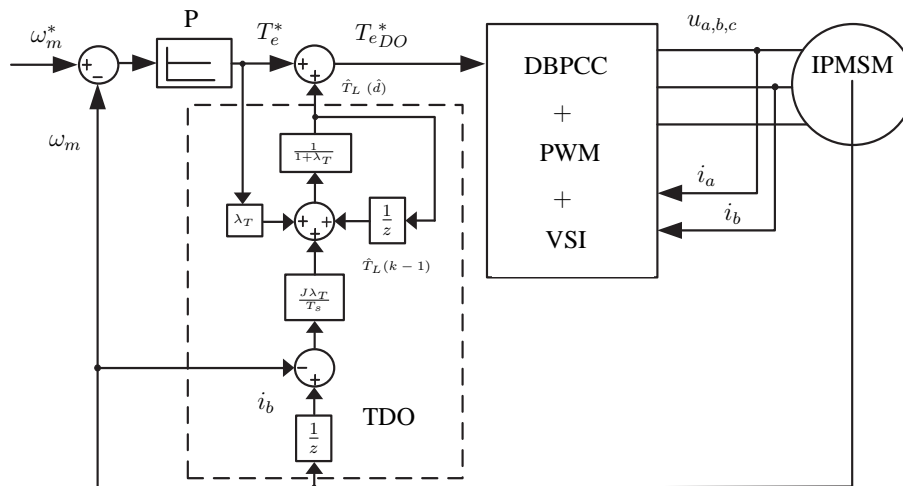


Figure 6.2: DBPCC drive system for IPMSM with TDO.

6.3.1 Simulation and Experimental Verification

Figure 6.3 shows the simulation of low speed (300 rpm) with rated load torque (12 Nm) variations. The torque is added to the system suddenly at 1 s when the motor is rotating with 300 rpm at steady state. When the system regains its stability, this load is removed immediately after 2 s. The dashed curves are the references. From this simulation, it is seen that TDO works with increasing effectiveness as the torque observer coefficient λ_T decreases from 0. Figure 6.4 is the same experimental test on the SPMSM with same λ_T variations. The experimental results are highly consistent to the simulation ones.

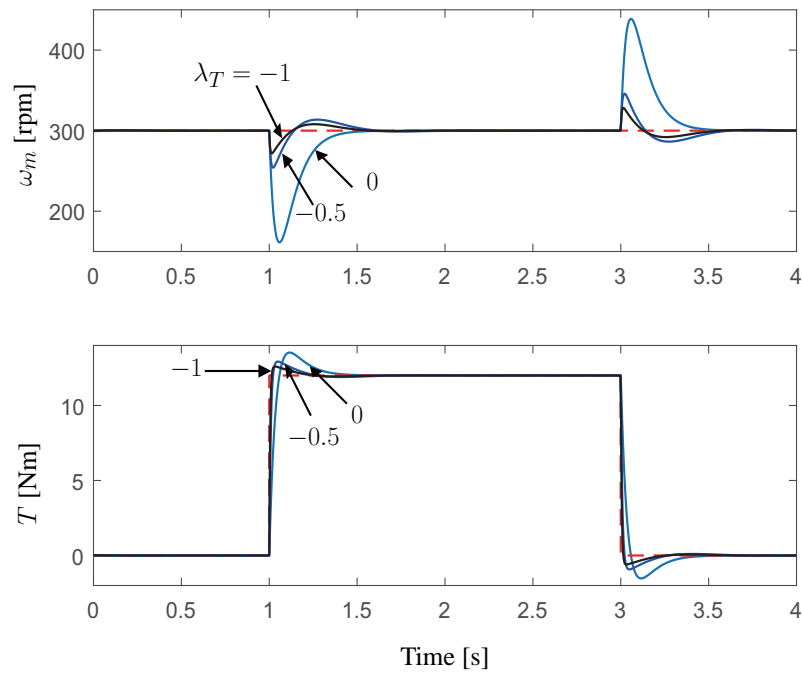


Figure 6.3: Simulation: low speed torque performance of DBPCC with TDO for IPMSM (values of λ_T are shown in figures).

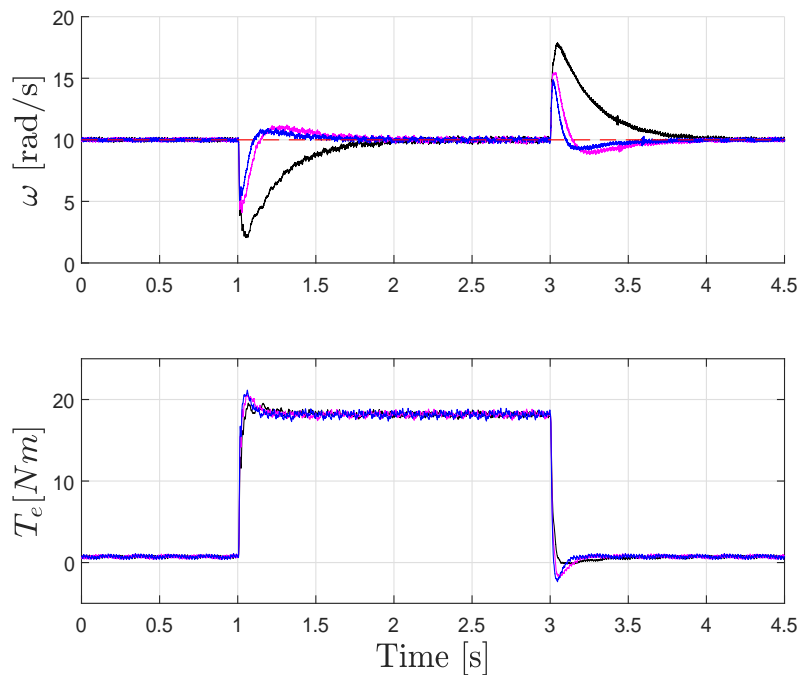


Figure 6.4: Experiment: low speed torque performance of DBPCC with TDO for SPMSM (black: $\lambda_T = 0$, violet: $\lambda_T = -0.5$, blue: $\lambda_T = -1$).

Figure 6.5 shows the same simulation of high speed (1500 rpm) conditions. As can be seen from the figure, the system performance and trend of TDO effects are of similar form as the

low speed situation. Figure 6.6 is the same experimental test on the SPMSM, which are also consistent to the simulation results. Moreover, the peak values of speed variations (-130, -30 and -15 rpm for $\lambda_T = 0, -0.5$ and -1) subject to torque disturbances for different TDO coefficients are almost same as the case of low speed simulations. This shows that the torque disturbances and the system's disturbance rejection ability have no close relationship with the motor speed. This discovery is further proved by the 3-D figure 6.7 showing the relationship among the max. speed drop/raise (absolute values), motor speeds and TDO coefficients, whose data are gained through a series of simulations with sudden load torque (12 Nm) variations. In this figure, the reduced TDO coefficient also leads to smaller speed ripples in transient while the motor speed itself has little influence on the speed variations caused by sudden load disturbance.

Moreover, the relationship between the max. speed drop/raise, load torque and TDO coefficient is also studied under constant speed (1500 rpm) condition, which is shown in figure 6.8. This figure is consistent to the previous simulations, in which the larger the torque disturbance is, more speed variations it causes. And the effect of varying TDO coefficient is accordant as that in figure 6.7 .

To properly and fully utilize the TDO, adjustment of λ_T is conducted to find out its range of sensible values. Figure 6.9 shows the adjustment process through the trail and error method. In figure 6.9, when the machine operates at steady state of rated speed, a time-varying load with both magnitude and frequency of time-ascending properties is added to the system to simulate an oscillating torque. When the values of λ_T decrease from 0 to negative, the speed maintains much more stable to its reference and the corresponding torque tracking capacity is stronger. As is illustrated by the figure, before λ_T is decreased to -9, system remains stable. Therefore, the theoretical range of proper λ_T is around $[-8,0)$.

In real system, the load torque is time-variant. Therefore, another simulation with noises in the torque reference is conducted. Figure 6.10 shows the system performance with different λ_T when the motor is operating at steady state during 1 second time period at rated speed and with rated torque including uniform random noises. The means and covariances of both variables for different λ_T are also measured and shown in table 6.1. The stator current THDs are also calculated. As can be seen from both the fig. 6.10 and table 6.1, the introduction of TDO maintains the stability of rotor speed, i.e. showing smaller variances with smaller λ_T values. In contrast, the electromagnetic torque of the system with TDO has larger oscillations, which shows the sensibility of the TDO and intensive control efforts of torque reacting quickly to load torque variations. This is confirmed by the torque variances, in which the stronger TDO is, the closer the torque variance is to that of the reference, i.e. load torque with random noises. The zoomed-in figure of 0.014 s shows the electromagnetic torque's trajectory for the load variations. It is seen that stronger TDO makes the output torque highly align with the disturbances, but with slight delay which is ignorable, when compared to the smooth torque curves of system with weaker or no TDO. The stator current THD with TDO is also larger with torque oscillations. This is understandable because the generation of the varying output torque depends on the output voltages and therefore also the currents. The increased THD in TDO system is undesired from the current quality view, however, it is sensible because in order to achieve acute torque disturbance rejection, it is unavoidable and therefore acceptable. A compromise of the current quality to the torque control should be made. This affirms again the purpose and importance of the range selection of TDO coefficient in the previous simulation.

The above simulation and experimental results match well with the theories and therefore

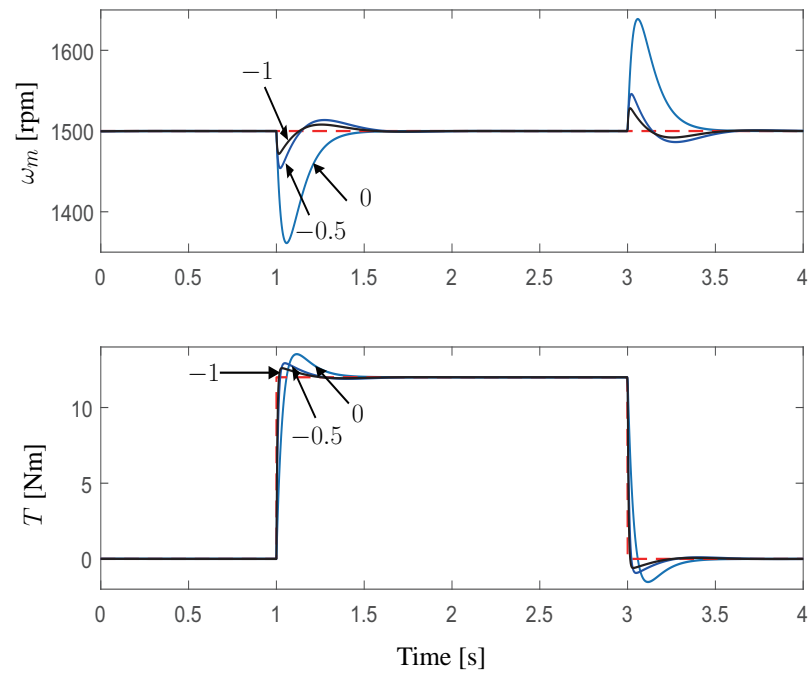


Figure 6.5: Simulation: high speed torque performance of DBPCC with TDO for IPMSM (values of λ_T are shown in figures).

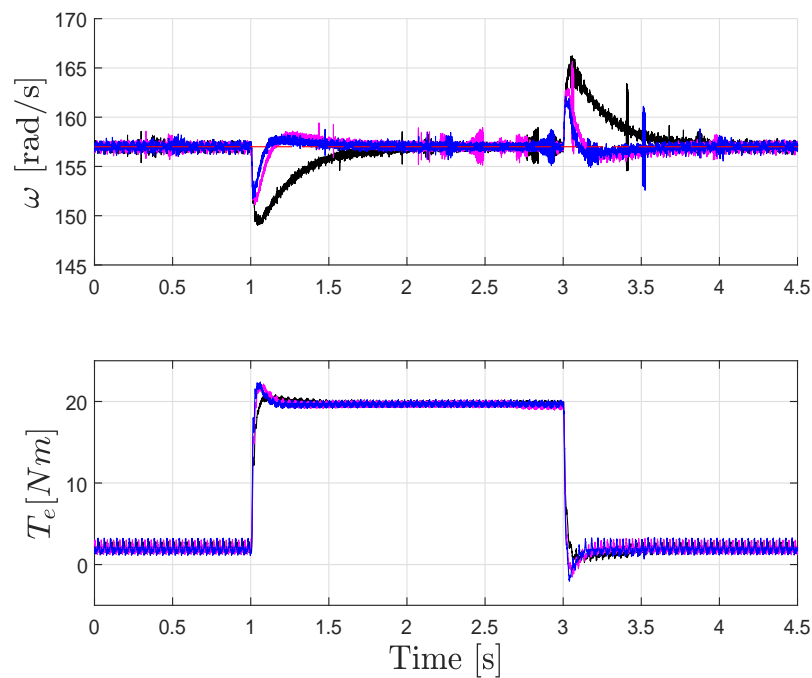


Figure 6.6: Experiment: high speed torque performance of DBPCC with TDO for SPMSM (black: $\lambda_T = 0$, violet: $\lambda_T = -0.5$, blue: $\lambda_T = -1$).

verify the feasibility and effectiveness of the proposed drive control algorithms.

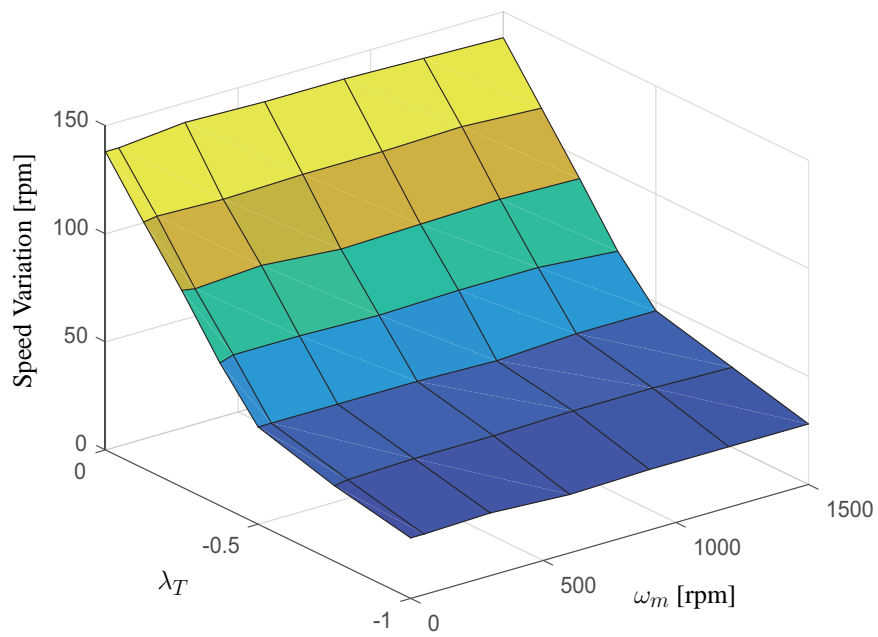


Figure 6.7: Simulation: Speed variations to different TDO coefficients and speeds of DBPCC for IPMSM.

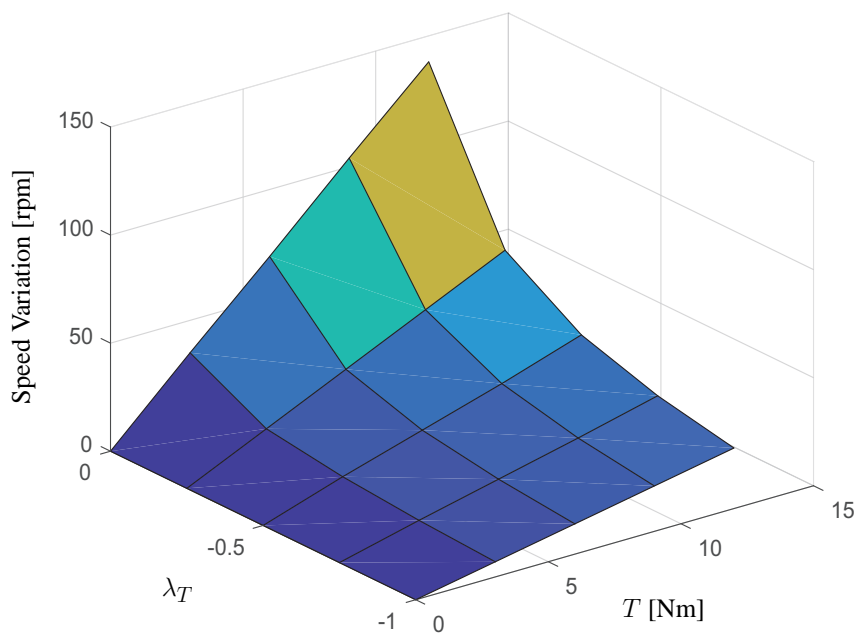
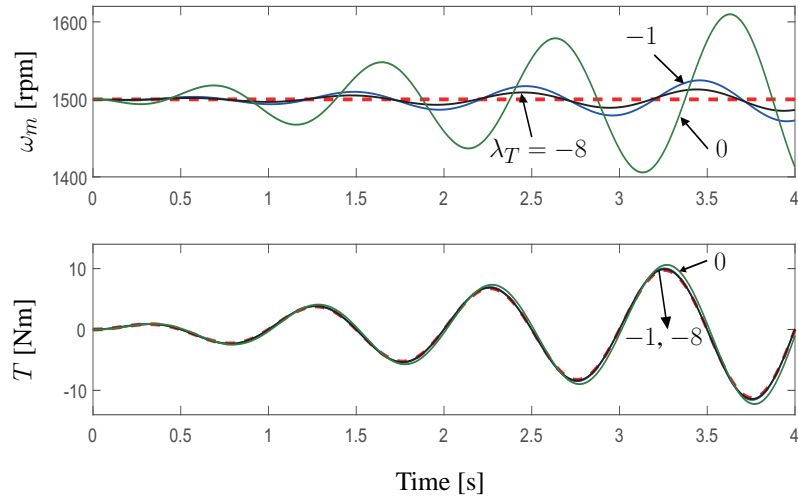
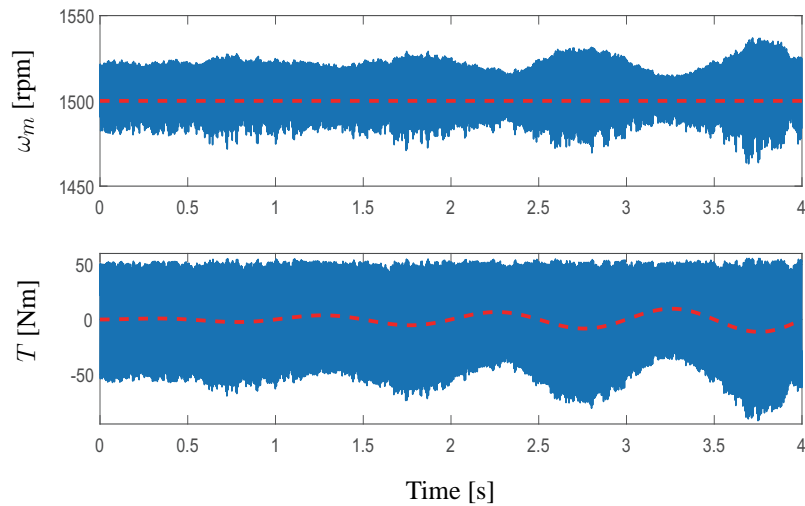


Figure 6.8: Simulation: Speed variations to different TDO coefficients and torques of DBPCC for IPMSM.

(a) $\lambda_T = 0, -1$ and -8 .(b) $\lambda_T = -9$.Figure 6.9: Simulation: Varying torque tracking performance with different λ_T values in TDO of DBPCC for IPMSM.Table 6.1: Statistic Analysis of Variables for Different λ_T .

λ_T	ω_m		T		THD
	mean	variance	mean	variance	
0	1500	0.1549	12.0053	0.0007	1.13%
-0.5	1500	0.0469	12.0056	0.023	1.58%
-1	1500	0.0275	12.0055	0.039	2.82%
reference	1500	0	12.0052	0.3325	—

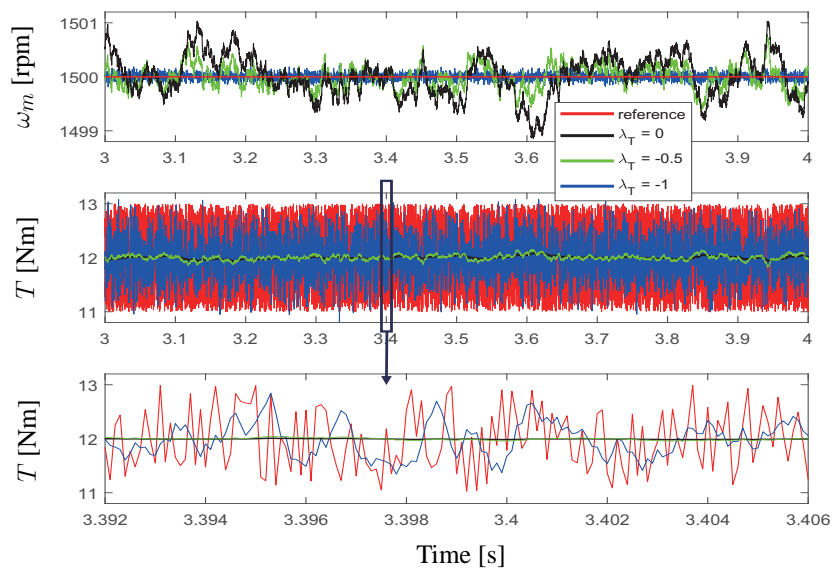


Figure 6.10: Simulation: System performance with random noises in torque in TDO of DBPCC for IPMSM.

6.4 FCS-PTC with TDO

The designed TDO is baseline controller as well as control strategy independent, therefore, this chapter tests its effectiveness on FCS-MPC. Take PTC as an example, figure 6.11 displays the PTC drive system for IPMSM with TDO integrated. The TDO of this system is exactly the same as the one applied in DBPCC.

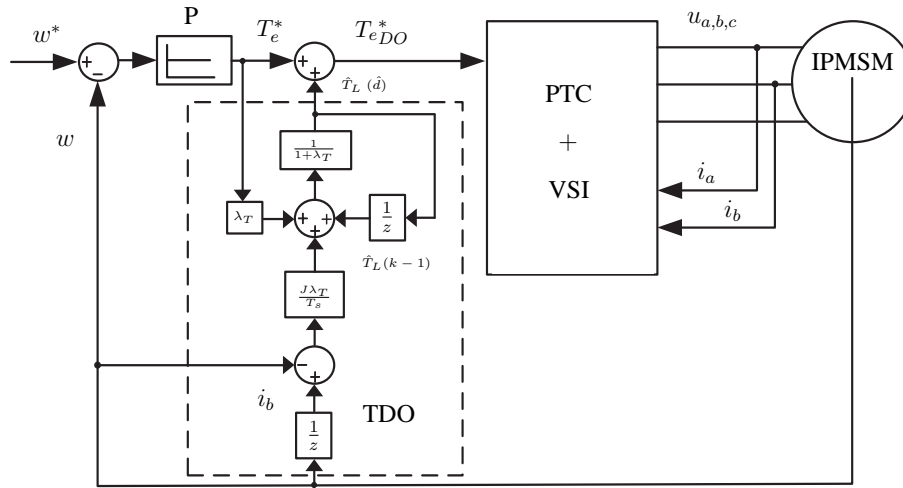


Figure 6.11: PTC drive system for IPMSM with TDO.

6.4.1 Maximum Torque Per Ampere Implementation

As IPMSM's current utilization and efficiency are crucial within rated speed and torque operations, especially for higher power applications. Therefore, the MTPA operation control for flux linkage reference tracking is adopted [28]. Instead of given fixed stator flux magnitude reference or using simple $i_d^* = 0$ control, MTPA calculates the optimal reference flux for maximum $\|\psi_s^*\|$ torque output. This is achieved through solving a pair of binary quadratic equations containing reference currents.

Review (2.26), the reference torque from TDO can be written as the integrated function of current references:

$$\hat{T}_e^* = \frac{3}{2} \cdot p[\psi_{PM}i_q^* + (L_d - L_q)i_d^*i_q^*] \quad (6.21)$$

And the MTPA trajectory derived from the torque equation corresponding to the local (i.e. absolute) maximum is:

$$i_d^* + \frac{(L_d - L_q)}{\psi_{PM}}(i_d^{2*} - i_q^{2*}) = 0 \quad (6.22)$$

with the condition:

$$\frac{2(L_d - L_q)}{\psi_{PM}}i_d^{2*} + 1 < 0 \quad (6.23)$$

Solve equations (6.21) and (6.22), the reference currents are calculated. Substitute these currents into (2.25), the reference stator flux dq components can be achieved and finally reference flux magnitude is calculated as:

$$\|\psi_{s(mtpa)}^*\| = \sqrt{\psi_d^{2*} + \psi_q^{2*}} \quad (6.24)$$

Apply the above reference as the flux magnitude reference in the following cost function of PTC with the above reference, the MTPA operation can be implemented as:

$$g_j = |T_e^* - \hat{T}_e(k+2)_j| + \lambda_g \cdot \|\psi_s^*\| - \|\hat{\psi}_s(k+2)_j\| + I_m(k+2)_j \quad (6.25)$$

where $\|\hat{\psi}_s(k+2)_j\|$ is obtained with the square root of the predicted fluxes (3.5) as follows:

$$\|\hat{\psi}_s(k+2)\| = \sqrt{\hat{\psi}_\alpha^2(k+2) + \hat{\psi}_\beta^2(k+2)} \quad (6.26)$$

6.4.2 MTPA-based FCS-PTC with TDO

However, it is found in implementation that if as in (6.25) where flux is chosen as the control term, there will have multiple values converging to the reference. Therefore, it should be replaced by the form of components, i.e. $\hat{\psi}_\alpha(k+2)$ and $\hat{\psi}_\beta(k+2)$. Actually in this system, only one of the two components is enough to force the system to track its reference without converging to the wrong optima.

Here, it is easier and intuitive to think of directly applying the reference current in the cost function design instead of adopting the flux term.

Therefore, a novel way of implementation for MTPA through a slight variation in cost function for PTC is designed and it will be realized through the following cost function:

$$g_j = |T_e^* - \hat{T}_e(k+2)_j| + \lambda_g \cdot |i_d^* - \hat{i}_d(k+2)_j| + I_m(k+2)_j \quad (6.27)$$

where i_d^* is the reference current calculated from (6.21) and (6.22). And $\hat{i}_d(k+2)_j$ is the predicted currents from (3.12) in the dq frame. Actually, in the above cost function, currents of $\alpha\beta$ frame can also be applied, with which it is found through simulation that the systems with both ways of implementation has almost the same error convergence capabilities. Therefore, only the case with i_d as control terms will be tested in this work for MTPA-based PCC with TDO.

The MTPA-based FCS-PTC system for IPMSM with TDO is shown in figure 6.12.

To further reduce the switching frequencies, the switching-minimization of RFCS-PCC as mentioned in chapter 5.2 is further applied for FCS-PTC.

6.4.3 Simulation and Experimental Verification

Similar as for deadbeat PCC, the observer gain λ_T is firstly obtained through a trail and error process to strike a balance between system dynamics and torque inhibition extent (i.e. convergence rate) after plenty of empirical adjustments, and its value is fixed. In the following simulations, if not specially assigned, $\lambda_T = -2.5$.

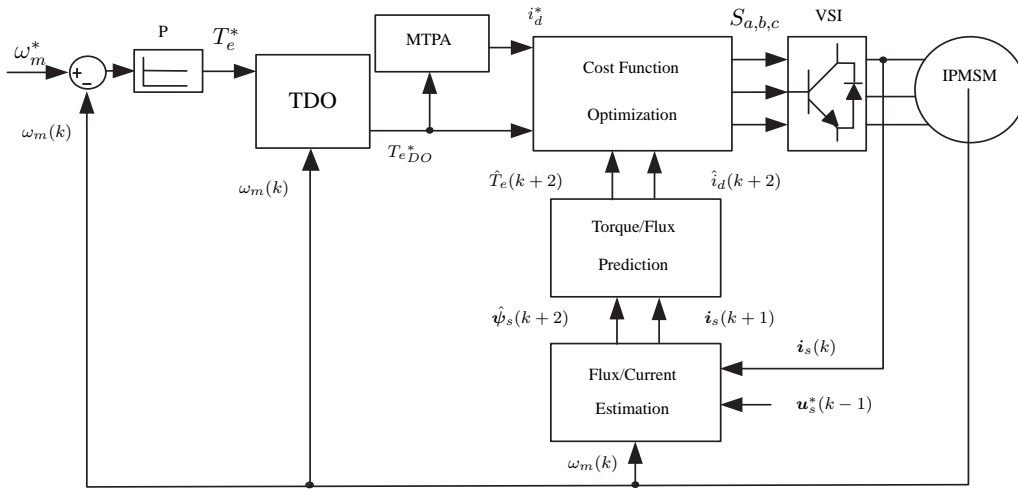


Figure 6.12: FCS-PTC drive system for IPMSM with TDO.

A speed start-up from standstill and reversal process from rated positive to negative speeds of the proposed system for IPMSM is shown in figure 6.13. It is seen from the figure that the rotor speed can properly track its ramp reference (dashed line) in short time. The reversal speed therein is around -6000 *rps*. And during the speedup and reversal process, the electromagnetic torque reaches its rated (maximum) at the beginning phase to achieve both prompt and smooth acceleration and deceleration. The currents are controlled within its rated (13.8 A) at the full load and speed condition. And stator flux is precisely maintained around the rated. This simulation shows that the system with TDO has similar performance and fast response as the conventional FCS-PTC drives. Figure 6.14 is the same experiment on SPMSM, which confirms again the non-deteriorated steady performance of TDO for the system.

The dynamic performances with sudden torque disturbances at rated speed condition are shown in figure 6.15. At 0.1 s, a step rated load torque is added to the system and after 0.5 s, this load is removed but an opposite rated torque is loaded for another 0.5 s. Figure 6.15 compares the performance of the torque dynamics of the system with and without TDO. It is obviously shown that the application of TDO can largely reduce the speed drop and rise time, rendering the torque adjustment time to be extremely short. And the torque ripples, currents magnitudes and flux tracing control capability of both systems are almost the same. This simulation verifies that the designed TDO works effectively to observe and compensate torque disturbances, without deteriorating the other system performances. Figure 6.16 is the same experiment on SPMSM, whose performance matches those in simulation.

In order to make the test harsher and closer to real stochastic processes and environments. The steady state performances with random unit torque noises of maximum magnitude of 3 Nm in torque reference at rated speed and rated torque condition are shown in figure 6.17, and figure 6.18 with switching frequency minimized. In these figures, the torque rejection capability of TDO integrated system is further confirmed. From the speed curves, it is seen that the TDO based system is more stable therefore with less speed oscillations against time-varying load torques.

The system's robustness under parameter deviations at rated condition are also tested through simulation. Since the TDO has only parameter's dependency on a single parameter J , the system's steady state performances with sudden changes of inertia J from 10% to 1000000% ,

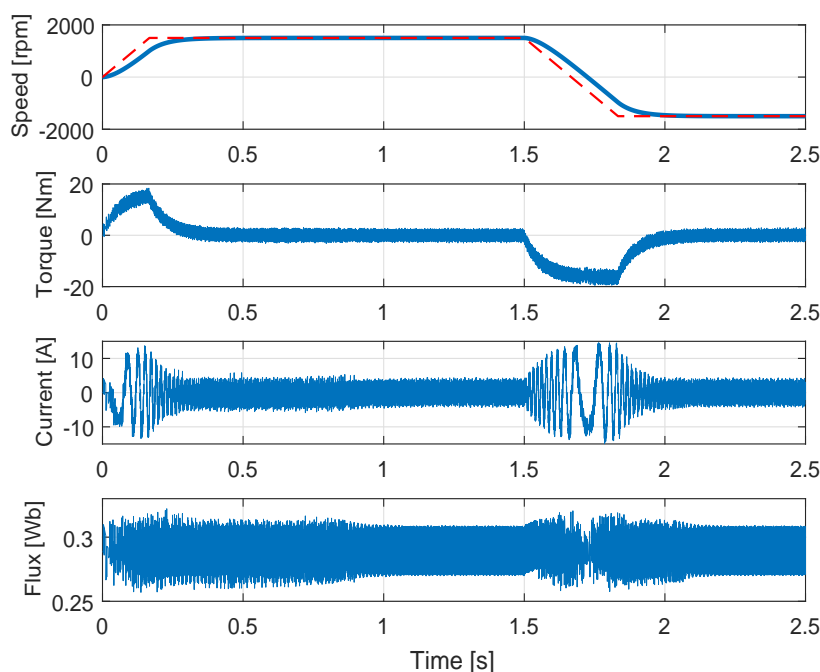


Figure 6.13: Simulation: speed reversal performance under FCS-PTC with TDO for IPMSM. (From top to down: rotor speed, electromagnetic torque, stator phase A current and stator flux.)

which are even harsher than the real parameter change, are shown in figure 6.19. As can be seen, the system is very robust against J variations of a wide range, even for erroneous huge J .

To achieve quantitative comparison, both systems' performance analysis data are shown in figure 6.20. The bar charts analyze the systems through their mean/variances of speeds/torques, stator current total harmonics distortion (THD), and the switching frequencies. In general, the systems with and without TDO have the same trend of variations in performance. Thus, there is no influence of TDO on system performance with different switching frequency strategies. Judging from the average values, both systems track their speed references correctly. It is seen that the torque means of frequency minimized system is slightly less than the noised torque reference, which is caused by the inappropriate speed controller's P parameter and TDO observer gain. However, for fair comparison in this work, all parameters in systems are kept as the same, which should be adjusted to achieve best general system performance. Similar as previous simulation, the system with TDO has better speed performance and less variations. However, the torque variance is correspondingly larger in TDO. This is actually not a phenomena of torque deterioration of TDO. Contrarily, it is the result of intensive torque control and disturbance compensation mechanism. Moreover, as expected, the speed of the system with switching minimization has larger but not much variance and increased current THD, when compared to the system that chooses the optimized voltage vectors without consideration of switching transitions. However, the increase of both values are not obvious and crucial. And the switching frequencies shown in the chart have been halved and calculation time is reduced. In light of this, the minimized system is preferred and therefore applied for further tests in the following simulation and experiments.

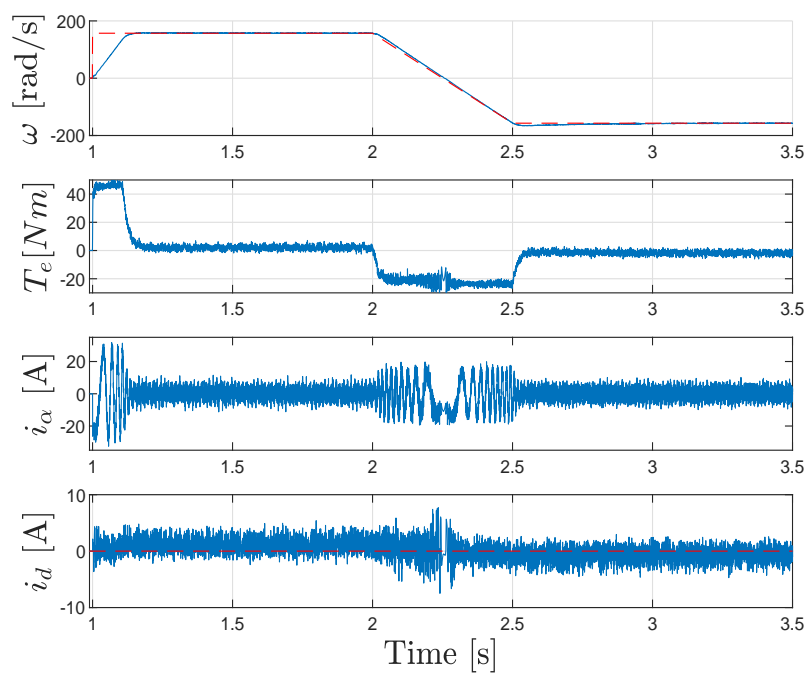


Figure 6.14: Experiment: speed reversal performance under FCS-PTC with TDO for SPMSM. (From top to down: rotor speed, electromagnetic torque, stator phase A current and stator flux.)

Simulation and experimental results match well with the theories, and therefore verify the feasibility of the proposed algorithms.

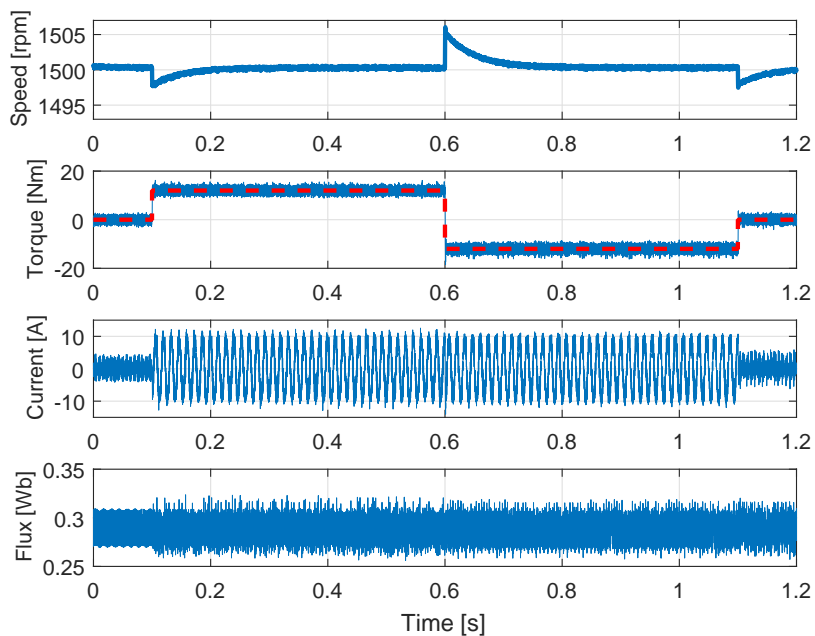
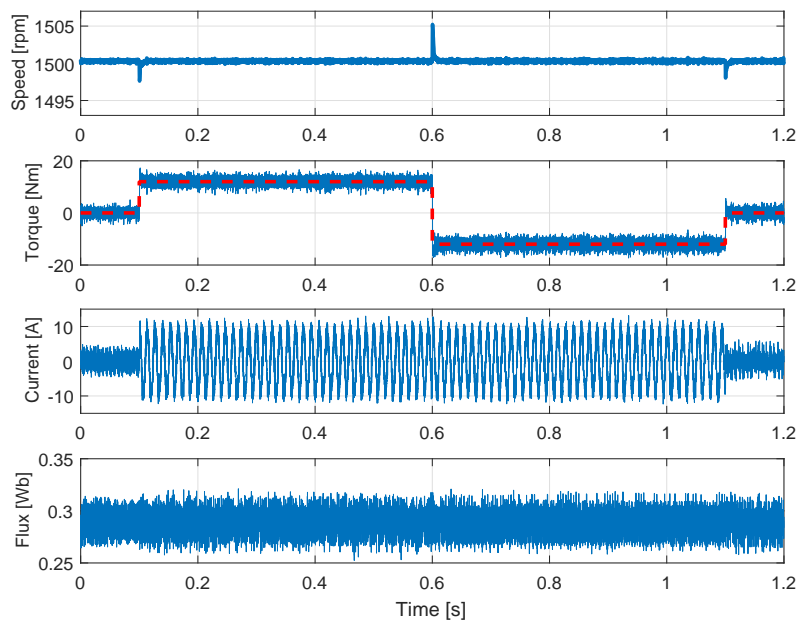
(a) $\lambda_T = 0$.(b) $\lambda_T = -2.5$.

Figure 6.15: Simulation: torque rejection performances under FCS-PTC with/without TDO for IPMSM.

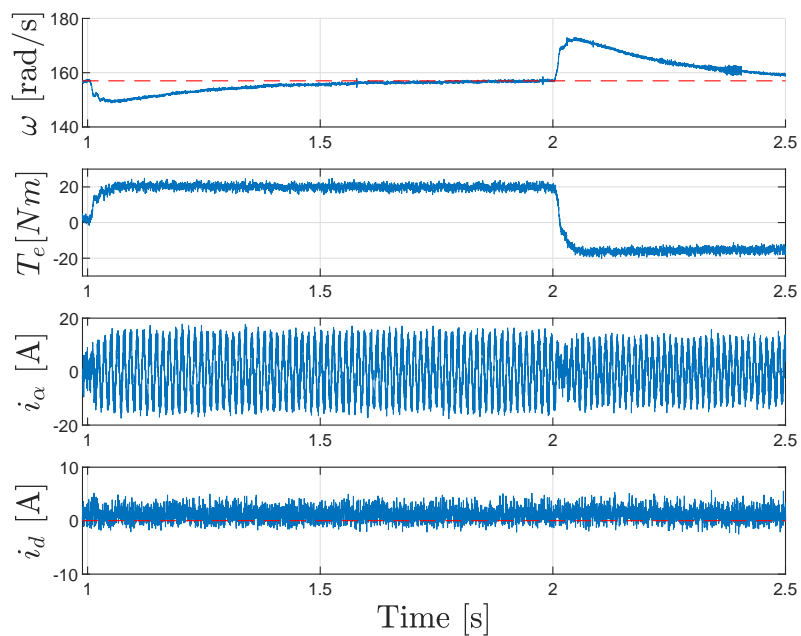
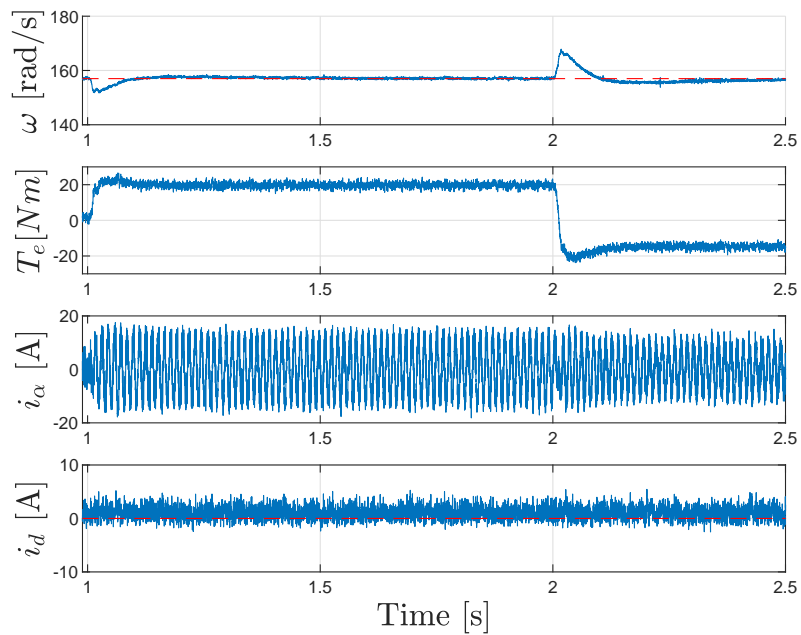
(a) $\lambda_T = 0$.(b) $\lambda_T = -2.5$.

Figure 6.16: Experiment: torque rejection performances under FCS-PTC with/without TDO for SPMSM.

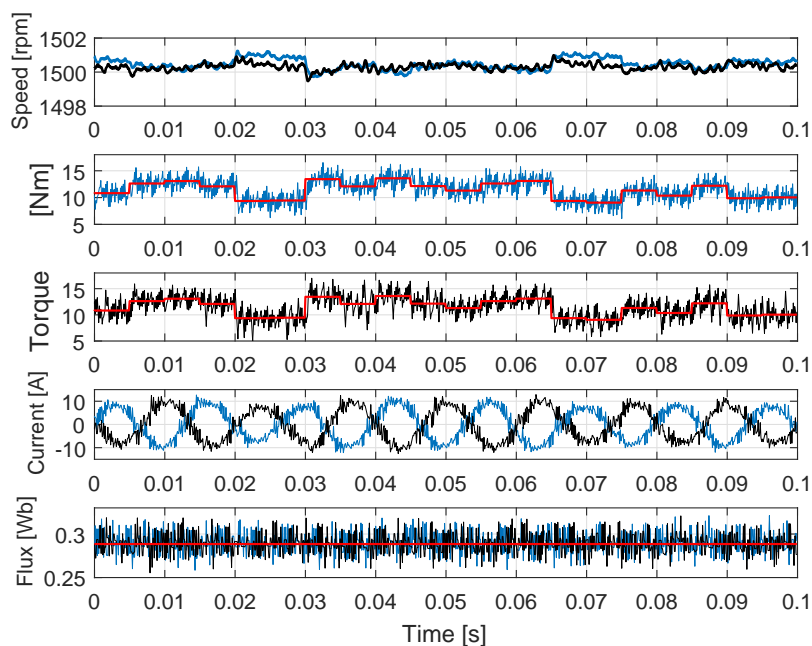


Figure 6.17: Simulation: system performance with random noises in torque under FCS-PTC for IPMSM. (blue: system without TDO. black: system with TDO.)

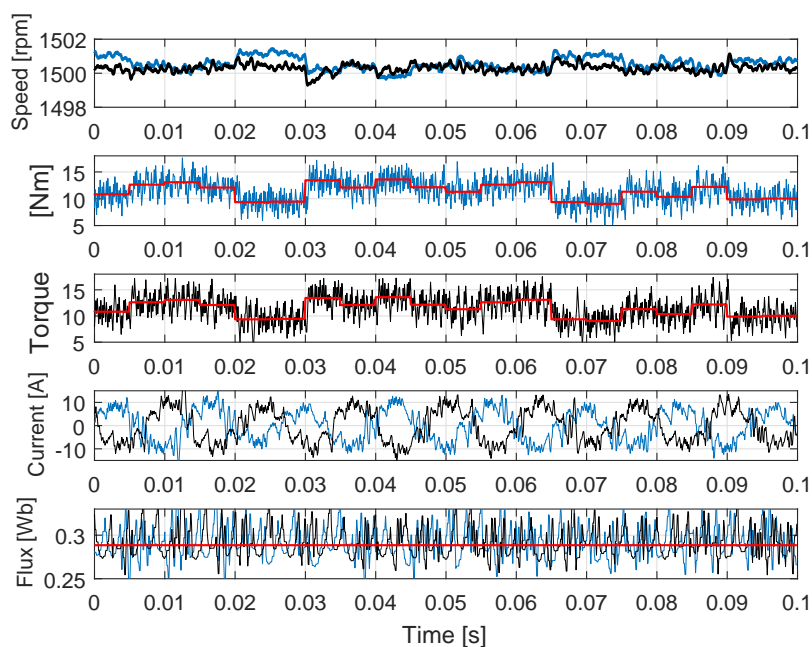


Figure 6.18: Simulation: switching frequency minimized system performance with random noises in torque under FCS-PTC for IPMSM. (blue: system without TDO. black: system with TDO.)

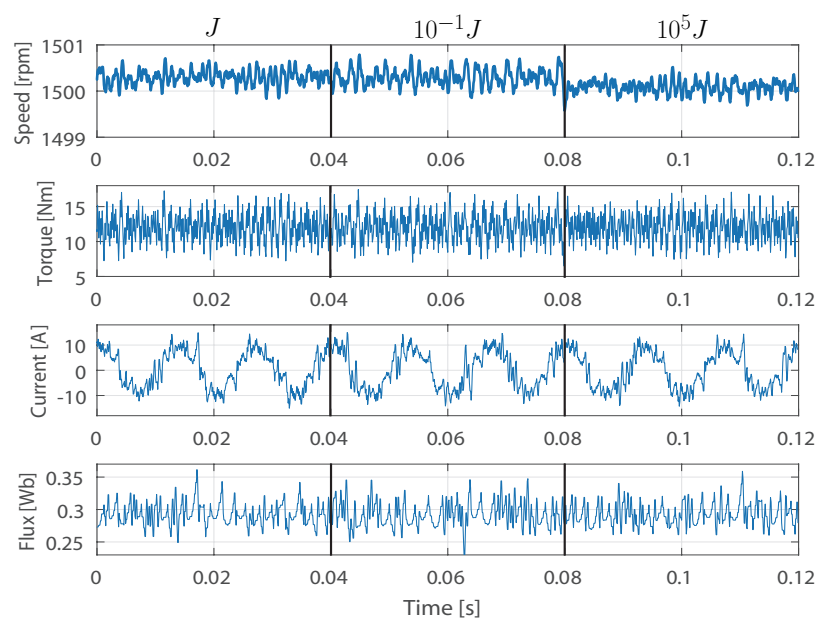


Figure 6.19: Simulation: system robustness test against parameter deviation with sharp changes of inertia.

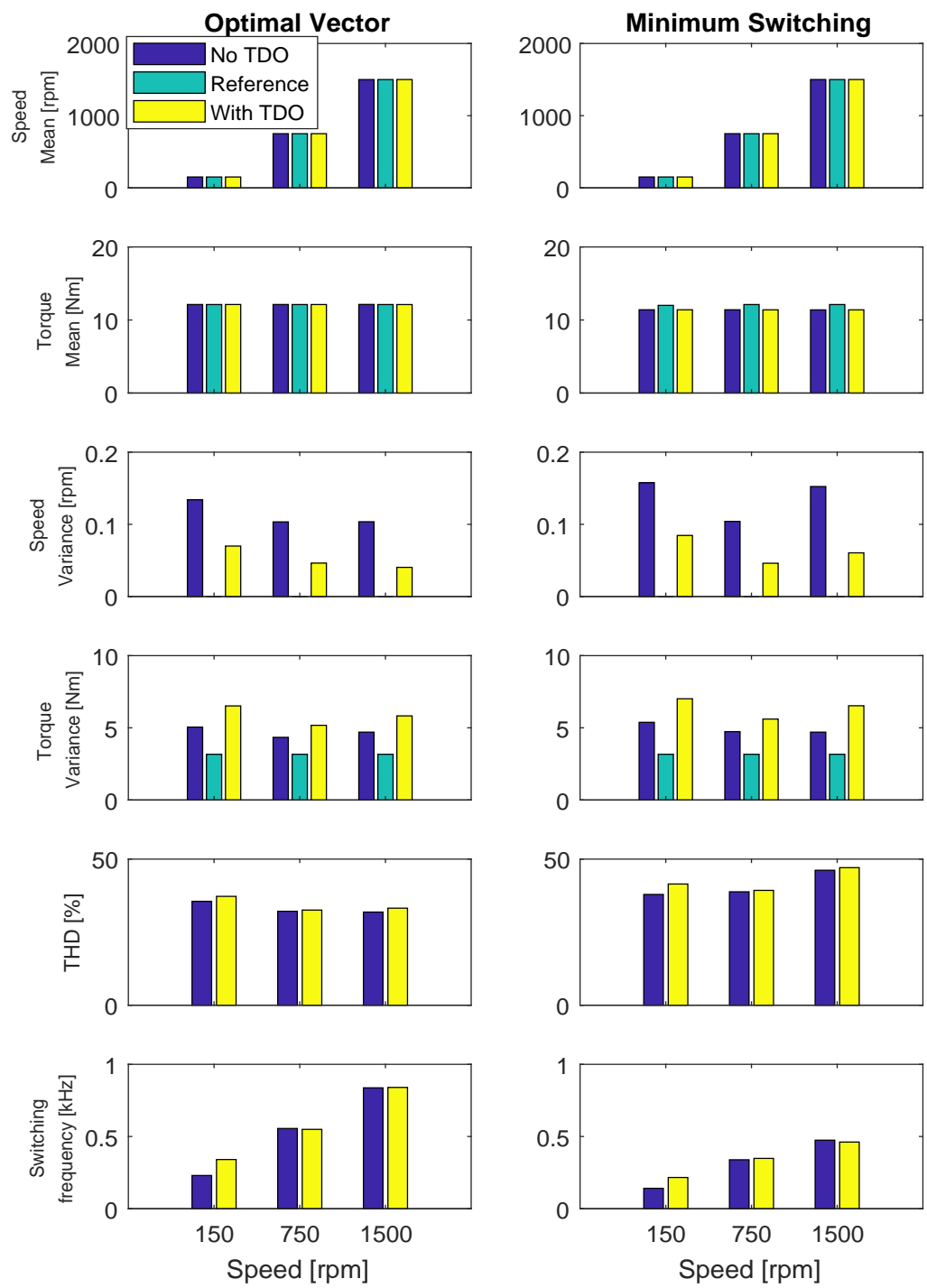


Figure 6.20: Simulation: both FCS-PCC systems' analysis with random noises in torque with/without TDO.

6.5 Conclusion

A DBPCC PMSM drive system with TDO has been proposed and verified by simulations and experiments. Through the application of TDO and combining with deadbeat control, and both the system's transient and steady state performances are improved. Moreover, the elimination of integral part of outer speed PI controller reduces the time-consuming integral error tracking time and tedious tuning work of parameter. And a FCS predictive torque controlled (FCS-PTC) IPMSM drive system with TDO has been also proposed and verified by simulations and experiments. The proposed system remains fast response characteristics of conventional FCS-PCC.

TDO can not only simplify the control by eliminating the I parameter, but also reduce the torque response time, thus it improves the transient dynamics. It doesn't depend on the slow integral process of speed or torque errors. Instead, it estimates the torque directly from the speed and electromagnetic torque, and compensate this torque variation instantly to the reference in a deadbeat manner, rendering the system to be "disturbance-free". Moreover, it is only rotor inertia J sensitive and has a strong robustness against this parameter deviation. It is proved to be a practical strategy to reduce the system complexity and improve system dynamics in industry.

Therefore, the proposed strategy is proved to be a very effective solution which can be easily implemented on existing drive systems. Moreover, it can be extensively applied to other drive systems with various machine types. And the TDO can also be independently adopted to the system based on different control methods, such as FOC, DTC and deadbeat MPC.

CHAPTER 7

FCS-MPC without Weighting Factor

For all FCS-MPCs, there is at least one weighting factor for the cost function as long as there are control terms of different physical natures [88]. Even for strategies with control terms of the same attribute, e.g. FCS-PCC, the weighting factor of 1 cannot be taken as the optimal for granted, which is also confirmed through adjustments experiences of the weighting factor of FCS-PCC. And it is found that usually 0.25~0.5 instead of 1 leads to better convergence/quality for both currents and torque. However, there exists no standard method or criteria with physical quantity for the tuning of weighting factor(s). Usually, they are simply set to be fixed values and normalized to achieve fair control between different terms, which is similar as per unit control. However, this is not a guarantee for optimal control for all conditions under different operation points. There are already some control strategies regarding the simplification or elimination of the weighting factor, which are essentially all variations for online tuning of the priority/importance for different control terms with specific criteria [89–92]. Among them, a recently proposed strategy—sequential FCS-MPC (SMPC) is a simple and promising realization of weighting-factor-less FCS-MPC [93]. In this chapter, tests of SMPC are conducted and an improved extension of it—SMPC with varying control sequence is also proposed and verified. Moreover, in order to fully study the possibilities of weighting-factor-less FCS-MPC, a novel analogue of SMPC—Parallel FCS-MPC (PMPC) will also be proposed and tested.

Instead of only using PMSM as control object as in previous chapters, IM will be controlled in this chapter for SMPC, because the rotor flux of IM is induced, whose flux control is more difficult and important than IPMSM with separated magnet. Therefore, the effectiveness of both SMPC will be more prominent. PMPC will be still tested on PMSM.

7.1 Sequential FCS-PTC

Because of the length limitation of this work, only PTC is taken as example to verify the algorithms in this chapter.

7.1.1 Conventional Sequential FCS-PTC

The recently proposed novel strategy of Sequential FCS-PTC for IM as in [93] will be introduced and explained in this sub-chapter, whose block diagram is shown in figure 7.1.

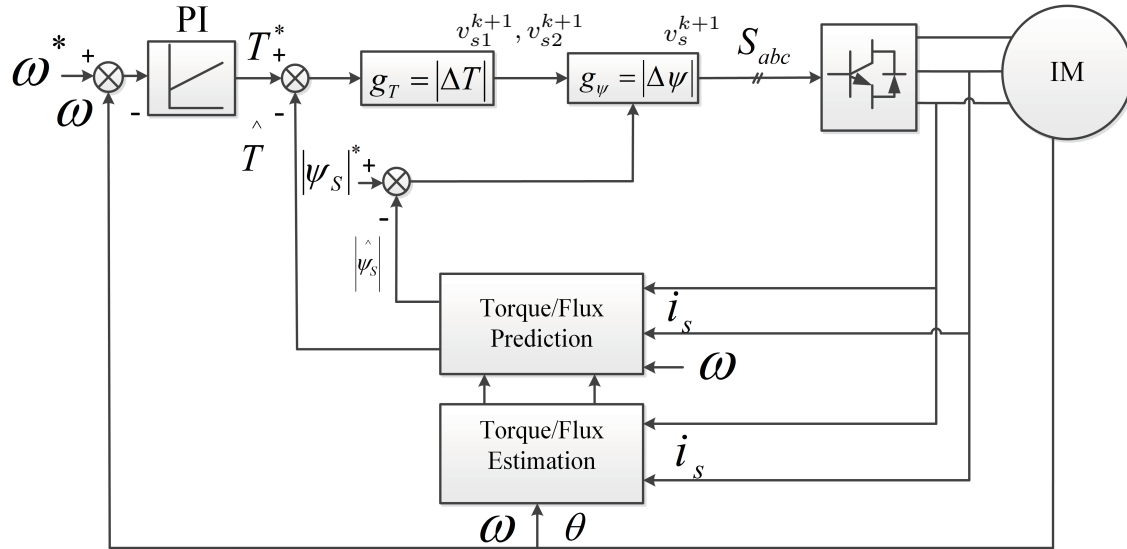


Figure 7.1: Sequential PTC for IM.

The basic mechanism of SPTC is to split the conventional "all in one" congregate cost function with weighting factor(s) into as many as the number of control terms. And through a cascade structure of sequential execution of cost functions' optimizations, some of the control terms are firstly calculated and the best optimal voltage vectors leading to minimum errors are firstly selected and serve as the reduced control set's candidate vectors for the cost function of the secondly controlled object.

For example, in this novel SPTC, two separate cost functions of control, i.e. g_T and g_ψ for the torque and stator flux terms, are adopted as follows:

$$g_T = |T_e(k+2) - T_e^*| \quad (7.1)$$

$$g_\psi = |\psi_d(k+2) - |\psi_s|^*| \quad (7.2)$$

Except the additional over current protection term in both cost functions' calculation processes, the torque cost function is firstly calculated and the best two vectors for it are pre-chosen for the flux optimization. Thereafter, these two optimal vectors are given to the stator flux's cost function to find out the optimal vector that will be output as the reference. For the IM under test, 2 is chosen as the ideal quantity of the pre-chosen voltage vectors that strikes a balance between the calculation amount and slightly higher emphasis on torque control. It is obtained after a trail and error process. More than two vectors is not suitable for torque optimization, while only 1 is absolutely abandoning the control of stator flux. Theoretically, the less vectors are chosen for the secondly executed cost function, the more emphasis is put on the first cost function's control object. However, this raises another problem and an extra factor to be tuned

for the SPTC, which is surely machine type and parameters dependent. Therefore, it comes to the motivation of extension for this method in the following sub-chapter.

For easiness of comparison, the simulation and experimental verification of both methods will be shown together in the later sub-chapter.

7.1.2 Sequential FCS-PTC with Varying Control Sequence

The basic principle of the extended method of SPTC to be proposed in this sub-chapter is similar as the previous method, whose block diagram is shown in figure 7.2. In order to improve the system precision and dynamics by avoiding the unbalanced control for either of the control objects (i.e. torque and stator flux), an sequence or order selection is conducted by a simple logic basing on the previous control cycle's cost functions' values. And these values serve as the input of a decision-making LUT that decides in each control cycle which cost function should be firstly calculated.

The rule is that the larger a control object's cost function's minimum value in the last control period is, the higher possibility its cost function will be firstly calculated in the next control period. Through the introduction of varying cost functions' execution sequence, the extended method considers the varying priorities of different control terms in different operation points. As a result, the system's control performances can be further improved through the tunings of the error band widths of torque and flux control's priorities. A flowchart in figure 7.3 illustrates this algorithm. And the cost functions' execution sequence is decided based on the the rule in LUT of table 7.1, where the error band width values of torque (εT) and flux ($\varepsilon \psi$) are chosen as half of the average peak-to-peak torque and flux ripple values in steady state of the system proposed in the last sub-chapter with fixed cost function sequence. These values are integrated into the logical rules, with whom the final decision can be achieved as a commend for an interlocking "switch" that changes the execution sequences of control terms.

From the flowchart in figure 7.3, it is seen that the extended method is almost identical as the previous method, except that in step 2 an additional LUT based sequence decision is made before the cascaded cost functions.

Table 7.1: Cost function executive order decision-making LUT.

min. g_T of last period (Nm)	min. g_ψ of last period (Wb)	Decision
≥ 0.025	≥ 0.5	same as last
≥ 0.025	< 0.5	g_T first
< 0.025	≥ 0.5	g_ψ first
< 0.025	< 0.5	same as last

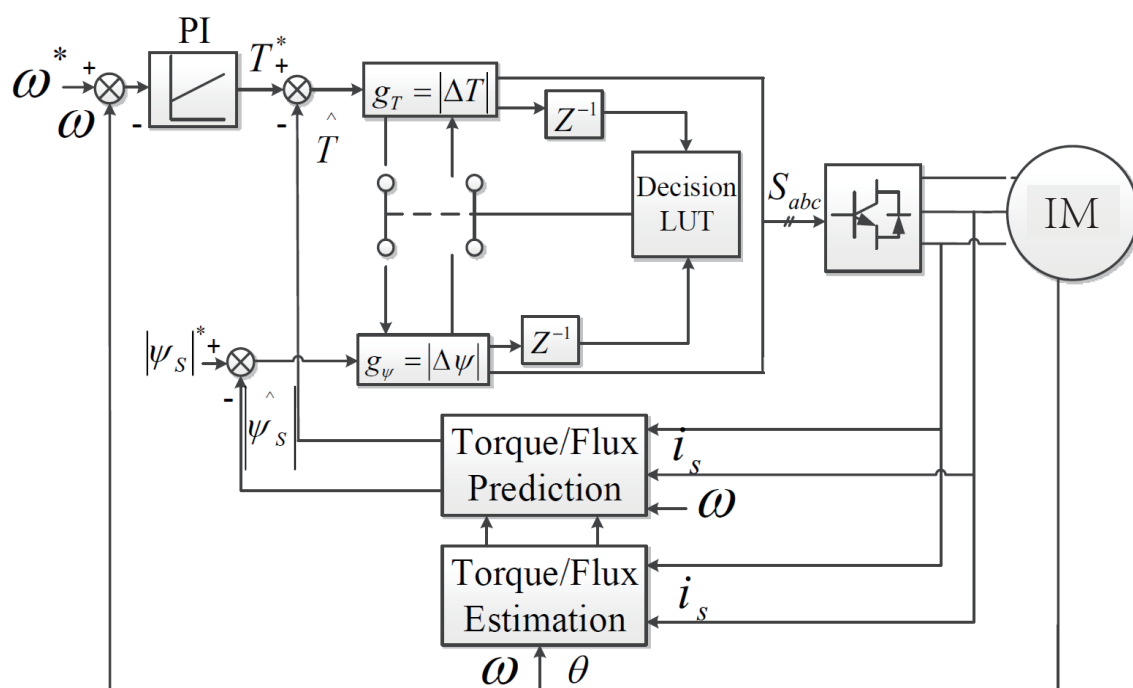


Figure 7.2: LUT based Sequential PTC for IM with varying control sequence.

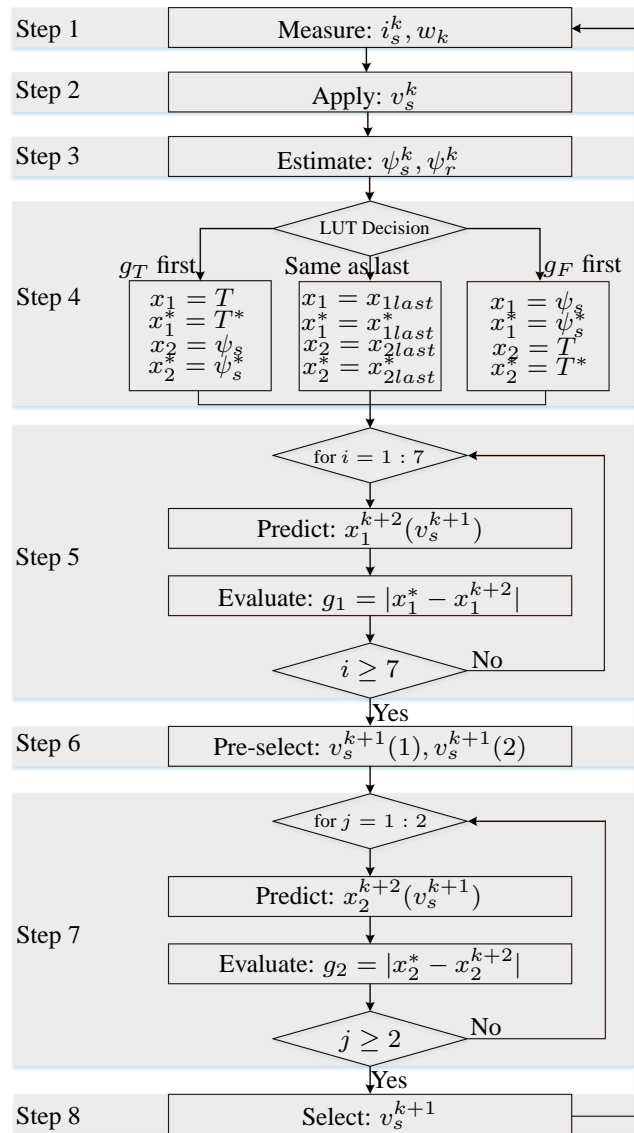


Figure 7.3: Flowchart of LUT based Sequential PTC for IM with varying control sequence.

7.1.3 Simulation and Experimental Verification

This chapter gives the simulation results of both conventional and extended sequential FCS-PTC with varying control sequence.

The parameters of the IM under test are shown in table 2.3 of chapter 2, which is the same as a real machine at laboratory. The other control data are set to be the same as in the test of IPMSM.

Simulation 1 is to find out the performance of the speed step-up and reversal process.

Figure 7.4 shows speed, torque, current and flux of this process. Both systems have similarly good dynamic and steady states performance as the conventional FCS-PTC of IM shown in figure 3.3.

Figure 7.5 shows the corresponding decisions for control sequences of sequential FCS-PTC with varying control sequence during this process. It is seen that the system automatically and frequently changes the orders of cost functions' execution according to the predefined error bandwidths of the previous control periods.

Figure 7.6 shows the corresponding torque and flux tracking performance. It is seen in this figure that both systems can track their references well.

Simulation 2 is to find out the speed performance under torque variations.

Figure 7.7 shows speed, torque, current and flux of this process. The differences of both methods are ignorable.

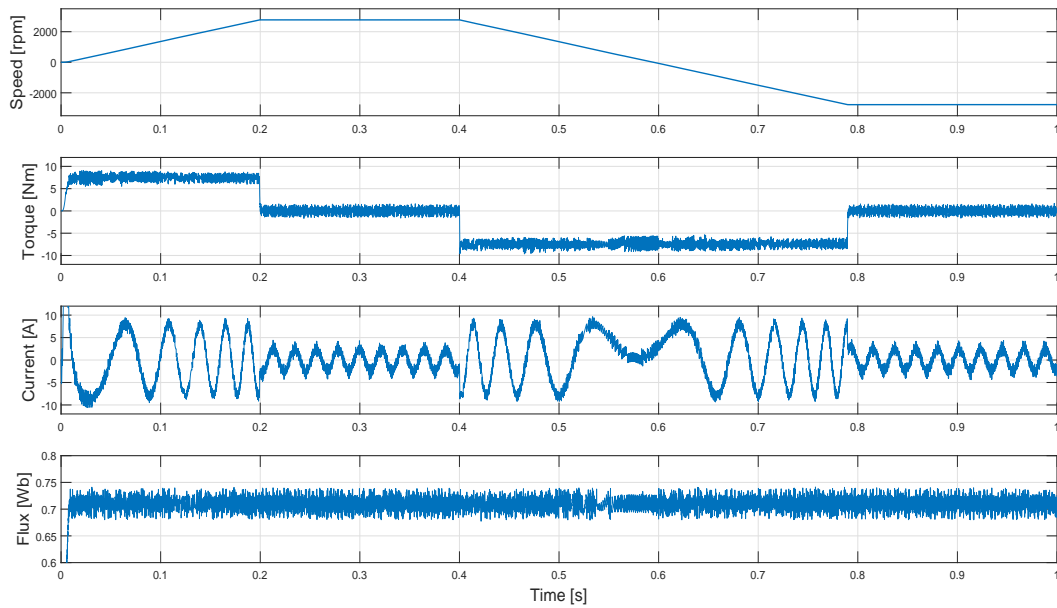
Experiments are conducted on IM with same parameters as in the previous IM model.

In experiment 1 as shown in figure 7.8, the system is operating at its steady state of nominal speed at no load condition, and a sudden load torque of rated value is added at 0.05s and removed at 0.25 s. Both systems can balance this load immediately with almost no time delay and minor speed drop/raise and regain. The flux performance is stable in spite of the load variations. This verifies the good and very similar torque rejection performances of both Sequential FCS-PTC systems.

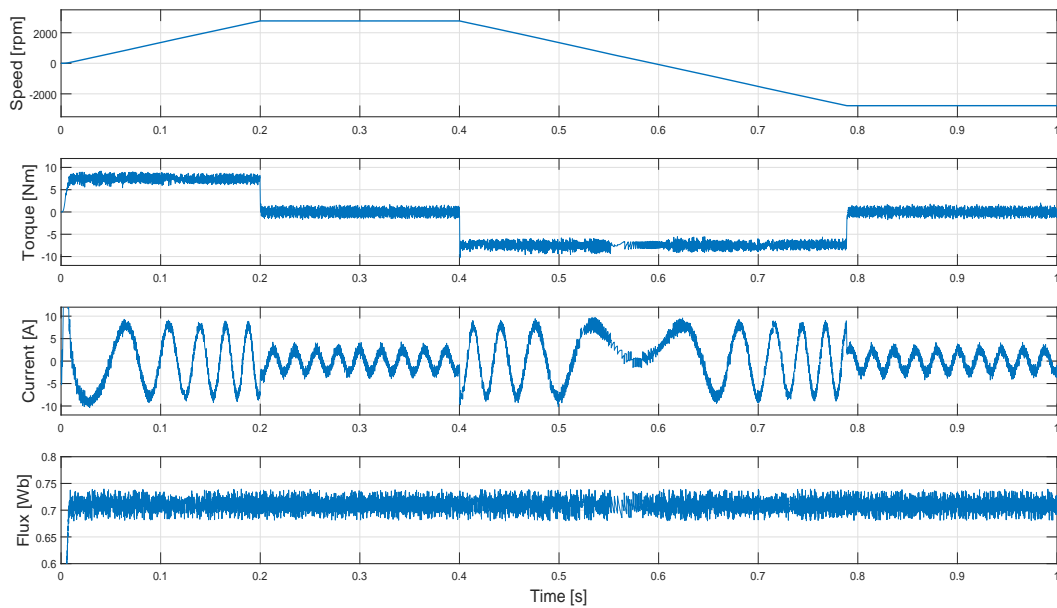
Experiment 2 finds out the influence of torque and flux expectations on the torque and current performances for SPTC with Varying Control Sequence. Figure 7.9 and figure 7.10 show the torque standard deviation and stator current THD for different εT and $\varepsilon \psi$. As can be seen that the torque deviation and current THD have very similar shape of contours, which confirms the torque's deciding and crucial influence to the current THD, with some difference because of the flux term's contribution. Therefore, experiment 2 serves as an instruction for the expectation values' selection of εT and $\varepsilon \psi$. As a result, in the following tests, the values of εT and $\varepsilon \psi$ are optimized by being reset to the minimum of both contours with $\varepsilon T = 0.2 Nm$ and $\varepsilon \psi = 0.015 Wb$, respectively.

In the following experiments, the system steady state performances under different conditions will be researched.

Experiment 3 investigates the system performances under different operation points with varying speeds under rated load. Figure 7.11 shows that both the electromagnetic torque ripples and stator current THDs will increase as the speed steps up. Theoretically, the system is more sensitive and susceptible at lower speed conditions. However, being different from the conventional PTC, the proposed SPTC with varying control sequence works even better at low speeds, with better torque and current qualities. The reason lies in the control effect's enhancement introduced by the self-adaptive control priority decision, i.e., at lower speed, because the torque's



(a) Sequential FCS-PTC.



(b) Sequential FCS-PTC with Varying Control Sequence.

Figure 7.4: Simulation: Rated speed start-up and reversal of conventional Sequential FCS-PTC and Sequential FCS-PTC with Varying Control Sequence for IM.

influence is enlarged by larger errors. Therefore, more control efforts are given to torque instead of flux.

Experiment 4 investigates the system performances under different operation points with

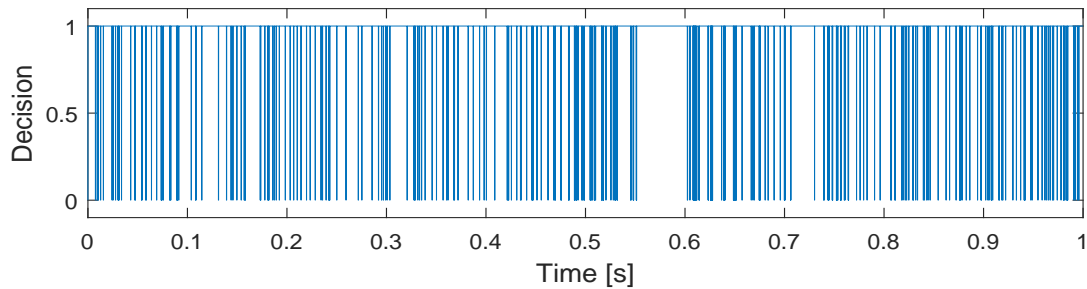
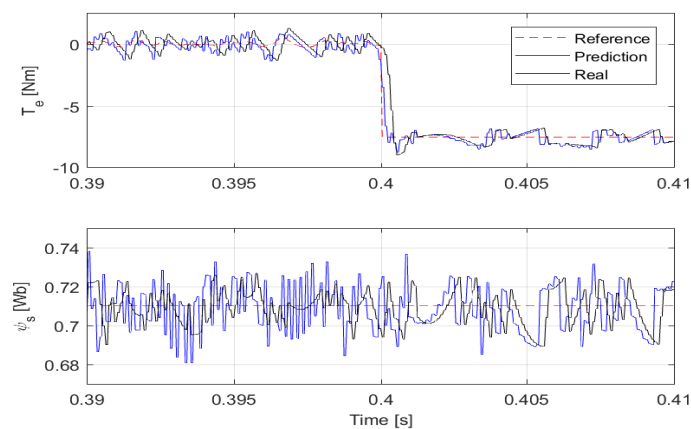
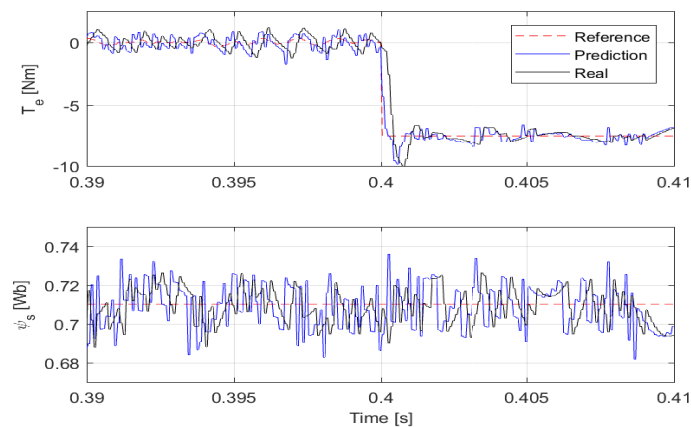


Figure 7.5: Simulation: Decisions of control sequence for Sequential FCS-PTC with Varying Control Sequence. (1/0: torque/flux cost function is executed first)



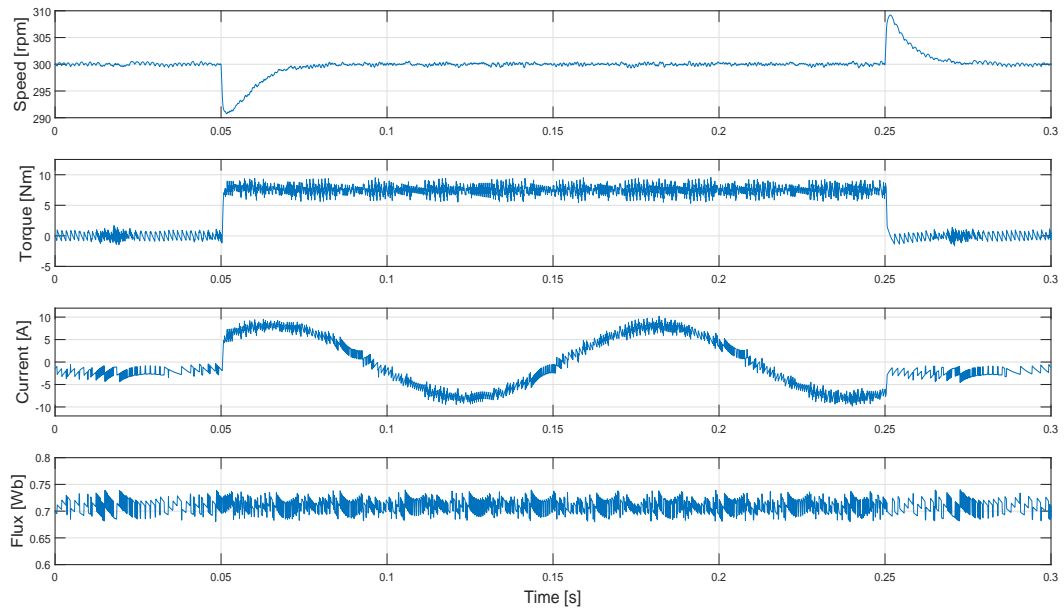
(a) Sequential FCS-PTC.



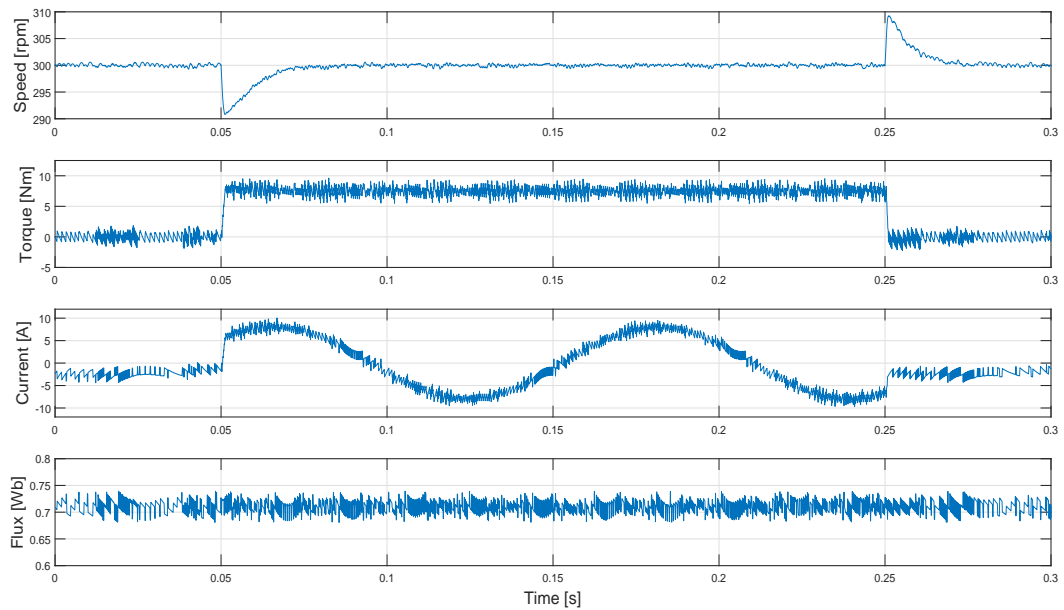
(b) Sequential FCS-PTC with Varying Control Sequence.

Figure 7.6: Simulation: Torque and Flux Tracking Performance of conventional Sequential FCS-PTC and Sequential FCS-PTC with Varying Control Sequence for IM.

different torques at nominal speed, which is shown in figure 7.12. From this figure, it is found that higher torque serves as the temporarily added inertia part and makes the system more stable and therefore leads to smaller current THD and even reducing switching frequency for intensive



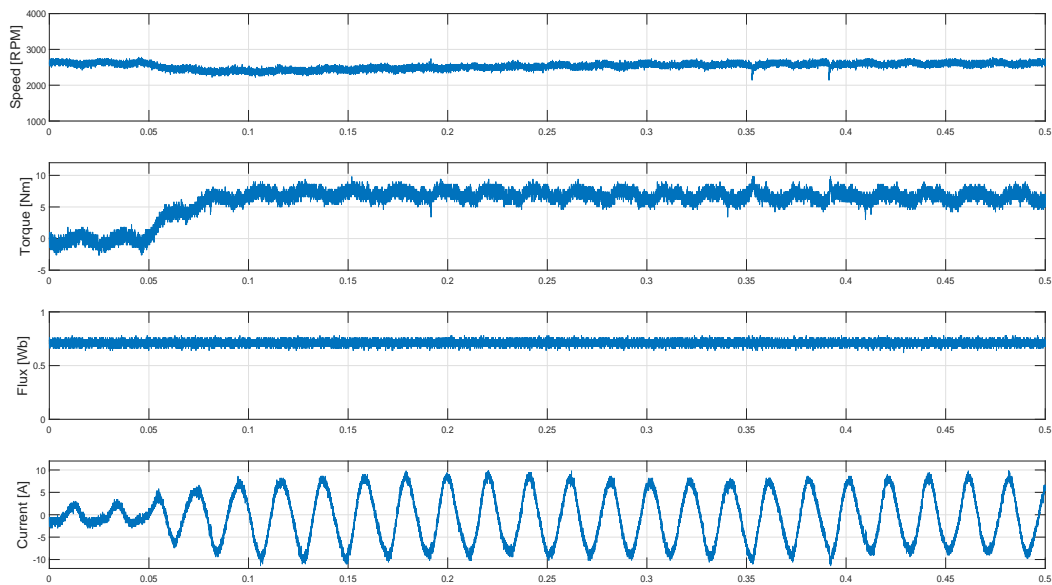
(a) Sequential FCS-PTC.



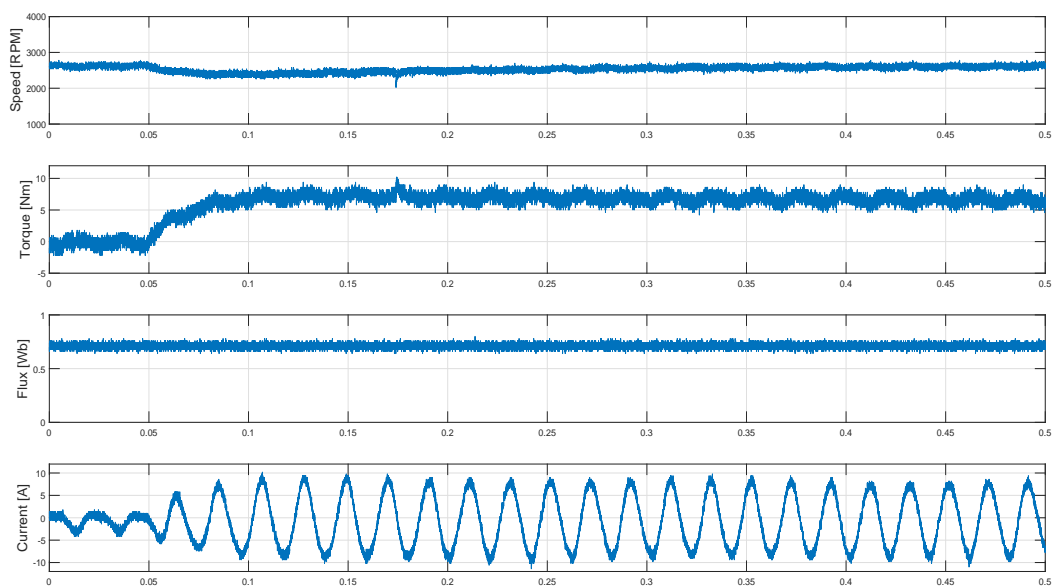
(b) Sequential FCS-PTC with Varying Control Sequence.

Figure 7.7: Simulation: Conventional Sequential FCS-PTC and Sequential FCS-PTC with Varying Control Sequence's Performances for IM under Torque Variations.

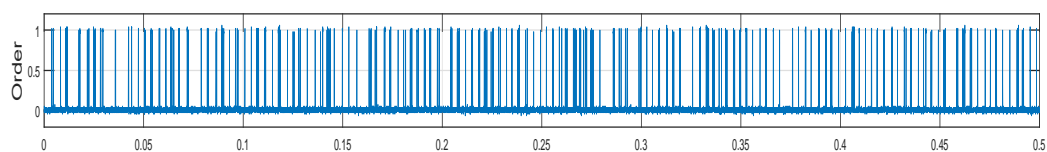
adjustments.



(a) Conventional SPTC.



(b) Proposed SPTC.



(c) Proposed SPTC Order.

Figure 7.8: Experiment: Conventional Sequential FCS-PTC and Sequential FCS-PTC with Varying Control Sequence for IM under load variations.

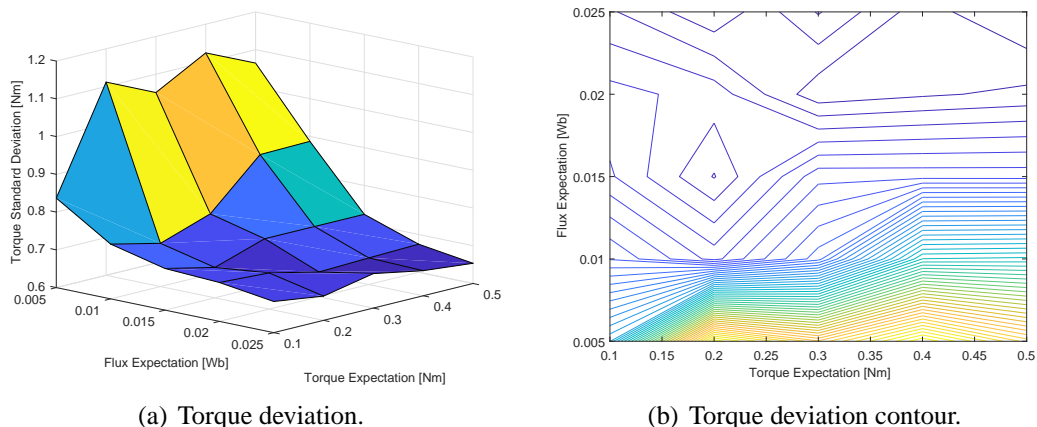


Figure 7.9: Experiment: Expectations' influences on torque standard deviation.

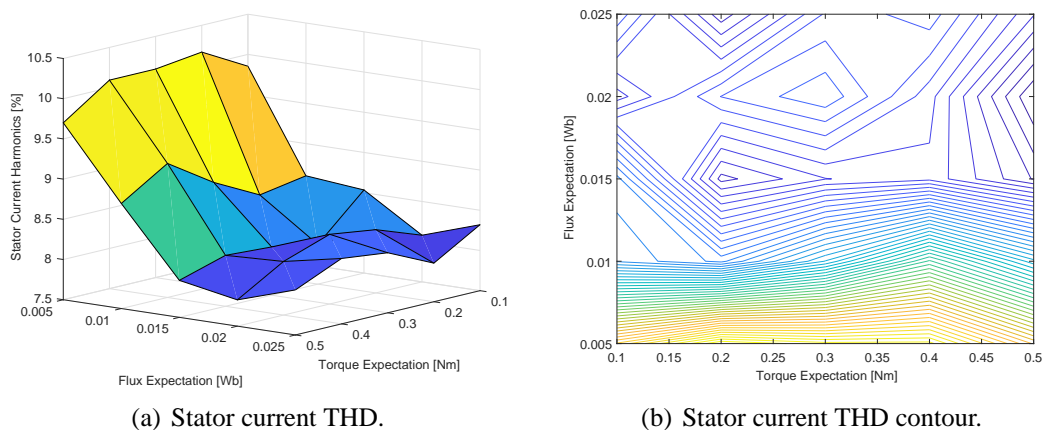


Figure 7.10: Experiment: Expectations' influences on stator current THD.

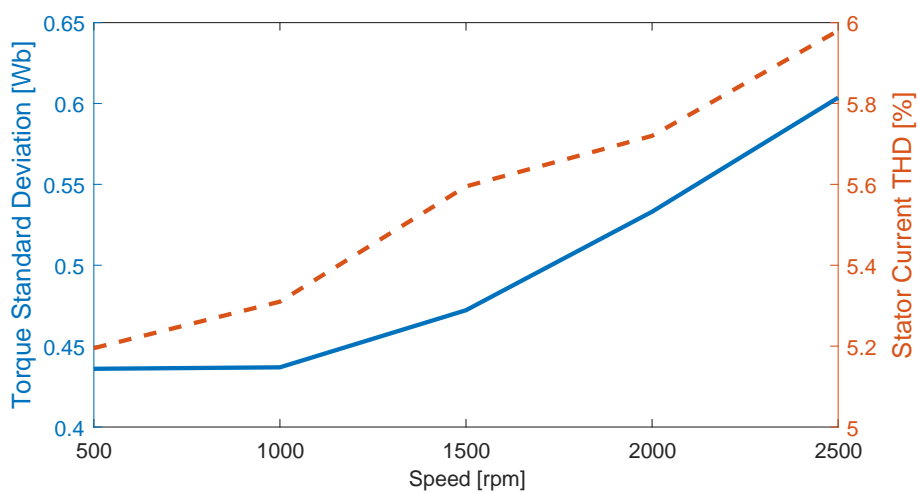


Figure 7.11: Experiment: Torque standard deviation and current THD under different speed operations.

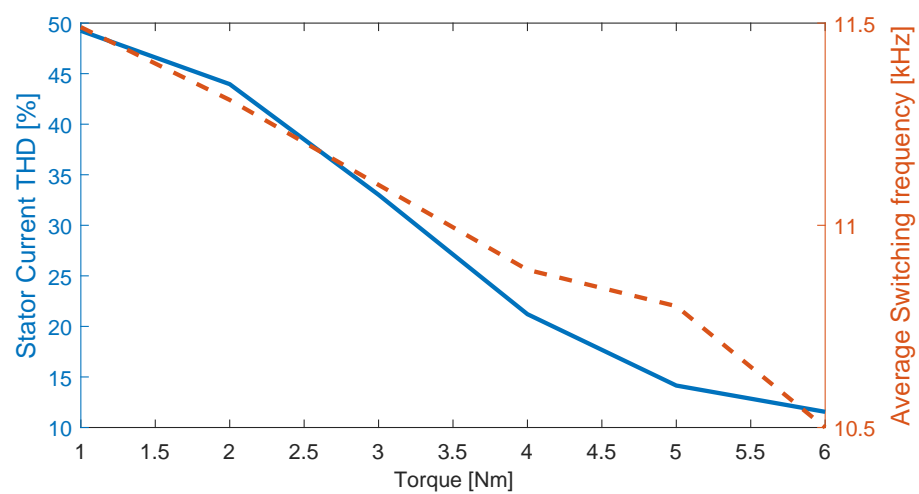


Figure 7.12: Experiment: Current THD and average switching frequency under different load conditions.

7.2 Parallel FCS-PTC

In this sub-chapter, PMPCs with both conventional full vectors based FCS for cost function and RFCSs introduced in chapter 5 will be proposed and verified for the purpose of calculation reduction. For RFCS based PMPC, only Deadbeat Triple and Deadbeat Double RFCS-MPCs are adopted, because for the Dichotomy-based RFCS-MPC, as is known from Chapter 5, the ripples are comparatively large, and for the Switching-minimized RFCS-MPC, the control performance is sacrificed as the cost for switching reduction. And Deadbeat Null RFCS-MPC calculates directly the reference voltage vector and contains no cost function, which is not suitable for PMPC requiring cost function.

Similar as SMPC, only PTC will be taken as example for implementation. The block diagram of Parallel FCS-PTC to be proposed in this chapter is illustrated in figure 7.13. The torque and flux related current estimation and prediction are the same as the conventional FCS-PTC as shown in the bottom area. The middle area is the PPTC mechanism, which are manipulated both laterally and vertically with separate torque and flux errors' sorting and integrated optimization procedures. Depending on the control set size, the system will optional apply the control set reduction algorithm shown inside the dotted area. Details of algorithms will be explained in the following parts.

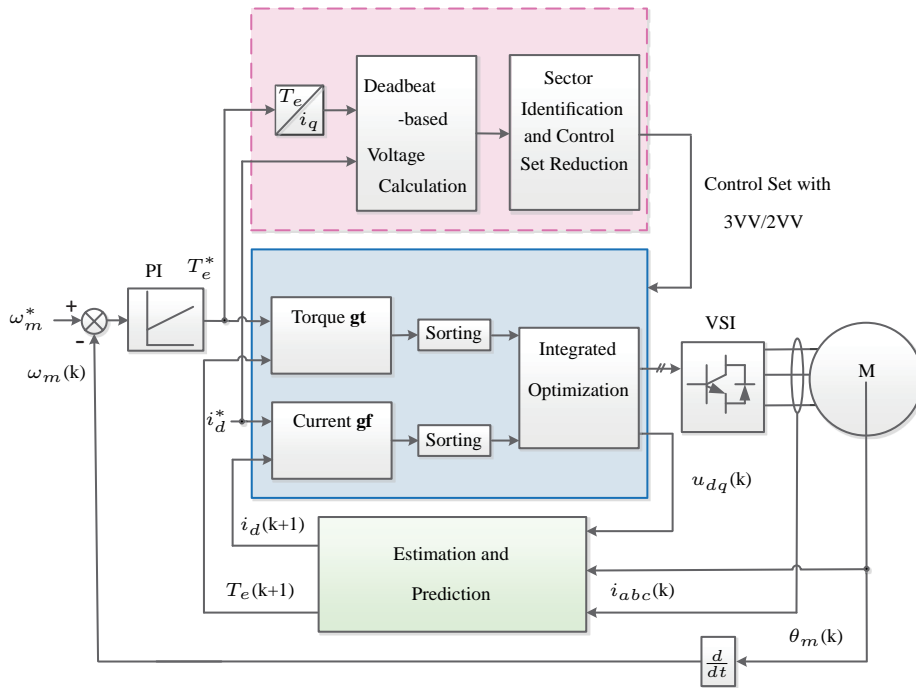


Figure 7.13: Parallell FCS-PTC.

7.2.1 Full-Vectors Parallel FCS-PTC

The basic idea of Full-Vectors Parallel PTC (or: Parallel FCS-PTC for short) applied in this chapter is to select the optimal/reference voltage vector from all 7 feasible vectors through the parallel optimization of both control terms with separate cost functions. Unlike the sequential methods in previous chapter that still require some parameters (e.g. control terms' error band widths for LUT decision), for parallel methods, in order to realize the real meaning of control "without weighting factor", neither weighting factor nor extra coefficients in other forms are required. The whole optimization process is conducted based on simple logical decision-makings that has reasonable theoretical bases. Figure 7.14 illustrates the principles of the optimization for the control set of FCS-Parallel PTC.

As is shown in this figure, the 7 voltage vectors are substituted into the absolute error terms of torque (torque error: gt) and flux (flux error: gf) separately. And these errors' corresponding vectors are then separately sorted into two lines, where the best one with minimum error value is on the right end.

Since for both PTC and PCC, the simulation and experimental experiences prove that the torque control is always more crucial than the flux control. Therefore, similar as SMPC, torque control is always given higher consideration and priority, while the flux control is also considered but with subordinate importance. Basic logic decision-makings are conducted with torque as the inferior control term and flux the superior one. Firstly, the best three vectors on the right side of both lines are analyzed for reference vector selection. And then, with these three options, there exist two possibilities. In case 1: if there exists 1~3 mutual vectors among the right vectors of both lines, the one that leads to better torque control (i.e. has smaller/smallest value of torque error) is chosen. For example, in figure 7.14, the mutual vector V_3 instead of the other mutual vector V_4 is selected and output as the reference. However, if there is no mutual vector among the right three vectors of both lines, it comes to case 2, where one of the best three of sorted torque vectors on right end leading to the smallest flux error is still selected. This emphasizes the importance of torque regulation, while it still limits the flux errors to the largest extent, i.e. the worst case is choosing the third worst voltage vector for the flux control.

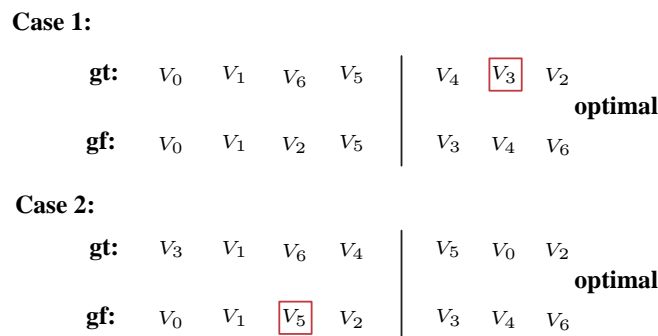


Figure 7.14: Optimization Principles for Full Control Set of PPTC.

7.2.2 Simulation and Experimental Verification

For fair comparison, in this chapter, conventional FCS-PTC and the proposed Parallel FCS-PTC for IM with an integrated cost function similar as (7.3) for IPMSM is firstly simulated.

And its cost function is:

$$g_j = |T_e^* - \hat{T}_e(k+2)_j| + \lambda_g \cdot | \| \psi_s^* \| - \| \hat{\psi}_s(k+2)_j \| | + I_m(k+2)_j \quad (7.3)$$

The systems are first control under speed control mode.

Simulation 1 is to find out the performance of the speed step-up and reversal process. Figure 7.15 shows speed, torque, current and flux of this process. It can be seen that the proposed full-vectors parallel FCS-PTC, even containing no cost function, has visible better torque and flux qualities than the conventional FCS-PTC.

Figure 7.16 shows the corresponding torque and flux tracking performance. It is seen in this figure, full-vectors parallel FCS-PTC's tracking performance is as good as that of the conventional FCS-PTC and it has even smaller flux oscillation band surrounding the reference.

Simulation 2 is to find out the speed performance under torque variations in simulation.

Figure 7.17 shows speed, torque, current and flux of this process. Similar as the speed dynamics process, in light of its smoother torque as well as current and flux, the proposed weighting factor-less method has better control performance.

The proposed method is than experimentally verified on SPMSM.

Experiment 1 as shown in figure 7.18 is the speed step reversal maneuver. Similar as in simulation, the proposed method has almost visibly same dynamics and steady performance as the conventional PTC.

Experiment 2 as shown in figure 7.19 is the torque variation test. Both the ripples band width and speed drop/rise in sudden torque varying transient are almost the same.

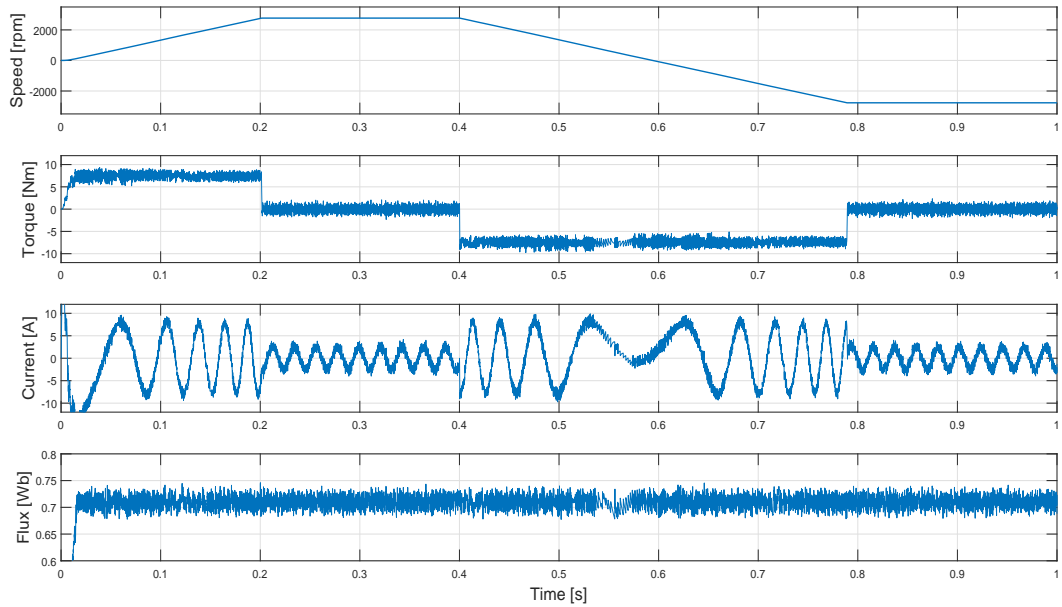
Experiment 3 is to find out the performance under torque control mode in experiment.

Figure 7.20 shows that both systems have instantly fast torque output capabilities.

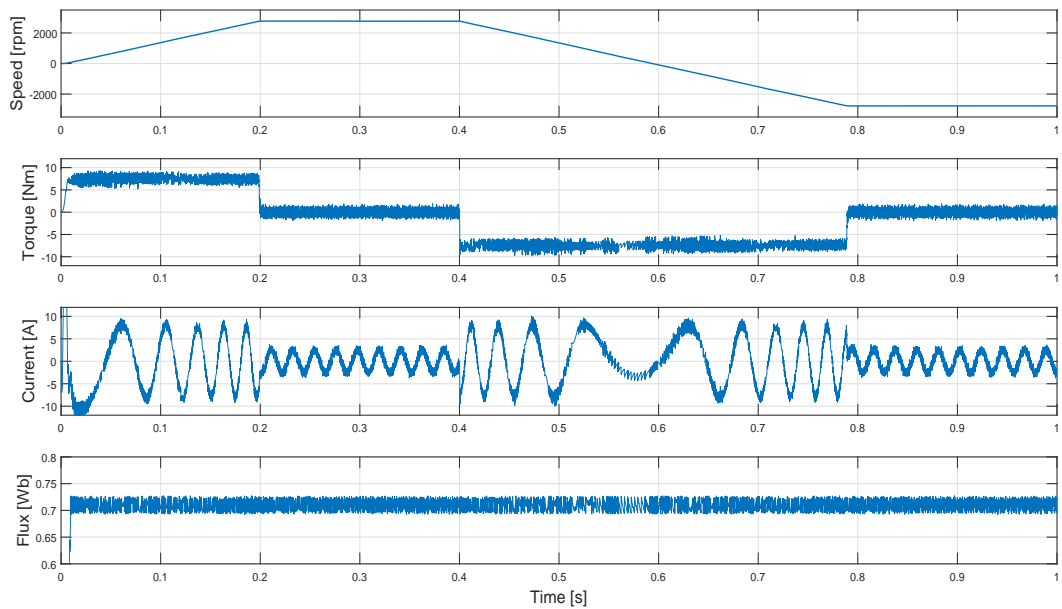
Experiment 4 is to find out the robustness of the conventional PTC and full-vectors parallel method in experiment.

Figure 7.21 and figure 7.22 shows speed, torque, current and flux under the R_s and ψ_{pm} variations, in which both system have same extent and sensitivities in robustness, i.e. somehow sensitive to the ψ_{pm} variation as with the previous methods.

All of the above simulations and experimental results verify the effectiveness and competitive performance of the full-vectors parallel FCS-PTC to the conventional FCS-PTC.

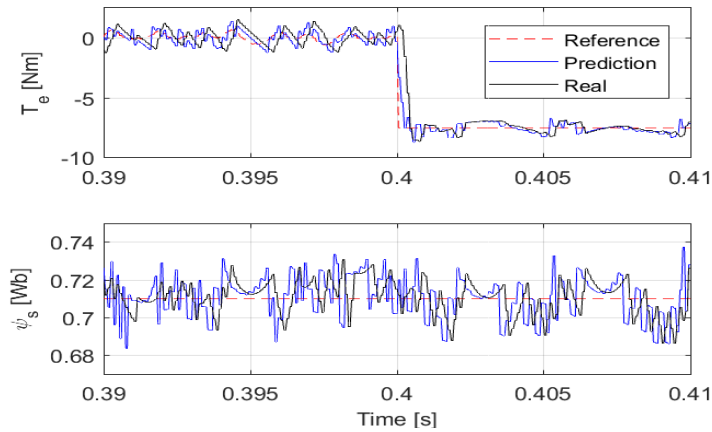


(a) FCS-PTC.

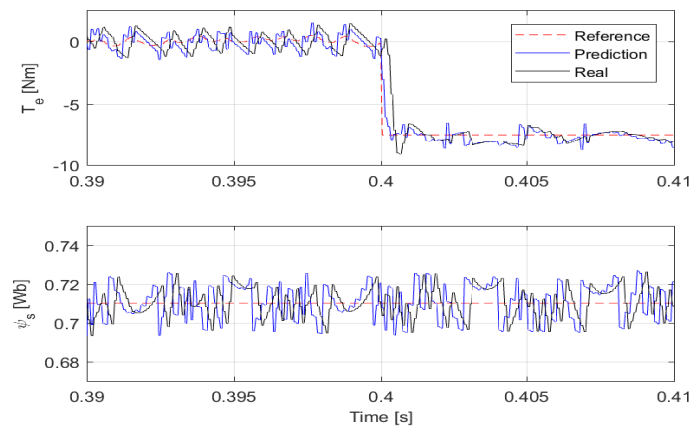


(b) FCS-Parallel PTC.

Figure 7.15: Simulation: Rated speed start-up and reversal of conventional FCS-PTC and Full-Vectors Parallel FCS-PTC for IM.

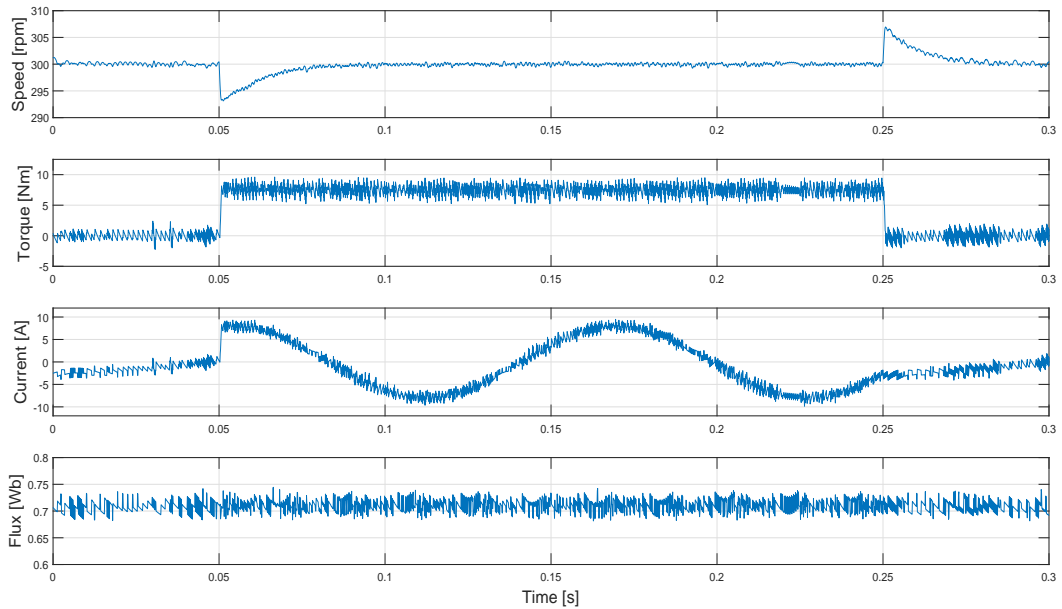


(a) FCS-PTC.

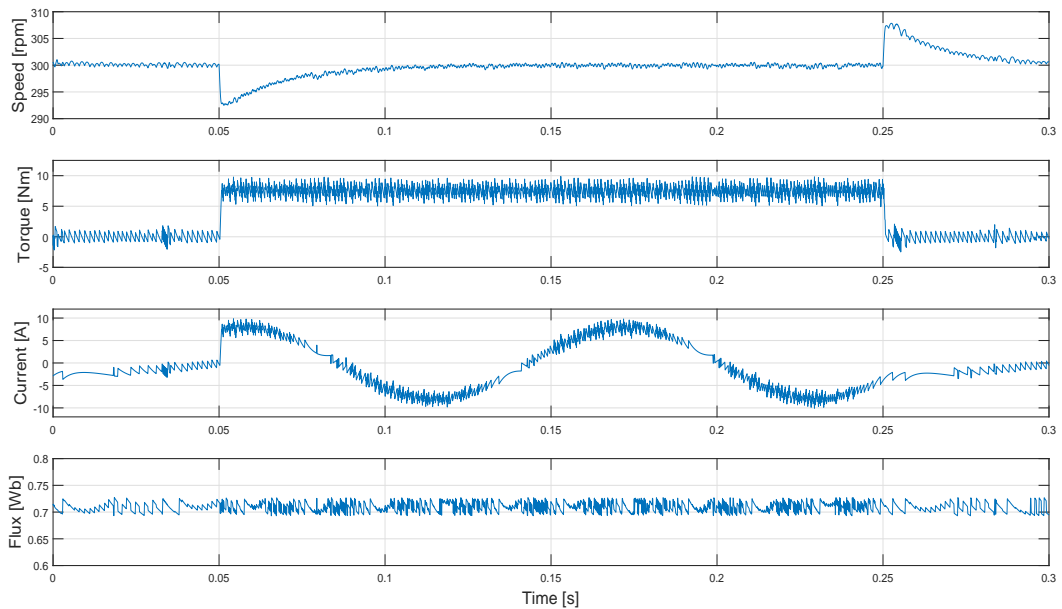


(b) FCS-Parallel PTC.

Figure 7.16: Simulation: Torque and Flux Tracking Performance of conventional FCS-PTC and Full-Vectors Parallel FCS-PTC for IM.

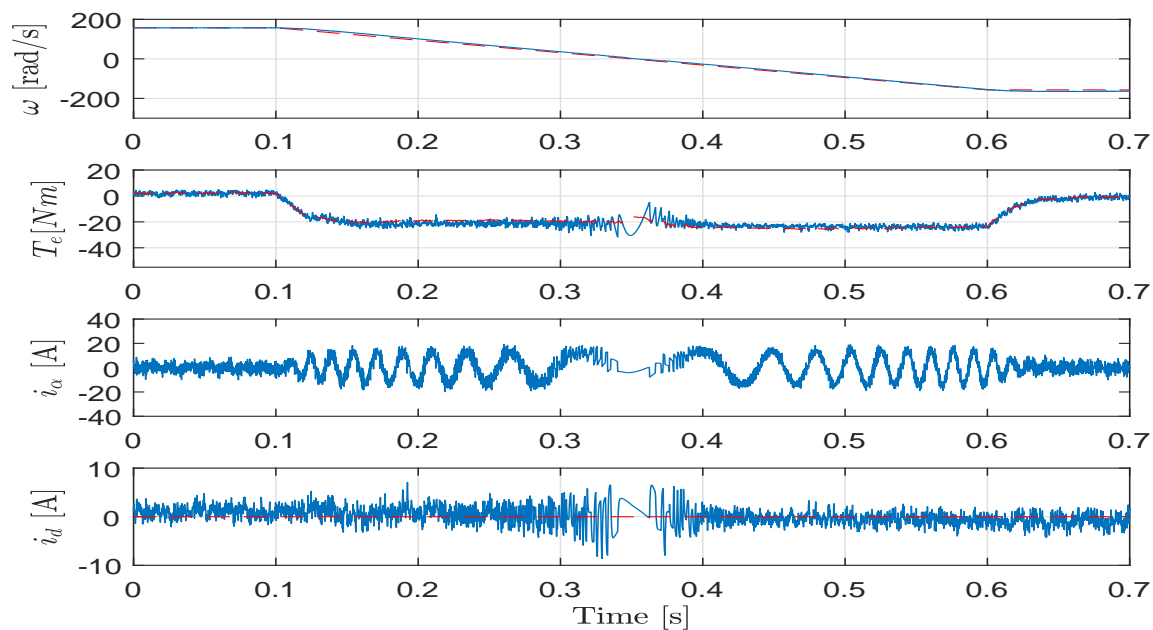


(a) FCS-PTC.

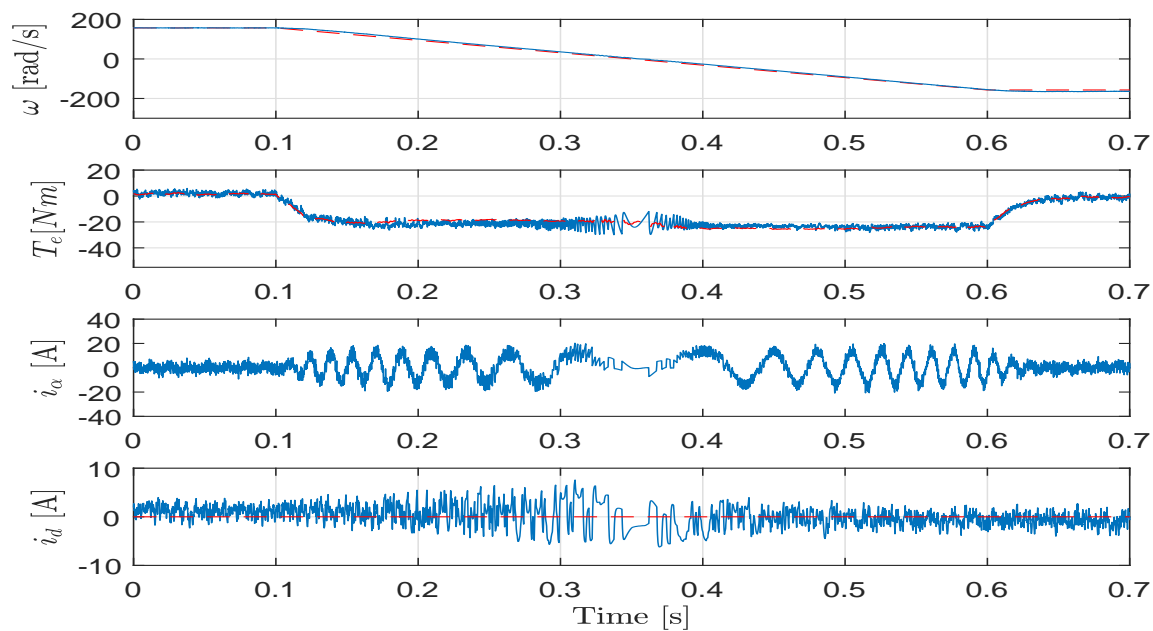


(b) FCS-Parallel PTC.

Figure 7.17: Simulation: Conventional FCS-PTC and Full-Vectors Parallel FCS-PTC Performance for IM under Torque Variations.

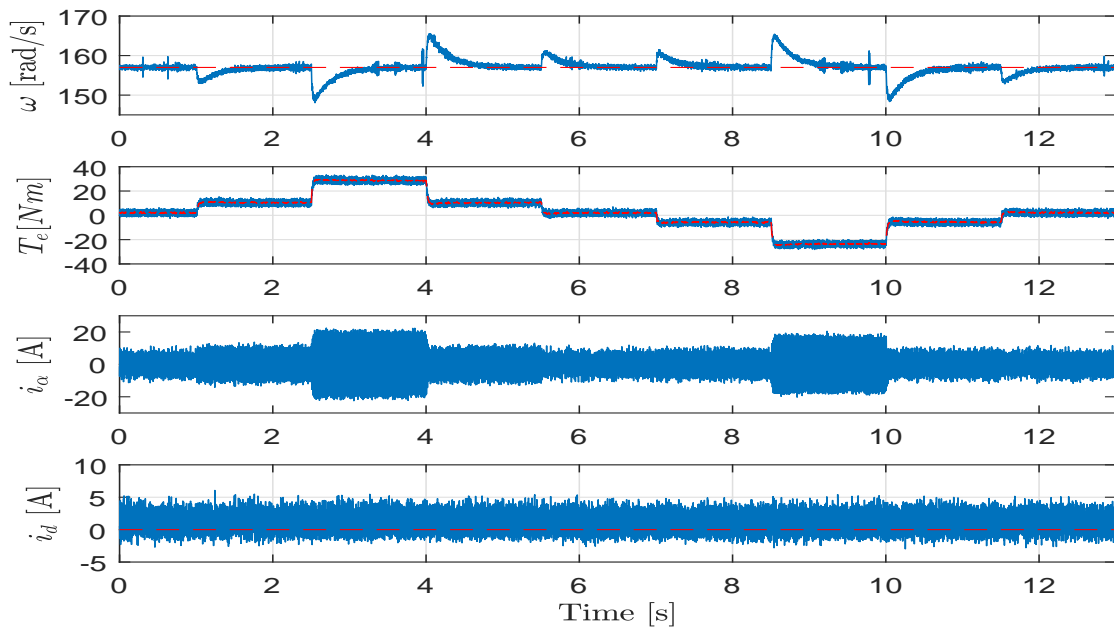


(a) FCS-PTC.

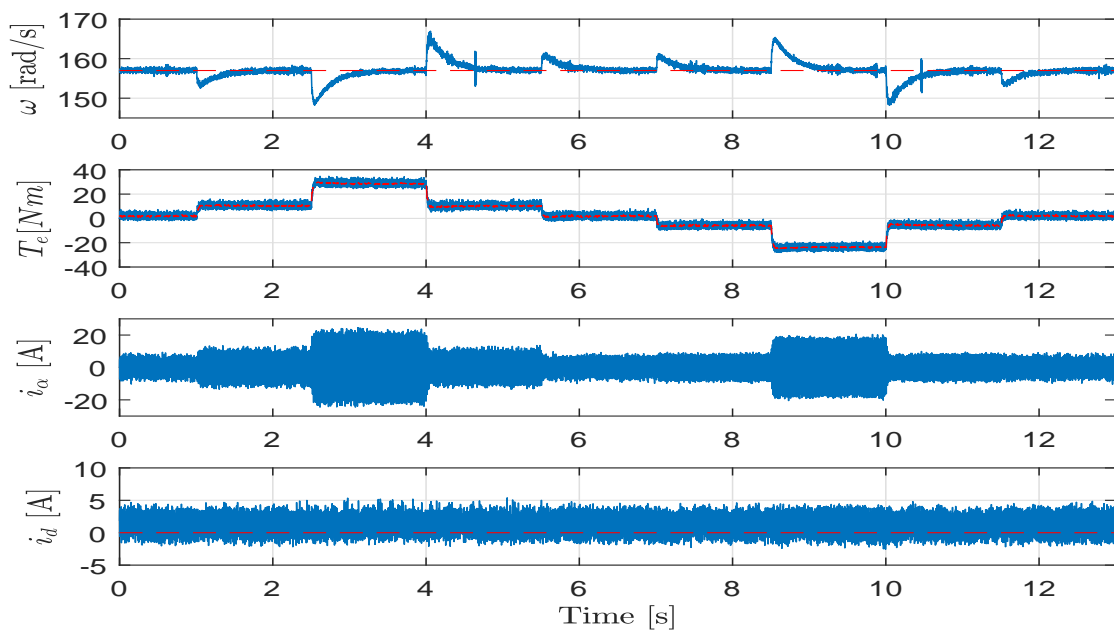


(b) FCS-Parallel PTC.

Figure 7.18: Experiment: Rated speed start-up and reversal of conventional FCS-PTC and Full-Vectors Parallel FCS-PTC for SPMSM.

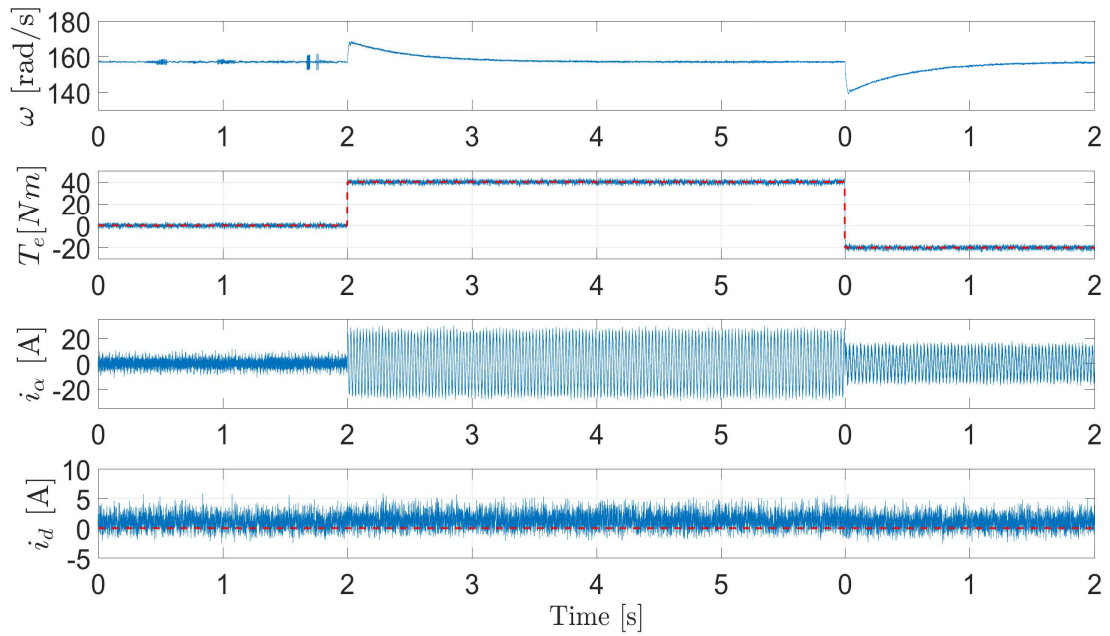


(a) FCS-PTC.

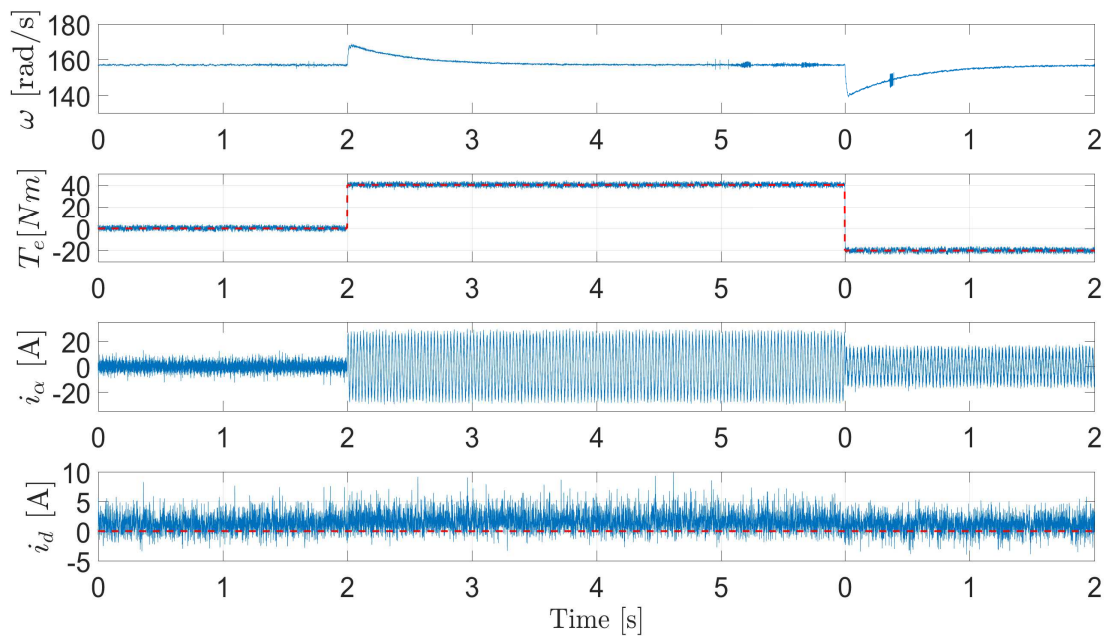


(b) FCS-Parallel PTC.

Figure 7.19: Experiment: Conventional FCS-PTC and Full-Vectors Parallel FCS-PTC Performance for SPMSM under Torque Variations.

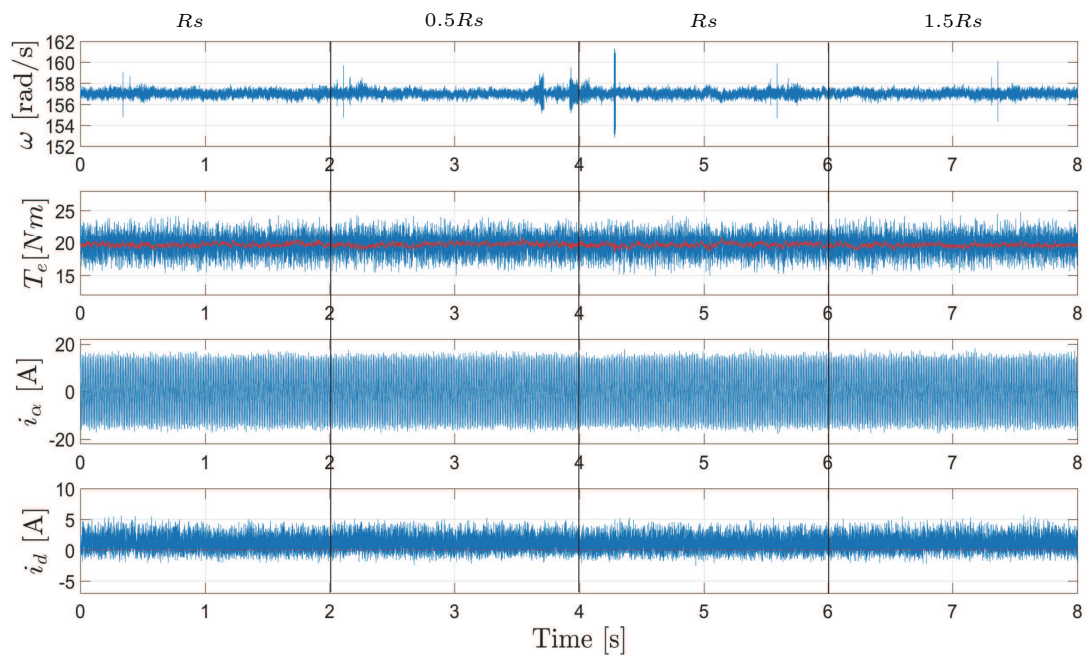


(a) FCS-PTC.

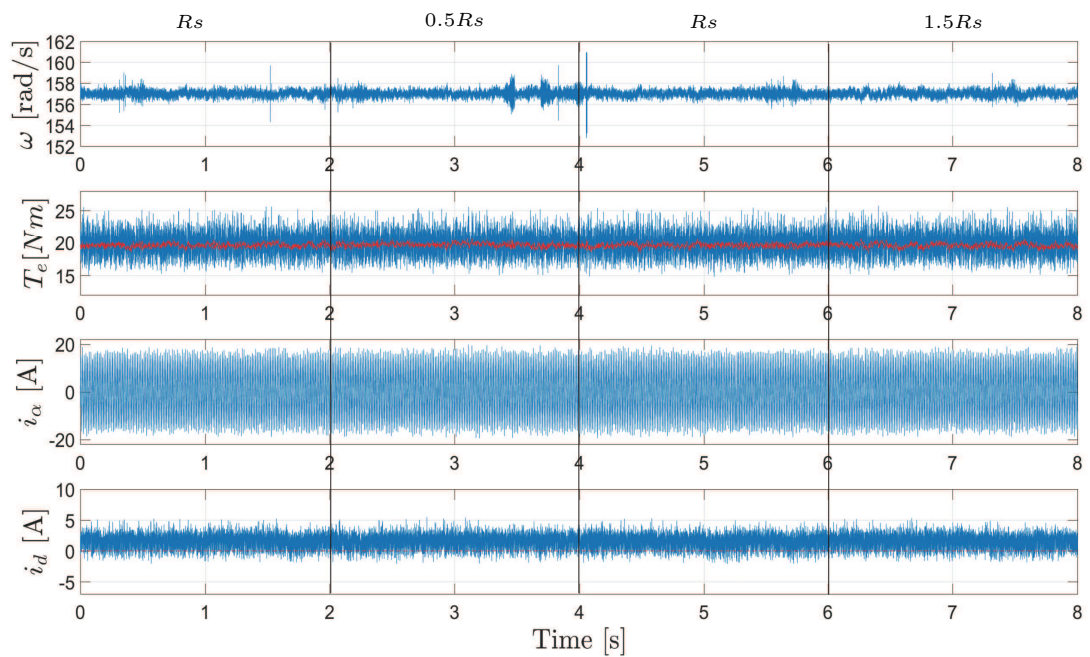


(b) FCS-Parallel PTC.

Figure 7.20: Experiment: Conventional FCS-PTC and Full-Vectors Parallel FCS-PTC Performance for SPMSM under Torque Control Mode.

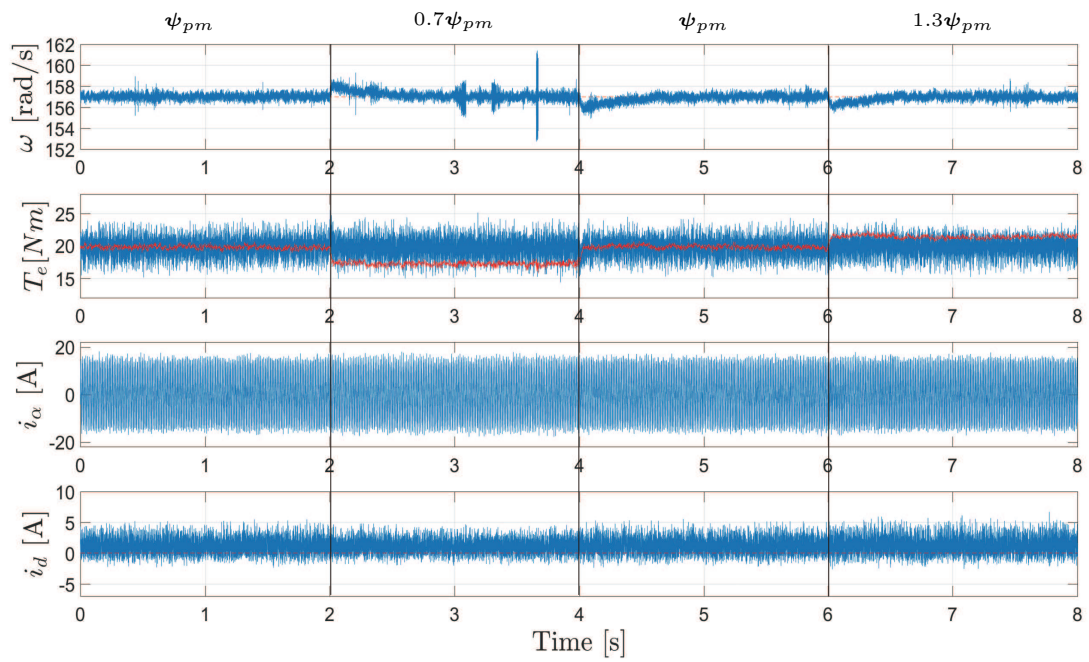


(a) FCS-PTC.

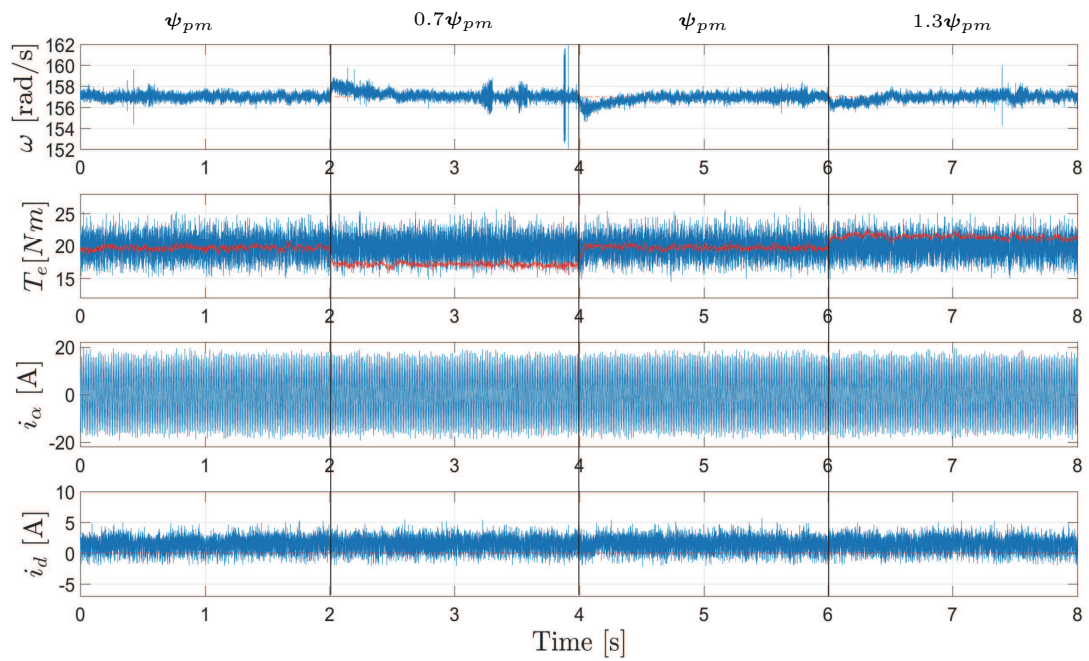


(b) FCS-Parallel PTC.

Figure 7.21: Experiment: Full-Vectors Parallel RFCS-PTC Performance for SPMSM under R_s Variation.



(a) FCS-PTC.



(b) FCS-Parallel PTC.

Figure 7.22: Experiment: Full-Vectors Parallel RFCS-PTC Performance for SPMSM under ψ_{pm} Variation.

7.2.3 Deadbeat Triple Parallel RFCS-PTC

Figure 7.23 illustrates the principles of the optimization for the control set of deadbeat triple RFCS-Parallel PTC. Similar as the previous method, firstly, only three vectors are left and sorted by their corresponding torque and flux errors respectively. Since the vector number is largely reduced, only the best two vectors of both lines are searched to find the optimal one. Because there must be at least one mutual vector among the best two vectors for both lines, no second case is to be discussed. The vector among these two vectors that minimizes the torque error will be chosen as reference, i.e. in this example, the only mutual vector V_6 is selected.

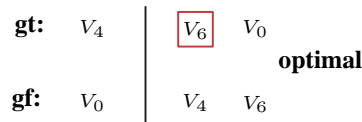


Figure 7.23: Optimization Principles for Control Set of Deadbeat Triple PPTC.

7.2.4 Simulation and Experimental Verification

Simulation 1 is to find out the performance during speed step start-up and reversal process in simulation.

Figure 7.24 shows speed, torque, current and flux of this process. This process has similarly comparable performance as the conventional FCS-PTC and previous methods, except the speed rise time is slightly longer.

Figure 7.25 shows the corresponding dynamics of torque and flux tracking performance, which is also fast and precise.

Simulation 2 is to find out the speed performance under torque variations in simulation.

Figure 7.26 proves that it is as good as the methods with larger control set and more vectors.

Deadbeat Triple Parallel RFCS-PTC are also experimented on SPMSM.

Experiment 1 is the speed start-up and reversal test shown in figure 7.27.

Experiment 2 is the system performance test under varying torque, which is given in figure 7.28.

Experiment 3 is to find out the performance under torque control mode in experiment.

Figure 7.29 shows speed, torque, current and flux of this process. It is as good as the case under deadbeat triple parallel RFCS-PTC.

Experiment 4 is to find out the robustness of the proposed method.

Figure 7.30 and figure 7.31 shows speed, torque, current and flux under the R_s and ψ_{pm} variations. The proposed method has almost the same robustness as previous method.

Therefore, deadbeat triple parallel RFCS-PTC works excellently as expected, and in light of its much smaller number of vectors in control set, it is easier in both calculation and concept of design. Containing no weighting factor, it is a very good alternative for the conventional and previous proposed methods for electric drives.

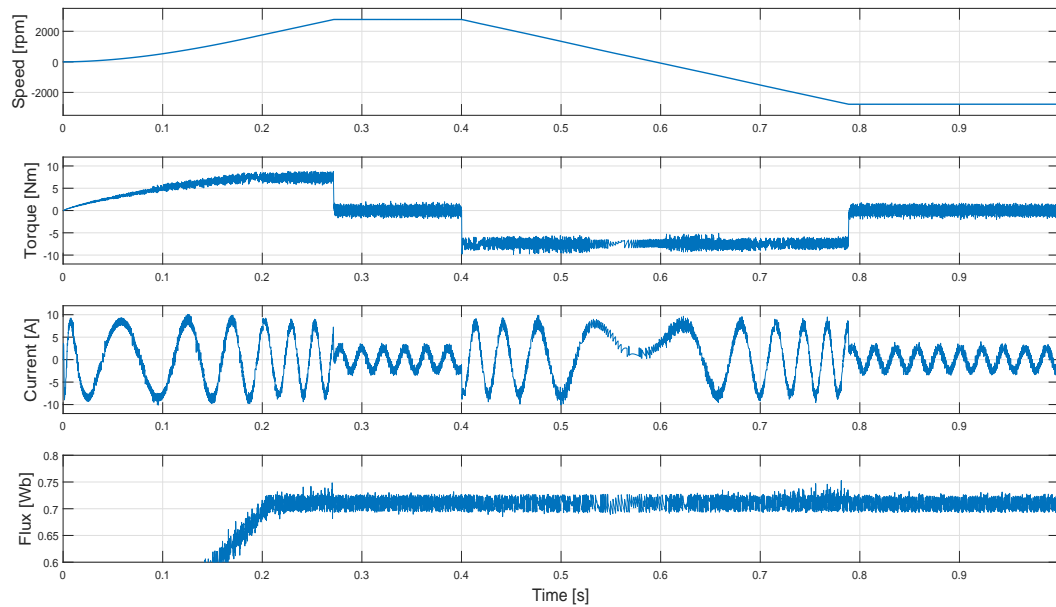


Figure 7.24: Simulation: Rated speed start-up and reversal of Deadbeat Triple Parallel RFCS-PTC for IM.

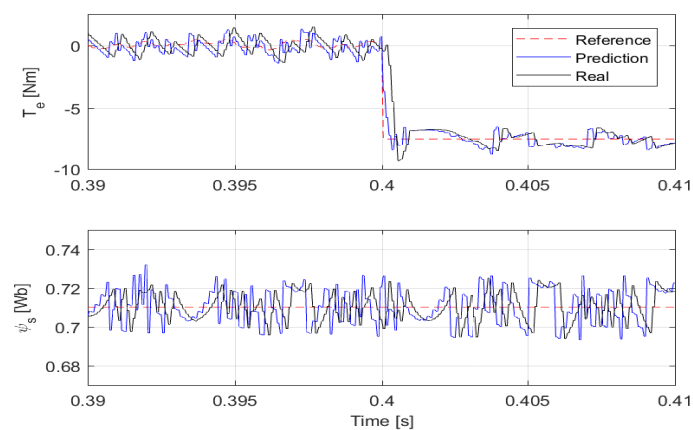


Figure 7.25: Simulation: Current Tracking Performance of Deadbeat Triple Parallel RFCS-PTC for IM.

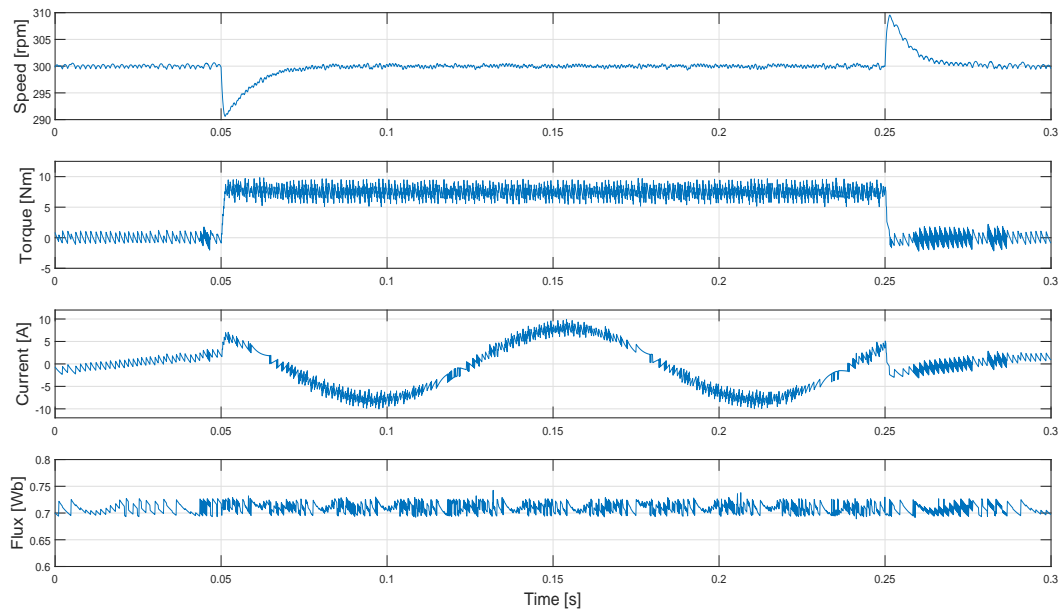


Figure 7.26: Simulation: Deadbeat Triple Parallel RFCS-PTC Performance under Torque Variations for IM.

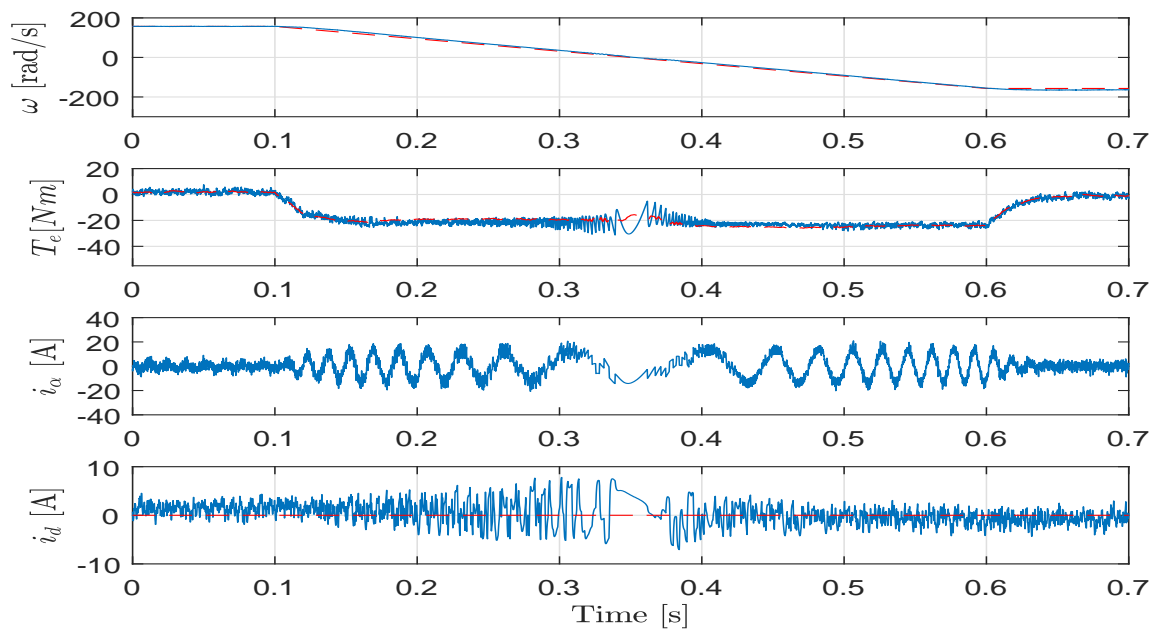


Figure 7.27: Experiment: Rated speed start up and reversal of Deadbeat Triple Parallel RFCS-PTC for SPMSM.

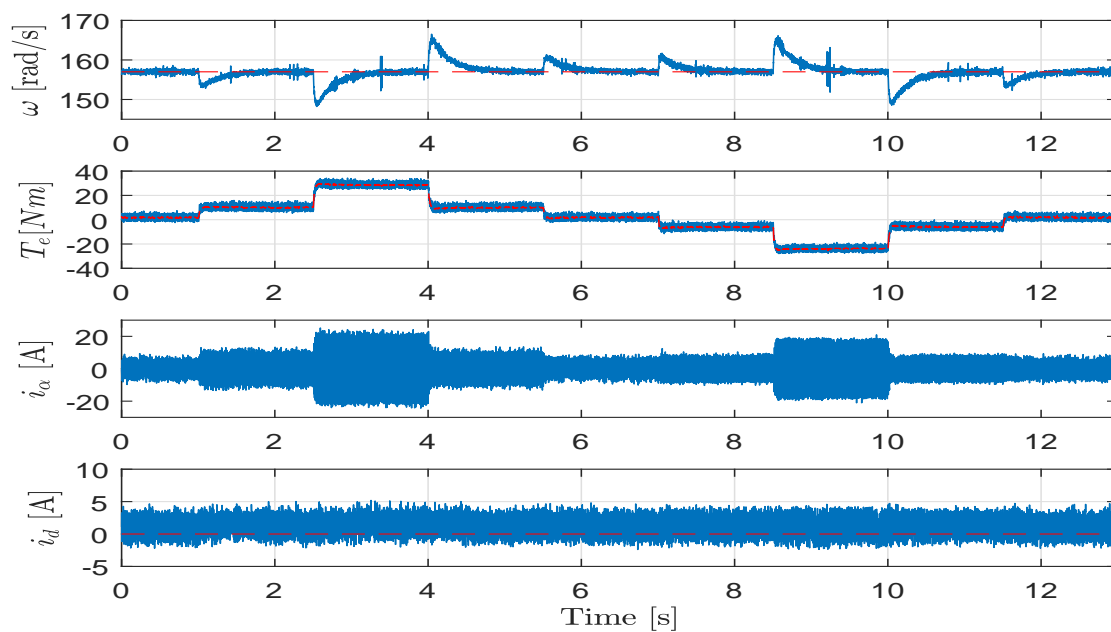


Figure 7.28: Experiment: Deadbeat Triple Parallel RFCS-PTC Performance under Torque Variations for SPMSM.

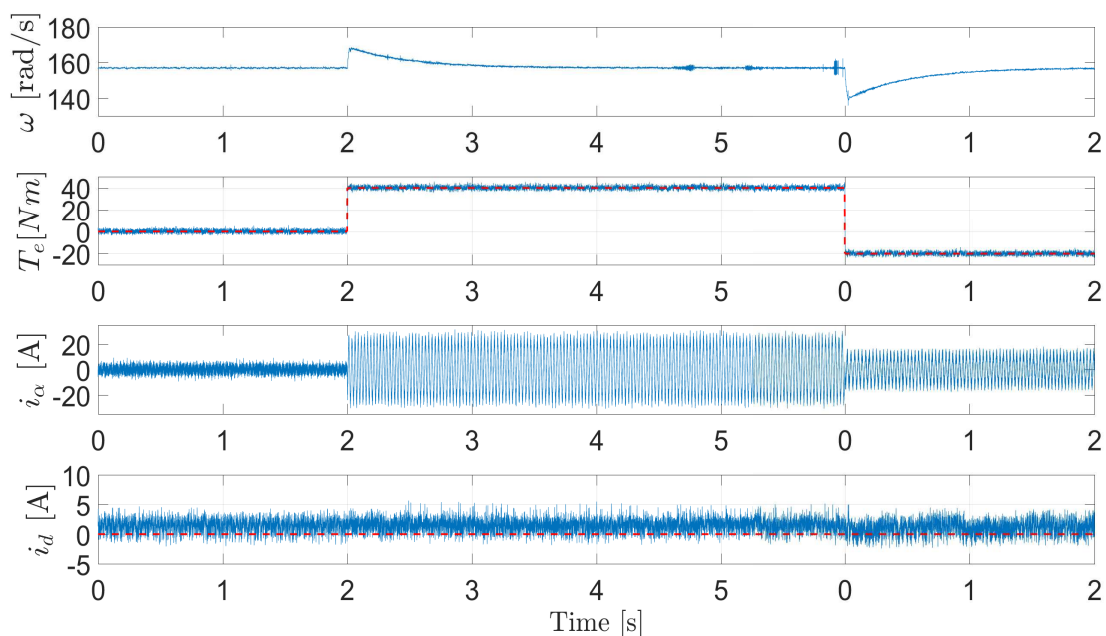


Figure 7.29: Experiment: Deadbeat Triple Parallel RFCS-PTC Performance for SPMSM under Torque Control Mode.

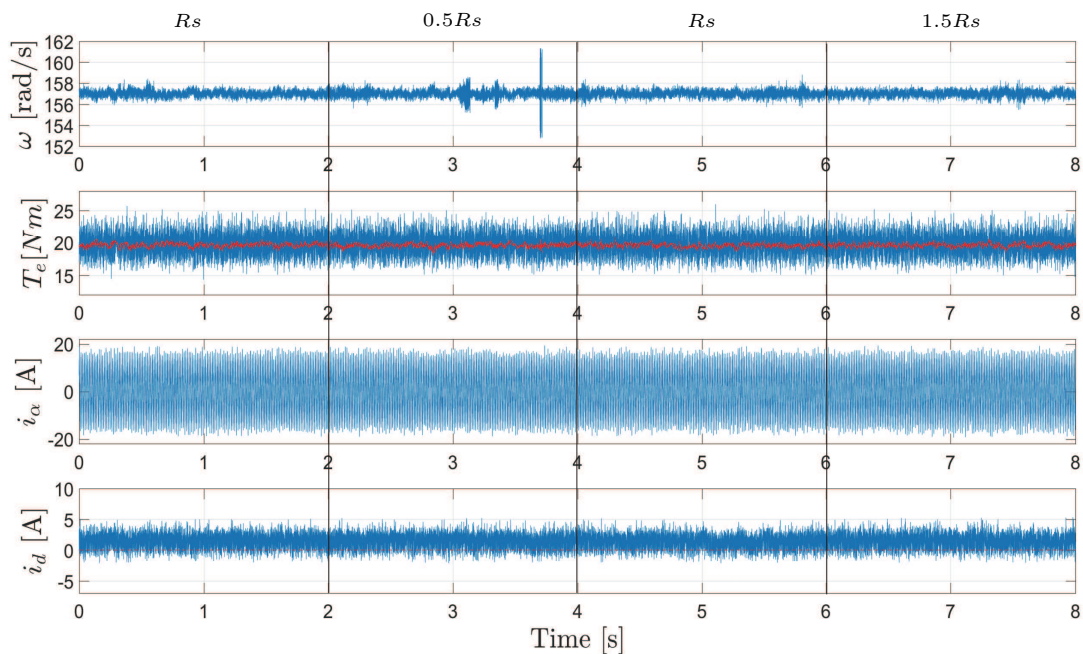


Figure 7.30: Experiment: Deadbeat Triple Parallel RFCS-PTC Performance under R_s Variation for SPMSM.

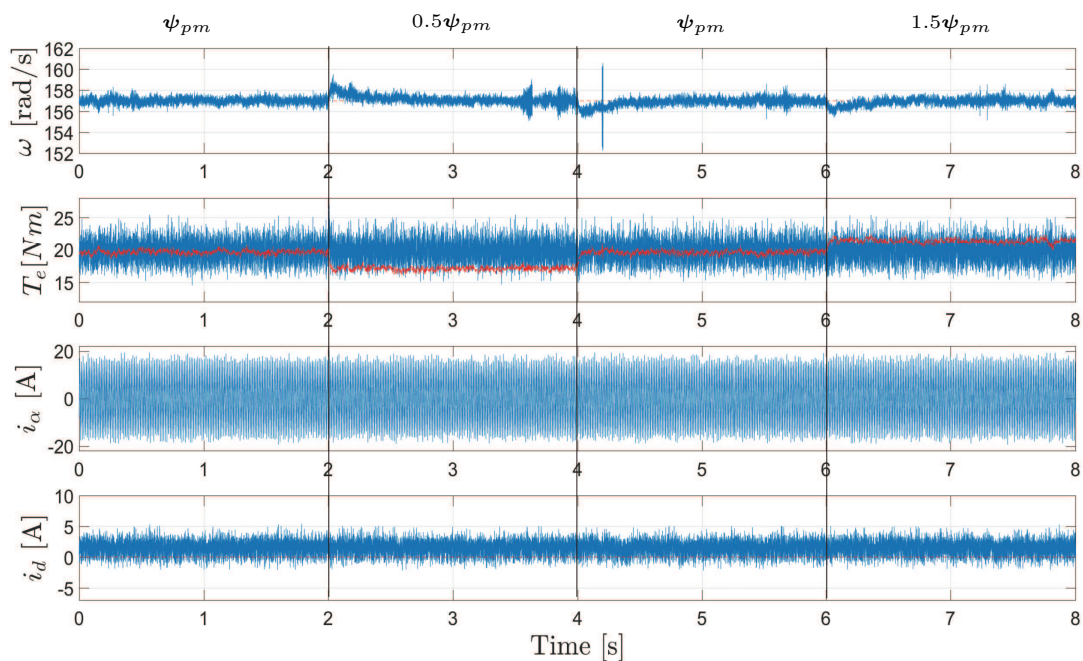


Figure 7.31: Experiment: Deadbeat Triple Parallel RFCS-PTC Performance under ψ_{pm} Variation for SPMSM.

7.2.5 Deadbeat Double Parallel RFCS-PTC

Figure 7.32 illustrates the optimization principles with the control set of deadbeat double parallel RFCS-PTC. Based on the core principle of giving higher torque priority, the best torque controlling vector, i.e., V_3 in this illustration, is selected.

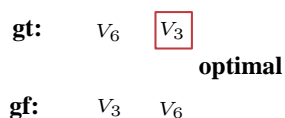


Figure 7.32: Optimization Principles for Control Set of Deadbeat Double PPTC.

7.2.6 Simulation and Experimental Verification

Simulation 1 is to find out the performance during speed step-up and reversal process in simulation.

Figure 7.33 shows speed, torque, current and flux of this process. Compared with previous figures of different solutions in the same process, the torque ripples' band is further reduced, but the flux control is not as good as previous ones, because it has slightly larger variations and slower flux dynamics.

Figure 7.34 shows the corresponding torque and flux tracking performance. Being consistent as the last test figure, the torque tracking performance is quite well but flux is not precisely controlled to align with its reference. However, since for IM, the flux can be strengthened or weakened flexibly according to system demands, this phenomenon is acceptable and even explicable for better torque control.

Simulation 2 is to find out the system performance under torque variations.

Figure 7.35 shows speed, torque, current and flux of this process. Similar as the previous test, the flux has comparatively larger value than its reference at loaded condition.

Deadbeat double parallel RFCS-PTC are also experimented on SPMSM.

Experiment 1 is the speed reversal performance test. Figure 7.36 shows that, though the flux ripples are slightly larger, the torque ripples are smaller than the previous method. Since the flux is only intermediate variable, it is not influential when its value is oscillating in larger range.

Experiment 2 is the torque variation test. The experimental results in figure 7.37 agrees with the discovery in experiment 1.

Experiment 3 is to find out the performance under torque control mode.

Figure 7.38 shows speed, torque, current and flux of this process, which shows the similar competitive performance of deadbeat double parallel RFCS-PTC as the triple one proposed in the previous sub-chapter.

Experiment 4 is to find out the robustness of the proposed method in experiment.

Figure 7.39 and figure 7.40 shows speed, torque, current and flux under the R_s and ψ_{pm} variations. Both figures show that the system is not less robust with the further reduction of voltage vectors in the control set.

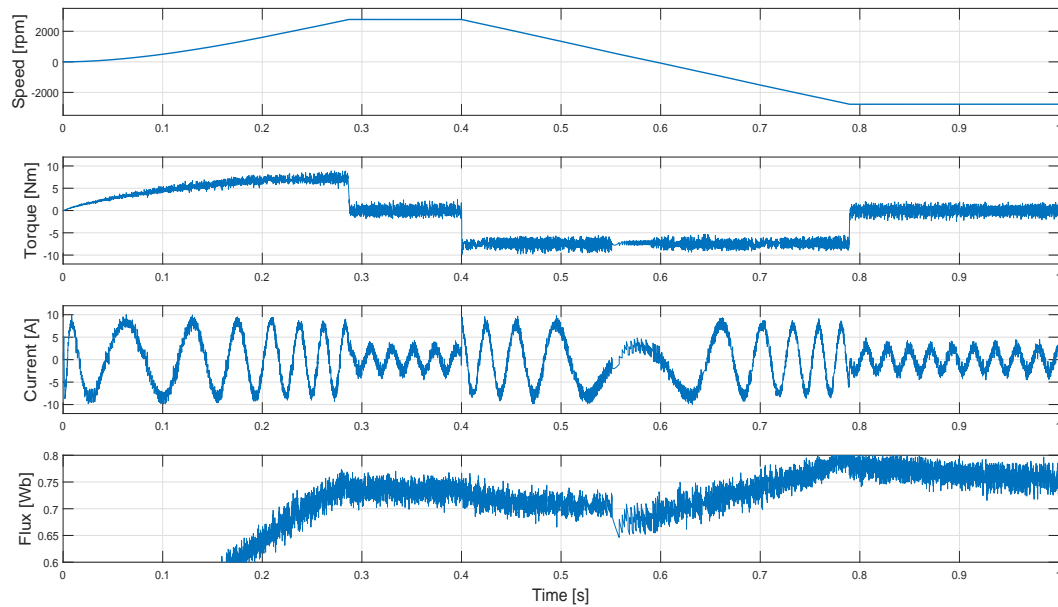


Figure 7.33: Simulation: Rated speed start up and reversal of Deadbeat Double Parallel RFCS-PTC for IM.

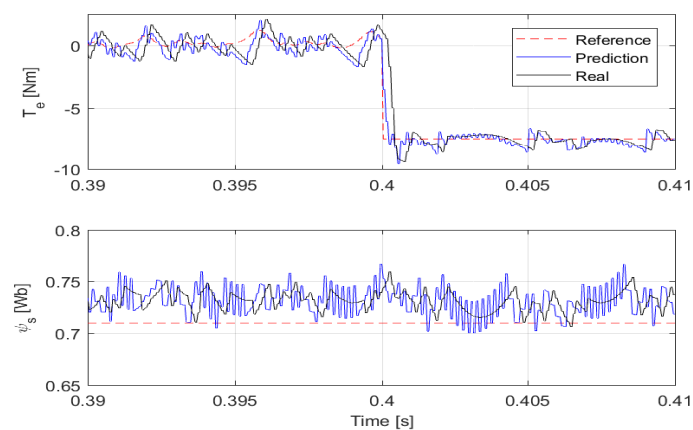


Figure 7.34: Simulation: Current Tracking Performance of Deadbeat Double Parallel RFCS-PTC for IM.

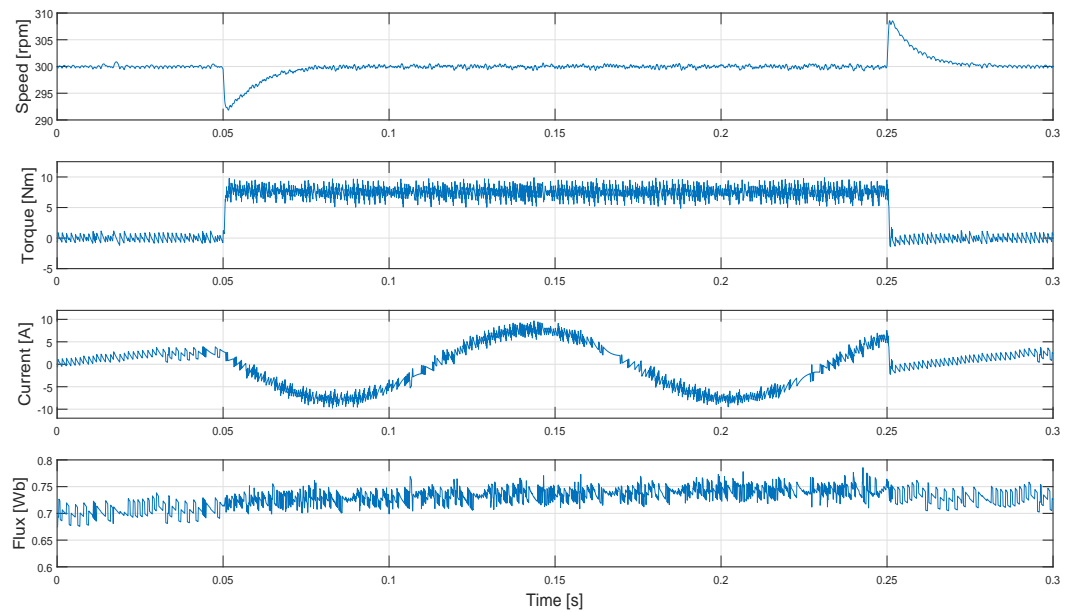


Figure 7.35: Simulation: Deadbeat Double Parallel RFCS-PTC Performance for IM under Torque Variations.

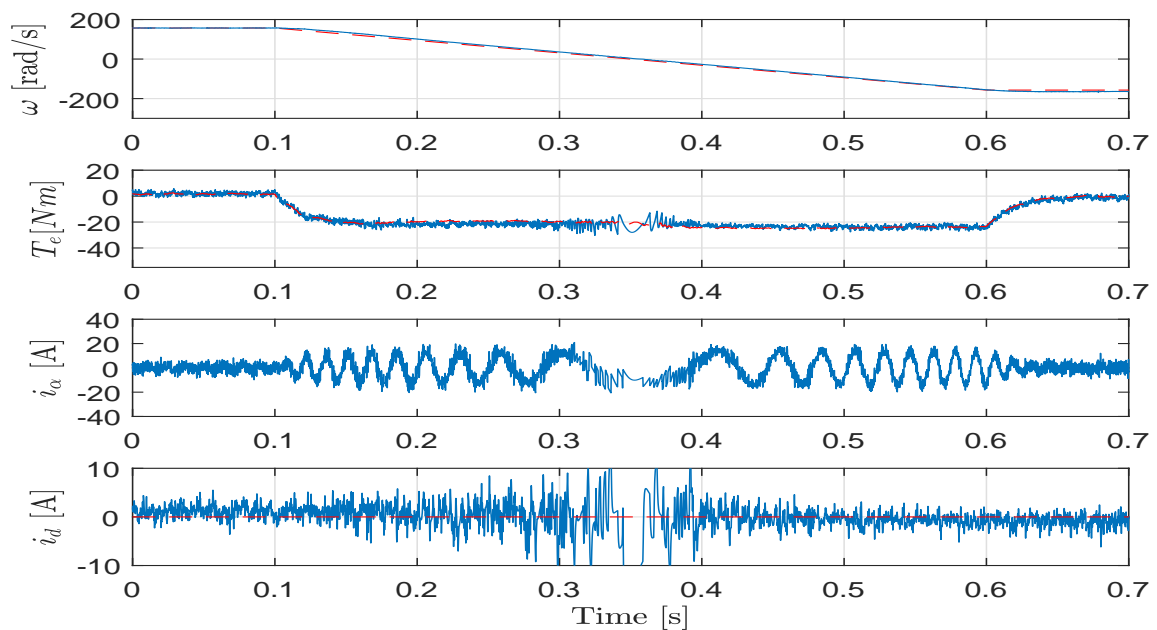


Figure 7.36: Experiment: Rated speed start up and reversal of Deadbeat Double Parallel RFCS-PTC for SPMSM.

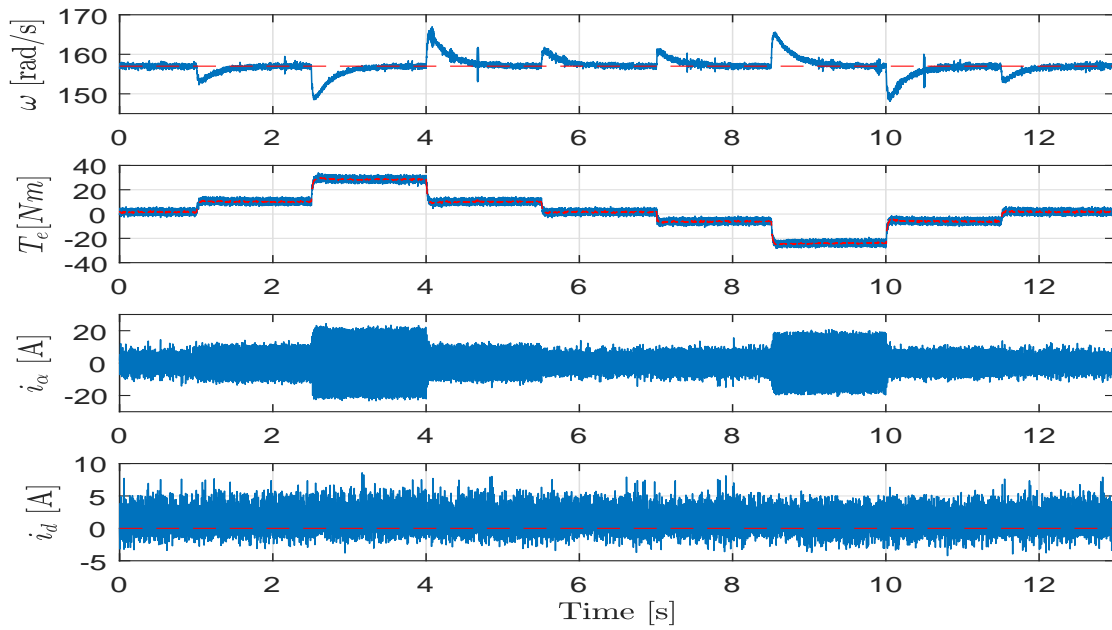


Figure 7.37: Experiment: Deadbeat Double Parallel RFCS-PTC Performance for SPMSM under Torque Variations.

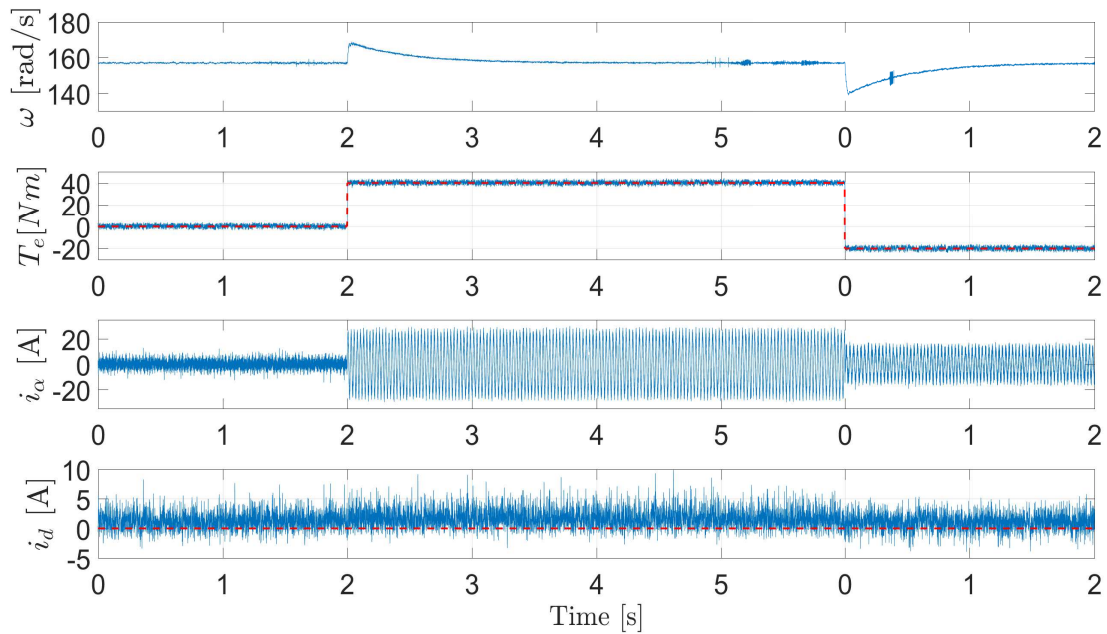


Figure 7.38: Experiment: Deadbeat Double Parallel RFCS-PTC Performance for SPMSM under Torque Control Mode.

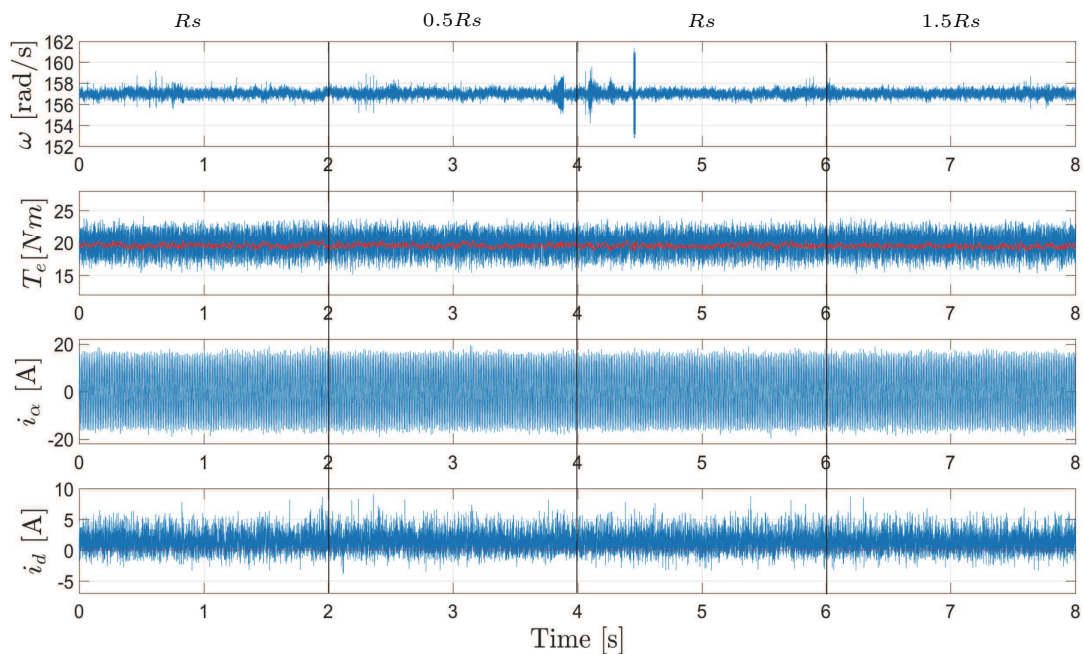


Figure 7.39: Experiment: Deadbeat Double Parallel RFCS-PTC Performance under R_s Variation for SPMSM.

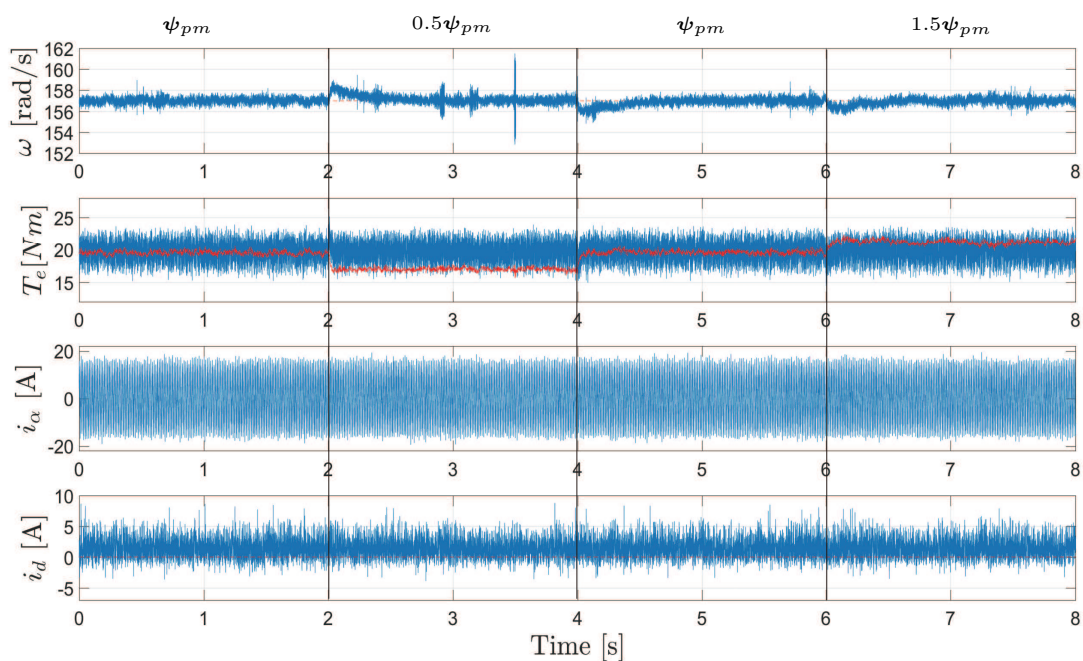


Figure 7.40: Experiment: Deadbeat Double Parallel RFCS-PTC Performance under ψ_{pm} Variation for SPMSM.

7.3 Conclusion

In this chapter, to eliminate the weighting factor and simplify/clarify the tuning process, one solution with online self-adjustive control priority for sequential FCS-PTC and three solutions for parallel FCS-PTCs including reduced calculation efforts and design simplification are proposed based on the previous works and verified by simulation and experiments.

Both sequential and parallel FCS-PTCs work satisfactorily as expected. Therefore, the goal to remove weighting factor for cost function in FCS-MPC is achieved with the proposed methods.

The proposed FCS-MPC without weighting factor in this chapter could be extensively devised and conducted for FCS-PCC.

CHAPTER 8

Summary and Outlook

In this dissertation, several different variations of model predictive controls and their extensive considerations in implementations for electric drives have been proposed and verified by simulations and experiments. Some methods, e.g., FCS-MPC without weighting factors, can not only be applied on electric machines, but also further applied on different AC/DC-DC/AC converters containing cost functions. In order to ensure the universality and extensibility of the proposed methods, three types of most commonly used AC machines are applied in tests, i.e., most simulations are conducted on an real IPMSM's model and all experiments are conducted on either an real IPMSM or an IM at the laboratory. Experiments are realized through an high performance dSPACE real time semi-physical simulation system. Moreover, the proposed control strategies or improvements can be further extended to other kinds of AC drives, for example, switched reluctance motors (SRM) or linear motor (LM) drives.

8.1 Conclusion

The work of this dissertation can be summarized as follows:

- **Chapter 3** has reviewed two main categories of MPCs: FCS-MPC and Continuous MPC. Three most popular examples of both categories, i.e., FCS-PTC, FCS-PCC and Deadbeat PCC have been explained, and their transient dynamics and steady state have been compared.

It has been found that both FCS-PTC and FCS-PCC have similar good performances in light of their dynamics, low switching frequencies and nonlinear control/constraint inclusion potential. And Deadbeat PCC, though contains PWM module, its amount of calculation is much less than the FCS-MPCs. Therefore, it is as good an option as FCS-MPC in light of its merits of similarly fast dynamics as FCS-MPCs.

- **Chapter 4** has proposed and verified two kinds of increased FCS-MPCs with continuous reference voltage, i.e., fan and circular dichotomy-based methods, which can generate quasi continuous voltage reference thus to be offered for the SVM.

Simulation and experimental verifications have proved that IFCS-MPCs can maintain the fixed switching frequency of the inverter, have better control accuracy, improves the current quality and reduces the torque ripples significantly. Therewith, the system's reliability can be ensured.

- **Chapter 5** has introduced five different realization of reduced FCS-MPCs so that the size of finite control set for cost functions is minimized. The number of candidate voltage vectors is reduced by these methods to 5, 4, 3, 2 and 0, respectively.

Simulation and experimental results have shown the effectiveness of all proposed reduced FCS-MPC methods. With reduction of calculation efforts and no deterioration of system performance or even better steady state characteristics, they could all be considered as ideal alternatives for the conventional FCS-MPC. Moreover, some of them have even better torque and speed ripples inhibitions ability than the conventional FCS-MPC.

- **Chapter 6** has proposed a TDO to improve the system's transient and steady state performances. By applying TDO to both deadbeat PCC and FCS-PTC, it is found that the integral part of outer speed PI controller could be eliminated to reduce the tuning of parameter.

Simulation and experimental results have verified that by making the system to be "disturbance-free", TDO can not only simplify the control, but also reduce the torque response time and the general transient dynamics. Moreover, it has a strong robustness against this parameter deviation. Therefore, the application of TDO to MPC has been proved to be a feasible and effective solution to reduce the system complexity and improve system dynamics.

- **Chapter 7** has introduced to ways of weighting factor-less FCS-PTC control strategies: sequential FCS-PTC and parallel FCS-PTC. In order to realize optimized torque and flux control by changing the cost functions' execution sequences online, a sequential FCS-PTC with self-adjustive control priority has been proposed and compared with the existing sequential FCS-PTC. Moreover, based on the reduced FCS-MPCs in chapter 5, three variations of weighting factor-less parallel FCS-PTCs have been proposed and tested.

Simulations and experiments have confirmed that both sequential and parallel FCS-PTCs work satisfactorily as expected. Therefore, the real meaning of FCS-MPC without weighting factor weighting factors in the cost function is achieved with the proposed methods, which significantly simplify the tuning work of the FCS-PTCs.

To conclude, according to the experimental results, all goals in chapter 2 have been achieved by the work in the dissertation. As is implied by the title of this work, it has fulfilled the gap on further studying MPC's applications on electric drive systems in depth and on the proposal of several extensive considerations and solutions for model predictive control.

8.2 Future Work

Several topics have been found as the future research directions as the extension of the topics discussed in this work and in the further considerations for MPCs' application to electric drives:

- **Calculation redundancy reduction/elimination.** For the increased FCS-MPC, the calculation effort is still the main problem. Further research should be the introduction of redundancy minimizing strategies such as those interdisciplinary algorithms for artificial intelligent, such as ant colony optimization and grey wolf optimization.
- **Improved disturbance observer.** Since the DO proposed in this work is only capable for torque disturbance's inhibition, more DO or more integrated DO with higher multiple disturbances inhibition potential should be designed and implemented. One possibility is to introduce a DO that can also remove the P parameter even require no extra parameter to be tuned.
- **Parameters identification.** For all model based predictive control strategies, the control variables thus the control performance is more or less sensitive to machine parameters' deviations, as shown in the previous chapters, in which most system is sensitive to L_s variations. Therefore, better robustness should be achieved through the online parameters identification.
- **Long horizon MPC.** Based on the existing methods on single step MPC, and with comparatively precise machine parameters, long horizon MPC should be applied to further improve system prediction range and control precision and system performance.

APPENDIX A

Nomenclature

General remark:

Scalars are italic letters:	x
Vectors are bold lower case letters:	\mathbf{x}
Matrices are bold upper case letters:	\mathbf{X}
References are marked with a star superscript:	x^*
Rated values are marked with a star subscript:	x_{nom}
Predictions are marked with a hat superscript: \hat{x}	
Time derivation: $\frac{dx}{dt}$ or \dot{x}	
Coordinate variable components are with a-b-c, α - β or d-q subscript:	$x_a, x_b, x_c, x_\alpha, x_\beta, x_d, x_q$

Symbols and parameters:

x	State vector
u	Input vector
y	Output vector
A	State matrix
B	Input matrix
C	Output matrix
a, b, c	Phases
α, β	Equivalent two-phase coordinates
j	$\sqrt{-1}$
v	Voltage
i	Current

R	Resistor
C	Capacitor
L	Inductor
J	Inertia
t	Time (continuous)
k	Time (discrete, current sample)
T_s	Sampling time

Machine variables and control coefficients:

v_s, v_r	Stator and rotor voltage
i_s, i_r	Stator and rotor current
ψ_s, ψ_r	Stator and rotor flux
ω_e	Electrical machine speed
ω_m	Mechanical machine speed
T_e	Electromagnetic torque
T_l	Mechanical load torque
p	Number of pole pairs
R_s, R_r	Stator and rotor resistance
L_s, L_r	Stator and rotor inductance
L_m	Mutual inductance
S_x/\bar{S}_x	Switching state of phase x upper/lower arm
λ_g	Weighting factor
λ_T	Observer gain
$\varepsilon T, \varepsilon \psi$	Error band width values of torque and flux

Acronyms:

AC	alternative current
AD	analog to digital
ASM	asynchronous machine
CPLD	complex programmable logic device
CSI	current source inverter
DA	digital to analog
DB	deadbeat
DC	direct current
DMTC	direct mean torque control
DO	disturbance observer
DSP	digital signals processor
DTC	direct torque control

EMF	electromotive field
FCS	finite control set
FOC	field oriented control
FPGA	field programmable gate array
FS	Finite Set
GPC	genetic predictive control
IFCS	increased-finite-control-set
IGBT	insulated gate bipolar transistor
IM	induction machine
IPMSM	interior permanent magnet synchronous machine
ISS	input to state stability
LM	linear motor
LUT	look-up-table
MCU	micro control unit
MMF	magnetomotive force
MPC	model predictive controls
MTPA	maximum torque per Ampere
OPA	operational amplifiers
PC	predictive control
PCC	predictive current control
PID	proportional–integral–derivative
PMPC	Parallel FCS-MPC
PTC	predictive torque control
PWM	pulse width modulator
RFCS	reduced-finite-control-set
SMPC	sequential FCS-MPC
SPMSM	surface-mounted permanent magnet synchronous machine
SPWM	sinusoidal pulse width modulation
SRM	switched reluctance motors
SVM	space vector modulation
THD	total harmonics distortion
VSI	voltage source inverter
VSP	varying-switching-point
VV	voltage vector

APPENDIX B

Pseudo Codes

Pseudo Codes of Sub-sector And RFCS Decision for Deadbeat Double RFCS-PCC:

Table B.1: Pseudo Codes of Sub-sector And RFCS Decision for Deadbeat Double RFCS-PCC (corresponding to figure 5.31)

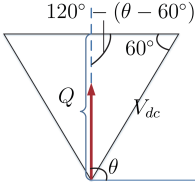
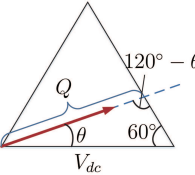
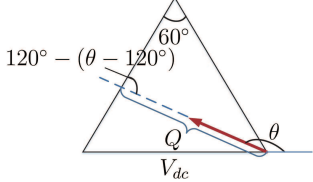
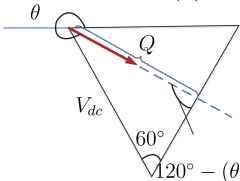
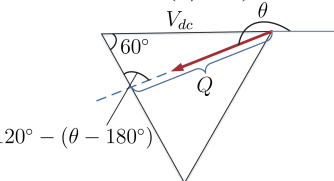
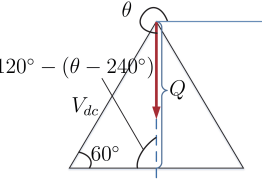
if sector (1)-II:	if sector (3)-I:	if sector (5)-III:
if $\theta^* > 0$ subsector II ₁ :V ₂ , V ₀ else subsector II ₂ :V ₃ , V ₀	if $\theta^* < \frac{\pi}{6}$ subsector I ₁ :V ₁ , V ₀ else subsector I ₁ :V ₂ , V ₀	if $\theta^* < -\frac{\pi}{6}$ subsector III ₁ :V ₃ , V ₀ else subsector III ₁ :V ₄ , V ₀
if sector (2)-VI:	if sector (4)-IV:	if sector (6) V:
if $\theta^* < -\frac{\pi}{6}$ subsector VI ₁ :V ₆ , V ₀ else subsector VI ₂ : V ₁ , V ₀	if $\theta^* < \frac{\pi}{6}$ subsector IV ₁ :V ₄ , V ₀ else subsector IV ₂ :V ₅ , V ₀	if $\theta^* < 0$ subsector V ₁ :V ₅ , V ₀ else subsector V ₂ :V ₆ , V ₀

Pseudo Codes of Deadbeat Null RFCS-PCC and Calculation of H :

Table B.2: Pseudo Codes of VV Decision for Deadbeat Null RFCS-PCC (corresponding to figure 5.46) and Rough H Calculation

<p>if sector (1)-II:</p> <p>if $\theta^* > 0$ $\theta_0 = \theta^*$ else $\theta_0 = \theta^* + \pi$ end $H = V_{dc} \cdot \frac{\sin(\pi/3)}{\sin\theta_0}$ if $V^* < \frac{H}{2}$ $V_{out} = V_0$ else if $\theta^* > 0$ $V_{out} = V_2$ else $V_{out} = V_3$ end end end</p>	<p>if sector (3)-I:</p> <p>$\theta_0 = \theta^*$ $H = V_{dc} \cdot \frac{\sin(\pi/3)}{\sin(\frac{2\pi}{3}-\theta_0)}$ if $V^* < \frac{H}{2}$ $V_{out} = V_0$ else if $\theta^* < \frac{\pi}{6}$ $V_{out} = V_1$ else $V_{out} = V_2$ end end</p>	<p>if sector (5)-III:</p> <p>$\theta_0 = \theta^* + \pi$ $H = -V_{dc} \cdot \frac{\sin(\pi/3)}{\sin(\frac{2\pi}{3}+\theta_0)}$ if $V^* < \frac{H}{2}$ $V_{out} = V_0$ else if $\theta^* < -\frac{\pi}{6}$ $V_{out} = V_3$ else $V_{out} = V_4$ end end</p>
<p>if sector (2)-VI:</p> <p>$\theta_0 = \theta^* + 2\pi$ $H = V_{dc} \cdot \frac{\sin(\pi/3)}{\sin(\frac{2\pi}{3}-\theta_0)}$ if $V^* < \frac{H}{2}$ $V_{out} = V_0$ else if $\theta^* < -\frac{\pi}{6}$ $V_{out} = V_6$ else $V_{out} = V_1$ end end</p>	<p>if sector (4)-IV:</p> <p>$\theta_0 = \theta^* + \pi$ $H = -V_{dc} \cdot \frac{\sin(\pi/3)}{\sin(\frac{2\pi}{3}+\theta_0)}$ if $V^* < \frac{H}{2}$ $V_{out} = V_0$ else if $\theta^* < -\frac{\pi}{6}$ $V_{out} = V_4$ else $V_{out} = V_5$ end end</p>	<p>if sector (6) V:</p> <p>if $\theta^* > 0$ $\theta_0 = \theta^* + \pi$ else $\theta_0 = \theta^* + 2\pi$ end $H = -V_{dc} \cdot \frac{\sin(\pi/3)}{\sin\theta_0}$ if $V^* < \frac{H}{2}$ $V_{out} = V_0$ else if $\theta^* < 0$ $V_{out} = V_5$ else $V_{out} = V_6$ end end</p>

Table B.3: Pseudo Codes of Precise H (for clarity, it is renamed as 'Q') Calculation for Deadbeat Null RFCS-PCC (corresponding to figure 5.48)

<p>if sector (1)-II:</p> $\frac{Q}{\sin(\pi/3)} = \frac{V_{dc}}{\sin(2\pi/3 - (\theta - \pi/3))}$ $\Rightarrow Q = \frac{V_{dc} \cdot \sin(\pi/3)}{\sin\theta}$ 	<p>if sector (3)-I:</p> $\frac{Q}{\sin(\pi/3)} = \frac{V_{dc}}{\sin(2\pi/3 - \theta)}$ $\Rightarrow Q = \frac{V_{dc} \cdot \sin(\pi/3)}{\sin(2\pi/3 - \theta)}$ 	<p>if sector (5)-III:</p> $\frac{Q}{\sin(\pi/3)} = \frac{V_{dc}}{\sin(2\pi/3 - (\theta - 2\pi/3))}$ $\Rightarrow Q = -\frac{V_{dc} \cdot \sin(\pi/3)}{\sin(2\pi/3 + \theta)}$ 
<p>if sector (2)-VI:</p> $\frac{Q}{\sin(\pi/3)} = \frac{V_{dc}}{\sin(2\pi/3 - (\theta - 5\pi/3))}$ $\Rightarrow Q = -\frac{V_{dc} \cdot \sin(\pi/3)}{\sin(\pi/3 - \theta)}$ 	<p>if sector (4)-IV:</p> $\frac{Q}{\sin(\pi/3)} = \frac{V_{dc}}{\sin(2\pi/3 - (\theta - \pi))}$ $\Rightarrow Q = -\frac{V_{dc} \cdot \sin(\pi/3)}{\sin(\pi/3 + \theta)}$ 	<p>if sector (6) V:</p> $\frac{Q}{\sin(\pi/3)} = \frac{V_{dc}}{\sin(2\pi/3 - (\theta - 2\pi/3))}$ $\Rightarrow Q = -\frac{V_{dc} \cdot \sin(\pi/3)}{\sin\theta}$ 

APPENDIX C

List of Publications

Journal Publications:

- F. Wang, S. Li, **X. Mei**, W. Xie, J. Rodríguez and R. M. Kennel, "Model-Based Predictive Direct Control Strategies for Electrical Drives: An Experimental Evaluation of PTC and PCC Methods," in IEEE Transactions on Industrial Informatics, vol. 11, no. 3, pp. 671-681, June 2015.
- F. Wang, **X. Mei**, P. Tao, R. Kennel and J. Rodriguez, "Predictive field-oriented control for electric drives," in Chinese Journal of Electrical Engineering, vol. 3, no. 1, pp. 73-78, 2017.
- F. Wang, **X. Mei**, J. Rodriguez and R. Kennel, "Model predictive control for electrical drive systems-an overview," in CES Transactions on Electrical Machines and Systems, vol. 1, no. 3, pp. 219-230, September 2017.

Conference Papers:

- **X. Mei**, F. Wang, Anjun Xia, Z. Ma, Zhenbin Zhang and R. Kennel, "Predictive current control of an induction machine by using dichotomy-based method," 2016 IEEE 8th International Power Electronics and Motion Control Conference (IPEMC-ECCE Asia), Hefei, 2016, pp. 3368-3373.
- **X. Mei**, F. Wang and R. Kennel, "A circular dichotomy-based method for model predictive control with fixed switching frequency for electric drives," IECON 2016 - 42nd Annual Conference of the IEEE Industrial Electronics Society, Florence, 2016, pp. 2594-2599.

- **X. Mei**, F. Wang and R. Kennel, "Deadbeat Boolean logic predictive current control for induction machine without cost function," IECON 2016 - 42nd Annual Conference of the IEEE Industrial Electronics Society, Florence, 2016, pp. 4331-4336.
- **X. Mei**, X. Lu, A. Davari, E. A. Jarchlo, F. Wang and R. Kennel, "Torque disturbance observer based model predictive control for electric drives," 2018 9th Annual Power Electronics, Drives Systems and Technologies Conference (PEDSTC), Tehran, 2018, pp. 499-504.
- **X. Mei**, R. Zu, F. Wang and R. Kennel, "Variable Cost Functions' Sequence Design for Model Predictive Control of IPMSM without Weighting Factor," 2018 IEEE International Conference on Information and Automation(ICIA), Wuyishan, 2018.
- F. Wang, **X. Mei**, H. Dai, S. Yu and P. He, "Sensorless finite control set predictive current control for an induction machine," 2015 IEEE International Conference on Information and Automation(ICIA), Lijiang, 2015, pp. 3106-3111.
- F. Wang, **X. Mei** and Z. Zhang, "Sensorless predictive control for an induction machine," 2016 IEEE International Conference on Information and Automation (ICIA), Ningbo, 2016, pp. 1320-1324.
- P. Tao, F. Wang, **X. Mei** and J. Lin, "PLL with Piecewise Judgement Function for SMO Beased Sensorless Control of PMSM," 2017 5th International Conference on Enterprise Systems (ES), Beijing, 2017, pp. 190-194.
- Z. Li, D. Ke, G. Hu, **X. Mei** and F. Wang, "Research on speed and torque parameter adaptive control system of permanent magnet synchronous motor," 2017 2nd International Conference on Robotics and Automation Engineering (ICRAE), Shanghai, 2017, pp. 311-316.
- G. Hu, A. Xia, Z. Li, **X. Mei** and F. Wang, "Research on injection molding machine drive system based on model predictive control," 2017 2nd International Conference on Robotics and Automation Engineering (ICRAE), Shanghai, 2017, pp. 161-167.

List of Figures

1.1	Close Loop Control System for Electrical Machine	3
2.1	Space-vector notation of three-phase currents	5
2.2	Space-vector notation of two-phase currents	6
2.3	Squirrel-cage induction machine model	8
2.4	Surface-Mounted Permanent Magnet Synchronous Machine	9
2.5	Interior Permanent Magnet Synchronous Machine	10
2.6	Three-phase Two-level VSI.	11
2.7	Voltage Vectors for VSI.	12
2.8	FOC Block Diagram.	13
2.9	DTC Block Diagram.	16
2.10	Determination of the DTC lookup table for sector 1	18
2.11	General Block Diagram of MPC for Electric Drives.	20
2.12	Test Bench.	21
3.1	Time Order and Compensation of FCS-MPC.	28
3.2	FCS-PTC for IPMSM.	29
3.3	Simulation: IPMSM Rated speed start up and reversal under FCS-PTC.	31
3.4	Simulation: IPMSM Torque and Flux Tracking Performance under FCS-PTC.	31
3.5	Simulation: IPMSM FCS-PTC Performance under Torque Variations.	32
3.6	Simulation: IPMSM Torque and Voltage Vectors of FCS-PTC under Torque Variations.	33
3.7	Simulation: IPMSM FCS-PTC performance with R_s Variations.	34
3.8	Simulation: IPMSM FCS-PTC performance with L_d Variations.	34
3.9	Simulation: IPMSM FCS-PTC performance with L_q Variations.	35
3.10	Experiment: SPMSM Rated speed startup and reversal under FCS-PTC.	35

3.11 Experiment: SPMSM Torque and Flux Tracking Performance under FCS-PTC.	36
3.12 Experiment: SPMSM FCS-PTC Performance under Torque Variations.	36
3.13 Experiment: SPMSM FCS-PTC Performance under R_s Variation.	37
3.14 Experiment: SPMSM FCS-PTC Performance under L_s Variation.	37
3.15 Experiment: SPMSM FCS-PTC Performance under ψ_{pm} Variation.	38
3.16 FCS-PCC for IPMSM.	39
3.17 Simulation: Rated speed start up and reversal of FCS-PCC.	40
3.18 Simulation: Current Tracking Performance of FCS-PCC.	41
3.19 Simulation: FCS-PCC Performance under Torque Variations.	41
3.20 Simulation: Torque and Voltage Vectors of FCS-PCC under Torque Variations.	42
3.21 Simulation: FCS-PCC performance with R_s Variations.	42
3.22 Simulation: FCS-PCC performance with L_d Variations.	43
3.23 Simulation: FCS-PCC performance with L_q Variations.	43
3.24 Experiment: Rated speed startup and reversal of FCS-PCC.	44
3.25 Experiment: Current Tracking Performance of FCS-PCC.	44
3.26 Experiment: FCS-PCC Performance under Torque Variations.	45
3.27 Experiment: FCS-PCC Performance under R_s Variation.	45
3.28 Experiment: FCS-PCC Performance under L_s Variation.	46
3.29 Experiment: FCS-PCC Performance under ψ_{pm} Variation.	46
3.30 DBPCC.	47
3.31 Simulation: Rated speed start up and reversal of DBPCC.	48
3.32 Simulation: DBPCC Performance under Torque Variations.	49
3.33 Simulation: Torque and Voltage Vectors of DBPCC under Torque Variations.	49
3.34 Simulation: DBPCC performance with R_s Variations.	50
3.35 Simulation: DBPCC performance with L_d Variations.	50
3.36 Simulation: DBPCC performance with L_q Variations.	51
3.37 Experiment: Rated speed start up and reversal of DBPCC.	51
3.38 Experiment: Stator Reference Voltages during speed deceleration of DBPCC.	52
3.39 Experiment: DBPCC Performance under Torque Variations.	52
3.40 Experiment: DBPCC Performance under R_s Variation.	53
3.41 Experiment: DBPCC Performance under L_s Variation.	53
3.42 Experiment: DBPCC Performance under ψ_{pm} Variation.	54
3.43 Analysis of FCS-PTC,FCS-PCC and DBPCC.	55
4.1 Dichotomy-based IFCS-PCC for IPMSM.	58

4.2	One iteration of the fan dichotomy-based IFCS-MPC's reference voltage vector selection.	59
4.3	One iteration of the circular dichotomy-based IFCS-MPC's reference voltage vector selection.	61
4.4	Simulation: Rated speed start up and reversal of Dichotomy-based IFCS-PCC for IPMSM.	62
4.5	Simulation: Current Tracking of Dichotomy-based IFCS-PCC for IPMSM	63
4.6	Simulation: Dichotomy-based IFCS-PCC Performance for IPMSM under Torque Variations.	64
4.7	Simulation: Dichotomy-based IFCS-PCC performance for IPMSM with Rs Variations.	65
4.8	Simulation: Dichotomy-based IFCS-PCC performance for IPMSM with Ld Variations.	66
4.9	Simulation: Dichotomy-based IFCS-PCC performance for IPMSM with Lq Variations.	67
5.1	Vector Selection of Dichotomy-based RFCS-MPC	70
5.2	Simulation: Rated speed startup and reversal of Dichotomy-based RFCS-PCC.	71
5.3	Simulation: Current Tracking Performance of Dichotomy-based RFCS-PCC.	71
5.4	Simulation: Dichotomy-based RFCS-PCC Performance under Torque Variations.	72
5.5	Simulation: Torque and Voltage Vectors of Dichotomy-based RFCS-PCC under Torque Variations.	72
5.6	Simulation: Dichotomy-based RFCS-PCC performance with Rs Variations.	73
5.7	Simulation: Dichotomy-based RFCS-PCC performance with Ld Variations.	73
5.8	Simulation: Dichotomy-based RFCS-PCC performance with Lq Variations.	73
5.9	Switching states transitions for 2-level 3-phase VSI.	74
5.10	Simulation: Rated speed start up and reversal of Switching-minimized RFCS-PCC.	75
5.11	Simulation: Current Tracking Performance of Switching-minimized RFCS-PCC.	75
5.12	Simulation: Switching-minimized RFCS-PCC Performance under Torque Variations.	76
5.13	Simulation: Torque and Voltage Vectors of Switching-minimized RFCS-PCC under Torque Variations.	76
5.14	Simulation: Switching-minimized RFCS-PCC performance with Rs Variations.	77

5.15 Simulation: Switching-minimized RFCS-PCC performance with Ld Variations.	77
5.16 Simulation: Switching-minimized RFCS-PCC performance with Lq Variations.	77
5.17 Vector Sector Location for Deadbeat Triple RFCS-PCC.	79
5.18 Simulation: Rated speed start-up and reversal of Deadbeat Triple RFCS-PCC.	80
5.19 Simulation: Current Tracking Performance of Deadbeat Triple RFCS-PCC.	80
5.20 Simulation: Deadbeat Triple RFCS-PCC Performance under Torque Variations.	81
5.21 Simulation: Torque and Voltage Vectors of Deadbeat Triple RFCS-PCC under Torque Variations.	81
5.22 Simulation: Deadbeat Triple RFCS-PCC performance with Rs Variations.	81
5.23 Simulation: Deadbeat Triple RFCS-PCC performance with Ld Variations.	82
5.24 Simulation: Deadbeat Triple RFCS-PCC performance with Lq Variations.	82
5.25 Experiment: Rated speed start-up and reversal of Deadbeat Triple RFCS-PCC.	83
5.26 Experiment: Current Tracking Performance of Deadbeat Triple RFCS-PCC.	83
5.27 Experiment: Deadbeat Triple RFCS-PCC Performance under Torque Variations.	84
5.28 Experiment: Deadbeat Triple RFCS-PCC Performance under Rs Variation.	84
5.29 Experiment: Deadbeat Triple RFCS-PCC Performance under Ls Variation.	85
5.30 Experiment: Deadbeat Triple RFCS-PCC Performance under ψ_{pm} Variation.	85
5.31 Hexagon of reference voltage vector selection for Deadbeat Double RFCS-PCC.	86
5.32 Flowchart of Deadbeat Double RFCS-PCC.	87
5.33 Simulation: Rated speed start up and reversal of Deadbeat Double RFCS-PCC.	88
5.34 Simulation: Current Tracking Performance of Deadbeat Double RFCS-PCC.	88
5.35 Simulation: Deadbeat Double RFCS-PCC Performance under Torque Variations.	89
5.36 Simulation: Torque and Voltage Vectors of Deadbeat Double RFCS-PCC under Torque Variations.	89

5.37 Simulation: Deadbeat Double RFCS-PCC performance with R_s Variations.	90
5.38 Simulation: Deadbeat Double RFCS-PCC performance with L_d Variations.	90
5.39 Simulation: Deadbeat Double RFCS-PCC performance with L_q Variations.	90
5.40 Experiment: Rated speed start-up and reversal of Deadbeat Double RFCS-PCC.	91
5.41 Experiment: Current Tracking Performance of Deadbeat Double RFCS-PCC.	91
5.42 Experiment: Deadbeat Double RFCS-PCC Performance under Torque Variations.	92
5.43 Experiment: Deadbeat Double RFCS-PCC Performance under R_s Variation.	92
5.44 Experiment: Deadbeat Double RFCS-PCC Performance under L_s Variation.	93
5.45 Experiment: Deadbeat Double RFCS-PCC Performance under ψ_{pm} Variation.	93
5.46 Hexagon of reference voltage vector selection for Deadbeat Null RFCS-PCC.	94
5.47 Flowchart of Deadbeat Null RFCS-PCC.	95
5.48 H approximation with V_{dc}	95
5.49 Simulation: Rated speed start-up and reversal of Deadbeat Null RFCS-PCC.	96
5.50 Simulation: Deadbeat Null RFCS-PCC Performance under Torque Variations.	97
5.51 Simulation: Torque and Voltage Vectors of Deadbeat Null RFCS-PCC under Torque Variations.	98
5.52 Simulation: Deadbeat Null RFCS-PCC performance with R_s Variations.	99
5.53 Experiment: Deadbeat Null RFCS-PCC performance with L_d Variations.	100
5.54 Deadbeat Null RFCS-PCC performance with L_q Variations.	101
5.55 Experiment: Rated speed start up and reversal of Deadbeat Null RFCS-PCC.	102
5.56 Experiment: Deadbeat Null RFCS-PCC Performance under Torque Variations.	103
5.57 Experiment: Deadbeat Null RFCS-PCC performance with R_s Variations.	104
5.58 Experiment: Deadbeat Null RFCS-PCC performance with L_s Variations.	105

5.59	Experiment: Deadbeat Null RFCS-PCC performance with ψ_{pm} Variations.	106
5.60	Analysis of FCS-PCC (7-PCC), Dichotomy-based RFCS-PCC (5-PCC), Switching-minimized RFCS-PCC (4-PCC), Deadbeat Triple RFCS-PCC (3-PCC), Deadbeat Double RFCS-PCC (2-PCC), Deadbeat Null RFCS-PCC (0-PCC) and its $H = V_{dc}$ approximated method (0H-PCC).	107
6.1	DO.	110
6.2	DBPCC drive system for IPMSM with TDO.	113
6.3	Simulation: low speed torque performance of DBPCC with TDO for IPMSM (values of λ_T are shown in figures).	114
6.4	Experiment: low speed torque performance of DBPCC with TDO for SPMSM (black: $\lambda_T = 0$, violet: $\lambda_T = -0.5$, blue: $\lambda_T = -1$).	114
6.5	Simulation: high speed torque performance of DBPCC with TDO for IPMSM (values of λ_T are shown in figures).	116
6.6	Experiment: high speed torque performance of DBPCC with TDO for SPMSM (black: $\lambda_T = 0$, violet: $\lambda_T = -0.5$, blue: $\lambda_T = -1$).	116
6.7	Simulation: Speed variations to different TDO coefficients and speeds of DBPCC for IPMSM.	117
6.8	Simulation: Speed variations to different TDO coefficients and torques of DBPCC for IPMSM.	117
6.9	Simulation: Varying torque tracking performance with different λ_T values in TDO of DBPCC for IPMSM.	118
6.10	Simulation: System performance with random noises in torque in TDO of DBPCC for IPMSM.	119
6.11	PTC drive system for IPMSM with TDO.	120
6.12	FCS-PTC drive system for IPMSM with TDO.	122
6.13	Simulation: speed reversal performance under FCS-PTC with TDO for IPMSM. (From top to down:rotor speed, electromagnetic torque, stator phase A current and stator flux.)	123
6.14	Experiment: speed reversal performance under FCS-PTC with TDO for SPMSM. (From top to down:rotor speed, electromagnetic torque, stator phase A current and stator flux.)	124
6.15	Simulation: torque rejection performances under FCS-PTC with/without TDO for IPMSM.	125
6.16	Experiment: torque rejection performances under FCS-PTC with/without TDO for SPMSM.	126
6.17	Simulation: system performance with random noises in torque under FCS-PTC for IPMSM. (blue: system without TDO. black: system with TDO.)	127

6.18	Simulation: switching frequency minimized system performance with random noises in torque under FCS-PTC for IPMSM.(blue: system without TDO. black: system with TDO.)	127
6.19	Simulation: system robustness test against parameter deviation with sharp changes of inertia.	128
6.20	Simulation: both FCS-PCC systems' analysis with random noises in torque with/without TDO.	129
7.1	Sequential PTC for IM.	132
7.2	LUT based Sequential PTC for IM with varying control sequence.	134
7.3	Flowchart of LUT based Sequential PTC for IM with varying control sequence.	135
7.4	Simulation: Rated speed start-up and reversal of conventional Sequential FCS-PTC and Sequential FCS-PTC with Varying Control Sequence for IM.	137
7.5	Simulation: Decisions of control sequence for Sequential FCS-PTC with Varying Control Sequence. (1/0: torque/flux cost function is executed first)	138
7.6	Simulation: Torque and Flux Tracking Performance of conventional Sequential FCS-PTC and Sequential FCS-PTC with Varying Control Sequence for IM.	138
7.7	Simulation: Conventional Sequential FCS-PTC and Sequential FCS-PTC with Varying Control Sequence's Performances for IM under Torque Variations.	139
7.8	Experiment: Conventional Sequential FCS-PTC and Sequential FCS-PTC with Varying Control Sequence for IM under load variations.	140
7.9	Experiment: Expectations' influences on torque standard deviation.	141
7.10	Experiment: Expectations' influences on stator current THD.	141
7.11	Experiment: Torque standard deviation and current THD under different speed operations.	141
7.12	Experiment: Current THD and average switching frequency under different load conditions.	142
7.13	Parallel FCS-PTC.	143
7.14	Optimization Principles for Full Control Set of PPTC.	144
7.15	Simulation: Rated speed start-up and reversal of conventional FCS-PTC and Full-Vectors Parallel FCS-PTC for IM.	146
7.16	Simulation: Torque and Flux Tracking Performance of conventional FCS-PTC and Full-Vectors Parallel FCS-PTC for IM.	147
7.17	Simulation: Conventional FCS-PTC and Full-Vectors Parallel FCS-PTC Performance for IM under Torque Variations.	148
7.18	Experiment: Rated speed start-up and reversal of conventional FCS-PTC and Full-Vectors Parallel FCS-PTC for SPMSM.	149

7.19	Experiment: Conventional FCS-PTC and Full-Vectors Parallel FCS-PTC Performance for SPMSM under Torque Variations.	150
7.20	Experiment: Conventional FCS-PTC and Full-Vectors Parallel FCS-PTC Performance for SPMSM under Torque Control Mode. . .	151
7.21	Experiment: Full-Vectors Parallel RFCS-PTC Performance for SPMSM under R_s Variation.	152
7.22	Experiment: Full-Vectors Parallel RFCS-PTC Performance for SPMSM under ψ_{pm} Variation.	153
7.23	Optimization Principles for Control Set of Deadbeat Triple PPTC. .	154
7.24	Simulation: Rated speed start-up and reversal of Deadbeat Triple Parallel RFCS-PTC for IM.	155
7.25	Simulation: Current Tracking Performance of Deadbeat Triple Parallel RFCS-PTC for IM.	155
7.26	Simulation: Deadbeat Triple Parallel RFCS-PTC Performance under Torque Variations for IM.	156
7.27	Experiment: Rated speed start up and reversal of Deadbeat Triple Parallel RFCS-PTC for SPMSM.	156
7.28	Experiment: Deadbeat Triple Parallel RFCS-PTC Performance under Torque Variations for SPMSM.	157
7.29	Experiment: Deadbeat Triple Parallel RFCS-PTC Performance for SPMSM under Torque Control Mode.	157
7.30	Experiment: Deadbeat Triple Parallel RFCS-PTC Performance under R_s Variation for SPMSM.	158
7.31	Experiment: Deadbeat Triple Parallel RFCS-PTC Performance under ψ_{pm} Variation for SPMSM.	158
7.32	Optimization Principles for Control Set of Deadbeat Double PPTC.	159
7.33	Simulation: Rated speed start up and reversal of Deadbeat Double Parallel RFCS-PTC for IM.	160
7.34	Simulation: Current Tracking Performance of Deadbeat Double Parallel RFCS-PTC for IM.	160
7.35	Simulation: Deadbeat Double Parallel RFCS-PTC Performance for IM under Torque Variations.	161
7.36	Experiment: Rated speed start up and reversal of Deadbeat Double Parallel RFCS-PTC for SPMSM.	161
7.37	Experiment: Deadbeat Double Parallel RFCS-PTC Performance for SPMSM under Torque Variations.	162
7.38	Experiment: Deadbeat Double Parallel RFCS-PTC Performance for SPMSM under Torque Control Mode.	162
7.39	Experiment: Deadbeat Double Parallel RFCS-PTC Performance under R_s Variation for SPMSM.	163
7.40	Experiment: Deadbeat Double Parallel RFCS-PTC Performance under ψ_{pm} Variation for SPMSM.	163

List of Tables

2.1	Voltages for Different Switching States	12
2.2	Lookup table for DTC	17
2.3	Data of Eletrical Drive Systems.	22
3.1	Classification of Predictive Controls for Electric Drives.	25
3.2	Comparison of FCS-PTC/PCC and DBPCC.	56
6.1	Statistic Analysis of Variables for Different λ_T	118
7.1	Cost function executive order decision-making LUT.	133
B.1	Pseudo Codes of Sub-sector And RFCS Decision for Deadbeat Double RFCS-PCC (corresponding to figure 5.31)	173
B.2	Pseudo Codes of VV Decision for Deadbeat Null RFCS-PCC (corresponding to figure 5.46) and Rough H Calculation	174
B.3	Pseudo Codes of Precise H (for clarity, it is renamed as 'Q') Calculation for Deadbeat Null RFCS-PCC (corresponding to figure 5.48)	175

Bibliography

- [1] Hasse, *Control of Electrical Drives*. Berlin: Springer-Verlag, 1996.
- [2] J. Holtz, "Pulsewidth modulation for electronic power conversion," *Proceedings of the IEEE*, vol. 82, no. 8, pp. 1194–1214, Aug 1994.
- [3] F. Blaschke, "The principle of field orientation as applied to the new transvector closed-loop control system for rotating machines," vol. 39, no. 5. Siemens Review, 1972.
- [4] J. Holtz, "Proceedings of 1994 ieee international symposium on industrial electronics (isie'94)," May 1994, pp. 1–6.
- [5] T. A. Lipo, *Vector Control and Dynamics of AC Drives*. Oxford University Press, 1996, vol. 41.
- [6] W. Leonhard, *Control of Electrical Drives*. Springer-Verlag New York, Inc., 1996.
- [7] A. Trzynadlowski, *Control of Induction Motors*. Academic Press, 2001.
- [8] B. K. Bose, "The past, present, and future of power electronics [guest introduction]," *IEEE Industrial Electronics Magazine*, vol. 3, no. 2, pp. 7–11, 14, June 2009.
- [9] P. Vas, *Sensorless Vector and Direct Torque Control*. Oxford University Press, 1998.
- [10] M. Preindl and E. Schartz, "Sensorless model predictive direct current control using novel second-order pll observer for pmsm drive systems," *IEEE Transactions on Industrial Electronics*, vol. 58, no. 9, pp. 4087–4095, Sept 2011.
- [11] S. A. Davari, D. A. Khaburi, F. Wang, and R. M. Kennel, "Using full order and reduced order observers for robust sensorless predictive torque control of induction motors," *IEEE Transactions on Power Electronics*, vol. 27, no. 7, pp. 3424–3433, July 2012.
- [12] D. Stando and M. P. Kazmierkowski, "Novel speed sensorless dtc-svm scheme for induction motor drives," in *2013 International Conference-Workshop Compatibility And Power Electronics*, June 2013, pp. 225–230.
- [13] L. Yacoubi, K. Al-Haddad, L. Dessaint, and F. Fnaiech, "Linear and nonlinear control techniques for a three-phase three-level npc boost rectifier," *IEEE*

- Transactions on Industrial Electronics*, vol. 53, no. 6, pp. 1908–1918, Dec 2006.
- [14] R. Dian, W. Xu, J. Zhu, D. Hu, and Y. Liu, “An improved speed sensorless control strategy for linear induction machines based on extended state observer for linear metro drives,” *IEEE Transactions on Vehicular Technology*, vol. 67, no. 10, pp. 9198–9210, Oct 2018.
- [15] M. Depenbrock, “Direct self-control (dsc) of inverter-fed induction machine,” *IEEE Transactions on Power Electronics*, vol. 3, no. 4, pp. 420–429, Oct 1988.
- [16] I. Takahashi and T. Noguchi, “A new quick-response and high-efficiency control strategy of an induction motor,” *IEEE Transactions on Industry Applications*, vol. IA-22, no. 5, pp. 820–827, Sept 1986.
- [17] I. Takahashi and Y. Ohmori, “High-performance direct torque control of an induction motor,” *IEEE Transactions on Industry Applications*, vol. 25, no. 2, pp. 257–264, March 1989.
- [18] F. U. Syed, M. L. Kuang, M. Smith, S. Okubo, and H. Ying, “Fuzzy gain-scheduling proportional–integral control for improving engine power and speed behavior in a hybrid electric vehicle,” *IEEE Transactions on Vehicular Technology*, vol. 58, no. 1, pp. 69–84, Jan 2009.
- [19] G.-J. Wang, C.-T. Fong, and K. J. Chang, “Neural-network-based self-tuning pi controller for precise motion control of pmac motors,” *IEEE Transactions on Industrial Electronics*, vol. 48, no. 2, pp. 408–415, April 2001.
- [20] A. Rubaai and P. Young, “EKF-based pi-/pd-like fuzzy-neural-network controller for brushless drives,” *IEEE Transactions on Industry Applications*, vol. 47, no. 6, pp. 2391–2401, Nov 2011.
- [21] R. Shahnazi, H. M. Shانهchi, and N. Pariz, “Position control of induction and dc servomotors: A novel adaptive fuzzy pi sliding mode control,” *IEEE Transactions on Energy Conversion*, vol. 23, no. 1, pp. 138–147, March 2008.
- [22] P. K. Singh, Y. V. Hote, and M. M. Garg, “Comments on “pi and sliding mode control of a cuk converter”,” *IEEE Transactions on Power Electronics*, vol. 29, no. 3, pp. 1551–1552, March 2014.
- [23] R. Kennel, A. Linder, and M. Linke, “Generalized predictive control (gpc)-ready for use in drive applications?” in *2001 IEEE 32nd Annual Power Electronics Specialists Conference (IEEE Cat. No.01CH37230)*, vol. 4, June 2001, pp. 1839–1844 vol. 4.
- [24] S. A. Davari, F. Wang, and R. M. Kennel, “Robust deadbeat control of an induction motor by stable mras speed and stator estimation,” *IEEE Transactions on Industrial Informatics*, vol. 14, no. 1, pp. 200–209, Jan 2018.
- [25] J. S. Lee and R. D. Lorenz, “Deadbeat direct torque and flux control of ipmsm drives using a minimum time ramp trajectory method at voltage and current limits,” *IEEE Transactions on Industry Applications*, vol. 50, no. 6, pp. 3795–3804, Nov 2014.
- [26] M. Morari and J. H. Lee, “Model predictive control: Past, present and future,” *Comp. Chem. Eng.*, vol. 24, p. 667–682, 1999.

- [27] J. H. Lee, "Model predictive control: Review of the three decades of development," *Int. J. Contr. Autom. Syst.*, vol. 9, no. 3, p. 415–424, 2011.
- [28] M. Preindl and S. Bolognani, "Model predictive direct torque control with finite control set for pmsm drive systems, part 1: Maximum torque per ampere operation," *IEEE Transactions on Industrial Informatics*, vol. 9, no. 4, pp. 1912–1921, Nov 2013.
- [29] P. Karamanakos, T. Geyer, and R. Kennel, "A computationally efficient model predictive control strategy for linear systems with integer inputs," *IEEE Transactions on Control Systems Technology*, vol. 24, no. 4, pp. 1463–1471, July 2016.
- [30] E. Liegmann, P. Karamanakos, T. Geyer, T. Mouton, and R. Kennel, "Long-horizon direct model predictive control with active balancing of the neutral point potential," in *2017 IEEE International Symposium on Predictive Control of Electrical Drives and Power Electronics (PRECEDE)*, Sept 2017, pp. 89–94.
- [31] Y. Wang, N. Niimura, and R. D. Lorenz, "Real-time parameter identification and integration on deadbeat-direct torque and flux control (db-dtfc) without inducing additional torque ripple," *IEEE Transactions on Industry Applications*, vol. 52, no. 4, pp. 3104–3114, July 2016.
- [32] M. S. Rafaq, F. Mwasilu, J. Kim, H. H. Choi, and J. Jung, "Online parameter identification for model-based sensorless control of interior permanent magnet synchronous machine," *IEEE Transactions on Power Electronics*, vol. 32, no. 6, pp. 4631–4643, June 2017.
- [33] Y. Yang, S. Tan, and S. Y. R. Hui, "Adaptive reference model predictive control with improved performance for voltage-source inverters," *IEEE Transactions on Control Systems Technology*, vol. 26, no. 2, pp. 724–731, March 2018.
- [34] W. Chen, J. Yang, L. Guo, and S. Li, "Disturbance-observer-based control and related methods—an overview," *IEEE Transactions on Industrial Electronics*, vol. 63, no. 2, pp. 1083–1095, Feb 2016.
- [35] J. Wang, F. Wang, Z. Zhang, S. Li, and J. Rodríguez, "Design and implementation of disturbance compensation-based enhanced robust finite control set predictive torque control for induction motor systems," *IEEE Transactions on Industrial Informatics*, vol. 13, no. 5, pp. 2645–2656, Oct 2017.
- [36] L. Xiaoquan, L. Heyun, and H. Junlin, "Load disturbance observer-based control method for sensorless pmsm drive," *IET Electric Power Applications*, vol. 10, no. 8, pp. 735–743, 2016.
- [37] Y. B. Zbede, S. M. Gadoue, and D. J. Atkinson, "Model predictive mras estimator for sensorless induction motor drives," *IEEE Transactions on Industrial Electronics*, vol. 63, no. 6, pp. 3511–3521, June 2016.
- [38] M. Abdelrahem, C. M. Hackl, and R. Kennel, "Finite position set-phase locked loop for sensorless control of direct-driven permanent-magnet synchronous generators," *IEEE Transactions on Power Electronics*, vol. 33, no. 4, pp. 3097–3105, April 2018.

- [39] S. A. Davari and J. Rodriguez, "Predictive direct voltage control of induction motor with mechanical model consideration for sensorless applications," *IEEE Journal of Emerging and Selected Topics in Power Electronics*, vol. 6, no. 4, pp. 1990–2000, Dec 2018.
- [40] F. Wang, S. Li, X. Mei, W. Xie, J. Rodríguez, and R. M. Kennel, "Model-based predictive direct control strategies for electrical drives: An experimental evaluation of ptc and pcc methods," *IEEE Transactions on Industrial Informatics*, vol. 11, no. 3, pp. 671–681, June 2015.
- [41] F. Wang, X. Mei, P. Tao, R. Kennel, and J. Rodriguez, "Predictive field-oriented control for electric drives," *Chinese Journal of Electrical Engineering*, vol. 3, no. 1, pp. 73–78, 2017.
- [42] J. Holtz, "Sensorless control of induction motor drives," *Proceedings of the IEEE*, vol. 90, no. 8, pp. 1359–1394, Aug 2002.
- [43] Z. Ma, J. Gao, and R. Kennel, "Fpga implementation of a hybrid sensorless control of smpmsm in the whole speed range," *IEEE Transactions on Industrial Informatics*, vol. 9, no. 3, pp. 1253–1261, Aug 2013.
- [44] W. Xie, F. Wang, X. Wang, G. Dajaku, D. Gerling, and R. Kennel, "Analysis of high efficiency and low cost drive system of ipmsm by using two-steps model predictive torque control," in *Proceedings of the 32nd Chinese Control Conference*, July 2013, pp. 4114–4119.
- [45] C. Wang, J. Xia, and Y. Sun, *Modern Control Technology for Electric Machines*. Beijing: China Machine Press, 2009.
- [46] B. K. Bose, *Power Electronics and Variable Speed Drives*. IEEE Press, 1997.
- [47] J. Kang and S. Sul, "New direct torque control of induction motor for minimum torque ripple and constant switching frequency," *IEEE Transactions on Industry Applications*, vol. 35, no. 5, pp. 1076–1082, Sept 1999.
- [48] E. F. Camacho and C. Bordons, *Model Predictive Control (Advanced Textbooks in Control and Signal Processing)*. 2nd ed. Springer, February 2008.
- [49] G. E. Moore, "Cramming more components onto integrated circuits," *Proceedings of the IEEE*, vol. 86, no. 1, pp. 82–85, Jan 1998.
- [50] P. Cortes, J. Rodriguez, C. Silva, and A. Flores, "Delay compensation in model predictive current control of a three-phase inverter," *IEEE Transactions on Industrial Electronics*, vol. 59, no. 2, pp. 1323–1325, Feb 2012.
- [51] J. Holtz and S. Stadtfeldt, "A predictive controller for the stator current vector of ac machines fed from a switched voltage source," *Proc. IEEE IPEC*, vol. 2, 1983.
- [52] R. Kennel and D. Schöder, "A predictive control strategy for converters," *Proc. IFAC Control Power Electron. Elect. Drives*, 1983.
- [53] P. Cortes, M. P. Kazmierkowski, R. M. Kennel, D. E. Quevedo, and J. Rodriguez, "Predictive control in power electronics and drives," *IEEE Transactions on Industrial Electronics*, vol. 55, no. 12, pp. 4312–4324, Dec 2008.

- [54] F. Wang, X. Mei, J. Rodriguez, and R. Kennel, "Model predictive control for electrical drive systems-an overview," *CES Transactions on Electrical Machines and Systems*, vol. 1, no. 3, pp. 219–230, September 2017.
- [55] P. Stolze, P. Karamanakos, M. Tomlinson, R. Kennel, T. Mouton, and S. Manias, "Heuristic variable switching point predictive current control for the three-level neutral point clamped inverter," in *2013 IEEE International Symposium on Sensorless Control for Electrical Drives and Predictive Control of Electrical Drives and Power Electronics (SLED/PRECEDE)*, Oct 2013, pp. 1–8.
- [56] M. Preindl and S. Bolognani, "Model predictive direct speed control with finite control set of pmsm drive systems," *IEEE Transactions on Power Electronics*, vol. 28, no. 2, pp. 1007–1015, Feb 2013.
- [57] T. Geyer, G. Papafotiou, and M. Morari, "Model predictive direct torque control—part i: Concept, algorithm, and analysis," *IEEE Transactions on Industrial Electronics*, vol. 56, no. 6, pp. 1894–1905, June 2009.
- [58] E. F. Camacho and C. Bordons, *Model-Based Predictive Control of Electric Drives*. Germany: Cuvillier Verlag Göttingen, 2010.
- [59] D. W. Clarke, "Generalized predictive control: A robust self-tuning algorithm," in *1987 American Control Conference*, June 1987, pp. 990–995.
- [60] —, "Application of generalized predictive control to industrial processes," *IEEE Control Systems Magazine*, vol. 8, no. 2, pp. 49–55, April 1988.
- [61] S. Mariethoz, A. Domahidi, and M. Morari, "Sensorless explicit model predictive control of permanent magnet synchronous motors," in *2009 IEEE International Electric Machines and Drives Conference*, May 2009, pp. 1250–1257.
- [62] J. Rodriguez and P. Cortes, *Predictive Control of Power Converters and Electrical Drives*. Wiley-IEEE Press, 2012.
- [63] Z. Ma, S. Saeidi, and R. Kennel, "Fpga implementation of model predictive control with constant switching frequency for pmsm drives," *IEEE Transactions on Industrial Informatics*, vol. 10, no. 4, pp. 2055–2063, Nov 2014.
- [64] X. Mei, F. Wang, and R. Kennel, "A circular dichotomy-based method for model predictive control with fixed switching frequency for electric drives," in *IECON 2016 - 42nd Annual Conference of the IEEE Industrial Electronics Society*, Oct 2016, pp. 2594–2599.
- [65] X. Mei, F. Wang, A. Xia, Z. Ma, Z. Zhang, and R. Kennel, "Predictive current control of an induction machine by using dichotomy-based method," in *2016 IEEE 8th International Power Electronics and Motion Control Conference (IPEMC-ECCE Asia)*, May 2016, pp. 3368–3373.
- [66] P. Karamanakos, A. Ayad, and R. Kennel, "A variable switching point predictive current control strategy for quasi-z-source inverters," *IEEE Transactions on Industry Applications*, vol. 54, no. 2, pp. 1469–1480, March 2018.
- [67] P. Karamanakos, T. Geyer, and R. Kennel, "Reformulation of the long-horizon direct model predictive control problem to reduce the computational effort," in

- 2014 *IEEE Energy Conversion Congress and Exposition (ECCE)*, Sept 2014, pp. 3512–3519.
- [68] P. Karamanakos, T. Geyer, T. Mouton, and R. Kennel, “Computationally efficient sphere decoding for long-horizon direct model predictive control,” in *2016 IEEE Energy Conversion Congress and Exposition (ECCE)*, Sept 2016, pp. 1–8.
- [69] P. Karamanakos, T. Geyer, and R. Kennel, “Constrained long-horizon direct model predictive control for power electronics,” in *2016 IEEE Energy Conversion Congress and Exposition (ECCE)*, Sept 2016, pp. 1–8.
- [70] S. J. Ovaska and O. Vainio, “Predictive compensation of time-varying computing delay on real-time control systems,” *IEEE Transactions on Control Systems Technology*, vol. 5, no. 5, pp. 523–526, Sept 1997.
- [71] G. Papafotiou, J. Kley, K. G. Papadopoulos, P. Bohren, and M. Morari, “Model predictive direct torque control—part ii: Implementation and experimental evaluation,” *IEEE Transactions on Industrial Electronics*, vol. 56, no. 6, pp. 1906–1915, June 2009.
- [72] J. Rodriguez, R. M. Kennel, J. R. Espinoza, M. Trincado, C. A. Silva, and C. A. Rojas, “High-performance control strategies for electrical drives: An experimental assessment,” *IEEE Transactions on Industrial Electronics*, vol. 59, no. 2, pp. 812–820, Feb 2012.
- [73] J. Rodriguez, J. Pontt, C. A. Silva, P. Correa, P. Lezana, P. Cortes, and U. Ammann, “Predictive current control of a voltage source inverter,” *IEEE Transactions on Industrial Electronics*, vol. 54, no. 1, Feb 2007.
- [74] A. A. Ahmed, J.-S. Kim, and Y. I. Lee, “Model predictive torque control of pmsm for ev drives: A comparative study of finite control set and predictive dead-beat control schemes,” in *2016 Eighteenth International Middle East Power Systems Conference (MEPCON)*, Dec 2016, pp. 156–163.
- [75] I. Şahin and O. Keysan, “A new model predictive torque control strategy with reduced set of prediction vectors,” in *2018 IEEE 12th International Conference on Compatibility, Power Electronics and Power Engineering (CPE-POWERENG 2018)*, April 2018, pp. 1–6.
- [76] X. Mei, F. Wang, and R. Kennel, “Deadbeat boolean logic predictive current control for induction machine without cost function,” in *IECON 2016 - 42nd Annual Conference of the IEEE Industrial Electronics Society*, Oct 2016, pp. 4331–4336.
- [77] Y. Wang, X. Wang, W. Xie, F. Wang, M. Dou, R. M. Kennel, R. D. Lorenz, and D. Gerling, “Deadbeat model-predictive torque control with discrete space-vector modulation for pmsm drives,” *IEEE Transactions on Industrial Electronics*, vol. 64, no. 5, pp. 3537–3547, May 2017.
- [78] S. Li, J. Yang, W. Chen, and X. Chen, *Disturbance Observer-Based Control: Methods and Applications*. CRC Press, 1997.
- [79] Z. Kai, K. Yong, X. Jian, and C. Jian, “Deadbeat control of pwm inverter with repetitive disturbance prediction,” in *APEC '99. Fourteenth Annual Applied*

- Power Electronics Conference and Exposition. 1999 Conference Proceedings (Cat. No.99CH36285)*, vol. 2, March 1999, pp. 1026–1031 vol.2.
- [80] P. Mattavelli, “An improved deadbeat control for ups using disturbance observers,” *IEEE Transactions on Industrial Electronics*, vol. 52, no. 1, pp. 206–212, Feb 2005.
- [81] P. M. Meshram and R. G. Kanojiya, “Tuning of pid controller using ziegler-nichols method for speed control of dc motor,” in *IEEE-International Conference On Advances In Engineering, Science And Management (ICAESM - 2012)*, March 2012, pp. 117–122.
- [82] S. A. Bhatti, S. A. Malik, and A. Daraz, “Comparison of p-i and i-p controller by using ziegler-nichols tuning method for speed control of dc motor,” in *2016 International Conference on Intelligent Systems Engineering (ICISE)*, Jan 2016, pp. 330–334.
- [83] E. K. Anto, J. A. Asumadu, and P. Y. Okyere, “Pid control for improving p amp; amp;o-mppt performance of a grid-connected solar pv system with ziegler-nichols tuning method,” in *2016 IEEE 11th Conference on Industrial Electronics and Applications (ICIEA)*, June 2016, pp. 1847–1852.
- [84] H. Du, X. Hu, C. Ma, and G. Zhang, “Numerical pi tuning method and its application in aircraft pitch control,” in *2017 12th IEEE Conference on Industrial Electronics and Applications (ICIEA)*, June 2017, pp. 1270–1274.
- [85] S. Li, J. Yang, W. Chen, and X. Chen, “Generalized extended state observer based control for systems with mismatched uncertainties,” *IEEE Transactions on Industrial Electronics*, vol. 59, no. 12, pp. 4792–4802, Dec 2012.
- [86] X. Mei, X. Lu, A. Davari, E. A. Jarchlo, F. Wang, and R. Kennel, “Torque disturbance observer based model predictive control for electric drives,” in *2018 9th Annual Power Electronics, Drives Systems and Technologies Conference (PEDSTC)*, Feb 2018, pp. 499–504.
- [87] J. Yang, W. Chen, S. Li, L. Guo, and Y. Yan, “Disturbance/uncertainty estimation and attenuation techniques in pmsm drives—a survey,” *IEEE Transactions on Industrial Electronics*, vol. 64, no. 4, pp. 3273–3285, April 2017.
- [88] J. B. Y. G. P. Liu and J. F. Whidborne, *Multiobjective Optimisation and Control*. Baldock, England: Research Studies Press Ltd., 2003.
- [89] P. Cortes, S. Kouro, B. L. Rocca, R. Vargas, J. Rodriguez, J. I. Leon, S. Vazquez, and L. G. Franquelo, “Guidelines for weighting factors design in model predictive control of power converters and drives,” in *2009 IEEE International Conference on Industrial Technology*, Feb 2009, pp. 1–7.
- [90] A. G. Bartsch, G. H. Negri, M. S. M. Cavalca, J. de Oliveira, and A. Nied, “Cost function tuning methodology for fcs-mpc applied to pmsm drives,” in *2017 Brazilian Power Electronics Conference (COBEP)*, Nov 2017, pp. 1–6.
- [91] T. Geyer, “Algebraic tuning guidelines for model predictive torque and flux control,” *IEEE Transactions on Industry Applications*, vol. 54, no. 5, pp. 4464–4475, Sept 2018.

- [92] S. Thielemans, T. J. Vyncke, and J. Melkebeek, "Weight factor selection for model-based predictive control of a four-level flying-capacitor inverter," *IET Power Electronics*, vol. 5, no. 3, pp. 323–333, March 2012.
- [93] M. N. GAE, J. Rodriguez, Z. Zhang, F. W. GAE, C. Garcia, and R. K. GAE, "A very simple strategy for high quality performance of ac machines using model predictive control," *IEEE Transactions on Power Electronics*, pp. 1–1, 2018.